MASSES AND PROPERTIES OF EXTRASOLAR PLANETS

A THESIS SUBMITTED TO THE GRADUATE DIVISION OF THE
UNIVERSITY OF HAWAI‘I AT MĀNOA IN PARTIAL FULFILLMENT
OF THE REQUIREMENTS FOR THE DEGREE OF

DOCTOR OF PHILOSOPHY

IN

ASTRONOMY

MAY 2018

By

Evan Sinukoff

Thesis Committee:

Andrew W. Howard, Chairperson
Christoph Baranec
Michael C. Liu
Jessica R. Lu
G. Jeffrey Taylor

Keywords: astronomy, exoplanets

ACKNOWLEDGMENTS

E.J.S. thanks all members of his thesis committee for their guidance over the course of his graduate school career. Thank you to members of the California Planet Search: Erik Petigura, BJ Fulton, Howard Isaacson, Lea Hirsch, Lauren Weiss, Ian Crossfield, Molly Kosiarek and Sarah Blunt. Thank you to the K2 collaboration: David Ciardi, Jessie Christiansen, Courtney Dressing, Joshua Schlieder, Justin Crepp, Erica Gonzales, John Livingston, Michael Werner, Michael Endl, William Cochran, Thomas Greene, Heather Knutson, Sebastien Lepine, and Leslie Rogers. Thank you to John Brewer and Eric Lopez for helpful analysis and discussions. We acknowledge R. Paul Butler and S. S. Vogt for many years of contributing to the Keck/HIRES data presented here. Some of the data presented here were determined directly from observations at the W. M. Keck Observatory, which is operated as a scientific partnership among the California Institute of Technology, the University of California, and NASA. We are grateful to the time assignment committees of the University of Hawaii, the University of California, the California Institute of Technology, and NASA for their generous allocations of observing time that enabled these projects. E. J. S. acknowledges that this material is based upon work supported by the Natural Sciences and Engineering Research Council of Canada (NSERC). We gratefully acknowledge the efforts and dedication of the Keck Observatory staff, especially Scott Dahm, Greg Doppman, Hien Tran, Grant Hill, and Josh Walawender for support of HIRES and Greg Wirth for support of remote observing. The authors wish to recognize and acknowledge the very significant cultural role and reverence that the summit of Maunakea has always had within the indigenous Hawaiʻian community. We are most fortunate to have the opportunity to conduct observations from this mountain. Finally, E.J.S. thanks his family, friends, and Jaclyn for their love and support.

ABSTRACT

NASA's Kepler Mission revealed that the majority of planets orbiting close to Sun-like stars are between the size of Earth and Neptune. Yet these "super-Earths" and "sub-Neptunes" are absent from our Solar System. The distributions of planet properties measured by *Kepler* — radii and orbital periods — have been precisely measured, but we do not yet have a good understanding of their masses and bulk compositions, which can ultimately be linked to their origins. Follow-up measurements of the masses of a few dozen *Kepler* planets demonstrated that planets smaller than ~ 1.5 Earth-radii are predominantly rocky, while larger planets typically have gaseous envelopes. Measurements of mass and radius do not provide a one-to-one relationship, indicating that compositions might depend on environmental parameters like temperature, and properties of the host star. Building on this, we leverage NASA's *K2* mission to identify and measure the masses of dozens more small planets orbiting bright stars. After nearly doubling the number of small planets with measured densities, and precisely characterizing each host star, we re-examined the distribution of planet bulk compositions, the transition from rocky to gas-dominated planets, and their dependencies on temperature and host star properties. Planet core mass is correlated with host star metallicity, suggesting that the availability of solids affects planet composition. There are two distinct planet populations — "super-Earths" consisting of 1–2 $R_\oplus$ cores with little to no gas, and larger "sub-Neptunes" with H/He envelopes comprising $\gtrsim 1\%$ of their total mass. The gap between these populations appears devoid of sub-Neptunes with the most tenuous atmospheres ($<1\%$ H/He), indicating that such planets experience complete photoevaporation.

TABLE OF CONTENTS

LIST OF TABLES

LIST OF FIGURES

CHAPTER 1
INTRODUCTION AND MOTIVATION

Our understanding of planet formation has grown via an explosion of exoplanet discoveries over the past few decades. Before the first exoplanets were confirmed (Mayor & Queloz, 1995), theories of planet formation had to explain just the planets in the Solar System, often grouped into three general classes: Cold gas giants (Jupiter, Saturn), ice giants (Uranus, Neptune), and rocky terrestrial planets (Mercury, Venus, Earth, Mars). However, the first detected exoplanet orbiting a Sun-like star was a hot, Jupiter-size planet orbiting 51 Pegasi, providing the first evidence that nature produces planets with a more diverse range of properties than those found in our Solar System. This new class of "hot Jupiter" planets was just the tip of the iceberg.

1.1 Lessons from Kepler

NASA's *Kepler* mission (2009–2013) discovered thousands of exoplanets transiting their host stars, enabling the first detailed study of planet demographics.

1.1.1 An abundance of small planets

Kepler revealed a surprising abundance of planets between the size of Earth and Neptune (hereafter "small" planets), which are absent from our Solar System. Approximately half of Sun-like stars have at least one small planet with an orbital period $P < 100$ days (Howard et al., 2012; Fressin et al., 2013; Petigura et al., 2013a). The large population of sub-Neptune-size planets orbiting close to their host stars poses fundamental challenges for planet formational theory. Small planets might form in-situ like the terrestrial planets in our Solar system, but this requires protoplanetary disks with surface densities several times that of the Minimum Mass Solar Nebula (MMSN) (Chiang & Laughlin, 2013; Hansen & Murray, 2013). Alternatively, these planets could have migrated inwards from several AU, where more material is available and ices speed the assembly of cores (Ida & Lin, 2010; Alibert et al., 2011; Rogers et al., 2011). Migration might occur via interactions with the protoplanetary disk ("Type-I" or "Type-II" migration, Terquem & Papaloizou, 2007; Ida & Lin, 2010), gravitational scattering (Kennedy & Kenyon, 2008; Ida & Lin, 2010), shepherding by giant planets (Tanaka & Ida, 1999; Mandell et al., 2007; Raymond et al., 2008), or Kozai oscillations (Rice, 2015). In any migration scenario, material from the outer disk—either planetary building blocks or whole planets—must be transported to sub-AU distances, but not fall onto the star. Of course, small planets might be a mix of both in-situ and migrated populations.

1.1.2 Planet compositions in the *Kepler* era

While the radius and orbital period distributions of small planets are well constrained from *Kepler*, our knowledge of their compositions — one of the best links to their formation histories — has been limited by a combination of observational challenges and measurement degeneracies. Compositions are often inferred from bulk densities, which combine radius and mass measurements. Masses can be measured from transit timing variations (TTVs), but this requires multiple transiting planets and the signals are typically weak unless the planets are close to orbital resonance (e.g. Carter et al., 2012; Hadden & Lithwick, 2017). In contrast, Doppler (radial velocity) measurements can probe planet masses in a diverse range of system architectures. However, only a small fraction of *Kepler* planet hosts are bright enough for RV follow-up. The study of bulk compositions of small planets is further complicated by degeneracies between mass, radius, and composition. For example, relative amounts of core rock, iron, and water can be traded with the H/He envelope mass fraction without changing mass or radius.

By the end of the prime *Kepler* mission in 2013, only a few dozen small planets had precisely measured masses. Even from this small population, compositional trends emerged, offering clues about the processes of planet formation. Figure 1.1 shows a mass-radius and density-radius diagram from Weiss & Marcy (2014) of all small planets whose mass and radius had been measured either by RVs or TTVs. While there are no well-characterized exoplanets smaller than Earth, the inner planets of the Solar System are all primarily rocky. At the other extreme, planets larger than Neptune (4 $R_\oplus$) have low densities consistent with H/He envelopes; there are no examples of rocky planets this large. In the 1–4 $R_\oplus$ domain, the mass-radius landscape is more complicated and poorly understood. Somewhere between $\sim$1.5 and 2.0 $R_\oplus$, planet density peaks and begins to drop with increasing radius, which has been interpreted as a transition point for atmospheric accretion (Weiss & Marcy, 2014; Marcy et al., 2014a,b).

There is significant scatter about the mean mass-radius relation, indicating compositional diversity, even for a fixed planet radius (e.g. Weiss & Marcy, 2014; Wolfgang & Lopez, 2015; Wolfgang et al., 2016). For example, Kepler-138d, a "fluffy", $\sim$ 1.3 g cm^{-3} planet, which seems to be an exception to the otherwise rocky population of planets smaller than $\sim$1.5 $R_\oplus$. The noticeable diversity raised many important questions: To what extent is the mass-radius relation influenced by environmental factors such as temperature? Does composition correlate with the overall system architecture or properties of the host star?

1.1.3 The Importance of Photoevaporation

There is growing evidence that the mass-radius relation is sculpted by the photoevaporation of planetary envelopes driven by incident stellar radiation at X-ray and EUV wavelengths. Such high-energy radiation is capable of heating a planet's upper atmosphere via ionization of atomic hydrogen (Hunten, 1982), which can produce hydrodynamic winds that drive significant mass loss

(Kasting & Pollack, 1983). The majority of envelope erosion is expected to occur during the first 100 Myr, when the star is most active at these high energies (Ribas et al., 2005) and the planet is still cooling and contracting (Lopez et al., 2012).

The rate of photoevaporative erosion strongly depends on planet composition, which makes it possible to break the degeneracies between mass, radius, and composition by studying the flux dependence of the mass-radius relation. For example, the susceptability of a planet to photoevaporation depends on the mass of its core and the chemical consitituents of its envelope. Massive cores have a stronger hold on their surrounding gas, making them more resistent to photoevaporation at a given level of incident flux. Moreover, H/He will be lost much more readily than heavier atmospheric constituents like water. The compositional dependency of this evolution is steepened by the fact that radii of low-mass planets are particularly sensitive to their H/He content (Fortney et al., 2013; Valencia et al., 2013). Therefore, if most small planets are solid cores surrounded by H/He envelopes, signatures of photoevaporation should be prominent in the mass-radius-temperature distribution.

Over the past few years, several observational signatures of photoevaporation have been discovered, suggesting that most small planets are rocky cores surrounded by varying amounts of H/He while water-dominated worlds are rare or non-existent. These signatures are outlined in the next three subsections:

1.1.4 Ultra-short-period Planets

The vast majority of known planets with orbital periods < 1 day, known as ultra-short-period (USP) planets, are smaller than $2R_\oplus$ (Sanchis-Ojeda et al., 2013). This suggests that they are remnant cores of planets stripped of any H/He they might have acquired during formation. If these planets formed with water-rich envelopes, a large fraction of them would not be eroded, leaving a significant population of USPs larger than $2R_\oplus$, which is at odds with observations (Lopez, 2017).

It has been argued that even some close-in giant planets can lose their entire envelopes via Roche lobe overflow (RLO) and become bare cores (e.g. Valsecchi et al., 2014, 2015; Jackson et al., 2016). However, the metallicity distribution of USP planets agrees with that of small planets on 1–10-day orbits, but not hot-Jupiters (Winn et al., 2017). This suggests the that the majority of USPs are more likely to be the remnants of photoevaporated Neptune- or sub-Neptune-size planets than cores of hot-Jupiters that experienced RLO.

1.1.5 The Sub-Neptune Desert

Supporting the claim that USPs are remnants of photoevaporation, there is a paucity of $\sim$ 2–4 $R_\oplus$ planets with $S_{\rm inc} \gtrsim 1000$, often referred to as the "sub-Neptune desert" (Mazeh et al., 2016; Lundkvist et al., 2016). While there are distinct populations of such highly irradiated planets with $R_P < 2\ R_\oplus$ and $R_P > 4\ R_\oplus$, intermediate-size planets are relatively rare at such temperature extremes, although not completely non-existent (Berger et al., 2018). This feature has been interpreted as a “photoevaporation desert”, in which hot planets that formed with modest H/He envelopes were completely stripped to their cores, shrinking to $< 2\ R_\oplus$ (Lopez, 2017). Consistent with the photoevaporation hypothesis, Fulton & Petigura (2018) find that the desert extends to lower $S_{\rm inc}$ for stars of lower mass, which emit a larger fraction of their total radiation in the X-ray and EUV.

1.1.6 The Planet Radius Valley

Another crucial clue that photoevaporation significantly influences the mass-radius relation is the discovery of gap in the planet radius distribution at 1.5–2.0 $R_\oplus$. By collecting spectra of 1300 *Kepler* planet hosts, the California Kepler Survey (CKS Petigura et al., 2017b; Johnson et al., 2017) shrunk the typical *Kepler* stellar radius uncertainties from $\sim$ 25–40% to 10%, revealing finer details of the planet radius distribution. Fulton et al. (2017) discovered a bimodal planet radius distribution with peaks at $\sim 1.2\ R_\oplus$ and $2.5\ R_\oplus$ and a valley between 1.5–2.0 $R_\oplus$. This valley divides the population of small planets into “super-Earths” comprised of bare cores, and “sub-Neptunes”, which contain low-density gaseous envelopes. Fulton & Petigura (2018) further improved the *Kepler* stellar radii by incorporating stellar parallaxes from Gaia and confirmed that the valley is not devoid of planets.

Numerical simulations by several studies had predicted that this radius valley should arise from the photoevaporation of H/He envelopes (Owen & Wu, 2013; Lopez & Fortney, 2014; Jin et al., 2014; Chen & Rogers, 2016; Lopez, 2017). After the valley was observed, Owen & Wu (2017) constructed a simple analytical model of photoevaporation to demonstrate it naturally produces one population of bare cores and a second population at twice the typical radius, where H/He envelopes comprise a few percent of the planet mass. This bifurcation occurs because planets are least susceptible to photoevaporation when the core radius is half of the total planet radius ($R_{\rm core} = 0.5R_P$). At lower envelope fractions ($R_{\rm core} > 0.5R_P$), the radius is minimally sensitive to changes in mass and so the photoevaporation cross-section remains constant as the envelope erodes until it is completely lost. At the other extreme, if the planet forms with $R_{\rm core} < 0.5R_P$, the radius (and therefore the irradiation cross-section) grows more quickly per addition of H/He mass, increasing the rate of photoevaporation. The end result is that puffier planets quickly shrink to twice the size of their core ($f_{\rm env} \approx 1\%$), while planets that form with modest envelopes ($f_{\rm env} \lesssim 1\%$) are rapidly stripped to their cores.

Alternative explanations to the photoevaporation hypothesis include the erosion of lighter envelopes driven by luminosities of cooling planet cores (Ginzburg et al., 2018). However, Fulton & Petigura (2018) observed that the sub-Neptune population shifts to higher bolometric incident fluxes for stars of higher mass, which emit a smaller fraction of radiation at the X-ray and EUV energies, consistent with photoevaporation.

1.1.7 The diversity of small planet cores

Much can be learned about planet formation by measuring the distribution of planet core masses and its dependence on host star properties. For example, it has been firmly established that metal-rich stars are more likely to host Jovian-mass planets (Gonzalez, 1997; Reid, 2002; Santos et al., 2004; Fischer & Valenti, 2005), which remains the best evidence that giant planets form by core accretion.

One way to constrain the distribution of core masses and compositions of small planets is to subject different simulated populations to a photoevaporation model and see which populations produce a radius distribution most consistent with observations. Using this approach, Owen & Wu (2017) argued that the specific location of the planet radius valley indicates that the majority of small planets have $\sim 3\ M_\oplus$ cores with Earth-like compositions ($\sim$ 30% iron, 70% rock by mass). However, Wu (2018) claim that the methodology of Owen & Wu (2017) was sensitive to the pipeline completeness corrections of Fulton et al. (2017). To circumnavigate this issue, Wu (2018) generated synthetic populations of observed planet radii by applying completeness corrections to their model predictions. They found that the super-Earth population has a typical core mass of $\sim$8 $M_\oplus$ with compositions likely similar to Earth.

It is important to consider that the typical core mass might change as a function of stellar properties such as mass and metallicity. Fulton & Petigura (2018) found that the radius valley shifts to larger radii with increasing stellar mass, suggesting that smaller planet cores form around smaller stars. However, they note that smaller stars tend to be metal-poor, so it could be a metallicity effect. The link between the properties and occurrence of small planet and stellar metallicity has been widely debated (Buchhave et al., 2012, 2014; Schlaufman, 2015). While the overall correlation between the radius of small planets and stellar metallicity is weak at best, the occurrence of small planets at short orbital periods does depend on metallicity. Petigura et al. (2018) found that the occurrence of planets $< 1.7 R_\oplus$ at $P < 10$ days increases with host star metallicity. For planets 1.7–$4 R_\oplus$, this correlation extends out to $P \sim 50$ days.

For small planets, the dependence between planet mass and stellar metallicity has been investigated much less extensively than the radius-metallicity relationship due to a limited sample of small planet masses. However, in principle, a mass-metallicity assessment would be more conclusive. In a universe where the core mass of small planets strongly correlates with stellar metallicity, the correlation between radius and metallicity would likely be more subtle because the radius of planet cores grows slowly with increasing mass — as ${M_P}^{1/4}$ after accounting for compression. Moreover, correlations between radius and metallicity could be influenced by differences in irradiation and photoevaporative effects around stars of different masses (and thus metallicities). Therefore, the lack of a strong radius-metallicity correlation does not preclude a strong mass-metallicity correlation.

In this work, I estimate the distribution of core masses and compositions of small planets directly from measurements of their masses. I present evidence that the masses of planet cores are dictated by stellar metallicity more than stellar mass.

1.2 From Kepler to K2

In 2013, the loss of a second reaction wheel on the *Kepler* telescope motivated a repurposing of the Kepler mission into a new mission called *K2*. Since February 2014, the two-reaction-wheel *Kepler* telescope has pointed at 19 different fields ("campaigns") spread along the ecliptic, each for 75 days. Despite the substantial pointing drift of the telescope, clever reduction pipelines have achieved photometric precision comparable to the prime *Kepler* Mission. Thanks to these efforts, hundreds of transiting planets have been discovered in the *K2* photometry, most of which are Earth- to Neptune-size (Vanderburg et al., 2015; Sinukoff et al., 2016; Crossfield et al., 2016).

Since *K2* covers significantly more sky than *Kepler*, it surveys more bright stars, which are amenable to RV follow-up. As high-precision RV measurements of the brightest and quietest planet hosts in the *Kepler* field had already been made, *K2* presented a new opportunity to measure the masses of small planets. To this end, I joined a collaborative effort to detect and precisely characterize *K2* planets. Our team has found hundreds of planet candidates, most of which we validated through spectroscopy and AO imaging. These observations yielded a fresh supply of bright planet hosts. I played a lead role in planning and conducting Doppler observations of more than 50 *K2* stars, nearly doubling the number of small planets with measured masses. Armed with a larger statistical sample, one can probe the transition from rocky to gaseous planets and its dependence on other parameters like temperature and the nature of the host star.

1.3 Plan

This thesis comprises four previously published papers on which I am first author, as well as one paper in preparation. Chapter 2 is a reproduction of Sinukoff et al. (2013), which reviews of planet formation and outlines prospects of detecting and characterizing planets smaller than Earth. Chapter 3 is a reproduction of Sinukoff et al. (2016). There, I present a catalog of 11 multiplanet systems from *K2* and quantify the *K2* planet "multiplicity boost" — the reduction in the false positive probability of a planet candidate by virtue of it being in a multi-planet system. I also report the first of many *K2* planet mass measurements. The masses and properties of seven additional *K2* planets are highlighted Chapters 4 and 5, which are reproductions of Sinukoff et al. (2017a) and Sinukoff et al. (2017b) respectively. In Chapter 6, I construct a catalog of $\sim$ 150 planets spanning 1–8 $R_\oplus$, constituting nearly all such planets with measured masses, and re-derive planet masses and radii using a precise and homogeneous catalog of host star properties. I use this catalog to answer key questions about the compositions of small planets at short orbital periods. I constrain the diversity of planet cores and discover a positive correlation between the core masses

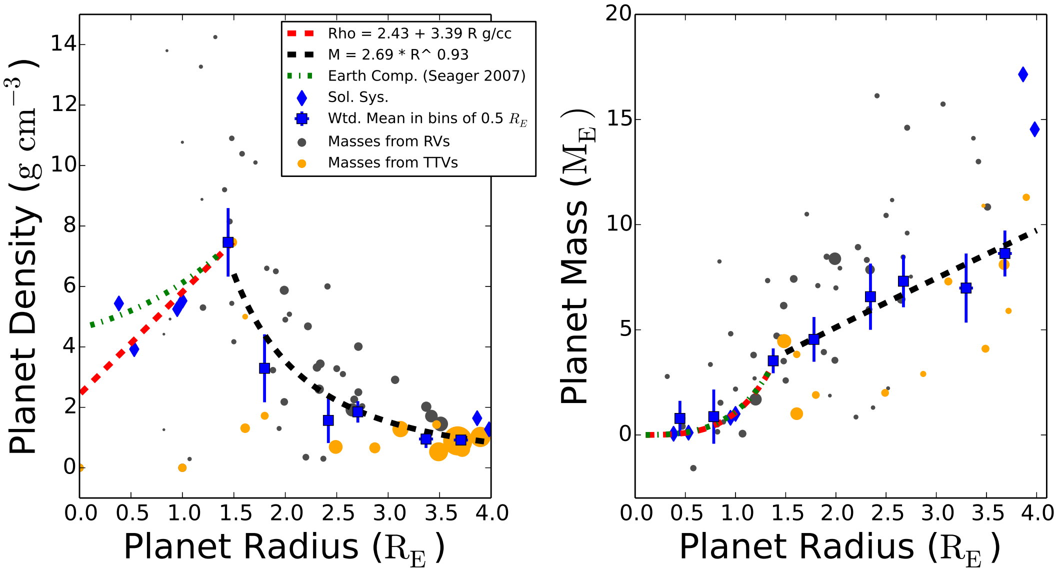

Figure 1.1: Copy of Figure 2 from Weiss & Marcy (2014). Updated versions of these plots are shown in Chapter 6.

of small planets and the metallicities of their host stars. The updated density-radius relation is characterized by two distinct populations — "super-Earths" consisting of 1–2 $R_\oplus$ cores with little to no gas, and "sub-Neptunes" with H/He envelopes comprising $\gtrsim 1\%$ of their total mass. The gap between these populations is where cores with <1% H/He would reside, indicating that such planets are quickly stripped of their envelopes by photoevaporation. This supports the leading interpretation of the observed planet radius valley.

CHAPTER 2
BELOW ONE EARTH: THE DETECTION, FORMATION, AND PROPERTIES OF SUBTERRESTRIAL WORLDS

This chapter is a reproduction of Sinukoff et al. (2013).

2.1 Uncovering the Sub-Earth Realm

The detection of Earth-size planets around other stars has long been a goal of astronomy. The *Kepler* space mission has discovered many such candidates (Borucki et al., 2011; Batalha et al., 2013), some of which are confirmed, and seeks to determine the fraction of solar-type stars that harbor Earth-size planets in their habitable zones (Borucki et al., 2010). While it is human nature to search for analogs of our home planet, the distribution of objects in our Solar System extends well below one Earth mass, i.e. Mars, Mercury, the "dwarf planets" Pluto and Ceres, and large planetary satellites such as Titan and Ganymede. However, the sub-Earth realm remains largely unexplored around other stars due to the limits of present detection methods. Like Mars, Europa and Titan, sub-Earth-mass objects in other planetary systems may prove to be of astrobiological interest.

For the purposes of this paper, we define sub-Earths or subterrestrial exoplanets (hereafter STEPs) as planets with radius $R_p < 0.95\ R_\oplus$. For a rocky planet this corresponds to a mass $M_p < 0.82\ M_\oplus$. Under this definition, a Venus twin ($0.95\ R_\oplus$, $0.82\ M_\oplus$) is not a STEP, while analogs to Mercury ($0.38\ R_\oplus$, $0.055\ M_\oplus$) and Mars ($0.53\ R_\oplus$, $0.11\ M_\oplus$) are[1]. Throughout this paper, we will refer to mass and radius interchangeably. Conceivably, planets might exist that have a radius smaller than 0.95 but a mass exceeding that of Earth (e.g. an "iron planet"), but we assume a single mass-radius relation appropriate for an Earth-like composition (i.e., Valencia et al., 2007, see §2.6 for more on expected STEP properties).

One of the first exoplanets discovered was the $0.02\ M_\oplus$ pulsar planet PSR B1257+12A (Wolszczan, 1994), however the *Kepler* mission is the primary source of STEP discoveries: As of April 2013, *Kepler* has discovered 7 STEPs and 36 candidates. Table 2.1 lists the parameters of all reported candidate and confirmed STEPs. Figure 3.4 plots the planets' radii R_p and orbital periods P. We include all confirmed and candidate planets with $R_p + \sigma_{R_p} < 1\ R_\oplus$, where σ_{R_p} is the uncertainty in radius.

STEPs may be very abundant. The distribution of planets rises steeply with both decreasing mass and decreasing radius down to $3\ R_\oplus$ (Howard et al., 2010b, 2012) but appears to be flat from $3\ R_\oplus$ to $1\ R_\oplus$, the completeness limit of *Kepler* (Fressin et al., 2013). A data pipeline sensitive to planets as small as $0.5\ R_\oplus$ suggests that the *Kepler* planet size distribution for $P =$ 5.0–10.8 days

---

[1] We discuss large satellites of exoplanets, or "exomoons" in §2.4.3.

either remains flat or increases below 1 $R_\oplus$ (Petigura et al., 2013b). Although the detection rate in this region of parameter space is <50%, these findings indicate that STEPs are relatively common.

STEPs occupy diverse environments. Three STEPs orbit the M dwarf Kepler-42 (Muirhead et al., 2012b). Kepler-20e is part of a five-planet system that includes three gas giants and an Earth-size planet (Fressin et al., 2012). Contrary to the configuration of the Solar System, the two smallest planets of Kepler-20 orbit amongst the giants. KOIs 55.01 and 55.02 orbit within 0.008 AU of a B subdwarf and have day side temperatures exceeding 8000 K, allowing *Kepler* to detect their thermal emission at visible wavelengths (Charpinet et al., 2011). They somehow survived or avoided engulfment by the star during its red giant phase. An object transiting *Kepler* star KIC 12557548 every 15.7 hr is thought to be a disintegrating Mercury-size planet surrounded by a cloud of dust (Rappaport et al., 2012).

STEPs are part of the complete picture of planet formation and evolution. Although planet formation is thought to be a stochastic process, statistical quantities and occurrence patterns, e.g. mass distribution or metallicity correlation, presumably reflect underlying processes common to all systems. Any planet formation theory is incomplete if it cannot account for such trends in the sub-Earth population. Historically, the study of exoplanets in previously unexplored regions of parameter space has provoked new ideas: The discovery of "hot Jupiters" (Mayor & Queloz, 1995) led to proposals for orbital migration (Lin et al., 1996), that of "super-Earths" (Rivera et al., 2005) kindled interest in volatile-rich "ocean planets" (Kuchner, 2003; Léger et al., 2004), and the hot rocky planet CoRoT-7b (Queloz et al., 2009) stimulated the concept of "lava planets" (Léger et al., 2011) and "Chthonian" planets, the remnant cores of evaporated gas giants (Hébrard et al., 2004). STEPS should likewise expand our appreciation for — and demand the explanation of — the diverse outcomes of planet formation.

In this review, we address the capability of both the *Kepler* space mission (§2.2) and ground-based Doppler observations (§2.3) to detect STEPs. In §2.4 we consider the original (pulsar timing) and one future (microlensing) method by which STEPs can be detected, as well as the potential for discovery of exomoons. In §2.5 we discuss the predictions of planet formation theory, and in §2.6 we speculate on the properties of STEPs and how they might be established by follow-up observations. We summarize our conclusions and recommend future studies in §5.4.

2.2 Detection of Sub-Earths by *Kepler*

Since most of the currently known sub-Earth planet candidates were discovered by *Kepler*, it is useful to study the sensitivity of *Kepler* observations to such planets. This will provide an estimate of the number of stars in the *Kepler* sample around which the mission could detect transiting sub-Earth planets as well as identify those stars most suitable for such a search.

The *Kepler* spacecraft was launched in 2009 with the primary goal of discovering an Earth-size exoplanet in the habitable zone of a solar-type star (Borucki et al., 2010; Koch et al., 2010).

Table 2.1: Confirmed and Candidate Sub-Earths (STEPs)[a]

Name	R_p ($R_\oplus$)	M_p ($M_\oplus$)[a]	Period (d)	Method	Reference[b]
Confirmed planets					
Kepler-20e [c]	0.87	0.59	6.10	transit	F12
Kepler-37b	0.30	0.01	13.37	transit	BA13
Kepler-37c	0.74	0.32	21.30	transit	BA13
Kepler-42b	0.78	0.39	1.21	transit	M12
Kepler-42c	0.73	0.30	0.45	transit	M12
Kepler-42d	0.57	0.12	1.87	transit	M12
Kepler-62c	0.54	0.10	12.44	transit	BO13
PSR B1257+12 A	0.36	0.02	25.27	pulsar	W94
Candidate planets[d]					
KIC 12557548b[e]	0.38	0.03	0.65	transit	R12
KOI 55.01[e]	0.76	0.35	0.24	transit	C11
KOI 55.02[e]	0.87	0.59	0.34	transit	C11
KOI 82.04	0.70	0.26	7.07	transit	NEA13
KOI 82.05	0.52	0.08	5.29	transit	NEA13
KOI 251.02	0.82	0.47	5.77	transit	NEA13
KOI 283.02	0.84	0.51	25.52	transit	NEA13
KOI 321.02	0.84	0.51	4.62	transit	NEA13
KOI 430.02	0.77	0.37	9.34	transit	NEA13
KOI 568.02	0.74	0.32	2.36	transit	NEA13
KOI 605.02	0.61	0.15	5.07	transit	NEA13
KOI 672.03	0.55	0.10	0.57	transit	NEA13
KOI 952.05	0.86	0.56	0.74	transit	NEA13
KOI 1499.02	0.66	0.20	0.84	transit	NEA13
KOI 1612.01	0.78	0.39	2.47	transit	NEA13
KOI 1618.01	0.77	0.37	2.36	transit	NEA13
KOI 1619.01	0.80	0.43	20.67	transit	NEA13
KOI 1692.02	0.84	0.51	2.46	transit	NEA13
KOI 1964.01	0.73	0.30	2.23	transit	NEA13
KOI 1977.02	0.69	0.24	7.42	transit	NEA13
KOI 2006.01	0.88	0.61	3.27	transit	NEA13
KOI 2013.01	0.86	0.56	2.41	transit	NEA13
KOI 2029.02	0.82	0.47	10.06	transit	NEA13
KOI 2059.01	0.80	0.43	6.15	transit	NEA13
KOI 2079.01	0.66	0.20	0.69	transit	NEA13
KOI 2169.04	0.50	0.07	2.19	transit	NEA13
KOI 2247.01	0.89	0.64	4.46	transit	NEA13
KOI 2421.01	0.72	0.29	2.27	transit	NEA13
KOI 2426.01	0.79	0.41	4.16	transit	NEA13
KOI 2527.01	0.57	0.12	1.39	transit	NEA13
KOI 2657.01	0.60	0.14	5.22	transit	NEA13
KOI 2693.01	0.70	0.26	4.08	transit	NEA13
KOI 2693.03	0.66	0.20	6.83	transit	NEA13
KOI 2792.01	0.61	0.15	2.13	transit	NEA13
KOI 2838.02	0.61	0.15	4.77	transit	NEA13
KOI 3083.03	0.59	0.13	8.29	transit	NEA13
UCF-1.01	0.66	0.20	1.37	transit	S12
UCF-1.02	0.65	0.19	—	transit	S12

---

[a] Assuming $M/M_\oplus = (R/R_\oplus)^{3.817}$ appropriate for an Earth-like composition (Valencia et al., 2007).

[b] BA13: Barclay et al. (2013), BO13: Borucki et al. (2013), C11: Charpinet et al. (2011), F12: Fressin et al. (2012), M12: Muirhead et al. (2012b), NEA13: NASA Exoplanet Archive (January 2013), R12: Rappaport et al. (2012), S12: Stevenson et al. (2012), W94: Wolszczan (1994).

[c] *Kepler* detections include Quarters 1-8 observations. We exclude *Kepler* candidates with Multiple Event Statistic (a measure of signal-to-noise) <7, which are statistically unreliable detections (Jenkins et al., 2010). We omit targets that are unclassified in the *Kepler* Input Catalogue (Brown et al., 2011).

[d] Candidate planets have estimated $R_p < 1.0\ R_\oplus$ to within 1σ.

[e] Quoted M_p and R_p are lower limits.

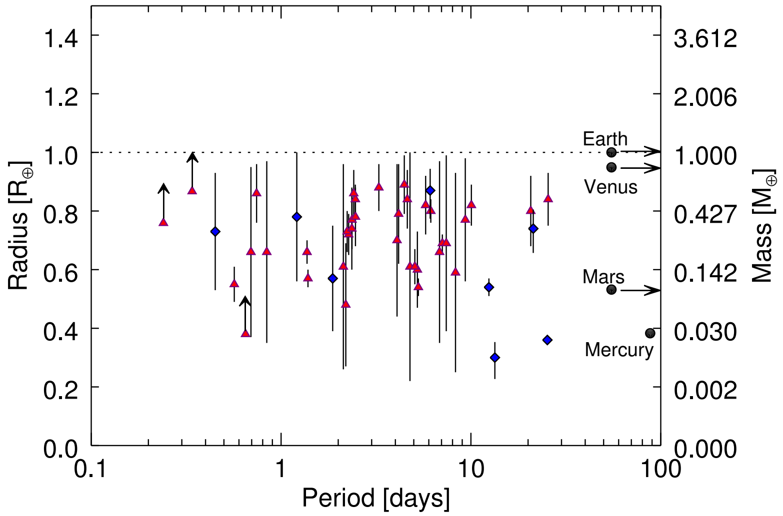

Figure 2.1: Radii and orbital periods of confirmed (blue diamonds) and candidate STEPs (red triangles). The latter, all but one of which are *Kepler* detections, are included only if they have estimated radii at least $1\sigma_{R_p}$ below 1 $R_\oplus$ according to the NASA Exoplanet Archive. The void near 1 $R_\oplus$ is a result of this criterion. Where uncertainties are unavailable, we include $R < 1\ R_\oplus$. We equate radii and mass using a relation for low-mass rocky planets with negligible water content (Valencia et al., 2007).

As of January 2013, the *Kepler* mission has discovered 105 bona fide planets and more than 2700 planetary candidates using the transit detection method, i.e. by detecting the decrease in flux as the planet passes in front of its host star. Most candidates are likely to be planets (Colón et al., 2012; Morton, 2012; Fressin et al., 2013), but the stars are either too faint or the planets too small to be confirmed by the radial velocity method (§2.3). The unsurpassed precision of *Kepler* photometry and the fact that the transit method is sensitive to the cross-section ($\propto R_p^2$) of the planet, not its mass ($\propto R_p^4$, Valencia et al., 2007) makes *Kepler* our most powerful tool for detecting STEPs.

2.2.1 Direct transit detection

We assess the ability of *Kepler* to directly detect STEPs via transits of their host stars. The transit signal is proportional to $(R_p/R_*)^2$, where R_* is the radius of the star. At a given detection limit for a transit signal, smaller planets can be found around smaller stars. For example, a 0.5 $R_\oplus$ planet produces a signal of ~20 parts per million (ppm) if it transits a G5 dwarf, but ~50 ppm if it transits an M2 dwarf. All else being equal, late-type M dwarf stars should be more desirable targets for searches for STEPs. We first consider the fraction of sub-Earths that would be detected around the planet-hosting *Kepler* M dwarfs characterized by Muirhead et al. (2012a) (hereafter M12). These stars have radii and masses inferred from a comparison of spectrocopically-determined effective temperatures $T_{\rm eff}$ and metallicities with stellar evolution models. These allow us to convert a detection threshold into equivalent planet radii. Furthermore, these stars are likely to host additional planets (Wright et al., 2009; Lissauer et al., 2011b), and these planets are also likely to transit because of orbital coplanarity (Sanchis-Ojeda et al., 2012; Hirano et al., 2012).

The radius of the smallest detectable planet R_p with an orbital period P observed for a time $t_{\rm obs}$ is:

$$R_p = R_* \sqrt{\left(\frac{P}{t_{\rm obs}}\right)^{1/2} \mathrm{S/N} \cdot \mathrm{CDPP}_d}, \tag{2.1}$$

where the threshhold signal to noise S/N for detection is 7.1 (Jenkins et al., 2010; Tenenbaum et al., 2012), and CDPP is the effective Combined Differential Photometric Precision over a time interval d (Koch et al., 2010). CDPP_d is a measure of the noise of a light curve within a specified time interval d and is similar to the standard deviation of the photometry binned over that interval.

To determine the sensitivity of the survey to sub-Earth planets around the M12 stars, we first calculate the transit duration (d) for a range of possible planet orbital periods using the stellar masses and radii from M12. To determine CDPP_d we fit a second-order polynomial in $1/\sqrt{d}$ to the $d = 3$, 6, and 12 hour CDPP values of each of the ~168,000 stars observed by *Kepler*. Assuming that every planet transits, and that the observing timespan is equal to the total length of the *Kepler* primary plus extended mission[2] ($t_{\rm obs} = 6.8$ yr), *Kepler* should be able to detect transiting sub-Earth-size planets with periods as long as ~60 days around ~50% of the stars in the M12 catalogue (Fig. 2.2).

Although the transit signal for a given planet size is inversely proportional to the square of the stellar radius, the transit signal-to-noise also depends on the noise due to both intrinsic stellar variability and photometric error (Gilliland et al., 2011). The smallest planets can be detected around the smallest, brightest, and most intrinsically quiet stars. All of the stars in the M12 catalogue are early- to mid-M-type stars: Gilliland et al. (2011) shows that only 7% of M dwarfs, but 76% of G5 dwarfs have $\mathrm{CDPP}_6 < 50$ ppm. In addition, late-type stars are much less luminous and thus under-represented in the magnitude-limited *Kepler* survey.

The results of Gilliland et al. (2011) motivate us to identify the subset of *Kepler* targets that are best suited for detecting transits of sub-Earth-sized objects. These same arguments will also apply to any future space-based transit survey if the photometric precision is limited by stellar variability. Since transit signal-to-noise scales inversely with the product of R_*^2 and CDPP, we define a parameter $D \equiv R_*^2 \mathrm{CDPP}_6$ to identify the most suitable stars for which to search for small planets. We use CDPP_6 as our reference because the corresponding orbital period of a transiting planet is 40 d, within the range considered here. (The other available precision metrics are for 3 hr and 12 hr, corresponding to orbital periods of 5 d and 320 d).

---

[2] The extended mission may be terminated due to the failure of a second reaction wheel on the spacecraft.

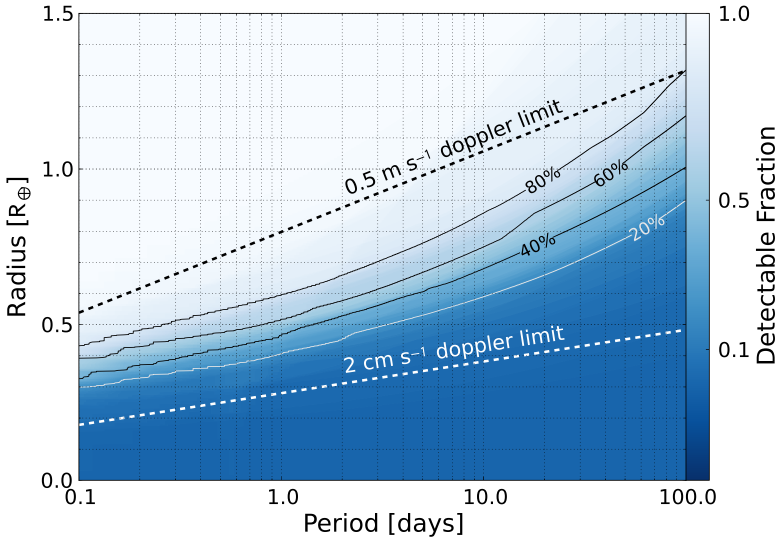

Figure 2.2: Detectable fraction vs. period and planet radius for hypothetical additional planets orbiting planet-hosting stars in the M12 catalogue. All planets are assumed to be on coplanar orbits and transiting. The dashed lines show the best current radial velocity capability (0.5 m s^{-1}) and future radial velocity capability (2 cm s^{-1}) for instruments such as CODEX (see §2.3) assuming the median stellar mass (0.53 $M_\odot$) of the M12 sample and a planet mass-to-radius relation for rocky planets from Valencia et al. (2007). The detectable fraction is defined as the fraction of M12 stars around which a planet of a given radius and period would produce a detectable (7.1 σ) transit signal over the course of the extended *Kepler* mission (6.8 yr, see section 2.1).

Smaller planets can be detected around stars with lower values of D. Figure 2.3 shows the distribution of D for those stars observed by *Kepler*, binned by the $T_{\rm eff}$ reported in the Kepler Input Catalogue (KIC, Brown et al., 2011). The curves are cumulative with $T_{\rm eff}$ from coolest to hottest: the uppermost curve is the total over all $T_{\rm eff}$. These distributions peak near $D \approx 80$ ppm, close to the signal from the single transit of an Earth twin around a solar analog (84 ppm). This means that the signal-to-noise of individual transits of an Earth twin would be ~1 and highlights the challenge of detecting such a planet with *Kepler*. Planets on shorter-period orbits will produce more transits and are more readily detected. About one quarter of all *Kepler* targets have $D < 70$ ppm. Figure 2.3 indicates that no particular spectral type is optimal, although stars with 5450 K $< T_{\rm eff} <$ 5700 K have a D distribution slightly skewed toward lower values. This contrasts with the common perception that M dwarfs are favorable targets because, among *Kepler* stars, M dwarfs are fainter and photometrically noisier. However, the stellar radii of very low-mass stars in the KIC catalogue are systematically too large (Muirhead et al., 2012a; Mann et al., 2012). If the radii were corrected, this would push the distribution of D for the M-dwarfs towards smaller values of D, making them slightly better targets.

In order to estimate the fraction of stars around which sub-Earth-size planets are detectable in the Kepler photometry via transits, we select the 25% (32,721) of stars with the smallest values of D and calculate the percentage of sub-Earth planets that would be detected if each star was orbited by a planet with a given period. We assume isotropically-oriented orbits, such that the transit probability is R_*/a, where a is the semi-major axis, using R_* from the KIC and the scaling relation $M_* \sim R_*^{0.8}$ (Cox & Pilachowski, 2000) to determine a from P. Figure 2.4 shows that *Kepler* should find $\sim$ 1% of planets with $R \sim 1\ R_\oplus$ out to $P \sim 80$ d around these stars. Thirty-six sub-Earths found by *Kepler* orbit at $1 < P < 10$ d where the detection efficiency is ∼5-10% (Fig. 3.4).

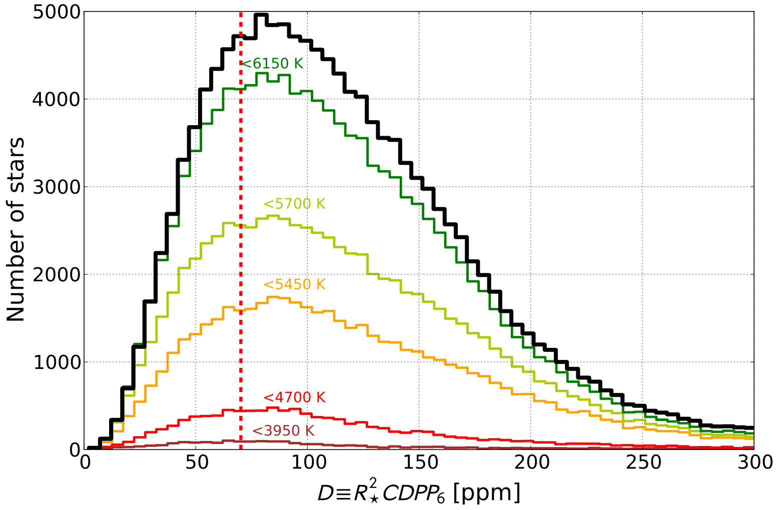

Figure 2.3: Distribution of $D \equiv R_*^2 CDPP_6$ for all ∼168,000 stars observed by *Kepler* in Quarter 10. The colored lines are cumulative bins of stars grouped by $T_{\rm eff}$ and the black line is the distribution of the entire sample. The vertical dashed red line indicates the 25th percentile cut of stars used to produce Fig. 2.4.

2.2.2 Detection by transit timing variations

Additional, non-transiting planets can be detected when mutual gravitational perturbations cause sufficient variation in the ephemeris of the transiting planet (Miralda-Escudé, 2002; Holman & Murray, 2005; Agol et al., 2005). The amplitude of these transit timing variations (TTVs) in the case of an inner transiting planet being perturbed by a longer period companion is (Holman & Murray, 2005):

$$\Delta t \simeq \frac{45\pi}{16}\left(\frac{M_p}{M_*}\right)\frac{P_1\alpha_e^3}{(1-\sqrt{2}\alpha_e^{3/2})^2}, \tag{2.2}$$

where the subscripts 1 and 2 indicate parameters of the transiting and perturbing planet, respectively, P is the orbital period, M_p is the perturbing planet mass, M_* is the mass of the host star,

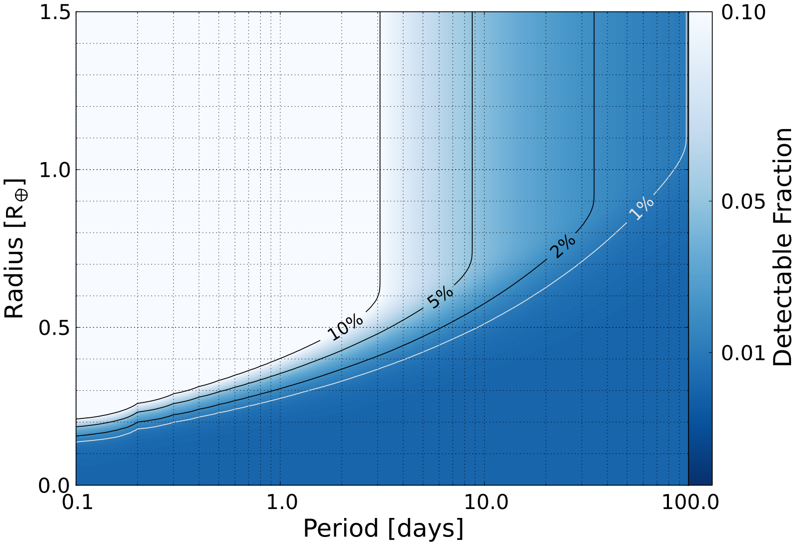

Figure 2.4: Detectable planet fraction vs. period and planet radius of the 25% most detection-favorable *Kepler* targets, i.e. smallest $D \equiv R_*^2 CDPP_6$, accounting for transit probability. The sharp rise of the contours (decrease in detectability) at long periods is a result of the geometric probability of transit being very low for long-period planets. The detectable fraction is defined as the fraction of KIC stars around which a planet of a given radius and period would produce a detectable (7.1 σ) transit signal (see Section 2.1).

$\alpha_e = a_1/[a_2(1-e_2)]$, and e is the eccentricity. Δt depends on the mass of the perturber (not the transiting planet), and sub-Earth-mass perturbers will produce only a very small TTV signal. The amplitude of a TTV signal also depends on the period ratio and orbital eccentricities of the two planets and is maximized when the periods are commensurate. Dynamical simulations show that the maximum TTV signal from an Earth-mass planet will be ~20 s (Holman & Murray, 2005).

Kepler can measure the time of transit center with a precision of ~20 s for the deepest transits of the brightest stars, but for the majority of stars the precision is much worse (Ford et al., 2011). The highest precision that has ever been achieved is ~5 s using the *Hubble* Space Telescope (Brown et al., 2001; Pont et al., 2007), and ground-based observations can achieve precisions of ~60 s (Fulton et al., 2011; Maciejewski et al., 2013). Although *Hubble* may be able to detect TTVs due to sub-Earths, the telescope's short observing window (due to its low Earth orbit) makes it less than ideal for this type of observation. It seems unlikely that TTVs will be a viable method to detect STEPs until the advent of a more capable observatory such as the *James Webb* Space Telescope (JWST).

2.3 Doppler detection

The radial velocity (RV) or Doppler method was used to discover and confirm the first exoplanet around a main-sequence star (Mayor & Queloz, 1995), and is responsible for nearly half of all exoplanet discoveries to date (Schneider et al., 2011). Although this statistic is changing because of the success of transit surveys such as *Kepler*, RV measurements are required to rule out certain false positive scenarios and measure planetary mass. For a circular orbit, RV semi-amplitude K scales as

$$K \approx 64 \frac{M_p \sin i}{M_\oplus} \left(\frac{P}{1 \text{ d}} \right)^{-1/3} \left(\frac{M_*}{M_\odot} \right)^{-2/3} \text{cm s}^{-1}. \tag{2.3}$$

where i is the orbital inclination of the planet with respect to the plane of the sky. As of January 2013, the smallest reported signal is 51 cm s^{-1} from a planet with a minimum mass of 1.3 $M_\oplus$ on a 3.2 d orbit around α Cen B (Dumusque et al., 2012, but see Hatzes (2013)). This detection was made by the High Accuracy Radial velocity Planet Searcher (HARPS) instrument installed on the ESO La Silla 3.6 m telescope in Chile, which represents the state of the art in operational spectrographs. Other instruments achieve an RV stability in the 1–3 m s^{-1} range (Table 2.2). This performance falls well short of what is needed to detect Earths or sub-Earths with $P \gg 1$ d around solar-type stars, but leaves open the possibility of discovering or confirming "hot" STEPs on extremely close orbits ($P \sim 1$ d) around M dwarfs (Fig. 2.2).

Detection of STEPs at larger orbital distances will require greatly improved sensitivity: A 0.5 $M_\oplus$ planet on a 10 d orbit around a $0.53 M_\odot$ star produces a maximum Doppler signal of ~ 22 cm s^{-1}, or roughly half that of the current best precision reported by HARPS. The same planet with the same orbit around a solar-type star would produce a Doppler signal of only ~ 14 cm s^{-1}. Although this precision is beyond the abilities of current instruments, there are already plans in place to improve the performance of existing instruments, such as HARPS, and to build new instruments which will achieve the precision needed to detect STEPs. In order to do this, new instruments must overcome both instrumental and stellar noise. The solutions come from multiple approaches, and we address each below.

Spectrographs mounted directly on telescopes experience flexure, pressure variations, and temperature variations that produce systematic errors. These effects can be minimized by placing the instrument in a temperature-stabilized dewar fed by a fiber from the telescope, as is done with HARPS (Lovis et al., 2006). Imaging a star directly onto a spectrograph slit engenders noise from guiding errors and changes in the point spread function (PSF) (Valenti et al., 1995; Endl et al., 2000). These issues can be partially addressed by high-cadence pointing corrections, but a more elegant solution is to stabilize the PSF by transmitting the light to the instrument by a fiber (e.g., Spronck et al., 2012; Bouchy et al., 2013). Isolating and finely controlling the environment of the instrument is necessary to maintain both short-term (single observation) and long-term (survey-spanning) instrumental precision.

Another source of error is the wavelength calibrator against which Doppler shifts are measured. A molecular iodine gas absorption cell, placed in the beamline, provides a forest of fiducial absorption lines at $\lambda < 650$ nm (Butler et al., 1996). While iodine works well for observations of solar-type stars, which have significant signal at blue wavelengths, it becomes a limiting factor for Doppler observations of M dwarfs, which have peak emission at redder ($\lambda > 800$ nm) wavelengths. An alternative gas is ammonia, which has a large number of lines in the K (2.2 μm) band (Reiners et al., 2010). An ammonia gas cell is used with the CRyogenic high-resolution InfraRed Echelle Spectrograph (CRIRES) at the ESO Very Large Telescope (VLT) for radial velocity searches for planets around M dwarfs (Bean et al., 2010).

There are also alternatives to gas absorption cells. The HARPS spectrograph uses the emission lines from a thorium-argon lamp, but such lamps also have fewer lines in the near infrared and the light from the lamp does not follow the exact same path as that from the star. A laser frequency "comb" combined with an etalon interferometer can create a uniform ladder of equally bright emission lines across a selectable wavelength range. Steinmetz et al. (2008) suggest that, with more development, laser combs should permit RV measurements with a precision of $\sim$1 cm s^{-1}.

The ultimate limit to the Doppler method is intrinsic stellar noise or "jitter" from granulation, oscillations, plages, and star spots. One strategy is to average over these noise terms. Dumusque et al. (2011) conclude that a scheme where three 10-minute spectra are obtained 2 hours apart on each of 10 nights per month yields the best radial velocity precision and minimizes problems from stellar variability.

Forthcoming instruments will take advantage of these technologies and strategies (Table 2.2). HARPS-North, installed on the Telescopio Nazionale Galileo (TNG) on La Palma Island in the Canary Islands (Cosentino et al., 2012), is based on the design of the original HARPS instrument but will use a laser comb to achieve a precision of $\sim$10 cm s^{-1} (Li et al., 2012). The Echelle SPectrograph for Rocky Exoplanet and Stable Spectroscopic Observations (ESPRESSO) on the ESO VLT is expected to reach an RV precision of at least 10 cm s^{-1}, with a goal of a few cm s^{-1} (Pepe et al., 2010). The design specifications of CODEX, planned for the European Extremely Large Telescope, call for $<$2 cm s^{-1} RV precision (Pasquini et al., 2010). If there is an equivalent suppression in the effect of stellar "jitter", such instruments should be able to find STEPs orbiting close ($P < 10$ d) to nearby bright stars (Fig. 2.2). However, estmating the yield of a survey is difficult because of the lack of data on stellar noise at such precision, and thus any empirical means to construct a suitable target catalog of Doppler "quiet" stars. However, should an instrument such as CODEX achieve ~ 2 cm s^{-1} precision it could, in principle, detect Mars-size planets with $P < 100$ d (Fig. 2.2).

Table 2.2: Current and Future Spectrographs for Radial Velocity Measurements.

Instrument	Precision (cm s^{-1})	First Light	λ (μm)	Resolution	Reference
Keck-HiRES	100	1996	0.3–1.0	85,000	Butler et al. (1996)
UCLES	300	1998	0.48–0.86	45,000	Butler et al. (2001)
HDS	300	2000	0.35–0.65	150,000	Kambe et al. (2008)
HARPS	50	2003	0.38–0.69	115,000	Rupprecht et al. (2004)
SOPHIE	200	2006	0.38–0.69	75,000	Bouchy et al. (2013)
CHRONIS	70[a]	2011	0.45–0.89	120,000	Schwab et al. (2012)
HARPS-N	50[a]	2012	0.38–0.69	115,000	Cosentino et al. (2012)
APF-Levy	∼200[a]	2013[b]	0.3–0.65	73,000	Radovan et al. (2010)
APF-HWS	∼100[a]	2014	0.38–0.69	100,000	A. Howard, priv. comm.
ESPRESSO	∼10[a]	2016	0.35–0.72	150,000	Pepe et al. (2010)
CODEX	∼2[a]	2025	0.37–0.72	150,000	Pasquini et al. (2010)

---

[a] Expected performance

[b] In commissioning phase

2.4 Other Detection Techniques and Sub-Earth Objects

2.4.1 Pulsar planets

Since the discovery of the three planets of pulsar PSR1257+12, including one of lunar mass, searches of several dozen other millisecond pulars have revealed no other systems of similar ilk (Wolszczan, 2012). Pulsar PSR1719-1328 has a single substellar ($\sim$2–3 M_J) companion on a 2.2 hr orbit (Bailes et al., 2011), but this may be the degenerate helium or carbon/oxygen remnant of a former "donor star" (van Haaften et al., 2012). Given the exquisite timing stability of millisecond pulsars, the lack of additional discoveries cannot be an artifact of sensitivity. Miller & Hamilton (2001) propose that the scarcity of planets around millisecond pulsars can be explained in terms of the "recycling" hypothesis where accretion of matter from a donor star spins up the pulsar and makes it emit extremely stable, detectable radio signals. Such accretion produces an X-ray luminosity sufficient to vaporize any planets, and Miller & Hamilton (2001) argue that PSR1257+12 must be a rare example of a high primordial spin. Even more problematic is developing a plausible mechanism for the formation of the planets, either via survival of the supernova explosion that created the neutron star, by accretion from the disk resulting from the disruption of a companion or supernova fallback, or by capture from a main-sequence star (Sigurdsson, 1993). We refer the reader to the review by Phillips & Thorsett (1994) and references therein, as well as the revisit by Hansen et al. (2009) to this issue. Although additional pulsar planets may be uncovered in the future, their rarity means that they will not significantly contribute to the catalog of known sub-Earths.

2.4.2 Microlensing

A small planet can also be detected by "microlensing", i.e. as its host star passes very close to the line of sight between an observer and a more distant star (Mao & Paczynski, 1991). The effect of the planet is to break the radial symmetry of the gravitational lens and produce a distinctive, hours-long deviation from the symmetric days-long amplification in the light curve of the background star. Microlensing events are rare and this technique requires simultaneous monitoring of millions of distant stars, e.g. in the Galactic Bulge.

The method is most sensitive to planets with semi-major axes of a few AU, i.e. the angular Einstein radius projected to the typical distance of a lens. Sensitivity to small planets is ultimately limited by the angular size of the background star compared to the Einstein radius of the planet. In principle, monitoring of giant stars in the Bulge permits the detection of planets as low as 1 $M_\oplus$ (Bennett & Rhie, 1996), but because of limited observing cadence and sensitivity, the smallest planet detected to date has a mass of a few Earths (Kubas et al., 2012). Routine detection of Earth-size planets will require a second generation of ground-based microlensing surveys (Wright & Gaudi, 2012).

For dwarf stars at the distance of the Bulge, the theoretical detection limit is a few lunar masses. However, these stars will be very faint ($V > 20$), and the projected surface density of such stars towards the Bulge is several per square arc-second. Therefore, a dedicated space telescope that can achieve diffraction-limited, high photometric precision observations is required (Bennett & Rhie, 2002; Bennett, 2008). Such aspirations may eventually be realized in the form of the *Euclid* mission (Penny et al., 2012), the Wide Field InfraRed Space Telescope (WFIRST) (Barry et al., 2011) mission, or the NEW-WFIRST mission (Dressler et al., 2012), which should be capable of detecting planets as small as Mars ($\sim$0.1 $M_\oplus$). In particular, two 2.4 m telescopes, built by the US National Reconnaissance Office and transfered to NASA offer diffraction limited imaging of 0.16 arc-seconds at $\lambda = 1.6$ μm and might triple the yield of Mars-size planets compared to the design reference mission of WFIRST (Dressler et al., 2012).

2.4.3 Exomoons

Satellites of exoplanets have yet to be discovered but the Copernican idea predicts that the Solar System is not unique in this way. Given that Ganymede, the largest satellite in our Solar System, has only 2.5% of Earth's mass, it seems likely that satellites in other Solar Systems will also be sub-Earth objects. Satellites can accrete from the circumplanetary disks of giant planets, which accrete inflowing gas and solid material from the circumstellar disk. Dynamical simulations suggest that if a satellite grows large enough it will migrate inward and be accreted by its host planet (e.g., Canup & Ward, 2006; Sasaki et al., 2010). Canup & Ward (2006) found that this process restricts the ratio of cumulative satellite mass to planet mass to $\lesssim 10^{-4}$ e.g. ~ 0.1 $M_\oplus$ for a Jupiter-mass planet. This limit depends weakly on model parameters including gas surface density, abundance of solids, inflow timescale and migration efficiency. If the Canup & Ward (2006) model is representative of typical circumplanetary disk accretion, we should not expect satellites formed in-situ around Jupiter-mass planets to greatly exceed the mass of Mars. On the other hand, Ogihara et al. (2012)

added an inner circumplanetary disk cavity to the model of Canup & Ward (2006), and found that, in some cases, inward migration was inhibited. An inner cavity can be caused by magnetic coupling of the planet to the disk, but it is unclear how frequently this occurs.

Not all exomoons would necessarily form in a circumplanetary disk. The irregular orbits of many Solar System satellites indicate that they were acquired by their giant planet hosts through one of several proposed capture mechanisms. Dynamical simulations by Ćuk & Burns (2004) suggest that if a planetesimal encountering a circumplanetary disk experiences sufficient gas drag, capture could occur. Alternatively, binary planetesimals could become separated by the tidal pull of a giant planet resulting in the capture of a single planetesimal. In fact, the inclined retrograde orbit of Neptune's moon Triton might be the result of the latter mechanism (Agnor & Hamilton, 2006). Even if capture events in exoplanet systems are rare, the rate of survival of captured moons might be high. Porter & Grundy (2011) considered the post-capture stability of satellites around non-migrating giant planets in stellar habitable zones and found that about 20–50% of Mars- to Earth-size satellites enter stable orbits. It is conceivable that terrestrial-size planets could also be captured by an inward migrating gas giant. However, simulations are needed to estimate the likelihood of such events as well as the likelihood of long-term orbital stability. As a gas giant moves closer to its host star, its Hill radius shrinks and stability is limited to tighter orbits.

Close encounters between giant planets might commonly eject their satellites: Gong et al. (2013) performed dynamical simulations consisting of three satellite-hosting giant planets, with varying planet mass, planet eccentricity, satellite mass, and satellite semi-major axis. In $\sim$75% of their simulations, planet-planet scattering resulted in the ejection of all satellites. If planet-planet scattering is common among giant planets they are unlikely to retain their primordial satellites. The prospect for satellites around hot Jupiters would be especially grim if the orbits of these planets is a result of strong dynamical interactions.

Moon-size or larger satellites could of course form in the manner of the Moon's proposed origin — from the collision of two (proto)planets. Elser et al. (2011) predict that satellites with $>$0.5 lunar masses form around approximately 1 in 12 rocky planets. The most massive satellite produced in their simulations has three lunar masses.

In principle, *Kepler* can discover massive exomoons in the same manner it finds sub-Earths. An exomoon can transit the host star, adding an additional transit signal differing in phase, amplitude, and duration from that of the planet. Satellites on wide orbits could induce detectable reflex motions in the planet (Kipping et al., 2009), while satellites on close-in orbits are more likely to transit the planet as the planet transits the star. The latter is called a "mutual event" during which the transit signal temporarily *decreases* (Ragozzine & Holman, 2010; Pál, 2012). Satellites with large orbital inclinations relative to their host planet's orbital plane could transit the star even if the planet does not.

Satellites can also be detected by TTVs as well as the transit duration variations (TDVs) that they induce on their planetary hosts. The TTV signal is shifted in phase by $\pi/2$ relative to the TDV signal, allowing it to be distinguished from the effect of another planet (Kipping et al., 2009). Moreover, TTV amplitudes scale differently with satellite mass and orbital distance than TDV amplitudes, and these complementary measures thus provide unique solutions for these two parameters. Mass-dependent TTV and TDV detections can be combined with a (radius-dependent) transit signal to calculate the satellite's bulk density and infer its composition. Kipping et al. (2009) found that, using TTV and TDV measurements alone, *Kepler* may be sensitive to exomoons $\geq 0.2\ M_\oplus$ or about $0.67\ R_\oplus$ for an Earth-like composition. Hence, *Kepler* should be able to detect both the transit (§2.2.1) and the TTV/TDV signals from such a massive exomoon — if they exist.

The Hunt for Exomoons with Kepler (HEK) has identified the most likely hosts of detectable exomoons based on *Kepler* light curves (Kipping et al., 2013). The light curves of selected stars are compared with planet-only or planet-satellite models in a Bayesian analysis. So far, the HEK team has shown that the 7 most likely candidates are unlikely to have moons comparable in mass to their 2–4 $R_\oplus$ planet hosts (Kipping et al., 2013).

2.5 Formation of Subterrestrial Planets

According to canonical theory, rocky planets accrete from a disk of gas and dust that surrounds a protostar. In the first $\sim 10^4$ years, micron-size dust grains coagulate and settle to the disk midplane. However, growth of particles to sizes larger than a few millimeters cannot be observed and is poorly understood. Laboratory experiments indicate that collisions of millimeter-size grains rarely lead to sticking and growth under the assumed dynamical conditions within disks (Blum & Wurm, 2000; Zsom et al., 2010; Weidling et al., 2012). Moreover, the motion of larger (meter-size) bodies decouples from the gas and they experience a headwind and orbital decay into the star (Weidenschilling, 1977a). In theory, meter-size bodies should be lost to the central star in ~100 years (Youdin & Kenyon, 2013). Possible mechanisms by which nature overcomes these growth barriers have been proposed (See Chiang & Youdin, 2010; Morbidelli et al., 2012; Youdin & Kenyon, 2013; Haghighipour, 2013, for reviews). Regardless, bodies large enough (km-size) to be impervious to this effect must form by some mechanism. Once mutual gravitation begins to dominate, larger objects experience runaway growth over $10^5 - 10^6$ years (Morbidelli et al., 2012). Growth of the largest bodies slows down as they accumulate most of the remaining material within a "feeding zone", becoming lunar-to martian-size protoplanets (Chambers, 2006; Kokubo & Ida, 1998, 2000). Once the mass in protoplanets exceeds that of planetesimals, their orbits begin to cross (Kenyon & Bromley, 2006). Chaotic scattering and collisions ensue for ~100 Myr until a few relatively isolated planets remain.

STEPS might emerge from the final stages of planet formation via the same mechanisms proposed for their Earth- and super-Earth-size brethren: (i) as the in-situ products of constructive and destructive collisions and scattering of smaller planetary embryos (Morbidelli et al., 2012; Kennedy

& Kenyon, 2008); (ii) from embryos that have migrated inwards as a result of gravitational torques exerted by the protoplanetary disk ("Type-I migration", Ida & Lin, 2010; Terquem & Papaloizou, 2007; O'Brien et al., 2006), (iii) by gravitational scattering (Ida & Lin, 2010; Kennedy & Kenyon, 2008; Raymond et al., 2008), or (iv) shepherding by inward-migrating giant planets (Zhou et al., 2005; Raymond et al., 2006; Fogg & Nelson, 2007; Mandell et al., 2007) or super-Earths (Kennedy & Kenyon, 2008). A fifth mechanism - evaporation of larger bodies (Valencia et al., 2010), is discussed in §2.6. The rate of Type-I migration of an object is proportional to its mass (Ward, 1997) whereas smaller planets are more susceptible to gravitational scattering and shepherding. For a more detailed review of rocky planet formation see Morbidelli et al. (2012).

Numerical N-body simulations are a popular tool for investigating the late stages of rocky planet formation (Morbidelli et al., 2012). Such simulations consistently produce planets that have masses between those of Mars and Venus over a wide range of orbits (e.g. Walsh et al. (2011); Raymond et al. (2009); Montgomery & Laughlin (2009); Kokubo et al. (2006)). These outcomes are plausible examples of other planetary systems produced by the stochastic nature of the planet formation process, suggesting that most STEPs are unlikely to be of similar mass or occupy similar orbits as Mercury or Mars.

The initial mass surface density of the disk is an important parameter of dynamical models and it may determine planet size. One common choice of initial condition is the Minimum Mass Solar Nebula (MMSN; Weidenschilling, 1977b; Hayashi, 1981). However, the MMSN is not necessarily representative of all disks. For example, Chiang & Laughlin (2013) derive a "Minimum-Mass Extrasolar Nebula" from the population of *Kepler*-detected super-Earths that is $\sim$5 times denser than the MMSN. Figure 2.5 shows the average mass of the largest and second-largest planets that form between 0.5 and 1.5 AU in simulations by Kokubo et al. (2006). The authors varied the mass surface density of the disk at 1 AU (Σ_1) while maintaining a power-law radial surface density profile with index -3/2. The MMSN corresponds to $\Sigma_1 = 7$ g cm^{-2}. The average masses follow power laws with disk surface density having indices close to unity. If low-mass stars have disks of lower surface density, then the results of Kokubo et al. (2006) predict that small planets are most common around M-dwarfs, at least at 0.5–1.5 AU. However, the evidence for a relation between disk surface density and stellar mass is tentative (Williams & Cieza, 2011; Andrews et al., 2013).

The limited supply of disk material and hence the surface density likely governs the in-situ formation of close-in and especially detectable planets. Raymond et al. (2007) show that a MMSN disk rarely forms planets more massive than Mars within $\simeq$0.1 AU of late M-dwarfs. However, Montgomery & Laughlin (2009) find that a disk three times denser than the MMSN instead produces 3-5 planets with an average mass of 0.7–0.8 $M_\oplus$. These results suggest that the formation of STEPs depends on surface density. However, *Kepler* observations show that the occurrence of Earth- to Neptune-size planets does not depend on stellar metallicity, a potential proxy for disk surface density (Buchhave et al., 2012; Mann et al., 2013b).

STEPs may also migrate to close-in orbits after forming at larger orbital distances. Kennedy & Kenyon (2008) conclude that the minimum mass of a planet able to migrate to a short-period orbit is proportional to the distance at which ice condenses in the disk (the "snow line"). This distance scales with stellar luminosity and hence stellar mass. The same study shows that planets also tend to scatter to smaller orbital distance around low-mass stars, again suggesting that low-mass stars might commonly host detectable STEPS. Because (Type I) orbital migration scales with planet mass and mutual gravitational interactions will preferentially scatter less massive planets, we expect scattering to be more efficient than migration in dispersing the orbits of STEPS.

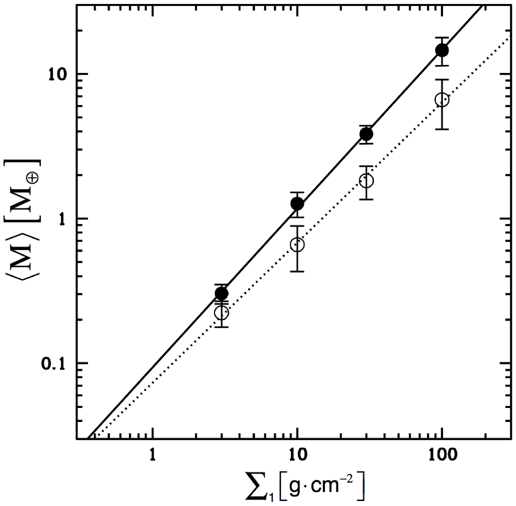

Figure 2.5: Mean masses $\langle M \rangle$ of the largest (filled circles) and second largest (open circles) planets formed in simulations of rocky planet formation as a function of disk surface density (Kokubo et al., 2006). The disk surface density depends on radius as a power-law with index -3/2, and is Σ_1 at 1 AU. Best-fit power law relations between Σ_1 and $\langle M \rangle$ have indices of 1.1 and 0.97 (solid and dashed lines, respectively).

2.6 Properties of Subterrestrial Planets

Although our Solar System lacks objects with radii between that of Mars and Venus, the diversity among smaller bodies (e.g., Ganymede, Titan, Mercury, and Mars) suggests that STEPs might have diverse characteristics depending on composition, distance from the star, and contingencies such as giant impacts. While there are many properties of such bodies that are of interest, we focus on two that may be ascertainable in the near future: mean density, and the presence or absence of an atmosphere.

The mean density $\bar{\rho}$ of a planet can be estimated if both radius and mass are measured (by the transit and Doppler methods, respectively). These can be compared with theoretical mass-radius relations to infer composition (e.g. Valencia et al., 2007; Seager et al., 2007; Grasset et al., 2009;

Rogers & Seager, 2010). Although such interior models have not been applied to STEPs per se, there have been detailed comparisons of similar models with Mercury (Hauck et al., 2013) and Mars (Sohl et al., 2005). Comparison with STEPS will be limited by Doppler precision (discussed in §2.3), sensitivity to planet radius and hence stellar radius ($\geq$3% Torres et al., 2010), and degeneracies between composition and mean density (Rogers & Seager, 2010). Because of these limitations, observations will likely be able to discriminate only between the most extreme compositions, i.e. very volatile-rich, rocky, or metal-rich planets.

Mercury, as the Solar System's smallest and innermost planet, is arguably the most appropriate analog to those sub-Earths that can be detected by the transit (§2.2) and Doppler (§2.3) methods. Mercury's salient bulk properties are a comparatively large iron core comprising most of its volume and mass (Hauck et al., 2013), and a lack of volatiles or substantial atmosphere. Whether its oversized core reflects a non-chondritic composition for the primordial disk close to the Sun (Lewis, 1972; Weidenschilling, 1978; Ebel & Alexander, 2011), or is a consequence of removal of most of the silicate mantle by a giant impact (Benz et al., 1988, 2007; Gladman & Coffey, 2009) is debated. Both of these mechanisms are more effective on orbits closer than Mercury (P = 88 d), where temperatures in a planet-forming disk and the kinetic energy of impacts, which scales with orbital velocity, are higher. This implies that STEPs close to their host stars may have comparatively large cores as well.

Like Mercury, STEPs on close-in orbits are likely to lack any substantial atmosphere because of their weak gravity and heating of their upper atmospheres by stellar X-ray, extreme ultraviolet (EUV) and Lyman-α radiation. Rapid atmospheric escape is predicted for their more massive super-Earth counterparts (Tian, 2009; Pierrehumbert & Gaidos, 2011). In the limit that the thermal speeds of atoms become comparable to escape speeds, hydrodynamic escape ensues and mass loss rate is limited only by the rate at which energy is absorbed by the atmosphere:

$$\dot{M} = \frac{3\epsilon F}{4G\bar{\rho}}, \tag{2.4}$$

where F is the incident flux absorbed by the atmosphere, G is the gravitational constant, and ϵ is an efficiency factor that accounts for the inflation of the atmosphere and radiative, conductive, and evaporative cooling. In this regime, absorption of energy E per unit area results in a loss of atmosphere (in units of pressure) of $E/(4\pi R_p)$. Given realistic models of the evolution of the X-ray and UV output of dwarf stars (Ribas et al., 2005; Sanz-Forcada et al., 2011), a Mercury-size planet on a 10-day orbit around its host star is expected to lose thousands of bars of atmosphere over billions of years.

Hydrodynamic escape will occur from the top of the atmosphere (the exobase) only if it is hot enough and the Jeans parameter $\lambda = GM_p\mu/(R_e k_B T)$, the ratio of the gravitational potential to the thermal energy, is <2.8 (Johnson, 2010), where μ is the atomic mass, R_e is the distance of the exobase from the planet's center, and k_B is the Boltzmann constant. As the thermal energy approaches the escape energy, the atmosphere inflates, $R_e > R_p$, and the escape energy decreases. Approximating this inflation as $R_e \approx R_p + h$, where $h = k_B T R_p^2/(GM_p\mu)$ is the atmospheric scale height, the required exobase temperature is $\sim 0.29 GM_p\mu/(R_p k_B)$. Under all plausible conditions, the light elements H and He will hydrodynamically escape from close-in planets, carrying some heavier elements with them.

A more germane question is whether hydrodynamic escape continues when H and He are exhausted, e.g., by the atomic oxygen produced by dissociation in a CO_2-dominated Venus-like atmosphere. For atomic oxygen on Venus, the required temperature is 3×10^4 K, but only $\sim$5000 K on a planet the size of Mercury. Figure 2.6 plots the $\lambda = 2.8$ condition for planets with CO_2 atmospheres and the expected combination of X-ray, EUV and Lyman-α irradiation (Ribas et al., 2005; Sanz-Forcada et al., 2011) for Sun-like (solid lines) and M0 dwarf (dashed lines) stars at three stellar ages. Hydrodynamic escape ($\lambda < 2.8$) occurs to the lower left of each boundary. These calculations assume that all incident X-ray plus UV (XUV) energy is absorbed at the top of the atmosphere and conducted downward, principally by atomic oxygen, to the homopause, then radiated away in the infrared by CO_2. We follow the procedure in Pierrehumbert & Gaidos (2011), except that by assuming a constant thermal conductivity k, an analytical solution is available for the required irradiation q as a function of λ:

$$q = \frac{GM_p\mu k}{R_p^2 k_b} \ln \frac{\sigma R_p p_0}{\lambda k_B T_0} \left[\ln \frac{GM_p\mu}{\lambda R_p k_B T_0} \right]^{-1}, \tag{2.5}$$

where p_0 and T_0 are the pressure and temperature at the homopause, and σ is the collision cross-section. We calculate the k of atomic O using Dalgarno & Smith (1962), assume a homopause pressure like that of Venus (10^{-3} Pa) and homopause temperature equal to the planet's equilibrium temperature, and adopt $\sigma = 2 \times 10^{-19}$ m^2 (Tully & Johnson, 2001). Equation 2.5 approximately reproduces the Jeans parameter for O on current Venus ($\lambda = 260$) and predicts that it lost atmosphere by hydrodynamic escape prior to 3.5 Ga (if indeed it had a CO_2 atmosphere). It also predicts the hydrodynamic escape of CO_2 from Mars in the past. Mercury would have suffered hydrodynamic escape of any CO_2 atmosphere throughout its history. Any sub-Earth on a closer orbit would have experienced yet greater loss. This is in addition to any removal by the stellar wind (Zendejas et al., 2010) or impacts (Ahrens, 1993).

The presence or absence of a substantial atmosphere might be discernable by follow-up observations, at least if the planet is very close to its star, very hot, and tidally locked. By detecting the infrared emission from the planet and measuring its variation with phase, the redistribution of heat around a synchronously rotating planet can be estimated (e.g., Gaidos & Williams, 2004; Lewis et al., 2010; Cowan & Agol, 2011; Demory et al., 2012). Planets lacking an atmosphere will have no redistribution, their substellar hemispheres will be hotter, and their phase curves more pronounced. Planets with a thick, circulating atmosphere will have cooler illuminated hemispheres because some

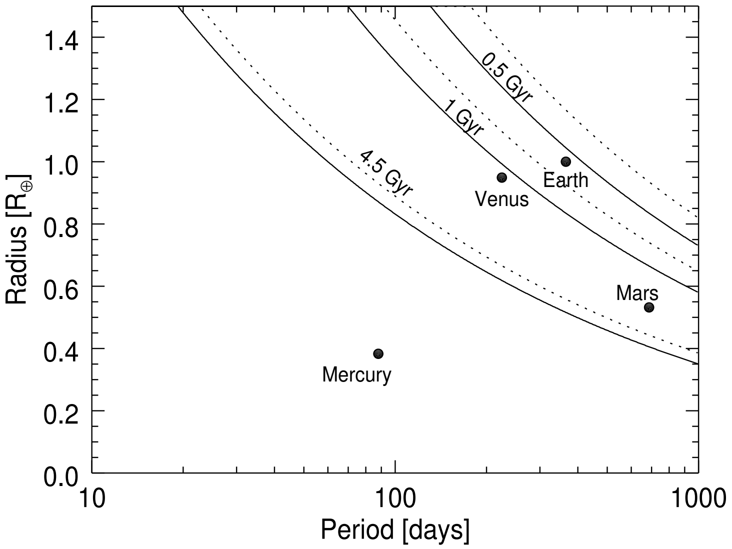

Figure 2.6: Combinations of rocky planet radius and orbital period for which the Jeans parameter λ of a CO_2 atmosphere is 2.8, the condition for hydrodynamic escape. The combined fluxes of stellar X-ray, EUV, and Lyman-α radiation at ages of 0.5, 1, and 4.5 Gyr are used (Ribas et al., 2005; Sanz-Forcada et al., 2011). Solid lines are for a Sun-like star and dashed lines are for an M0 dwarf star host. Atmospheres below and to the left of these lines will have $\lambda < 2.8$ and be hydrodynamically escaping. The inner planets of the Solar System are plotted.

of the heat is transferred to the night side, and their emission will exhibit little or no variation with phase. The boundary between these two regimes has not been theoretically established for planets on close-in orbits but is probably equivalent to a surface pressure of a fraction of a bar. The emission from an unresolved transiting planet can be detected by differencing the signal in and out of secondary eclipse. In exceptional cases, it might be possible to determine the planet's phase curve by measuring the small variation in total flux over a complete orbit.

The most promising (and perhaps only) tool with which to carry out such observations will be JWST using either the Near Infrared Camera (NIRCam) or the Mid Infrared Instrument (MIRI) (Clampin, 2012). Figure 2.7 shows estimated detection thresholds vs. orbital period for sub-Earths orbiting an M0 dwarf star at 10 pc. Breaks in the curves mark transitions between the regimes where one instrument is favored over the other. Two cases are considered: a Venus-like planet with an albedo of 0.9 and efficient heat redistribution (black curves), and a Mercury-like planet with an albedo of 0.068 and no heat redistribution (grey curves). For each case, we calculate a 10σ detection threshold in terms of the minimum angular radius of the planet, i.e. its physical radius at a distance of 10 pc (solid curves). We assume blackbody emission, a 10^4 s integration and the sensitivities from the JWST website[3]. In principle, JWST can detect the thermal emission

---

[3] http://www.stsci.edu/jwst/science/sensitivity/jwst-phot

from very small hot planets. However a more relevant measure of sensitivity is the accuracy with which the stellar signal can be subtracted, i.e. the photometric stability. The dotted curves in Fig. 2.7 correspond to a fractional detection threshold of 10^{-4} relative to the host star. This level of stability has been achieved with the *Spitzer* infrared space telescope (Demory et al., 2012). The two dashed curves are for a hypothetical stability of 10^{-5} (the actual stability will not be known until JWST is in space). It appears that sub-Earths can be detected by JWST only if its stability significantly exceeds that of *Spitzer* and only if the planets lack substantial atmospheres.

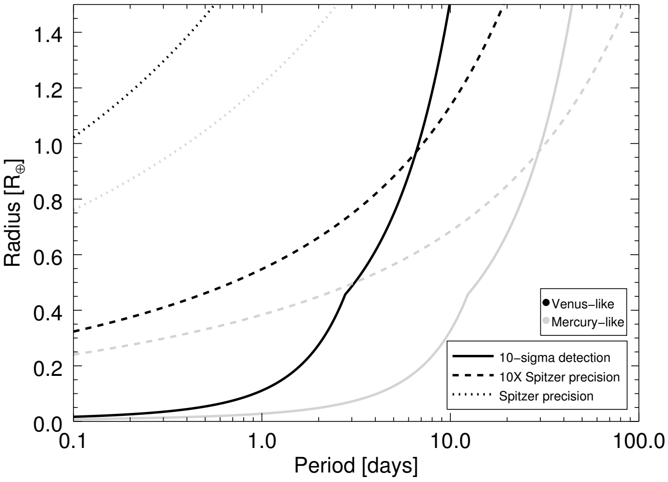

Figure 2.7: Detection by differential photometry of an eclipsing STEP around a M0 dwarf star at 10 pc with the *James Webb* Space Telescope and either MIRI or NIRCam. Two cases are considered: a Venus-like albedo and efficient re-distribution of heat around the planet (black lines), and a Mercury-like albedo, no redistribution of heat, and isotropic emission (grey lines). The solid lines are the 10σ detection of an isolated source, while the dotted and dashed lines are the detection limits if the stellar signal is removed with a photometric accuracy of 10^{-4} (typical of *Spitzer* observations) or 10^{-5}. The actual stability of these instruments will not be known until JWST is launched.

Removal of mass from sub-Earths may not stop with a CO_2 atmosphere. On close-in, tidally-locked planets, substellar surface temperatures are $T \approx 2800(L_*/L_\odot)^{1/4}(P/1\mathrm{d})^{-1/3}$ where L_* is the stellar luminosity and a weak dependence on stellar mass is ignored, and a Mercurian albedo (0.068) is assumed. If temperatures exceed the melting point of silicates, a magma "sea" would be present (Léger et al., 2011), and a tenous silicate vapor (SiO, O, and Si) atmosphere would form (Miguel et al., 2011). Continuous escape of this atmosphere would cause gradual mass loss[4]. Valencia et al. (2010) assumed $\epsilon \approx 0.4$ in Eqn. 2.4 and estimated that the hot "super-Earth" CoRoT-7b ($P = 0.85$ d) may have lost about half of its mass. This phenomenon would occur even more readily on smaller planets. Extreme rates of evaporation and a coma of silicate condensates have been proposed to explain the variable transit depth of whatever object orbits the *Kepler* star 12557548 with a period of 0.65 d (Rappaport et al., 2012).

In this scenario, the silicate mantles of sub-Earths close to solar-type stars may largely evaporate. As evaporation proceeds, the residual mantle, mixed by melting, would become steadily enriched in more refractory, heavier elements. It could eventually founder and/or dissolve into the core, whereupon the object would become an "iron planet", a naked core with a relatively high mean density. Without a comparatively light element such as O, hydrodynamic escape would halt, although the stellar wind might continue to erode an iron vapor atmosphere. This scenario would not unfold around M dwarfs with L_* as low as $10^{-4}L_\odot$; the equilibrium temperatures of sub-Earths around such stars would be up to 10× cooler and they would retain their silicate mantles.

2.7 Discussion

Over the past two decades, successive discoveries enabled by improvements in ground-based instruments and space missions such as *Hubble*, *Spitzer*, CoRoT, and *Kepler* have uncovered brown dwarfs, Jupiter-like gas giants, volatile-rich Neptunes, "super-Earths", and now Earth-size and presumably rocky planets. The discovery and characterization of sub-Earths, planets with masses significantly less than that of Earth, is the next and perhaps ultimate leg of the scientific journey to enumerate the worlds on close-in orbits around main-sequence stars. This step has just begun, but we can already draw the following conclusions:

- Several dozen confirmed or candidate sub-Earths have already been discovered by *Kepler* (plus 3 others by the Arecibo telescope and *Spitzer*). We expect that number to grow as the remaining *Kepler* data is analyzed. Studies of *Kepler* transit light curves may also reveal exomoons, if sufficiently massive ones exist.

---

[4] Cameron (1985) and Fegley & Cameron (1987) proposed that the mantle of Mercury was evaporated, but this is inconsistent with the MESSENGER estimate of volatile radioactive potassium in the Mercurian crust (Peplowski et al., 2011).

- Enumeration of *Kepler* sub-Earths will determine whether the planet distribution with radius remains flat (Fressin et al., 2013), rises, or falls below $\sim 1\ R_\oplus$ (Petigura et al., 2013b). Based on the number of *Kepler* discoveries to date (∼40), and a detection efficiency of 5% among the ∼33,000 most suitable stars (Fig. 2.4), we estimate that at least 2–3% of stars have planets with $0.5\ R_\oplus < R_p < 1\ R_\oplus$ and $P < 10$ d.

- Sub-Earths are at the limit of *Kepler*'s detection threshold and any estimate of their occurrence is sensitive to completeness for very small signals, which is still being determined (Petigura et al., 2013b). Moreover, the estimated radii of transiting planets depend on the radii of the host stars; those of *Kepler* targets are being refined as stellar parameters are measured and improved models are applied (Muirhead et al., 2012a; Mann et al., 2012). As a result, our estimate of 2–3% should be considered very tentative and probably a lower limit.

- With forseeable instruments, only STEPs with orbital periods of a few days will be detectable by Doppler (Fig. 2.2). *Kepler* stars are too faint for observations of such precision, but it is conceivable that a sample of nearby, much brighter stars could be interrogated by the Doppler method and the two populations compared by statistical techniques (e.g., Gaidos et al., 2012). The occurrence of close-in STEPs could be compared with the number of such objects detected on wider orbits by a microlensing mission such as WFIRST or NEW-FIRST. Such a study would investigate whether sub-Earths preferentially form on close-orbits, or are dynamically scattered onto distant orbits by their more massive counterparts.

- Planet formation theory predicts that the surface density of disks influences the size of planets that form in-situ. This linkage may be difficult to reconcile with the apparent independence of small (Earth- to Neptune-size) planet occurrence and host star metallicity, unless migration is common. Determining whether or not these parameters remain independent in the sub-Earth regime, where orbital migration is expected to be less efficient, will help resolve this apparent discrepancy.

- If the mass or surface density of planet-forming disks scales with that of the star, then M dwarfs may preferentially host sub-Earths, boding well for their detection (Fig. 2.2). However, this premise is only weakly supported by the available data and the occurrence of small planets may not depend on stellar mass (Fressin et al., 2013), as was originally thought (Howard et al., 2012). The Atacama Large Millimeter Array (ALMA) will help to clarify any relation between surface density and stellar mass in the context of planet formation. Other millimeter arrays have already yielded masses and surface density profiles of many tens of disks by measuring continuum dust emission, e.g. Isella et al. (2009); Guilloteau et al. (2011). ALMA is expected to increase the yield to hundreds or thousands of disks on account of its order of magnitude better sensitivity and angular resolution (Williams & Cieza, 2011).

- STEPs may be diverse objects with compositions that reflect initial conditions, formation mechanism, and environment. Sub-Earths close to their parent stars may be rich in water and other volatiles if they originated on wider orbits past the "snow line" and subsequently migrated or were scattered inwards. However, stellar XUV heating and winds are expected to remove their atmospheres (Fig. 2.6), and, around solar-type stars, the silicate mantles of these planets may evaporate, leaving bare iron cores. Indeed, some sub-Earths may be the product of evaporation of more massive planets. Observations of nearby transiting sub-Earths by JWST may be able to discriminate between tidally-locked planets lacking atmospheres, which will be hotter and brighter, and those with atmospheres, which will be fainter and perhaps undetectable (Fig. 2.7).

The immediate scientific return from the study of sub-Earths will be tests of models of planet formation and evolution. Descriptions of their occurrence and distributions with mass and orbital period is essential for a complete description of the planetary kingdom, and any over-arching theory must explain them. The possible role of subterrestrial planets as habitats for life should also not be overlooked. Although sub-Earths on very close orbits may not be suitable abodes for life, those further out may orbit in the circumstellar habitable zone and retain atmospheres and water. We who inhabit a comparatively small planet around a "dwarf" star should not presume that one Earth mass is the optimum for life.

CHAPTER 3
ELEVEN MULTI-PLANET SYSTEMS FROM *K2* CAMPAIGNS 1 & 2 AND THE MASSES OF TWO HOT SUPER-EARTHS

This chapter is a reproduction of Sinukoff et al. (2016).

3.1 Introduction

The prime *Kepler* mission (2009–2013) demonstrated that compact, multi-planet systems are common (Howard et al., 2012; Fressin et al., 2013; Petigura et al., 2013a). Of the 4,000+ planet candidates from *Kepler*, roughly 1500 are in systems with multiple candidates (Mullally et al., 2015). Some exceptional systems include the high-multiplicity Kepler-11 (Lissauer et al., 2011a) and Kepler-90 (Schmitt et al., 2014) systems that host six and seven planets, respectively, all within 1 AU. Another noteworthy system is Kepler-36 which hosts two planets with semi-major axes differing by 10% but densities differing by a factor of eight (Carter et al., 2012).

The ensemble properties of *Kepler* multi-planet systems ("multis") have provided key insights into the formation, evolution, and architectures of planetary systems (Lissauer et al., 2011b, 2012, 2014; Rowe et al., 2014). Most of the *Kepler* multis have low ($\lesssim$ 3%) mutual inclinations (Fang & Margot, 2012). Many multi-planet systems are dynamically packed, i.e. adding an additional planet on an intermediate orbit leads to dynamical instability (Fang & Margot, 2013). While the distribution of orbital period ratios of *Kepler* multis is roughly uniform, Fabrycky et al. (2014) observed an excess of planet pairs with orbital period ratios exterior to first order mean motion resonance (MMR) and a deficit of planets lying interior to resonance. This feature may be the outcome of eccentricity damping of resonant planet pairs by the protoplanetary disk (Lithwick & Wu, 2012; Batygin & Morbidelli, 2013).

Systems with multiple transiting planets are particularly valuable because they are a clean sample with nearly zero false positive detections (Lissauer et al., 2012, 2014). This is due to the low probability of having multiple stars with a false positive signals in the same photometric aperture, i. e. eclipsing binaries are distributed sparsely on the sky.

Given the photometric precision and four year baseline of the prime *Kepler* mission, dynamical interactions between pairs of planets are often detected as transit timing variations (TTVs), which can constrain planet properties such as mass and eccentricity (Holman & Murray, 2005; Agol et al., 2005). The analysis of the Kepler-36 system by Carter et al. (2012) demonstrated the power of TTV observations. They measured a mass of $4.45^{+0.33}_{-0.27}$ $M_{\oplus}$ for Kepler-36b, a planet with $R_P = 1.486 \pm 0.035$ $R_{\oplus}$. Currently, Kepler-36b has the best-constrained mass of any exoplanet smaller than 2 $R_{\oplus}$.

The prime *Kepler* mission came to an end in 2013, following the failure of a second reaction wheel. Beginning in March, 2014, NASA began operating the telescope in a new mode called *K2* (Howell et al., 2014). During *K2* operations, the spacecraft observes a different region of the ecliptic plane every ~ 85 d.

Kepler planet catalogs (Borucki et al., 2011; Batalha et al., 2013; Burke et al., 2014; Rowe et al., 2015; Mullally et al., 2015) spawned numerous statistical studies on planet occurrence, the distribution of planet sizes, and the diversity of system architectures. These studies deepened our understanding of planet formation and evolution. Continuing in this pursuit, *K2* planet catalogs will provide a wealth of planets around bright stars that are particularly favorable for studying planet compositions—perhaps the best link to their formation histories.

The first four *K2* campaigns (C0–C3) plus an additional engineering test campaign have yielded over 230 planet candidates at the time of writing [1]. Moreover, ~ 40 of these planet candidates have been either statistically validated as planets at better than 99% confidence or confirmed via radial velocity (RV) or TTV detection, including several noteworthy discoveries. Super-Earth HIP 116454b, discovered in the *K2* engineering test field, orbits a bright K dwarf. Its mass is well-constrained from follow-up RV measurements (Vanderburg et al., 2015). From C1, Crossfield et al. (2015) announced three super-Earths orbiting a nearby M0 dwarf, K2-3. Almenara et al. (2015) and Dai et al. (2016) detected the RV signature of the inner planet, which is consistent with a mostly rocky composition, although the water fraction could be as large as 60%. Foreman-Mackey et al. (2015) discovered two planets of Neptune- and Saturn-size near a 3:2 MMR around K2-19. Armstrong et al. (2015) used TTVs to constrain the mass of the larger outer planet and the masses of both planets were measured by Dai et al. (2016) using RVs. Vanderburg et al. (2016a) reported a third Earth-size planet candidate, K2-19d, at P=2.5 d. The first *K2* planet catalogs have already been assembled; Foreman-Mackey et al. (2015) reported 36 planet candidates, 21 of which were validated at $> 99\%$ confidence by Montet et al. (2015b). These include four validated multi-planet systems (K2-3, K2-5, K2-16, K2-19) and one system, K2-8, with one validated planet and a second planet candidate. More recently, Vanderburg et al. (2016a) presented 234 planet candidates in C0–C3, including 20 systems with multiple planet candidates.

In this paper, we present 11 multi-planet systems with a total of 26 planets detected by our team in *K2* photometry from Campaigns 1 and 2 (C1 and C2). We detected no multi-planet systems in Campaign 0. We adopt a "confirmed" disposition for planet candidates with detected RV or TTV signatures and, following Montet et al. (2015b), a "validated" disposition for planet candidates found to have a false positive probability, FPP $< 1\%$. Under this definition, 13 of the 26 planet candidates are previously confirmed or validated, 11 are newly validated, and two are newly discovered and confirmed. Most importantly, 9 of the 13 newly validated or confirmed planet candidates orbit stars $V \leq 12.5$ mag, amenable to RV follow-up. For one system, K2-38, we obtained radial velocity measurements using Keck/HIRES to constrain planet masses. The remainder of this

---

[1] NASA Exoplanet Archive, UT 28 April 2016, http://exoplanetarchive.ipac.caltech.edu.

paper is organized as follows: In Section 5.2 we describe the photometric detection of multis in *K2* photometry along with follow-up observations that confirm the planets and characterize the their stellar hosts. Section 3.3 details the physical properties of stellar hosts. Section 3.4 outlines our validation of each planet via AO images, archival images, as well as vetting of the light curves and spectra. In Section 3.5, we describe our light curve modeling and present derived planet properties. We present our RV measurements of K2-38 and the derived planet masses in Section 3.6. In Section 3.7, we summarize the most noteworthy characteristics of each system, including additional findings of other studies where relevant. We discuss the likely compositions of the K2-38 planets, summarize the ensemble properties of our planet sample, and compare our results to other studies in Section 5.4. Our RVs, spectra, AO images and contrast curves will be uploaded to the ExoFOP-K2 website[2]. We note that throughout this paper, systems are ordered by EPIC number.

3.2 Detection and Observations of *K2* Multis

3.2.1 *K2* Planet Search Program

During the prime *Kepler* mission, the project office selected nearly all of the stars that were observed. This target list was dominated by a magnitude-limited set of F, G, K, and M dwarfs ($Kp < 16$) from which the major planet catalogs and occurrence analyses were derived. *K2* is entirely community-driven with all targets selected from Guest Observer proposals. Our team has proposed large samples of G, K, and M dwarfs for every *K2* Campaign (to date, Campaigns 0–10). For the G and K dwarfs, our proposed sets of stars are magnitude-limited at $Kp < 13$ or 14 (depending on crowding) and ∼3,500–10,000 stars per Campaign have been selected for *K2* observations. During each *K2* Campaign, the *Kepler* telescope observes the selected stars nearly continuously for ∼75 d.

This catalog of multi-planet systems is based on photometry collected by *K2* during Campaign 1 (2014 May 30–2014 Aug 21) and Campaign 2 (2014 Aug 23–2014 Nov 13). The stars were part of *K2* Guest Observer proposals led by I. Crossfield, R. Sanchis-Ojeda, A. Scholz, A. Sozzetti, P. Robertson, D. Stello, V. Sanchez Bejar, N. Deacon, B.-O. Demory (Campaign 1) and E. Petigura, R. Sanchis-Ojeda, and D. Stello (Campaign 2). We searched for transiting planets in the photometry of all stars observed by *K2*, not just those in the above programs.

3.2.2 *K2* Photometry & Transit Detection

During *K2* observations, solar radiation pressure exerts a torque on the spacecraft that causes the telescope to roll around its boresight. Consequently, stars trace out small arcs of ∼1 pixel every ∼6 hr. As the stars sample different pixel phases, inter-pixel sensitivity variations cause their

---

[2] https://cfop.ipac.caltech.edu/k2/

apparent brightnesses to change. Disentangling stellar variability from spacecraft systematics is non-trivial when working with *K2* data.

We extracted the photometry from the *K2* target pixel files, which are available at the Mikulski Archive for Space Telescopes (MAST)[3]. Our photometric extraction procedure is detailed in Crossfield et al. (2015). In brief, for a given target star we compute raw aperture photometry using a soft-edged circular aperture. For every frame in a *K2* campaign, we solve for the roll angle between the target and an arbitrary reference frame using several hundred stars. We model the time- and roll-dependent variations using a Gaussian process, which are then subtracted from the raw photometry to produce calibrated photometry. This process is repeated for different aperture sizes, and we adopt the aperture size which minimizes photometric noise on three-hour timescales. Specifically, we use the median absolute deviation (MAD) of the three-hour Single Event Statistic (SES) as our noise metric. We define the SES as the depth of a box-shaped dimming relative to the local photometric level. Conceptually, this is similar to the three-hour Combined Differential Photometric Precision (CDPP-3) metric used by the *Kepler* project. We compute a three-hour SES at every long cadence measurement as part of our transit search [4]. This method of aperture selection favors small apertures for faint stars (where background noise dominates) and large apertures for bright targets.

To search the calibrated photometry for planetary transits, we use the `TERRA` algorithm (Petigura et al., 2013a). We have adapted `TERRA` to search for multi-planet systems. When `TERRA` identifies a candidate transit, it flags that star for additional analysis. `TERRA` masks out the transit of the first candidate along with a buffer of ΔT on either side, where ΔT is the transit duration. `TERRA` then repeats the transit search in the masked photometry. This process continues until no transits with signal-to-noise ratio (SNR) > 8 are detected or when the number of iterations exceeds 5.

Table 3.1 lists coordinates, proper motions, and multi-band photometry for the 11 stars around which we detect multiple transiting planets.

3.2.3 AO Imaging

We obtained near-infrared adaptive optics images of the 11 EPIC sources at the W. M. Keck Observatory on the nights of 1 April 2015 UT (K2-8, K2-36, K2-19, K2-35, K2-24, K2-37, K2-32), 7 April 2015 UT (K2-3, K2-5), and 25 July 2015 UT (K2-38) UT, and at Palomar Observatory on the night of 29 May 2015 UT (K2-19). The observations were obtained with the 1024 × 1024 NIRC2 array at Keck Observatory behind the natural guide star AO system and the 1024 × 1024 PHARO array behind the PALM-3000 natural guide star system (Dekany et al., 2013). In all cases, the target star was bright enough to be used as the guide star. NIRC2 has a pixel scale of 9.942

---

[3] https://archive.stsci.edu/k2/

[4] As an example, to compute the SES on 1 hour timescales (corresponding to 2 Kepler long cadence measurements), we construct the following kernel, $g = \frac{1}{2}[0.5, 0.5, -1, -1, 0.5, 0.5]$, which is convolved with the measured photometry. See Petigura & Marcy (2012) for further details.

Table 3.1. *K2* multi-planet host stars

K2 Name	EPIC No.	C#	RA (J2000)	Dec. (J2000)	μ_{RA}[a] (mas yr^{-1})	μ_{dec}[a] (mas yr^{-1})	V[b] (mag)	Kp[a] (mag)	J[a] (mag)	Ks[a] (mag)
K2-5	201338508	C1	11:17:13	− 01:52:41	-10.3 ± 4.4	$+32.6 \pm 4.6$	14.91 ± 0.03	14.36	12.45 ± 0.03	11.60 ± 0.02
K2-3	201367065	C1	11:29:20	− 01:27:17	$+88.3 \pm 2.0$	-73.6 ± 2.7	12.17 ± 0.01	11.57	9.42 ± 0.03	8.56 ± 0.02
K2-8	201445392	C1	11:19:10	− 00:17:04	-34.7 ± 4.9	-16.7 ± 4.1	14.61 ± 0.03	14.38	12.83 ± 0.03	12.25 ± 0.03
K2-19	201505350	C1	11:39:50	+ 00:36:13	-18.7 ± 1.7	$+4.5 \pm 2.0$	13.00 ± 0.01	12.81	11.60 ± 0.02	11.16 ± 0.03
K2-35	201549860	C1	11:20:25	+ 01:17:09	$+10.4 \pm 6.4$	-16.8 ± 5.2	14.35 ± 0.06	13.92	12.14 ± 0.02	11.42 ± 0.02
K2-36	201713348	C1	11:17:48	+ 03:51:59	-17.5 ± 2.3	$+23.5 \pm 2.5$	11.80 ± 0.03	11.53	10.03 ± 0.02	9.45 ± 0.03
K2-16	201754305	C1	11:40:23	+ 04:33:26	-3.8 ± 3.2	$+21.8 \pm 3.9$	14.67 ± 0.04	14.30	12.76 ± 0.03	12.09 ± 0.02
K2-24	203771098	C2	16:10:18	− 24:59:25	-60.6 ± 2.5	-65.4 ± 2.4	11.07 ± 0.11	11.65	9.64 ± 0.02	9.18 ± 0.02
K2-37	203826436	C2	16:13:48	− 24:47:13	-9.4 ± 1.9	$+3.8 \pm 2.6$	12.52 ± 0.06	12.24	10.69 ± 0.02	10.14 ± 0.02
K2-38	204221263	C2	16:00:08	− 23:11:21	-55.6 ± 3.4	-38.3 ± 3.7	11.39 ± 0.03	11.21	9.91 ± 0.02	9.47 ± 0.02
K2-32	205071984	C2	16:49:42	− 19:32:34	-16.4 ± 1.2	-52.5 ± 1.3	12.31 ± 0.04	12.01	10.40 ± 0.02	9.82 ± 0.02

[a] From Ecliptic Plane Input Catalog (EPIC)

[b] From AAVSO Photometric All-Sky Survey (APASS) 9th Data Release

mas/pixel with a field of view of $10''$; PHARO has a pixel scale of 25 mas/pixel with a field of view of $25\farcs6$. The observations were taken in either the Ks or Br-γ filters; Br-γ has a narrower bandwidth (2.13–2.18 μm), but a similar central wavelength (2.15 μm) compared the Ks filter (1.95–2.34 μm; 2.15 μm) and allows for longer integration times before saturation. For the Keck observations, a 3-point dither pattern was utilized to avoid the noisier lower left quadrant of the NIRC2 array; the 3-point dither pattern was observed three times for a total of 9 frames. The Palomar observations were obtained with a 5-point dither pattern with 3 observations at each dither pattern position for a total of 15 frames.

To optimize our use of NIRC2 and PHARO, we pre-screened three of the targets by acquiring visible-light adaptive optics images of K2-3, K2-19, and K2-36 on 8–9 March 2015 using the Robo-AO system (Baranec et al., 2013, 2014) on the 1.5 m Telescope at Palomar Observatory. Observations comprise a sequence of full-frame-transfer EMCCD detector readouts at the maximum rate of 8.6 Hz for a total of 120 s of integration time with a long-pass filter cutting on at 600 nm, with longer wavelength sensitivity limited by the quantum efficiency of the silicon detector out to 1000 nm. The individual $44'' \times 44''$ images are corrected for detector bias and flat-fielding effects before being combined using post-facto shift-and-add processing using the source as the tip-tilt star with 100% frame selection to synthesize a long-exposure image (Law et al., 2014). Sensitivity to faint stellar companions matched that of the high-performance detectable magnitude ratio in Law et al. (2014), typically $\Delta\,\mathrm{mag} = 5$ at 5σ at $0\farcs5$. For these three sources, no stellar companions were detected.

3.2.4 Spectroscopy

Keck/HIRES

We used HIRES (Vogt et al., 1994) at the W. M. Keck Observatory to measure high resolution optical spectra of all 11 stars except for the coolest and faintest star, K2-5. Our observations followed standard procedures of the California Planet Search (CPS; Howard et al., 2010a). We used the "C2" decker ($0\farcs87 \times 14''$ slit) for a spectral resolution R = 55,000 and subtracted the faint sky spectrum from the stellar spectrum. The HIRES exposure meter was set to achieve the desired SNR, which varied with stellar brightness. For our *K2* follow-up program we generally obtain spectra of stars $V \leq 13.0$ mag having SNR = 45 per pixel at 550 nm, while spectra of fainter stars (K2-8, K2-35) have SNR = 32 per pixel. These exposure levels were chosen to be sufficient for determination of stellar parameters while keeping exposure times relatively short (1–10 min). Figure 3.1 shows a wavelength segment of our HIRES spectra. Some of these spectra are higher SNR than prescribed because we obtained additional HIRES spectra for potential Doppler campaigns.

IRTF/SpeX

For two *K2* multi-planet candidates with near-IR spectral types consistent with M dwarfs ($J - K_s \gtrsim 0.8$), we obtained spectra using the near-infrared cross-dispersed spectrograph SpeX (Rayner et al., 2003) on the 3.0-m NASA Infrared Telescope Facility (IRTF). These stars are K2-3 and K2-5. Our SpeX observations and analyses of K2-3 are described in detail in Crossfield et al. (2015) and we adopt those results here.

We observed K2-5 on 2015 May 5 UT under clear skies with an average seeing of $0\farcs5$. We used SpeX in short cross-dispersed mode using the $0\farcs3 \times 15''$ slit which provides wavelength coverage from 0.68 to 2.5 μm at a resolution of $R \approx 2000$. The star was dithered to two positions along the slit following an ABBA pattern for sky subtraction. The K2-5 observing sequence consisted of 8×75 s exposures for a total integration time of 600 s. We also observed an A0 standard and flat and arc lamp exposures immediately after the target star for telluric correction and wavelength calibration.

The data were reduced using the SpeXTool package (Vacca et al., 2003; Cushing et al., 2004). SpeXTool performs flat fielding, bad pixel removal, wavelength calibration, sky subtraction, spectral extraction and combination, telluric correction, flux calibration, and order merging. The final calibrated K2-5 spectrum had JHK-band signal-to-noise ratios $\sim$ 50/75/60. The spectrum is compared to late-type standards from the IRTF Spectral Library[5] (Cushing et al., 2005; Rayner et al., 2009) in Figure 3.2.

---

[5] `http://irtfweb.ifa.hawaii.edu/\mytildespex/IRTF\_Spectral\_Library/`

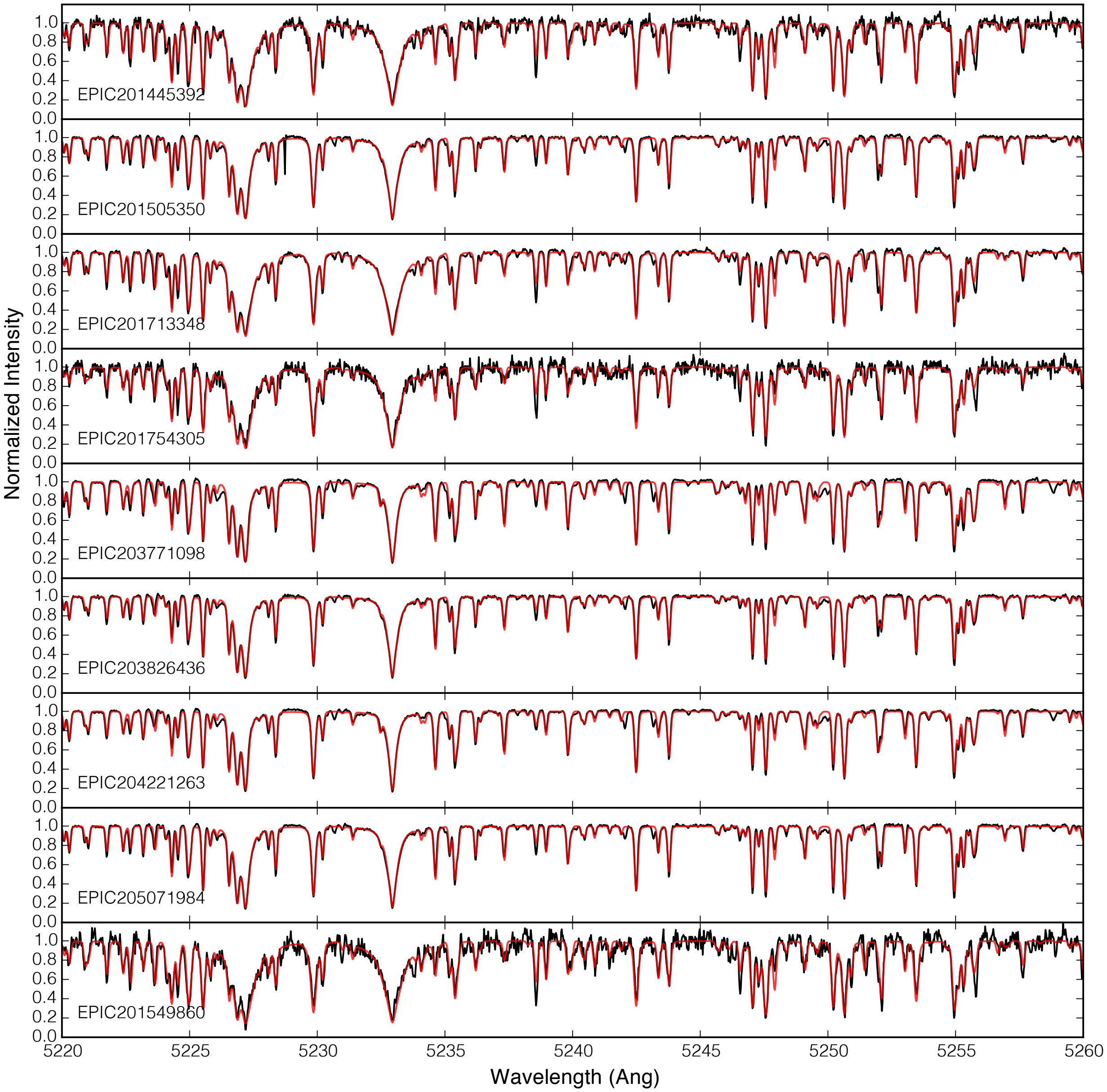

Figure 3.1: A representative segment of our HIRES spectra spanning λ = 5220–5260 Å. The observed stellar spectra are shown in black and the best-fit `SpecMatch` models (Petigura, 2015) are overplotted in red. Note that this represents only about 10% of the wavelength coverage modeled by `SpecMatch`.

3.3 Host Star Characterization

We used `SpecMatch` (Petigura, 2015) to determine stellar properties from our HIRES spectra for nine stars with spectral types of ∼K4 and earlier. `SpecMatch` estimates effective temperatures,

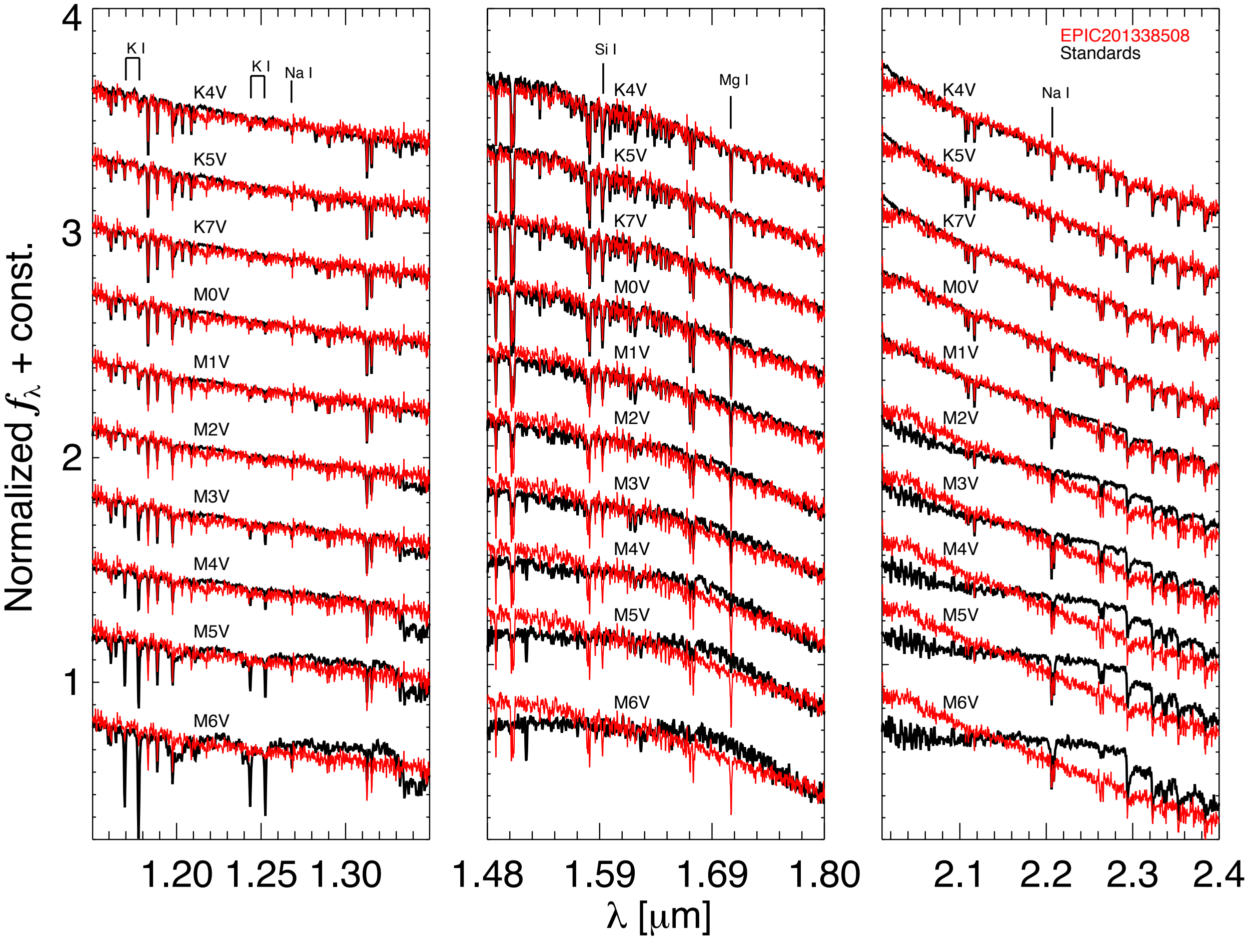

Figure 3.2: *JHK*-band IRTF/SpeX spectra of K2-5 compared to late-type standards from the IRTF spectral library. All spectra are normalized to the continuum in each of plotted regions. The star is a best visual match to spectral type ∼K7 across the three near-IR bands. This is consistent with the results from our analyses using spectroscopic indices.

surface gravities, metalicities, and rotational velocities by matching HIRES spectra to an interpolated library of model spectra from Coelho et al. (2005). These models are in good agreement with the spectra of well-characterized stars for $T_{\rm eff} > 4700\,{\rm K}$. See Petigura (2015) for details on `SpecMatch` including demonstration that the uncertainties on $T_{\rm eff}$, $\log g$, and [Fe/H] are 60 K, 0.08–0.10 dex, and 0.04 dex, respectively. Figure 3.1 shows the best-fit `SpecMatch` model spectra for all nine stars with results.

We estimated stellar masses and radii from spectroscopic parameters ($T_{\rm eff}$, $\log g$, [Fe/H]) by fitting them to a grid of models from the Dartmouth Stellar Evolution Database (Dotter et al., 2008). We used the `isochrones` Python package (Morton, 2015a), which interpolates the Dartmouth model grid (mass-age-[Fe/H]) and estimates uncertainties via the `emcee` Markov Chain Monte Carlo (MCMC) package (Foreman-Mackey et al., 2013). This procedure gives mass and radius uncertainties as small as $\sim 2\%$, not accounting for the intrinsic uncertainties of the Dartmouth models, which are most uncertain for cool stars. For $M_\star < 0.8$ M$_\odot$, Feiden & Chaboyer (2012) find that most Dartmouth evolution models agree with observed stellar radii to within $\sim$4%. Therefore, for the nine stars analyzed with `SpecMatch`, we conservatively adopt minimum uncertainties for stellar mass and radius of 5%. Our final stellar mass and radius uncertainties range from $\sim 5-10\%$.

We also used the HIRES spectra to measure stellar activity. The HIRES spectra span the Ca 2 H & Klines (3969 Å, 3934 Å) that are sensitive to chromospheric activity (Wilson, 1968). Following Isaacson & Fischer (2010), we measured $S_{\rm HK}$indices—the ratio of flux in Ca 2 H & Kline cores to flux in nearby continuum bands. These are converted into $\log R'_{\rm HK}$values (tabulated in Table 3.2), which account for differences in continuum flux levels with spectral type (Noyes et al., 1984; Middelkoop, 1982). Since the conversion to $\log R'_{\rm HK}$is only calibrated for stars with $B - V < 0.9$ ($T_{\rm eff} \sim 5000$ K), we provide only $\log R'_{\rm HK}$values for stars $T_{\rm eff} > 5000$ K and $S_{\rm HK}$values for the cooler stars. For reference, the Sun varies in the range $\log R'_{\rm HK}= -4.85$ to -5.05 dex through the solar cycle (Meunier et al., 2010). K2-19 and EPIC 201713348 are moderately active ($\log R'_{\rm HK}= -4.66$ dex and $S_{\rm HK}= 0.46$, respectively), while the other GK dwarfs are inactive.

Stellar parameters for the two cooler stars (K2-3, K2-5) are derived from infrared spectra discussed in Section 3.2.4. Determination of stellar parameters for K2-3 are detailed in Crossfield et al. (2015). Here we discuss characterization of K2-5 using similar methods.

We used our SpeX spectrum to measure the near-IR H_20-K2 index (Rojas-Ayala et al., 2012) to estimate a spectral type for K2-5 of K7.5 ± 0.5. This index-based measurement is consistent with the visual best match presented in Figure 3.2. Following Crossfield et al. (2015) and Petigura et al. (2015), we estimated metallicity ([Fe/H]), effective temperature ($T_{\rm eff}$), radius ($R_\star$), and mass ($M_\star$) using the methods presented in Mann et al. (2013a) and Mann et al. (2013b). Metallicity is estimated using spectroscopic index and equivalent width based methods (Rojas-Ayala et al., 2012; Terrien et al., 2012; Mann et al., 2013b) that were calibrated using a sample of M dwarfs having wide, co-moving FGK companions with well determined [Fe/H]. We use IDL software made publicly available by A. Mann[6] to calculate the H- and K-band metallicities of K2-5. We average the H and K metallicities and add the measurement and systematic uncertainties in quadrature to arrive at the final value of [Fe/H] $= -0.33 \pm 0.20$ dex. This star is metal poor. Effective temperature, radius, and mass are calculated using temperature sensitive spectroscopic indices in the JHK-bands (Mann et al., 2013a) and empirical relations calibrated using nearby, bright M dwarfs with interferometrically measured radii (Boyajian et al., 2012). We calculated $T_{\rm eff}$ in the JHK-bands and averaged the results. Conservative $T_{\rm eff}$ uncertainties were estimated by adding in quadrature the RMS scatter in the JHK-band values and the systematic errors in the empirical fits for each band (Mann et al., 2013a). The stellar radius and mass were computed using publicly available software from A. Mann[7]. The resulting fundamental parameters for K2-5 are: $T_{\rm eff} = 3930 \pm 375$ K,

---

[6] `https://github.com/awmann/metal`

[7] `https://github.com/awmann/Teff\_rad\_mass\_lum`

Table 3.2. Spectroscopic Stellar Properties

K2 Name	EPIC Number	T_{eff} (K)	$\log g$ (cgs)	[Fe/H] (dex)	$v \sin i$ (m s^{-1})	$\log R'_{\mathrm{HK}}$ (dex)	$M_\star$ (M$_\odot$)	$R_\star$ (R$_\odot$)
K2-5	201338508	3930 ± 375	4.71 ± 0.21	-0.33 ± 0.19	–	–	0.61 ± 0.13	0.57 ± 0.12
K2-3	201367065	3896 ± 189	4.72 ± 0.13	-0.32 ± 0.13	–	–	0.60 ± 0.09	0.56 ± 0.07
K2-8	201445392	4870 ± 60	4.52 ± 0.10	-0.02 ± 0.04	< 2	–	0.78 ± 0.04	0.74 ± 0.04
K2-19	201505350	5430 ± 60	4.63 ± 0.10	$+0.10 \pm 0.04$	< 2	-4.66	0.93 ± 0.05	0.86 ± 0.04
K2-35	201549860	4680 ± 60	4.56 ± 0.10	$+0.04 \pm 0.04$	3 ± 1	–	0.76 ± 0.04	0.72 ± 0.04
K2-36	201713348	4924 ± 60	4.65 ± 0.10	-0.03 ± 0.04	2 ± 1	–	0.80 ± 0.04	0.74 ± 0.04
K2-16	201754305	4742 ± 60	4.51 ± 0.10	-0.33 ± 0.04	2 ± 1	–	0.68 ± 0.03	0.66 ± 0.03
K2-24	203771098	5743 ± 60	4.29 ± 0.08	$+0.42 \pm 0.04$	< 2	-5.15	1.12 ± 0.06	1.21 ± 0.12
K2-37	203826436	5413 ± 60	4.52 ± 0.10	-0.03 ± 0.04	< 2	-4.85	0.90 ± 0.05	0.85 ± 0.04
K2-38	204221263	5757 ± 60	4.35 ± 0.08	$+0.28 \pm 0.04$	< 2	-5.13	1.07 ± 0.05	1.10 ± 0.09
K2-32	205071984	5315 ± 60	4.43 ± 0.10	$+0.00 \pm 0.04$	< 2	-4.94	0.87 ± 0.04	0.87 ± 0.05

[a] For K2-5 and K2-3, T_{eff}, [Fe/H], $M_\star$, $R_\star$ are derived using spectroscopic indices of (Mann et al., 2013a) and empirical relations of (Boyajian et al., 2012). For the other stars T_{eff}, $\log g$, [Fe/H], and $v \sin i$ are derived using `SpecMatch` (Petigura, 2015), $\log R'_{\mathrm{HK}}$ is derived using the recipe of Isaacson & Fischer (2010), $M_\star$ and $R_\star$ are derived using the `isochrones` Python package (Morton, 2015a).

[b] We only list $\log R'_{\mathrm{HK}}$ for stars with $T_{\mathrm{eff}} > 5000$ K, for which this activity metric is well-calibrated. S_{HK} values for cooler stars K2-8, K2-35, K2-36, and K2-16 are 0.33, 0.33, 0.46, and 0.18, respectively. Spectra of K2-5 and K2-3 come from observations with IRTF/SpeX and do not contain Ca 2 H & Klines.

$R_\star = 0.57 \pm 0.12\ R_\odot$, and $M_\star = 0.61 \pm 0.13\ M_\odot$.

K2-5 was presented as a multi-planet system in Montet et al. (2015b) where their fundamental parameters were estimated using broadband photometry and model fits. Our spectroscopic parameter estimates are consistent within uncertainties.

Table 3.2 lists spectroscopically derived stellar parameters.

3.4 Validation of Planet Candidates

There are several potential astrophysical events whose light curves can be confused with transiting planets. One example is a blended eclipsing binary (EB) system, either bound to the primary or in the background of the target star's photometric aperture. Some of these astrophysical false positives can be distinguished from planet transits by secondary eclipses (SEs), but SEs do not always occur and are often undetectably small. Even if the primary star does host a planet, blending of other stars within the photometric aperture can dilute the transit depth causing the planet radius to be underestimated (Ciardi et al., 2015). Follow-up observations are crucial for identifying any sources blended within the same 4″ *Kepler* pixels.

All of the multi-planet systems presented in this catalog passed a series of complementary vetting tests: First, from the *K2* light curves, we identified eclipsing binaries (EBs) via their characteristic "V-shaped" dimming profiles and secondary eclipses. We also searched for nearby companions in AO images and archival images. In addition, we searched for multiple sets of stellar lines in the high resolution optical spectra. We also estimate false positive probabilities (FPPs) of each planet candidate, which are constrained by these follow-up observations.

Even without AO imaging or spectroscopy to screen for these blends, the FPPs for multi-planet systems are intrinsically lower compared to systems with a single planet candidate (Lissauer et al., 2012, 2014). For the prime *Kepler* mission the FPP for a single planet candidate system is $\sim 10\%$ (Morton & Johnson, 2011; Fressin et al., 2013), but is reduced by factors of ~ 25 and ~ 100 for systems with one and two additional planet candidates respectively (Lissauer et al., 2012). These FP rates apply to the prime *Kepler* mission and cannot be blindly applied to *K2*, which has a different degree of source crowding as well as different photometric noise properties, target selection criteria, and vetting procedures, all of which factor into the FP rate and "multiplicity boost" estimation.

In this section, we summarize the results of our AO and archival image searches, spectroscopic validation efforts, and FPP assessment. We estimate multiplicity boosts for *K2* fields C1 and C2 using available *K2* planet candidate catalogs.

3.4.1 AO imaging

For each target star, our AO images were combined using a median average. Typical final FWHM resolutions were 4–6 pixels for a resolution of $\approx 0\overset{''}{.}05$ with Keck/NIRC2 and $\approx 0\overset{''}{.}1$ for Palomar/PHARO. For every target considered here, no other stars were detected within the fields of view of the cameras. For each final combined image, we estimated the sensitivities by injecting fake sources with a signal-to-noise ratio of 5 at distances of $N \times$ FWHM from the central source, where N is an integer. The 5σ sensitivities, as a function of radius from the stars, are shown in Figure 4.1 along with a full field of view combined image. Typical sensitivities yield contrasts of 2–3 mag within 1 FWHM of the target star and contrasts 4–6 mag within 3–4 FWHM. In the "flat" (> 6 FWHM) of the image, the typical contrasts were 8–9 mag fainter than the target star.

3.4.2 Archival imaging

We also searched for neighboring stars at separations beyond the edges of our AO images (typically $10''$), but within the *K2* photometric apertures (typically 10–$15''$). We downloaded $60'' \,\mathrm{x}\, 60''$ r_{P1}-band images from the Pan-STARRS1 3π survey (Kaiser et al., 2010), surrounding each of the EPIC target stars. The images have a plate scale of $0\overset{''}{.}25$ per pixel and average seeing-limited resolution of $\sim 1''$. The target stars are generally saturated in these images but background sources can be easily identified down to a limiting magnitude of $r_{\mathrm{P1}} \approx 23$ mag. We used the magnitude zero points in the FITS headers and performed our own aperture photometry on the images to estimate the magnitudes of nearby sources. Secondary sources are detected within the *K2* aperture of four systems. For three of these systems (K2-19, K2-37, K2-32) secondary sources were bright enough to produce observed transit depths. In these three cases, we regenerated the light curves using

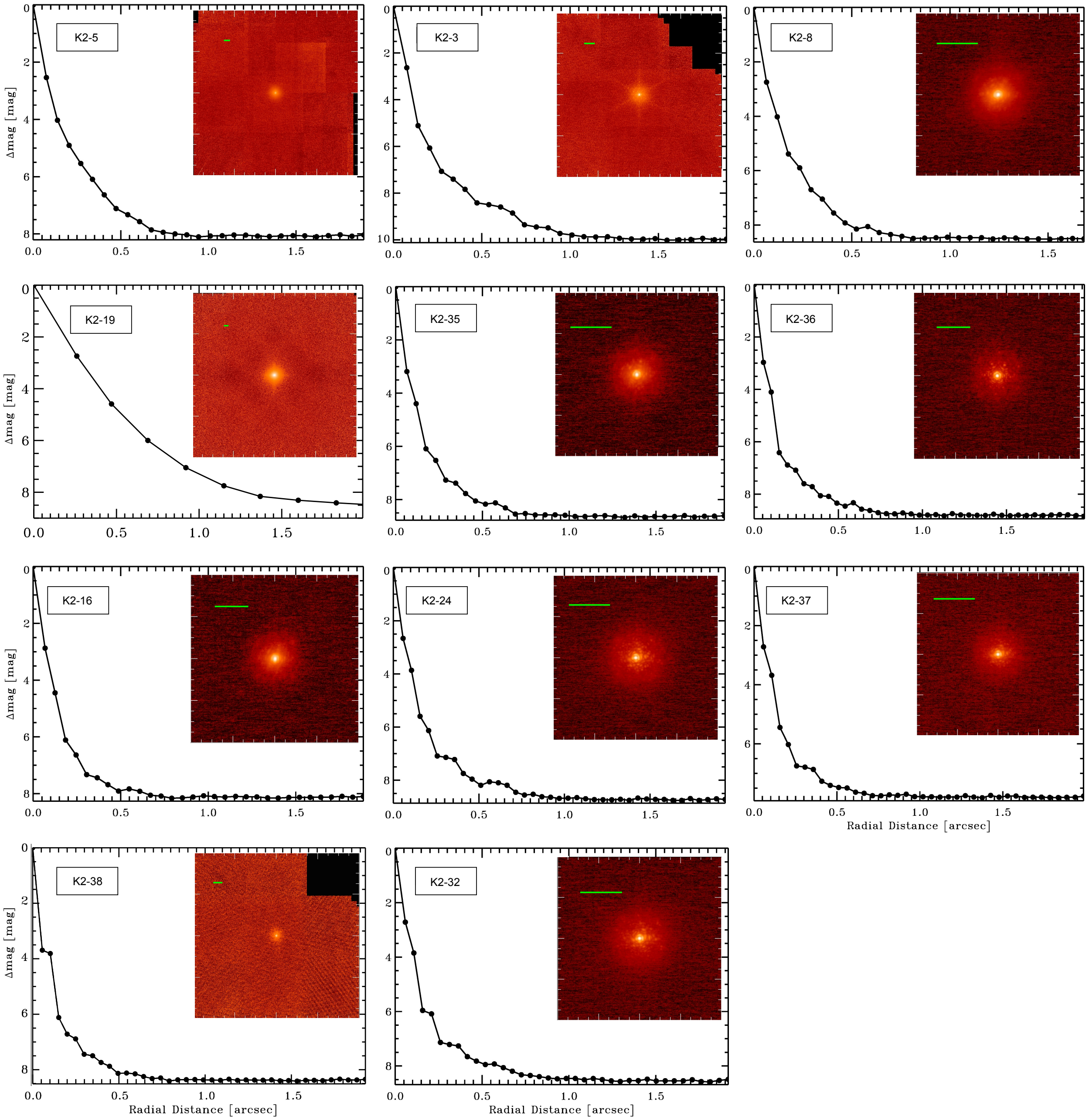

Figure 3.3: AO images and contrast curves for all multi-planet hosts. Targets were imaged using Keck/NIRC2 AO, with the exception of K2-19, which was observed with Palomar/PHARO. Green horizontal lines correspond to 1″in each field. Dotted black lines indicate where companions would be detectable with 5-σ confidence. No companions were detected near any of the 11 stars.

smaller apertures that excluded those other stars and verified that the transit signals remained. We note that all listed transit parameters derive from light curves produced with the original (larger) apertures because of reduced photometric noise. All secondary sources are sufficiently faint such that dilution corrections would have negligible effects on measured transit depths — correction factors would be more than an order of magnitude less than uncertainties on $R_p/R_\star$. An analysis of each EPIC target is given below.

K2-5: No sources fall within the $12''$ aperture to a limiting magnitude of $r_{\rm P1} \approx 23$ mag. The nearest bright source is $15''$ to the NE with $r_{\rm P1}$=18.9 mag.

K2-3: No stellar sources fall within the $16''$ aperture to a limiting magnitude of $r_{\rm P1} \approx 22$ mag. The nearest star detected in the Pan-STARRS1 imaging is $26''$ to the NE with $r_{\rm P1}$=17.2 mag.

K2-8: No sources fall within the $12''$ aperture to a limiting magnitude of $r_{\rm P1} \approx 22$ mag. No stars or galaxies brighter than $r_{\rm P1}$=21.6 mag fall within $30''$ of the target.

K2-19: One faint star falls within the $12''$ aperture $10.7''$ to the NWW with $r_{\rm P1}$=20.7 mag. We estimate that this source is contributing 0.6 ppt to the *K2* photometry. An eclipse of the secondary source would not be deep enough to produce the observed transits of K2-19 b or c. Moreover, Narita et al. (2015) measure a contrast of $\sim$ 0.1 ppt in H-band and detect the transits of K2-19 b and c when the faint star lies outside the photometric aperture, localizing them to the primary. However, an eclipse of the secondary could produce the observed 0.1 ppt transits of K2-19 d. We re-extracted the photometry using an $8''$ aperture, small enough to exclude the faint nearby source. The transit signals of all three planets were detected and their depths were consistent with those measured using the original (larger) aperture. The transits of all three planets are therefore localized to the bright star of interest. Dilution correction factors are negligible compared to measurement uncertainties on $R_p/R_\star$, so we do not apply them.

K2-35: No sources fall within the $12''$ aperture to a limiting magnitude of $r_{\rm P1} \approx 22$ mag. There are two nearby stars just outside the *K2* aperture. One star is $22''$ to the WNW with $r_{\rm P1}$ = 15.1 mag, and the other is $27''$ to the NNW with $r_{\rm P1}$ = 14.3 mag.

K2-36: There are two very bright sources $24''$ to the NE and $24''$ to the SE of K2-36 but both fall outside the $12''$ *K2* aperture. These sources are saturated in the Pan-STARRS1 data but are of comparable brightness to K2-36.

K2-16: No sources fall within the $8''$ *K2* aperture to a limiting magnitude of $r_{\rm P1} \approx 22$ mag. The nearest detected source is $29''$ to the W with $r_{\rm P1}$=20.3 mag.

K2-24: One faint star falls within the $12''$ *K2* aperture $6''$ to the W of the target. This star is badly blended with the wings of the saturated PSF of K2-24 so reliable photometry can not be extracted. However, we estimate that the star is no brighter than $r_{\rm P1} \approx 18.5$ mag, which would contribute only 0.8 ppt to the light in the *K2* aperture and could not be the source of the 2 ppt and 4 ppt transits of K2-24 b and c, respectively. We do not apply a dilution correction to the measured transit depths because it would have negligible effect.

K2-37: Two other stars fall within the 12″ aperture. One star, $r_{\rm P1}$=19.1 mag, is located 9.4″ to the ESE and the other, $r_{\rm P1}$=19.8 mag, is 8.3″ to the WNW. Combined, the contaminating sources contribute 3 ppt to the flux in the *K2* aperture. We regenerated the photometry using an 8″ aperture that excluded the two other stars, and the transits were still visible, confirming that the primary star is being transited. We do not correct the transit depths for dilution as this would have negligible effect.

K2-38: No stars brighter then $r_{\rm P1} \approx 20.3$ mag fall within the 12″ *K2* aperture. The nearest comparably bright source is a $r_{\rm P1} = 19.1$ mag star 29″ to the NW.

K2-32: Several faint sources fall within the 16″ *K2* aperture. The brightest of these is 15″ to the south with $r_{\rm P1}$=18.9 mag. This contaminating source contributes 2 ppt to the *K2* aperture flux and is bright enough to account for the transit depths of planets c and d but not planet b. We re-extracted the photometry using an 8″ aperture, small enough to exclude the other nearby stars and the transits were still visible. The transits are therefore localized to the target of interest. Changes in transit depths caused by dilution from the secondary sources are negligible.

3.4.3 Spectroscopic vetting

We searched the HIRES spectra for multiple sets of stellar lines using the algorithm of Kolbl et al. (2015). The algorithm is sensitive to blends from secondary stars in the 0.87″ × 14″ HIRES slit that have effective temperatures $T_{\rm eff}$ = 3400–6100 brightness ratios $\gtrsim$1% in V and R bands, and differ in radial velocity by $\gtrsim$10 km s^{-1} from the primary star. For the 10 targets with HIRES spectra, no spectroscopic blends were detected.

3.4.4 False Positive Assessment

We estimate the False Positive Probability (FPP) of each planet candidate signal using the Python package `VESPA` (Morton, 2015a). We supply `VESPA` with the phase-folded *K2* light curve, photometry from APASS, 2MASS, and WISE, stellar parameters derived from spectroscopy (§3.3), the contrast curve from AO imaging (§3.4.1), and the maximum allowed contrast and velocity offset determined by our spectroscopic vetting (§3.4.3). Given these constraints, `VESPA` estimates the FPP — the likelihood that the transit signal was produced by a true planet around the target star and not by an eclipsing binary, hierarchical triple system, or non-associated star with a transiting planet. The FPPs returned by `VESPA` are listed in Table 3.3 as well as planet candidate dispositions. Dispositions take into account this study as well as other previously published studies.

For planet candidates that are not "confirmed" by mass detection, we rely on computing a FPP as a means of validation. Following Montet et al. (2015b), we assign a "validated" disposition to planet candidates with FPP <1%. All planet candidates are validated by VESPA to better than 99% confidence, except for K2-8b and K2-32c, which have FPPs of 1.3% and 2.2% respectively. However, these estimates neglect the "multiplicity boost" — an additional factor of confidence in the planet hypothesis gained from the detection of multiple planet candidates in these systems. For the prime *Kepler* mission, Lissauer et al. (2012) estimate that the a priori FPP is $\sim 50\times - 100\times$ lower for systems with three or more planet candidates and $\sim 25\times$ lower for systems with two planet candidates compared to those with one planet candidate. These were derived using two different methods, each of which assumes that false positives (FPs) are randomly distributed among Kepler targets, and that the presence of FPs and detectable planet signals are uncorrelated.

We apply the same methods to *K2* planets. Following Lissauer et al. (2012), for a system with two planet candidates, if P_1 is the probability of a candidate's planethood before considering multiplicity, then the probability of planethood after accounting for multiplicity is

$$P_2 \approx \frac{X_2 P_1}{X_2 P_1 + (1 - P_1)}, \tag{3.1}$$

where X_2 is the "multiplicity boost" for systems of two planet candidates. K2-32c is part of a three-candidate system but, for argument sake, it is sufficient to assume that the multiplicity boost for three-candidate systems will be at least as large as that for two-candidate systems. Lissauer et al. (2012) estimate X_2 using two different methods:

The first method compares the fraction of Kepler targets with planet candidates ($F_{\mathrm{cand}} \sim 1/150$) to the fraction of planet candidate hosts with more than one planet candidate ($F_{\mathrm{multi}} \sim 1/6$). If planets and FPs were randomly distributed among Kepler targets, the detection rate of Kepler multis would be much lower ($F_{\mathrm{multi}} \sim F_{\mathrm{cand}}$). Assuming that FPs are randomly distributed and that planets are not, Lissauer et al. (2012) estimate $X_2 \sim F_{\mathrm{multi}}/F_{\mathrm{cand}} = 25$. We make the same assumptions to estimate X_2 for *K2* fields C1 and C2 using the catalog of Vanderburg et al. (2016a), who adopt a transit detection threshold of SNR > 9. We assume that the target sample in a given *K2* field consists of all objects denoted as a "STAR" in the EPIC catalog. Combining C1 and C2, we compute $F_{\mathrm{cand}} \sim (116/32264) = 0.4\%$ and $F_{\mathrm{multi}} \sim (10/116) = 8.6\%$. These suggest $X_2 \sim 24$, similar to *Kepler*. Substituting $X_2 = 24$ into Equation 3.1 and setting P_1 according to our `VESPA` constraints give corrected FPPs, $(1 - P_2) = 0.06\%$ and 0.09% for K2-8b and K2-32c respectively. We repeated these estimates for C1 and C2 independently, with similar results. We also applied these methods to our own catalog of ∼100 planet candidates in C1 and C2 detected by TERRA (Crossfield et al., submitted), requiring SNR > 12 and three transits. This yields $X_2 \sim 34$ and corrected FPPs (1-P_2) = 0.04% and 0.07% for K2-8b and K2-32c respectively. The multiplicity boosts estimated using either catalog are an order of magnitude larger than those needed to validate K2-8b and K2-32c to better than 99% confidence.

As an additional check, we estimate the multiplicity boost using a second method of Lissauer et al. (2012). This method assumes that some fraction of candidates F_{true} are true planets in order to estimate the expected fraction of multi-candidate systems that have at least one FP. Note that F_{true} is denoted as P in Lissauer et al. (2012) Equations 2 and 4. Those two equations are used to estimate the expected number of FPs in two-candidate systems based on F_{true} as well as the total numbers of observed targets and planet candidates. Subsequently dividing by the number of candidates in two-planet systems yields the fraction of candidates in two-candidate systems expected to be true planets. Using this method, Lissauer et al. (2012) estimated $X_2 \sim 25$ for the prime Kepler mission, consistent with the first method above. We apply this same method to our own catalog of *K2* planet candidates — unlike Vanderburg et al. (2016a), we compute FPPs for all candidates, most of which have been vetted via spectroscopy and high-resolution imaging. By integrating over all FPPs, we estimate $F_{\text{true}} \sim 90\%$ and $\sim 60\%$ and $X_2 \sim 70$ and ~ 20 for C1 and C2 respectively. These are similar to the prime Kepler mission ($F_{\text{true}} \sim 90\%$). Plugging these X_2 values into Equation 3.1 and setting P_1 according to our VESPA constraints yields corrected FPPs, $(1 - P_2) = 0.02\%$ and 0.12% for K2-8b and K2-32c. For this method, the multiplicity boost is still effective at validating these two planet candidates to FPP $< 1\%$ as long as $F_{\text{true}} \gtrsim 15\%$.

In summary, the multiplicity boosts estimated via both methods, when combined with `VESPA` constraints, are large enough to validate K2-8b and K2-32c to much better than 99%.

3.5 Derived Planet Properties

Our light curve analysis follows Crossfield et al. (2015), which we summarize here. Starting with the detrended light curves from `TERRA` (Section 3.2.2), we perform a sliding median subtraction to removes variability on several-day timescales, including stellar modulation. We fit `JKTEBOP` transit models (Southworth et al., 2004; Southworth, 2011) to the light curves, using the `emcee` MCMC package (Foreman-Mackey et al., 2013) to generate posterior probability distributions for the transit model parameter. We use the best-fitting transit depth, phase, and orbital period from `TERRA` for the initial model guess.

We assume circular orbits and adopt a linear limb-darkening model, imposing a Gaussian prior on the limb darkening coefficient u. The mean of this Gaussian is selected by interpolating the limb darkening tables of Claret et al. (2012, 2013) to our spectroscopically measured T_{eff} and $\log g$. The standard deviation was taken to be 0.05. We tested standard deviations of 0.1 and also tried propagating our T_{eff} and $\log g$ uncertainties through the interpolation procedure, but our results were insensitive to the chosen method. The use of a quadratic limb darkening model also resulted in negligible changes to the posteriors.

Detrended light curves, fitted transit models, and derived planet parameters are presented for all 11 systems in Figures 3.10–3.20 and Tables 3.7–3.17 in the Appendix. Derived parameters include orbital distance, a, incident flux $S_{\oplus}$, and equilibrium temperatures, T_{eq}. The discoveries of K2-3 and K2-24 planets are reported in Crossfield et al. (2015) and Petigura et al. (2016), based on the same data products and analysis methods presented here. We include them in our catalog for completeness. All stellar and planet parameters will be provided in an online supplementary table.

Table 3.3 lists key parameters for each multi-planet system. The 26 planets are plotted in

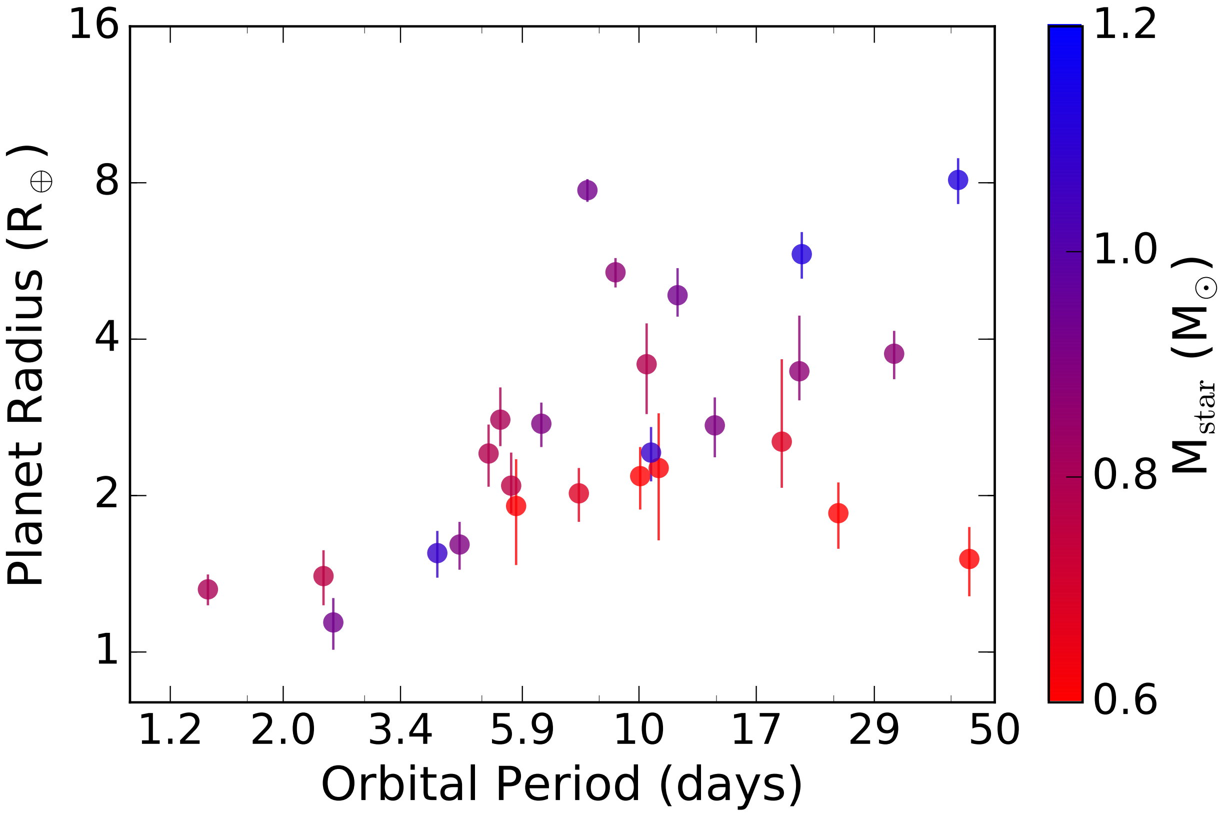

Figure 3.4: Radii and orbital periods of all 26 planets detected in 11 multi-planet systems in *K2* Campaigns 1 and 2. The points are colored according to host star mass, with redder colors corresponding to less massive stars. Twenty-one of the 26 planets are likely smaller than 4 $R_\oplus$.

radius versus orbital period in Figure 3.4. The points are colored according to host stellar mass. Twenty-one of the planets are likely smaller than Neptune ($R_p < 3.8\ R_\oplus$).

Figure 3.5 displays the architectures of all systems. Systems are ordered top to bottom by decreasing orbital period of the inner planet. The largest planet in each system is colored red, the second largest planet is green and, the third largest planet (if present) is blue. This ranking scheme considers posterior medians and does not account for uncertainties, thus providing the most likely ranking. In six out of seven systems having only planets $R_p < 3\ R_\oplus$, planet size increases with P.

3.6 Masses of K2-38 Super-Earths

3.6.1 Doppler Measurements

In an initial campaign with Keck/HIRES, we obtained 14 radial velocity (RV) measurements of K2-38 between 24 June 2015 UT and 3 October 2015 UT. These observations followed the standard procedures of the California Planet Search (CPS; Howard et al., 2010a). We used the "C2" decker

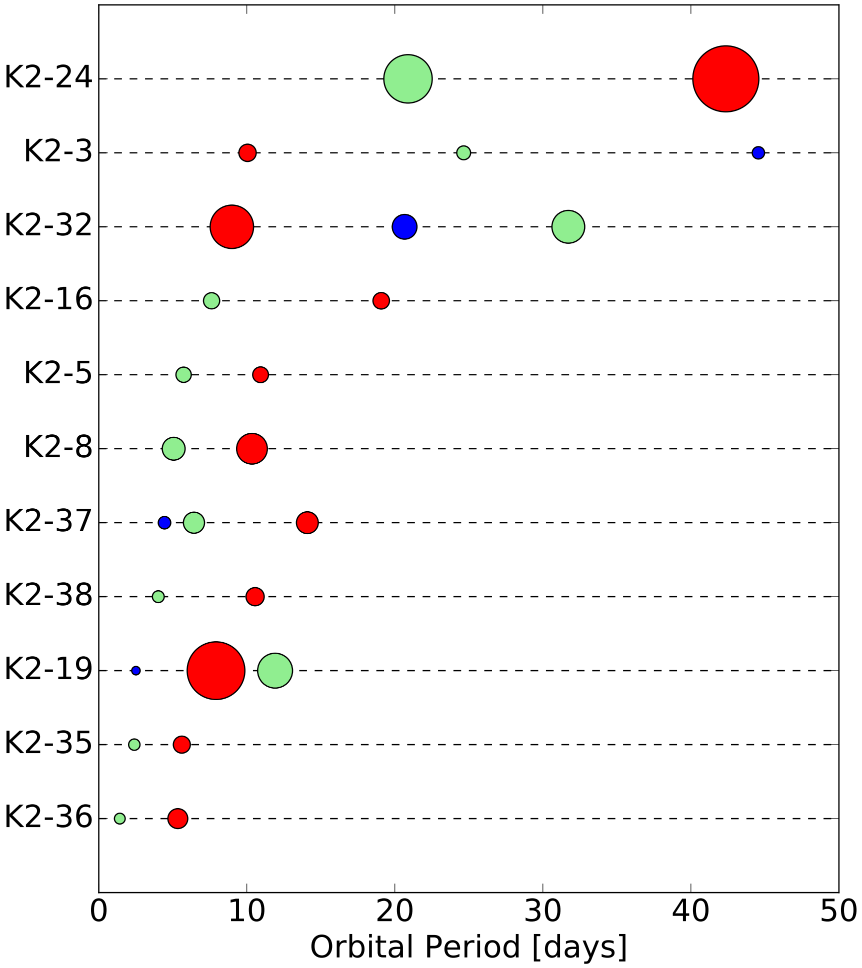

Figure 3.5: Architecture of the 11 *K2* multi-planet systems in this study. Each row shows the planets in a particular system ordered top to bottom by decreasing orbital period of the inner planet. The symbol sizes are proportional to planet sizes. The largest planet in each system is colored red, the second largest planet is green and the third largest planet (if present) is blue.

Table 3.3. Summary of *K2* multi-planet systems

K2 Name	EPIC No.	$T_{\rm eff}$ (K)	Kp (mag)	T_0 (BJD$_{\rm TDB}$−2456000)	P (d)	R_p ($R_\oplus$)	$T_{\rm eq}$ (K)	FPP	Disposition[a]
K2-5	201338508	3930 ± 375	14.36						
K2-5b	201338508b			808.8600 ± 0.0048	5.73594 ± 0.00064	1.91 ± 0.44	565 ± 84	< 0.001	Valid.
K2-5c	201338508c			814.6010 ± 0.0052	10.93241 ± 0.00134	2.26 ± 0.62	456 ± 68	< 0.001	Valid.
K2-3	201367065	3896 ± 189	11.57						
K2-3b	201367065b			813.4173 ± 0.0011	10.05449 ± 0.00026	2.18 ± 0.30	463 ± 39	< 0.001	Conf.
K2-3c	201367065c			812.2812 ± 0.0022	24.64354 ± 0.00117	1.85 ± 0.27	344 ± 29	< 0.001	Valid.
K2-3d	201367065d			826.2288 ± 0.0034	44.55983 ± 0.00590	1.51 ± 0.23	282 ± 24	< 0.001	Valid.
K2-8	201445392	4870 ± 60	14.38						
K2-8b	201445392b			813.6114 ± 0.0030	10.35239 ± 0.00086	3.58 ± 0.71	631 ± 18	0.013	Valid.[b]
K2-8c	201445392c			813.0707 ± 0.0033	5.06416 ± 0.00041	2.41 ± 0.33	801 ± 23	0.008	Valid.
K2-19	201505350	5430 ± 60	12.81						
K2-19b	201505350b			813.3837 ± 0.0003	7.91940 ± 0.00005	7.74 ± 0.39	854 ± 24	< 0.001	Conf.
K2-19c	201505350c			817.2755 ± 0.0051	11.90715 ± 0.00150	$4.86^{+0.62}_{-0.44}$	745 ± 21	< 0.001	Conf.
K2-19d	201505350d			808.9207 ± 0.0086	2.50856 ± 0.00041	1.14 ± 0.13	1252 ± 36	< 0.001	Valid.
K2-35	201549860	4680 ± 60	13.92						
K2-35b	201549860b			810.5871 ± 0.0085	2.39984 ± 0.00039	1.40 ± 0.17	979 ± 29	< 0.001	Valid.
K2-35c	201549860c			812.1158 ± 0.0049	5.60912 ± 0.00071	$2.09^{+0.33}_{-0.24}$	737 ± 22	< 0.001	Valid.
K2-36	201713348	4924 ± 60	11.53						
K2-36b	201713348b			809.4684 ± 0.0017	1.42266 ± 0.00005	1.32 ± 0.09	1232 ± 36	< 0.001	Valid.
K2-36c	201713348c			812.8422 ± 0.0008	5.34059 ± 0.00010	$2.80^{+0.43}_{-0.31}$	793 ± 23	< 0.001	Valid.
K2-16	201754305	4742 ± 60	14.30						
K2-16b	201754305b			811.6871 ± 0.0038	7.61880 ± 0.00087	2.02 ± 0.24	658 ± 19	< 0.001	Valid.
K2-16c	201754305c			809.4800 ± 0.0091	19.07863 ± 0.00327	$2.54^{+1.12}_{-0.47}$	485 ± 14	0.002	Valid.
K2-24	203771098	5743 ± 60	11.65						
K2-24b	203771098b			905.7950 ± 0.0007	20.88508 ± 0.00036	5.83 ± 0.60	709 ± 36	< 0.001	Conf.
K2-24c	203771098c			915.6250 ± 0.0005	42.36342 ± 0.00063	8.10 ± 0.82	560 ± 29	< 0.001	Conf.
K2-37	203826436	5413 ± 60	12.24						
K2-37b	203826436b			893.7013 ± 0.0080	4.44117 ± 0.00075	1.61 ± 0.17	974 ± 32	0.009	Valid.
K2-37c	203826436c			898.8603 ± 0.0023	6.42904 ± 0.00036	2.75 ± 0.27	861 ± 28	< 0.001	Valid.
K2-37d	203826436d			907.2315 ± 0.0031	14.09189 ± 0.00135	2.73 ± 0.36	663 ± 22	< 0.001	Valid.
K2-38	204221263	5757 ± 60	11.21						
K2-38b	204221263b			896.8786 ± 0.0054	4.01593 ± 0.00050	1.55 ± 0.16	1184 ± 51	< 0.001	Conf.
K2-38c	204221263c			900.4752 ± 0.0033	10.56103 ± 0.00090	2.42 ± 0.29	858 ± 37	< 0.001	Conf.
K2-32	205071984	5315 ± 60	12.01						
K2-32b	205071984b			900.9258 ± 0.0009	8.99218 ± 0.00020	5.38 ± 0.35	769 ± 25	< 0.001	Conf.
K2-32c	205071984c			899.4306 ± 0.0101	20.65614 ± 0.00598	$3.48^{+0.97}_{-0.42}$	583 ± 19	0.022	Valid.[b]
K2-32d	205071984d			903.7846 ± 0.0031	31.71922 ± 0.00236	3.75 ± 0.40	505 ± 16	< 0.001	Valid.

T_0 = mid-transit time, $T_{\rm eq}$ = equilibrium temperature assuming albedo = 0.3.

[a] Conf. = planet candidate confirmed by RV and/or TTV detections. Cand. = planet candidate (FPP > 1%). Valid. = Statistically validated planet candidate, >99% confidence (FPP < 1%). Dispositions take into account this study as well as other previously published studies.

[b] Although the FPPs of K2-8b and K2-32c exceed our 1% threshold for a "validated" disposition, FPP values do not account for the "multiplicity boost" (reduction in FPP) resulting from the presence of additional planet candidates around the same star. We estimate that the multiplicity boosts for C1 and C2 are large enough by an order of magnitude to validate K2-8b and K2-32c to better than 99% confidence (See §3.4.4).

($0.87'' \times 14''$ slit) with a cell of molecular iodine gas placed in front of the spectrometer slit to imprint a dense set of molecular absorption lines on the stellar spectrum, subjected to the same instrumental effects. Exposure times were typically ~20 min and were determined by an exposure meter that terminated exposures when an SNR per pixel of 160 in the continuum near 550 nm was reached. The iodine lines serve as a wavelength reference and calibration for the point spread function (PSF) over the entire spectral formal. We also gathered an iodine-free spectrum with the "B3" decker ($0\rlap{.}''57 \times 14''$ slit). RVs were determined by forward-modeling the iodine-free spectrum, a high-resolution/high-SNR spectrum of the iodine transmission, and the instrumental response (Marcy & Butler, 1992; Valenti et al., 1995; Butler et al., 1996; Howard et al., 2009). Our measured RVs are listed in Table 5.3. Individual RV measurement uncertainties are in the range 1.3–1.8 $\mathrm{m\,s^{-1}}$.

Figure 3.6 shows the measured RV time series for K2-38. The star has low astrophysical jitter and we were able to make initial mass measurements of the two planets. We fit a two-planet model using the IDL package `RVLIN` (Wright & Howard, 2009). Our RV model assumes two planets with circular orbits, with the orbital periods and phases fixed to the values measured from transits. We used a likelihood function constructed as in Howard et al. (2014). The model has five free parameters including the RV semi-amplitude of planets b and c, K_b and K_c, a constant RV offset, γ, and a constant radial acceleration (RV changing linearly with time), dv/dt. We also include an RV "jitter" parameter, σ_{jitter}, to account for additional Doppler noise, which might have astrophysical or instrumental origins. We estimate a jitter of $2.4^{+1.0}_{-0.7}$ $\mathrm{m\,s^{-1}}$ that is consistent with expectations for old, solar-type star (Wright, 2005; Isaacson & Fischer, 2010).

The RV time series has a negative slope, suggesting that we are seeing a small orbital segment of a third companion with a wider orbital separation. To test this hypothesis, we compared models with and without the constant RV acceleration parameter using the Bayesian Information Criterion (BIC; Schwarz, 1978; Liddle, 2007). Comparing the the best-fitting models, we find $\mathrm{BIC}_{\mathrm{dv/dt}} - \mathrm{BIC}_{\mathrm{dv/dt=0}} = -5.6$, indicating that the model that includes constant acceleration is strongly preferred. There is very likely to be a third, more distant companion in this system, and we constrain its properties in Section 3.6.2. Additional RV measurements in early 2016, when the target is next observable, will provide a stronger test of the long-term trend.

Using the same RV model and likelihood function, we performed an MCMC analysis of the RVs to determine parameter uncertainties. We used `emcee` (Foreman-Mackey et al., 2013) and adopted Gaussian priors on the orbital periods and phases, with means and widths matching the posteriors derived from fitting the light curve (Section 3.5). We adopted uninformed priors for K_b, K_c, σ_{jitter}, γ, and dv/dt. By allowing the model to explore unphysical solutions with $K < 0$, we did not bias the analysis to positive planet masses. We used the best fits from `RVLIN` to initialize the process. We discarded the first 500 steps. Every 2000 MCMC steps thereafter, we computed the Gelman-Rubin statistic (GRS, Gelman & Rubin, 1992) to assess convergence. We adopted

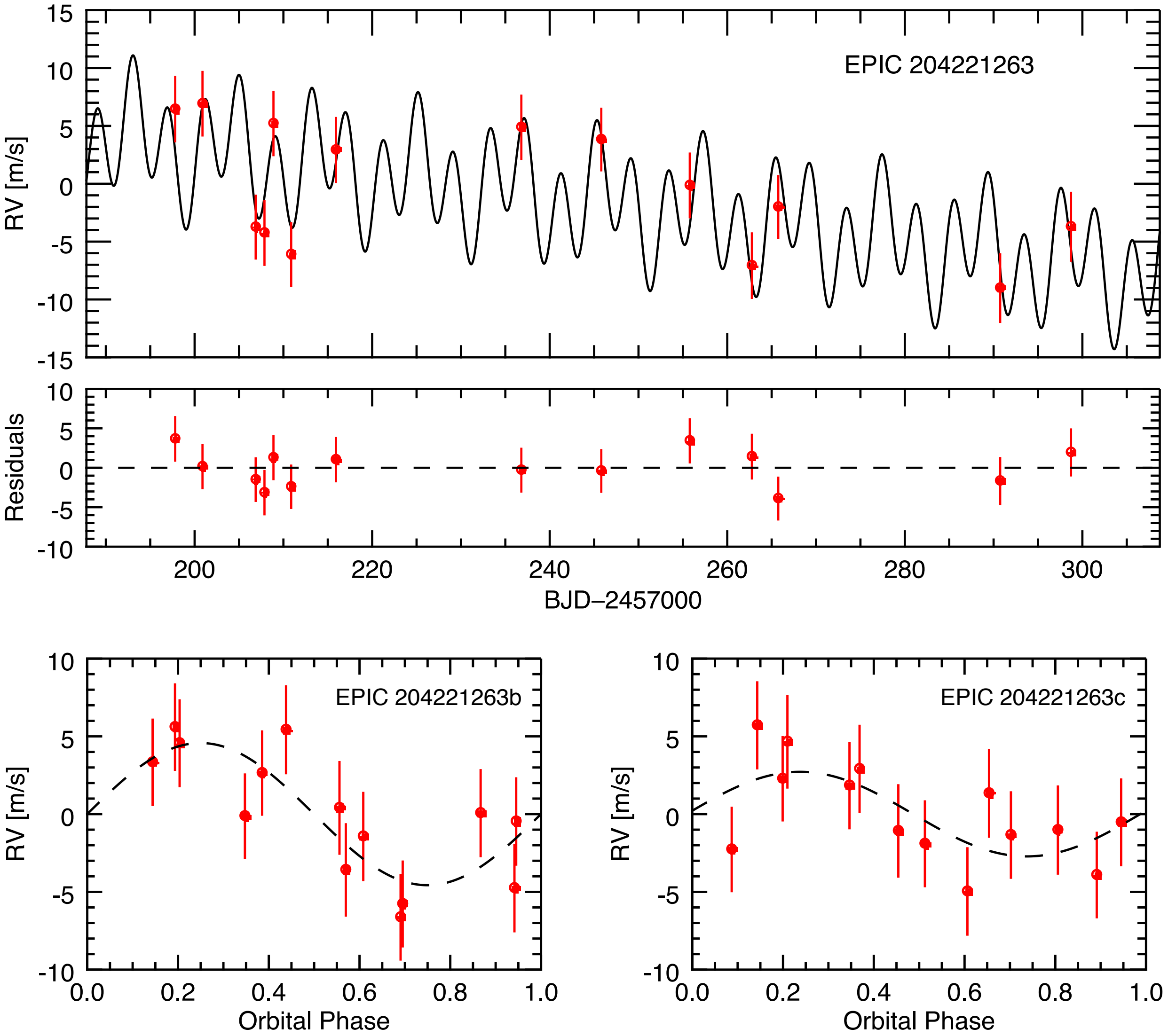

Figure 3.6: *Top*: RV time series observed with Keck/HIRES (red points), and the best two-planet fit, which includes a significant constant acceleration, dv/dt, evidence of a third bound companion at larger orbital distances. RV error bars represent the quadrature sum of individual measurement uncertainty and the best-fit jitter ($2.4\ \mathrm{m\,s^{-1}}$). *Bottom*: RV time series of planets b (left) and c (right), folded at the orbital period of each planet with the linear trend and the Keplerian signal from the other planet subtracted. Transits occur at an orbital phase of 0.5.

Table 3.4. Relative radial velocities, K2-38

BJD−2457000	Radial Velocity ($\mathrm{m\,s^{-1}}$)	Uncertainty ($\mathrm{m\,s^{-1}}$)
197.81009	6.49	1.49
200.88524	6.96	1.42
206.87767	−3.70	1.36
207.86695	−4.20	1.46
208.87926	5.25	1.40
210.87654	−6.06	1.34
215.91724	2.97	1.46
236.80323	4.93	1.40
245.80773	3.87	1.26
255.77713	−0.10	1.44
262.77317	−7.03	1.51
265.74243	−1.96	1.27
290.74044	−8.97	1.75
298.71937	−3.67	1.76

convergence criterion GRS < 1.03 and generated posteriors once this condition was satisfied.

Table 3.5 lists measured RV semi-amplitudes, masses, and bulk densities of K2-38 b and c. We list posterior medians, with quoted uncertainties being 15.87 and 84.13 percentiles. For the inner planet, we measure a mass of $12.0 \pm 2.9 M_\oplus$. Combining this our planet radius measurement gives a bulk density of $17.5^{+8.5}_{-6.2}$ $\mathrm{g\,cm^{-3}}$.The mass and bulk density of the outer planet are $9.9 \pm 4.6 M_\oplus$ and $3.6^{+2.7}_{-1.9}$ $\mathrm{g\,cm^{-3}}$, respectively. We discuss possible compositions for both planets in Section 5.4.

The marginalized posterior distribution for the linear trend gives $dv/dt = -37 \pm 11 \mathrm{m\,s^{-1}}$ $\mathrm{yr^{-1}}$. This linear trend contributes a change in RV of ∼10 $\mathrm{m\,s^{-1}}$ over the ∼100-day time baseline of our RV campaign. This suggests a Keplerian signal with semi-amplitude $K \gtrsim 5\,\mathrm{m\,s^{-1}}$, and $P \gtrsim 200\,\mathrm{d}$

Table 3.5. RV model, K2-38

Parameter	Planet b		Planet c	Units
K	4.6 ± 1.1		2.8 ± 1.3	$\mathrm{m\,s^{-1}}$
M_p	12.0 ± 2.9		9.9 ± 4.6	$M_\oplus$
ρ_p	$17.5^{+8.5}_{-6.2}$		$3.6^{+2.7}_{-1.9}$	$\mathrm{g\,cm^{-3}}$
σ_{jit}		$2.4^{+1.0}_{-0.7}$		$\mathrm{m\,s^{-1}}$
γ		-1.7 ± 0.9		$\mathrm{m\,s^{-1}}$
dv/dt		-37 ± 11		$\mathrm{m\,s^{-1}yr^{-1}}$

K = RV semi-amplitude, M_p = planet mass, ρ_p = planet density, σ_{jit} = RV "jitter", γ = constant RV offset, dv/dt = constant RV acceleration

($a \gtrsim 0.7\,\mathrm{AU}$).

3.6.2 Constraints on an additional body

We considered the possibility that the source of the linear RV trend is a companion star that contributes enough light to the *K2* photometry to significantly dilute the observed transit depths. In this scenario we would underestimate the planet radii and overestimate of planet densities (Ciardi et al., 2015). We assessed this possibility using our AO images and HIRES spectra. We confined the companion properties to a small domain of companion mass (or contrast with the primary) and orbital separation. These constraints are summarized in Figure 3.7 and suggest a low likelihood that the companion is bright enough to affect our measured density by more than 20%. The non-detection of secondary lines in the HIRES spectrum allows us to exclude stars close in proximity and mass to the primary, specifically $\Delta Kp \leq 5$ and $\Delta\mathrm{RV} \gtrsim 10$ m s^{-1} (red dashed line). The plotted boundary (dashed red line) assumes that the HIRES spectrum was acquired at an orbital phase of maximum ΔRV. Our Keck/NIRC2 AO contrast curve (blue solid line) extends the exclusion region to fainter companions at larger separations. Horizontal dotted lines show stellar companions that would cause planet densities to be overestimated by 10% and 20%. There is a small window of unvetted parameter space, spanning companion masses ∼0.6–0.7 $\mathrm{M}_{\odot}$, orbital separations ∼4–5 AU, which would cause planet densities to be overestimated by 10–20% (planet radii underestimated by 3% and 6%, respectively). This potential underestimate is smaller than our measurement uncertainties. There are a few noteworthy caveats: If the AO imaging happened to take place when the projected separation was small, then a brighter companion could go undetected. The same applies if the HIRES spectrum was taken when the difference between the RVs of the primary star and its companion was low or if the orbit is near face-on (misaligned with the transiting planets). Note that while a near face-on orbit would limit spectroscopic constraints, it would maximize detectability by AO imaging.

For the above analysis, we used *riJHK* photometric calibrations of Kraus & Hillenbrand (2007) to convert angular separation to orbital distance ($\sim 170\,\mathrm{pc}$) and to convert contrasts in the NIRC2-AO bandpass to contrasts in the Kepler bandpass and to companion masses. Following Winn et al. (2010), if we assume the companion has a circular orbit and mass $M_2 \ll M_\star$, then our measured $dv/dt = -37 \pm 11\mathrm{m\,s^{-1}}\ \mathrm{yr}^{-1}$ implies

$$M_2 \sin i \sim 0.2\, M_{\mathrm{Jup}} \left(\frac{a}{1\,\mathrm{AU}}\right)^2, \tag{3.2}$$

where M_{Jup} is the mass of Jupiter. If the companion is $1\,M_{\mathrm{Jup}}$ it would be located at ~ 2 AU. The constraints given by Equation 3.2 are also shown in Figure 3.7 (green dashed line). However, we stress that these assume the companion has a circular orbit in the same plane as the planets b and c, and a mass much lower than that of the primary star. Therefore, it does not decrease the likelihood of close-in companions bright enough to significantly dilute the transit depth.

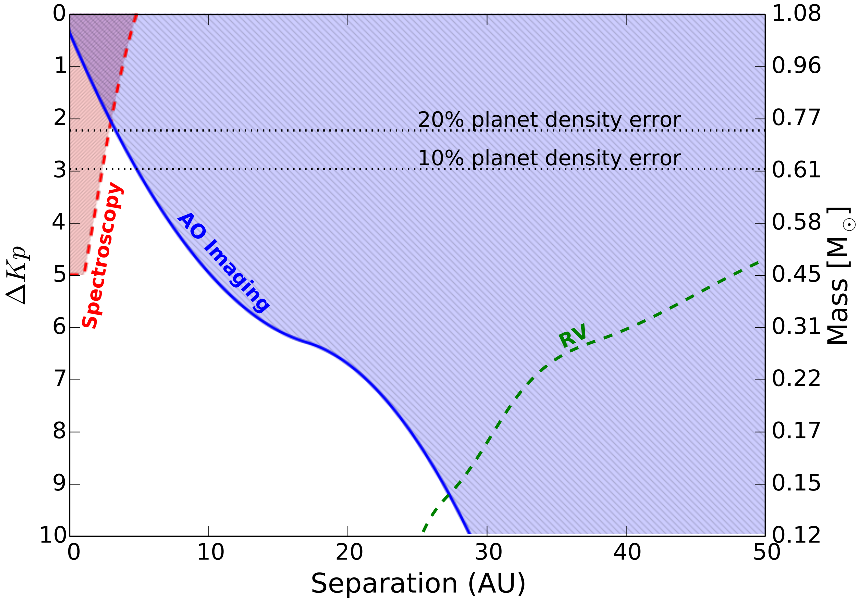

Figure 3.7: Constraints on the properties of an unseen companion. The axes denote a parameter space of brightness contrast of the companion with K2-38 (alternatively the mass of the companion) and the orbital separation between the two bodies. AO imaging excludes companions in the hatched blue region. The dashed red line shows the limits of our search for secondary lines in the high-resolution optical spectrum from HIRES. The dashed green line (lower right) corresponds to the masses and orbital semi-major axes consistent with the measured linear RV trend, assuming a circular, edge-on orbit and a companion mass much lower than that of the primary star (Equation 3.2). The horizontal dashed lines represent companion contrasts at which the dilution of the observed transit depths would cause planet densities to be overestimated by 10% and 20%. AO imaging and spectroscopy rule out companions that would cause systematic errors of $>$ 20% in planet density with high confidence (see Section 3.6.2 for discussion).

3.7 Individual systems

Here we summarize some of the most important characteristics of each system determined from this study, as well as other studies where relevant.

K2-5 is a ∼K7.5V star, hosting at least two planets with $P = 5.7$ and 10.9 d and $R_p = 1.91 \pm 0.44 R_\oplus$ and $2.26 \pm 0.62 R_\oplus$, respectively (Figure 3.10, Table 3.7). Both planets were reported by Foreman-Mackey et al. (2015), and Vanderburg et al. (2016a) and validated by Montet et al. (2015b). The large uncertainties on planet radii ($\sim 20 - 30\%$) relative to the rest of our targets is due to the modest SNR of our IRTF-SpeX stellar spectrum (see Section 3.2.4).

K2-3 is a nearby, ∼M0V star hosting three super-Earths with $P = 10.1$, 24.6, and 44.6 d and $R_p = 2.18 \pm 0.30$, 1.85 ± 0.27, and $1.51 \pm 0.23 R_\oplus$, respectively (Figure 3.11, Table 3.8). All three planets were first reported in Crossfield et al. (2015). Spitzer observations independently confirmed transits of each planet Beichman et al. (2016). Almenara et al. (2015) and Dai et al. (2016) measured masses of $8.4 \pm 2.1\ M_\oplus$ and $8.1^{+2.0}_{-1.9}\ M_\oplus$ respectively for the inner planet, K2-3b, which suggests it is composed mostly of rock, but possibly as much as 60% water. The outer planet receives ∼50% more stellar flux than Earth receives from the Sun, with an equilibrium temperature, $T_{\rm eq} \sim 282\,{\rm K}$.

K2-8 is a ∼K3V star hosting two planets with $P = 5.1$ and 10.4 d, near a 2:1 MMR. These planets have radii of 2.41 ± 0.33 and $3.58 \pm 0.71\,R_\oplus$, respectively (Figure 3.12, Table 3.9). Both planets were reported in Foreman-Mackey et al. (2015) and Vanderburg et al. (2016a). Montet et al. (2015b) estimated FPPs using `VESPA`. In their study, only the outer planet candidate (K2-8b) was given a "validated" disposition. They listed the inner planet as a "planet candidate" because the FPP exceeded 1%, dominated by the 1.9% probability of a background eclipsing binary (BEB). They looked for companions using images from data release nine of the Sloan Digital Sky Survey (SDSS), which has a 1.4″ PSF (Ahn et al., 2012). Our NIRC2 AO imaging excludes the possibility of BEBs several times closer to the star and we compute a lower FPP of 0.8%. Surprisingly, for the outer planet candidate validated by Montet et al. (2015b) (FPP=0.2%), we compute a higher FPP of 1.3%, despite better constraints from AO imaging and spectroscopy. The reason for this discrepancy is unclear but possibly the result of having slightly different stellar parameter constraints or photometry. Nevertheless, `VESPA` does not account for the multiplicity of this system, which would reduce our FPP estimate below 1% (See 4.4). Therefore, we assign validated dispositions to both K2-8b and K2-8c.

K2-19 is a ∼G9V star hosting three planets. The star is magnetically active; we measure $\log R'_{\rm HK} = -4.66\,{\rm dex}$ and the light curve exhibits quasi-periodic variations in brightness by $\sim 1\%$ over 15–20 d. The inner planet, $P = 2.5$ d, is near Earth-size with $R_p = 1.14 \pm 0.13 R_\oplus$. The outer two planets are larger and near 3:2 MMR having $P = 7.9$ and 11.9 d and $R_p = 7.74 \pm 0.39 R_\oplus$ and $4.86^{+0.62}_{-0.44}\ R_\oplus$, respectively (Figure 3.13, Table 3.10). The two outer planets were reported as planet candidates by Foreman-Mackey et al. (2015) and first confirmed by Armstrong et al. (2015), who used ground based telescopes to detect additional transits and measure hour-long TTVs for the middle planet. A similar study by Narita et al. (2015) found consistent TTVs and precisely characterized the star via AO imaging with Subaru-HiCIAO and high resolution spectroscopy with Subaru-HDS. Barros et al. (2015) simultaneously modeled *K2* and ground-based photometry and RVs from the SOPHIE spectrograph of $\sim$16 $\mathrm{m\,s^{-1}}$ precision. They find that planet b has mass $44 \pm 12\ M_\oplus$ and radius $7.46 \pm 0.76\ R_\oplus$, while planet c has mass $15.9^{+7.7}_{-2.8}\ M_\oplus$ and radius $4.51 \pm 0.47\ R_\oplus$. Dai et al. (2016) measured $M_b = 28.5^{+5.4}_{-5.0}\ M_\oplus$ and $M_c = 25.6 \pm 7.1\ M_\oplus$. Planet d was first reported as a planet candidate by Vanderburg et al. (2016a). The 2.5-day period of the transits is $\sim$10x the spacecraft thruster firing period of 6 hours. However, in our planet search and light curve fitting, we omit all photometry collected during a thruster firing. Thus, we are confident that thruster firings are not the source of the transit. As an additional test, we visually inspected the complete set of photometric measurements phased at the transit period and found there was no excess of thruster firings during the transits. Thus, even if these data points were included in our fitting, they would not significantly bias the derived planet properties. We also verified that the photometric scatter during the transit phase is not systematically different than the out-of-transit phase.

K2-35 is a bright $\sim$K4V star hosting two close-in super-Earths with $P = 2.4$ and 5.6 d. The planets are $1.40 \pm 0.17 R_\oplus$ and $2.09^{+0.33}_{-0.24}\ R_\oplus$ respectively (Figure 3.14, Table 3.11). The outer planet was reported as a planet candidate by Foreman-Mackey et al. (2015) and Montet et al. (2015b). Both were listed as planet candidates by Vanderburg et al. (2016a).

K2-36 is a bright $\sim$K2V star hosting two hot super-Earths with $P = 1.4$ and 5.3 d, first reported as planet candidates by Vanderburg et al. (2016a). The inner planet, $R_p = 1.32 \pm 0.09 R_\oplus$, has T_eq $\sim$1200 K and the outer planet, $R_p = 2.80^{+0.43}_{-0.31}\ R_\oplus$ has $T_\mathrm{eq} \sim 800$ K (Figure 3.15, Table 3.12). The light curve shows 1–2% modulation with a period of $\sim$10 d and the spectrum has strong Ca 2 H & Kemission lines (S_HK=0.46), indicating that the star is magnetically active.

K2-16 is a faint, $\sim$K3V star having two planets with P =7.6 and 19.1 d and $R_p = 2.02 \pm 0.24 R_\oplus$ and $2.54^{+1.12}_{-0.47}\ R_\oplus$, respectively (Figure 3.16, Table 3.13). These planets are near 5:2 MMR. They were first detected by Foreman-Mackey et al. (2015) and validated by Montet et al. (2015b). Both planets were detected by Vanderburg et al. (2016a).

K2-24 is a bright $\sim$G9V star with two cool, sub-Saturn-size planets near 2:1 MMR, $P = 20.9$ and 42.4 d, $R_p = 5.83 \pm 0.60\, R_\oplus$ and $8.10 \pm 0.82\, R_\oplus$ (Figure 3.17, Table 3.14). Using Keck/HIRES RVs, Petigura et al. (2016) measured masses of $21 \pm 5.4\, M_\oplus$ and $27 \pm 6.9\, M_\oplus$ and densities of $0.63 \pm 0.25\ \mathrm{g\,cm^{-3}}$ and $0.31 \pm 0.12\ \mathrm{g\,cm^{-3}}$ for inner and outer planets, respectively. Dai et al. (2016) measured masses of $19.8^{+4.5}_{-4.4}\ M_\oplus$ and $26.0^{+5.8}_{-6.1}\ M_\oplus$ respectively. The transit signals of both planets were also detected by Vanderburg et al. (2016a).

K2-37 is a bright $\sim$G3V star with three small, tightly packed planets having $P = 9.0$ d, 24.6 d, and 44.6 d and $R_p = 1.61 \pm 0.17$, $R_\oplus$ $2.75 \pm 0.27 R_\oplus$ and $2.73 \pm 0.36 R_\oplus$, respectively (Figure

3.18, Table 3.15). These were reported as planet candidates by Vanderburg et al. (2016a).

K2-38 is a bright ~G2V star, with two hot super-Earths, $P = 4.0$ and 10.6 d and $R_p = 1.55 \pm 0.16 R_\oplus$ and $2.42 \pm 0.29 R_\oplus$, respectively (Figure 3.19, Table 3.16). We measure planet masses of $12.0 \pm 2.9 M_\oplus$ and $9.9 \pm 4.6 M_\oplus$ and densities of $17.5^{+8.5}_{-6.2}\,\mathrm{g\,cm^{-3}}$ and $3.6^{+2.7}_{-1.9}\,\mathrm{g\,cm^{-3}}$ (Table 3.5). These indicate that the inner planet is likely rocky and possibly iron-rich, while the outer planet is likely to have an envelope of low-density volatiles (Section 3.8.1). A linear RV trend also suggests a third companion at larger orbital distances (Section 3.6). None of these planets were previously reported.

K2-32 is a bright ~G9V star with three planets, $P = 9.0$, 24.6, and 44.6 d, $R_p = 5.38 \pm 0.35$, $R_\oplus$ $3.48^{+0.97}_{-0.42}$, $R_\oplus$ and $3.75 \pm 0.40 R_\oplus$, respectively (Figure 3.20, Table 3.17). Vanderburg et al. (2016a) reported these as planet candidates. The outer two planets are near 3:2 MMR. Dai et al. (2016) confirmed the inner planet b, using RVs to measure a mass of $21.1 \pm 5.9\ M_\oplus$. For planet c, `VESPA` returns a FPP of 2.2%, which does not meet our criterion for a "validated" disposition (FPP < 1%). However, `VESPA` does not account for the "multiplicity boost", which is more than the factor of 2.2 necessary to reduce the FPP of K2-32c below 1% (See discussion in §3.4.4). Therefore we deem all three planet candidates in this system "validated".

3.8 Discussion & Conclusions

We have detected, validated, and characterized 11 multi-planet systems comprised of 26 planets in *K2* fields C1 and C2. Seven of these systems have two detected planets and four of them have three detected planets, the majority of which are smaller than Neptune. Moreover, seven of the stars have $Kp < 13$ and are amenable to RV follow-up to measure planet masses and densities. This study is distinguished from previous *K2* catalogs because it focuses on multi-planet systems with intrinsically low false positive probabilities and we have characterized each host star with high contrast imaging and spectroscopy. We detected the RV signatures of K2-38b and K2-38c, allowing us to constrain their masses and densities and infer their bulk compositions.

3.8.1 Compositions of K2-38 Super-Earths

Figure 5.2 shows the mass-radius and density-radius distributions of all planets with R_p ¡ 4.0 $R_\oplus$ whose mass and radius are measured to better than 50% precision (2σ) either by RVs or TTVs [8]. Solar System planets are included as well as theoretical mass-radius relations for pure iron, rock, and water compositions, based on models by Zeng & Sasselov (2013). The red points in Figure 5.2 show our mass and radius constraints of K2-38b and K2-38c.

The measured mass and radius of K2-38b are consistent with a rocky or iron-rich composition, matching K2-3d and KOI-94b within uncertainties. Comparing mass and radius estimates to com-

---

[8] NASA Exoplanet Archive, UT 13 November 2015, http://exoplanetarchive.ipac.caltech.edu

positional models of Zeng & Sasselov (2013) gives a 97.7% probability that the planet is denser than pure rock. With a bulk density of $17.5^{+8.5}_{-6.2}$ g cm^{-3}, K2-38b could be the densest planet discovered to date, but additional RV measurements are needed to confirm this. While our 1σ measurement errors do not rule out densities exceeding that of pure iron, we can reject such compositions on the basis that there are incompatible with planet formation theory and the low abundances of heavy elements in planet-forming disks. Iron-rich planets (e.g., Mercury) might result from collisional stripping of the rocky mantle of a larger, differentiated, planet. Simulations by Marcus et al. (2010) suggest that collisional stripping is unlikely to produce super-Earths with iron mass fractions exceeding $\sim 70\%$. The initial assembly of an iron-rich core might be expedited by photophoretic segregation of metals and silicates in the inner protoplanetary disk, which preferentially drives the rocky material outward (Wurm et al., 2013). With an equilibrium temperature, T_{eq} ~1200 K, K2-38b is perhaps a remnant core of a larger planet whose atmosphere was removed by photoevaporation. In such a scenario, the precursor could have been a gas giant that formed beyond the snow line and migrated inwards. Indeed, such a massive core would have rapidly accreted nebular gas, if still present. Alternatively, if the planet assembled in-situ, photoevaporation might have been less important to its present composition; nebular gas might have dispersed before the core was massive enough to accrete, or atmospheric accretion could have been limited by the creation of a gap in the disk (Hansen & Murray, 2012).

The mass and radius of the outer planet, K2-38c, are consistent with many other planets, including GJ 1214b, Kepler-68b, Kepler-96b, Kepler102-e, Kepler-106c, HD 97658b, and HIP 116454b. Its equilibrium temperature of 858 ± 37 K is intermediate to those of the other planets, which have T_{eq} spanning ~550–1150 K. This planet is unlikely to have experienced significant atmospheric photoevaporation. We measure the planet's mass to ~50% (2σ) precision, which allows for a range of possible compositions — even with smaller measurement uncertainties, planet compositions in this region of the mass-radius diagram are highly degenerate (Seager et al., 2007; Adams et al., 2008; Valencia et al., 2013). K2-38c likely contains an outer envelope comprised of low-density volatiles. It could have a small rocky core, with an extended H/He envelope or steam atmosphere. Alternatively, since the measured density is consistent with pure water, the planet could be a "water-world", with a core rich in water ice and interior to a mostly steam atmosphere. A more precise mass is needed to meaningfully constrain core to envelope mass ratios and possible mass fractions of rock, water, and H/He. Due to the mass-radius degeneracies between water-worlds and rocky cores with extended H/He atmospheres, the atmospheric composition must be measured by other means (e.g. transmission spectroscopy) in order to distinguish between these two different archetypes.

3.8.2 Orbital Stability

We analytically assess the orbital stability of each system by comparing orbital separations of each planet pair to their mutual Hill radii, which is the length scale applicable to dynamical interactions:

$$R_H = \left[\frac{M_{\rm in} + M_{\rm out}}{3M_\star}\right]^{1/3} \frac{(a_{\rm in} + a_{\rm out})}{2}. \tag{3.3}$$

Here, $M_{\rm in}$ and $M_{\rm out}$ are the masses of the inner and outer planets and $a_{\rm in}$ and $a_{\rm out}$ are their respective orbital distances from the host star. For planets $R_p = 1.4$–4.0 $R_\oplus$, we use the power-law scaling $M_p = 2.69R_p^{0.93}$ from Weiss & Marcy (2014)to convert radii to masses. For planets $R_p > 4.0$ $R_\oplus$ we use $M_p = 1.6R_p^{1.8}$ (Wolfgang & Lopez, 2015). The one exception is K2-38, for which we use our measured RV masses (Section 3.6). We compute orbital separations in units of R_H:

$$\Delta = \frac{a_{\rm out} - a_{\rm in}}{R_H}. \tag{3.4}$$

For a two-planet system, if $\Delta < 2\sqrt{3}$ then even circular orbits are likely to be unstable on short timescales (Gladman, 1993). All of our *K2* multis have $\Delta > 5$, so we have no reason to suspect that their orbits are unstable. While there are no such analytic criterion to assess the orbital stability of three planet systems, Fabrycky et al. (2014) suggest $\Delta_{\rm in} + \Delta_{\rm out} > 18$ as a conservative requirement. All four of the triple-planet systems presented here satisfy this criterion.

3.8.3 Orbital Resonances

In multi-planet systems, the distribution of planet orbital period ratios contains important clues regarding their formation and evolution. Fabrycky et al. (2014) found that the distribution of period ratios among Kepler multis was fairly uniform. They noted, however, a slight overabundance of planet pairs just outside first order mean-motion resonances, and an underabundance of pairs just inside. Lithwick & Wu (2012) and Batygin & Morbidelli (2013) interpreted this feature as a natural outcome of resonant pairs of planets that experience eccentricity damping. Figure 3.9 shows the distribution of period ratios for planet pairs discovered during the prime Kepler mission. In order to make a more direct comparison to our *K2* planets, we have restricted to orbital periods < 50 d. We have indicated the period ratios for the planet pairs presented in this paper. While there are too few planet pairs for a detailed comparison, the distribution of period ratios is qualitatively similar: fairly uniform with a few planet pairs lying just out side the 2:1 and 3:2 MMR.

Two planet pairs, K2-19 bc and K2-32 cd, are just wide of 3:2 MMR, having $P_{\rm rel} = 1.5036$ and 1.5351, respectively. Two pairs, K2-24 bc and K2-8 bc, orbit just outside of 2:1 resonance ($P_{\rm rel} = 2.0284$, 2.0441). The TTV signals of these planet pairs will be significantly enhanced by their near-resonant orbits (Holman & Murray, 2005; Lithwick & Wu, 2012).

Table 3.6. Comparison with other studies

EPIC	R_p (this study)	R_p (other)	$R_\star$ (this study)	$R_\star$ (other)	Reference[a]
201338508b	1.91 ± 0.44	1.92 ± 0.23	0.57 ± 0.12	0.52 ± 0.01	M15
201338508c	2.26 ± 0.62	1.92 ± 0.20	0.57 ± 0.12	0.52 ± 0.01	M15
201367065b	2.18 ± 0.30	1.98 ± 0.10, 2.14 ± 0.27	0.56 ± 0.07	0.52 ± 0.02, 0.56 ± 0.07	M15, C15
201367065c	1.85 ± 0.27	1.56 ± 0.10, 1.72 ± 0.23	0.56 ± 0.07	0.52 ± 0.02, 0.56 ± 0.07	M15, C15
201367065d	1.51 ± 0.23	1.52 ± 0.21	0.56 ± 0.07	0.56 ± 0.07	C15
201445392b	3.58 ± 0.71	2.97 ± 0.51	0.74 ± 0.04	$0.74^{+0.02}_{-0.03}$	M15
201445392c	2.41 ± 0.33	2.31 ± 0.33	0.74 ± 0.04	$0.74^{+0.02}_{-0.03}$	M15
201505350b	7.74 ± 0.39	7.11 ± 0.81, 7.23 ± 0.54, 7.46 ± 0.76	0.86 ± 0.04	$0.81^{+0.09}_{-0.05}$, 1.03 ± 0.2, 0.91 ± 0.09	M15, A15, B15
201505350c	$4.86^{+0.62}_{-0.44}$	4.31 ± 0.49, 4.21 ± 0.31, 4.51 ± 0.47	0.86 ± 0.04	$0.81^{+0.09}_{-0.05}$, 1.03 ± 0.2, 0.91 ± 0.09	M15, A15, B15
201549860c	$2.09^{+0.33}_{-0.24}$	2.20 ± 0.40	0.72 ± 0.04	0.69 ± 0.02	M15
201754305b	2.02 ± 0.24	2.13 ± 0.37	0.66 ± 0.03	0.64 ± 0.03	M15
201754305c	$2.54^{+1.12}_{-0.47}$	2.14 ± 0.41	0.66 ± 0.03	0.64 ± 0.03	M15
203771098b	5.83 ± 0.60	5.68 ± 0.41	1.21 ± 0.12	1.21 ± 0.11	P15
203771098c	8.10 ± 0.82	7.82 ± 0.72	1.21 ± 0.12	1.21 ± 0.11	P15

[a] Citation key: M15 = Montet et al. (2015b), C15 = Crossfield et al. (2015), A15 = Armstrong et al. (2015), B15 = Barros et al. (2015), P15 = Petigura et al. (2016)

3.8.4 Comparison with other studies

Table 3.6 compares our measured planet radii and host star radii with those published in other studies. All measurements agree within 1σ. Montet et al. (2015b) derive the radii of all 11 stars from photometry, yet their quoted uncertainties are often comparable to or smaller than our spectroscopic constraints. For example, for the two reddest stars (K2-3, K2-5) they estimate uncertainties $\lesssim 2\%$. They interpolate Dartmouth stellar evolution models, which, as the authors acknowledge, might systematically underestimate M-dwarf radii by as much as 15% (Montet et al., 2015a; Newton et al., 2015). Moreover, below $\sim 0.8 M_\odot$, the scatter relative to precisely measured stellar radii is ~4% (Feiden & Chaboyer, 2012). For the nine hotter stars, uncertainties from our stellar characterization algorithm Specmatch are well calibrated large samples of exquisitely characterized stars (Petigura, 2015). Therefore, we believe that our typical ~5–10% uncertainties are appropriate. Although the photometric derived uncertainties of Montet et al. (2015b) agree with our measurements, as both studies acknowledge, one should be cautious of adopting them for other analysis.

This appendix provides light curves and parameters for each planetary system. We show *K2* aperture photometry corrected for spacecraft systematics, de-trended photometry with planet transits identified by colored vertical ticks, and photometry phased to the orbital period of each planet. We also provide a table of physical, orbital, and model parameters for each planetary system. The most important stellar and planetary properties are summarized in Table 3.3.

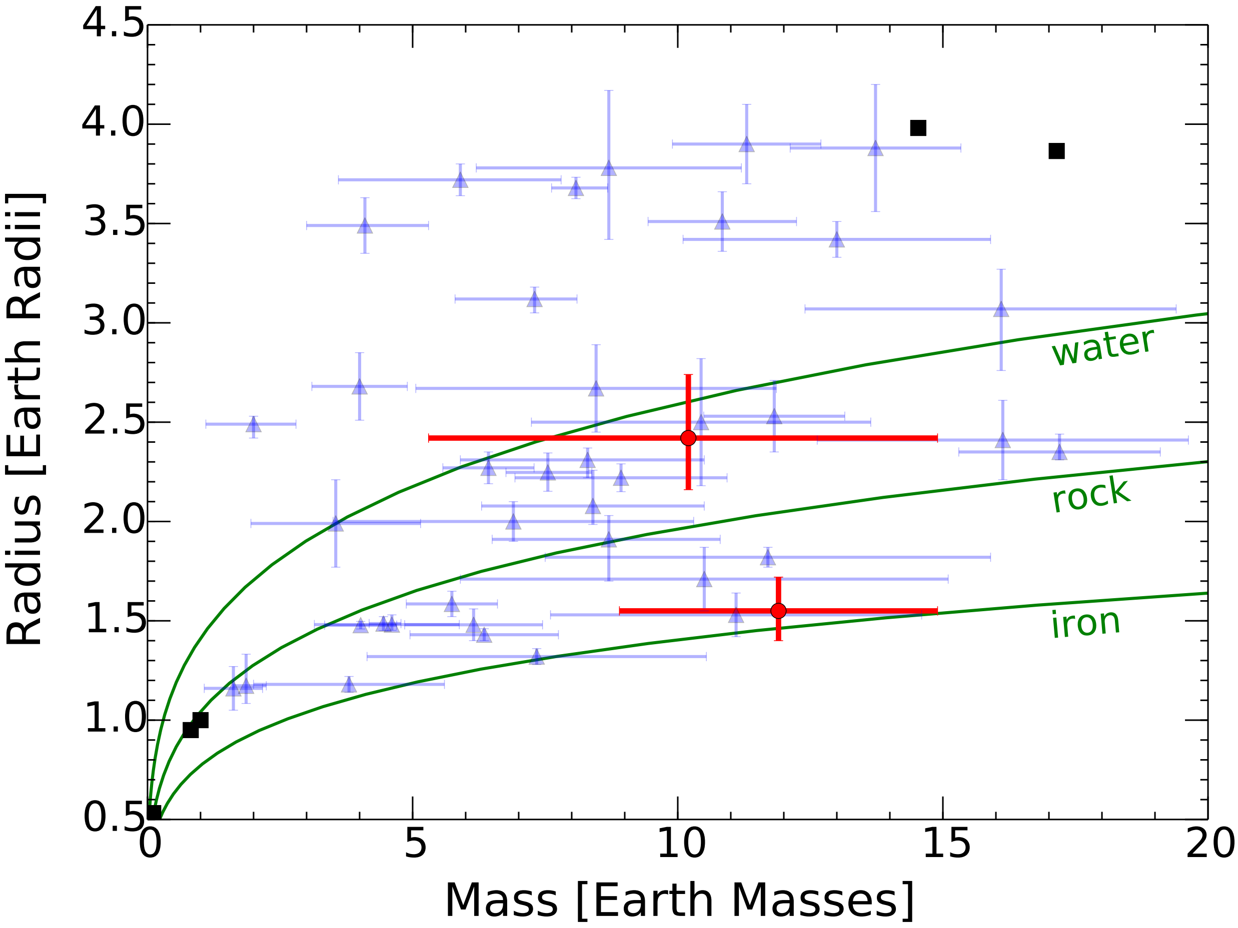

Figure 3.8: Radii and masses of all confirmed planets whose mass and radius are measured to better than 50% (2σ) precision (blue triangles). Solar System planets are represented as black squares. Red circles indicate our measurements of K2-38b and c (top and bottom points, respectively). Green curves show the expected planet mass-radius curves for pure iron, rock, and water compositions according to models by Zeng & Sasselov (2013). K2-38b likely has a large iron fraction and could be the densest planet detected to date. The composition of K2-38c is less certain, but the planet likely possesses an outer envelope comprised of low-density volatiles.

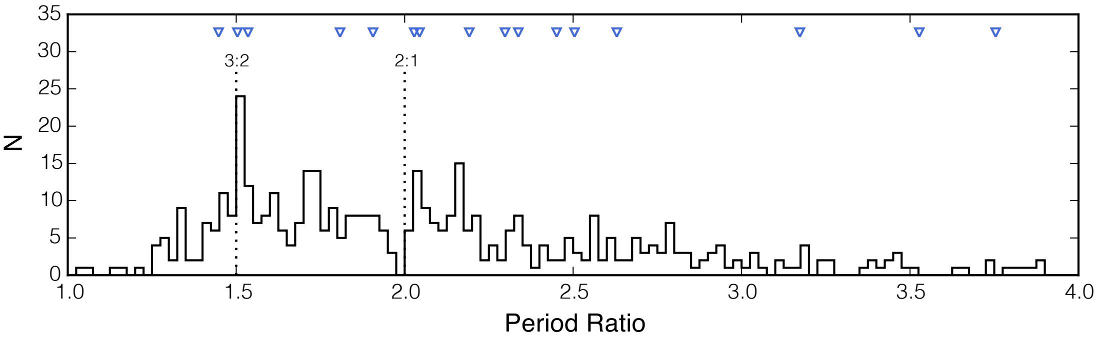

Figure 3.9: Histogram of the distribution of period ratios for planets from the prime *Kepler* mission (Fabrycky et al., 2014). In systems with three or more transiting planets, all pairs of planets are considered, not only adjacent pairs. In order to make a more direct comparison to the population probed by *K2*, we have only shown *Kepler* planets having $P < 50$ d. The period ratios of *K2* planet pairs presented in this work are shown using blue triangles. The *K2* distribution of period ratios is qualitatively similar to the period ratios from the Kepler prime mission.

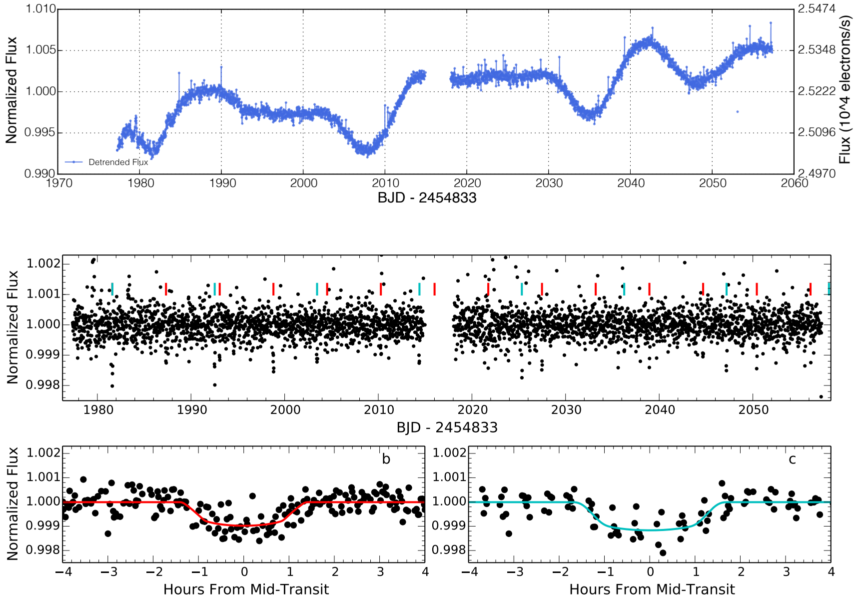

Figure 3.10: *Top*: *K2* photometry for K2-5 after subtracting variations caused by telescope roll. *Middle*: Calibrated *K2* photometry. Vertical ticks indicate times of planet transits. *Bottom*: Phase-folded photometry and best fitting light curves for each planet.

Table 3.7. Planet properties, K2-5

Parameter	Planet b	Planet c	Units
Transit Model			
T_0	808.8600 ± 0.0048	814.6010 ± 0.0052	$\mathrm{BJD_{TDB}}$−2456000
P	5.73594 ± 0.00064	10.93241 ± 0.00134	d
i	$87.35^{+1.88}_{-3.37}$	86.95 ± 2.47	deg
$R_p/R_\star$	$0.03031^{+0.00412}_{-0.00236}$	$0.03601^{+0.00805}_{-0.00475}$	–
$R_\star/a$	$0.0712^{+0.0487}_{-0.0159}$	$0.0639^{+0.0448}_{-0.0272}$	–
u	0.62 ± 0.05	0.62 ± 0.05	–
b	$0.65^{+0.22}_{-0.41}$	$0.83^{+0.09}_{-0.43}$	–
t_{14}	$2.654^{+0.607}_{-0.268}$	$3.498^{+1.420}_{-0.580}$	hrs
R_p	1.91 ± 0.44	2.26 ± 0.62	$R_\oplus$
$\rho_{\star,\mathrm{circ}}$	$1.59^{+1.80}_{-1.25}$	$0.60^{+2.59}_{-0.48}$	$\mathrm{g\,cm^{-3}}$
Derived Properties			
a	0.0532 ± 0.0038	0.0818 ± 0.0059	AU
S_{inc}	$24.1^{+18.4}_{-11.3}$	$10.2^{+7.8}_{-4.8}$	$S_\oplus$
T_{eq}	565 ± 84	456 ± 68	K

T_0 = mid-transit time, i = orbital inclination, a = orbital semi-major axis, u = linear limb-darkening coefficient, b = impact parameter, t_{14} = transit duration, $\rho_{\star,\mathrm{circ}}$ = stellar density, S_{inc} = incident stellar flux, T_{eq} = equilibrium temperature

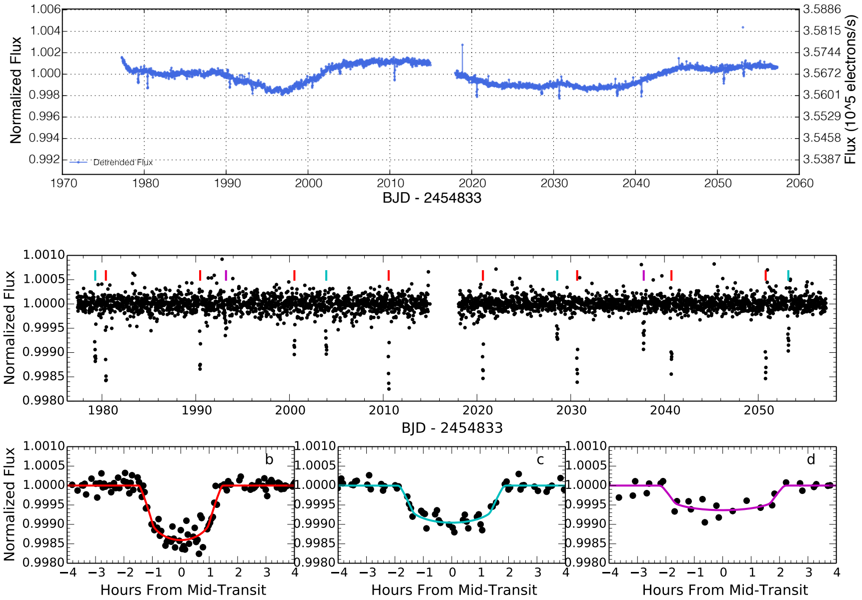

Figure 3.11: *Top*: *K2* photometry for K2-3 after subtracting variations caused by telescope roll. *Middle*: Calibrated *K2* photometry. Vertical ticks indicate times of planet transits. *Bottom*: Phase-folded photometry and best fitting light curves for each planet.

Table 3.8. Planet properties, K2-3

Parameter	Planet b	Planet c	Planet d	Units
Transit Model				
T_0	813.4173 ± 0.0011	812.2812 ± 0.0022	826.2288 ± 0.0034	$\mathrm{BJD_{TDB}}{-}2456000$
P	10.05449 ± 0.00026	24.64354 ± 0.00117	44.55983 ± 0.00590	d
i	$88.80^{+0.84}_{-1.12}$	$89.12^{+0.62}_{-0.86}$	$89.38^{+0.43}_{-0.64}$	deg
$R_p/R_\star$	$0.03534^{+0.00286}_{-0.00153}$	$0.03007^{+0.00304}_{-0.00203}$	$0.02453^{+0.00267}_{-0.00182}$	–
$R_\star/a$	$0.0391^{+0.0138}_{-0.0057}$	$0.0237^{+0.0123}_{-0.0053}$	$0.0161^{+0.0093}_{-0.0038}$	–
u	0.60 ± 0.05	0.60 ± 0.05	0.59 ± 0.05	–
b	$0.54^{+0.23}_{-0.35}$	$0.65^{+0.20}_{-0.40}$	$0.67^{+0.20}_{-0.40}$	–
t_{14}	$2.726^{+0.252}_{-0.111}$	$3.633^{+0.491}_{-0.191}$	$4.325^{+0.552}_{-0.256}$	hrs
R_p	2.18 ± 0.30	1.85 ± 0.27	1.51 ± 0.23	$R_\oplus$
$\rho_{\star,\mathrm{circ}}$	3.12 ± 1.87	$2.34^{+2.64}_{-1.67}$	$2.28^{+2.82}_{-1.70}$	$\mathrm{g\,cm^{-3}}$
Derived Properties				
a	0.0769 ± 0.0039	0.1399 ± 0.0070	0.2076 ± 0.0104	AU
S_{inc}	10.9 ± 3.7	3.3 ± 1.1	1.5 ± 0.5	$S_\oplus$
T_{eq}	463 ± 39	344 ± 29	282 ± 24	K

Same footnotes as Table 3.7

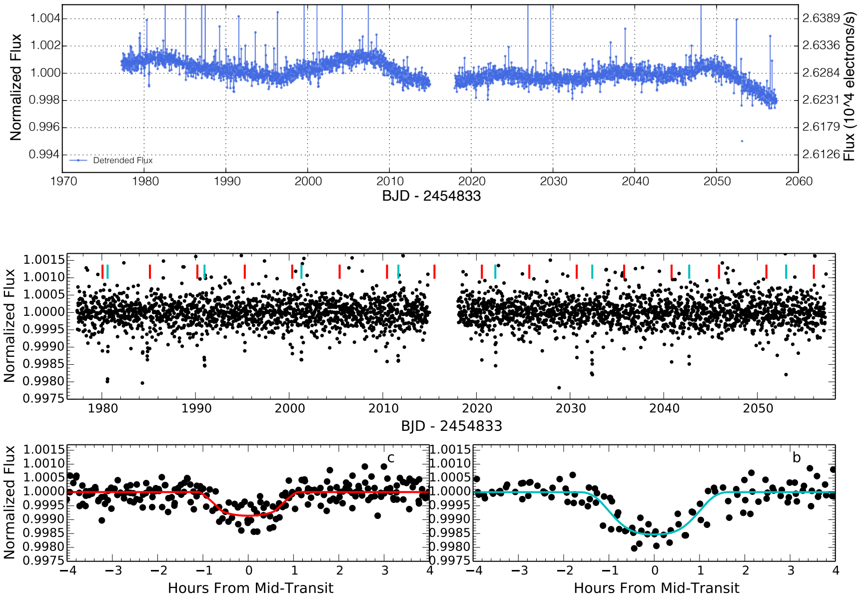

Figure 3.12: *Top*: *K2* photometry for K2-8 after subtracting variations caused by telescope roll. *Middle*: Calibrated *K2* photometry. Vertical ticks indicate times of planet transits. *Bottom*: Phase-folded photometry and best fitting light curves for each planet.

Table 3.9. Planet properties, K2-8

Parameter	Planet b	Planet c	Units
Transit Model			
T_0	813.6114 ± 0.0030	813.0707 ± 0.0033	$\mathrm{BJD_{TDB}}{-}2456000$
P	10.35239 ± 0.00086	5.06416 ± 0.00041	d
i	$86.42^{+2.56}_{-1.37}$	86.70 ± 2.48	deg
$R_p/R_\star$	0.04457 ± 0.00861	0.02990 ± 0.00385	–
$R_\star/a$	$0.0710^{+0.0233}_{-0.0366}$	$0.0743^{+0.0415}_{-0.0251}$	–
u	0.70 ± 0.05	0.70 ± 0.05	–
b	$0.88^{+0.04}_{-0.36}$	$0.78^{+0.12}_{-0.42}$	–
t_{14}	3.362 ± 0.885	$2.080^{+0.498}_{-0.253}$	hrs
R_p	3.58 ± 0.71	2.41 ± 0.33	$R_\oplus$
$\rho_{\star,\mathrm{circ}}$	$0.49^{+3.85}_{-0.28}$	$1.79^{+4.39}_{-1.32}$	$\mathrm{g\,cm^{-3}}$
Derived Properties			
a	0.0856 ± 0.0014	0.0532 ± 0.0009	AU
S_inc	37.7 ± 4.4	97.8 ± 11.4	$S_\oplus$
T_eq	631 ± 18	801 ± 23	K

Same footnotes as Table 3.7

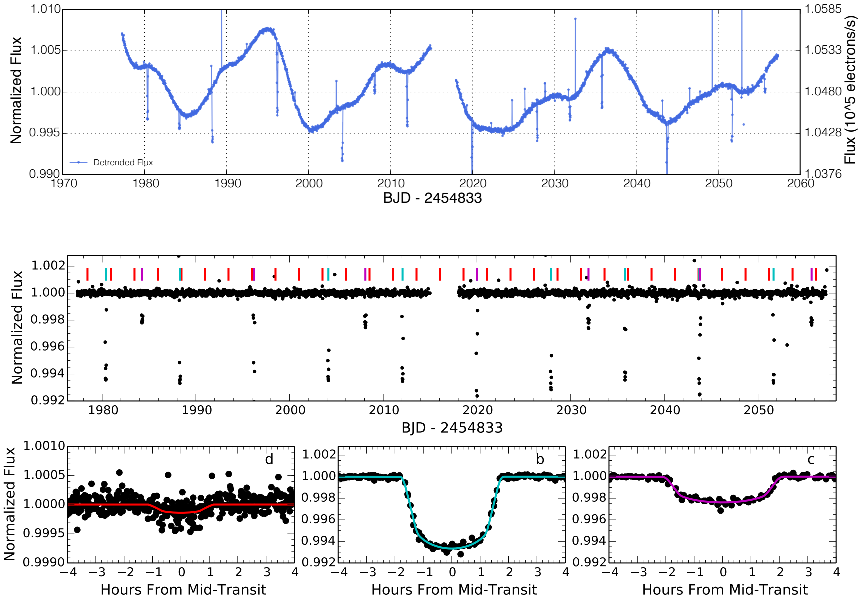

Figure 3.13: *Top*: *K2* photometry for K2-19 after subtracting variations caused by telescope roll. *Middle*: Calibrated *K2* photometry. Vertical ticks indicate times of planet transits. *Bottom*: Phase-folded photometry and best fitting light curves for each planet.

Table 3.10. Planet properties, K2-19

Parameter	Planet b	Planet c	Planet d	Units
Transit Model				
T_0	813.3837 ± 0.0003	817.2755 ± 0.0051	808.9207 ± 0.0086	$\mathrm{BJD_{TDB}}{-}2456000$
P	7.91940 ± 0.00005	11.90715 ± 0.00150	2.50856 ± 0.00041	d
i	89.47 ± 0.41	$87.99^{+1.42}_{-1.99}$	$85.83^{+2.97}_{-4.74}$	deg
$R_p/R_\star$	$0.07540^{+0.00060}_{-0.00043}$	$0.04727^{+0.00568}_{-0.00352}$	0.01109 ± 0.00116	–
$R_\star/a$	$0.0540^{+0.0021}_{-0.0010}$	$0.0553^{+0.0287}_{-0.0121}$	$0.1277^{+0.0586}_{-0.0254}$	–
u	0.48 ± 0.03	0.64 ± 0.05	0.64 ± 0.05	–
b	0.17 ± 0.12	$0.63^{+0.20}_{-0.39}$	$0.59^{+0.26}_{-0.38}$	–
t_{14}	3.502 ± 0.063	$4.371^{+0.939}_{-0.396}$	2.170 ± 0.328	hrs
R_p	7.74 ± 0.39	$4.86^{+0.62}_{-0.44}$	1.14 ± 0.13	$R_\oplus$
$\rho_{\star,\mathrm{circ}}$	$1.91^{+0.12}_{-0.21}$	$0.79^{+0.87}_{-0.56}$	$1.44^{+1.36}_{-0.97}$	$\mathrm{g\,cm^{-3}}$
Derived Properties				
a	0.0740 ± 0.0012	0.0971 ± 0.0016	0.0344 ± 0.0006	AU
S_{inc}	125.9 ± 14.4	73.1 ± 8.4	583.5 ± 66.7	$S_\oplus$
T_{eq}	854 ± 24	745 ± 21	1252 ± 36	K

Same footnotes as Table 3.7

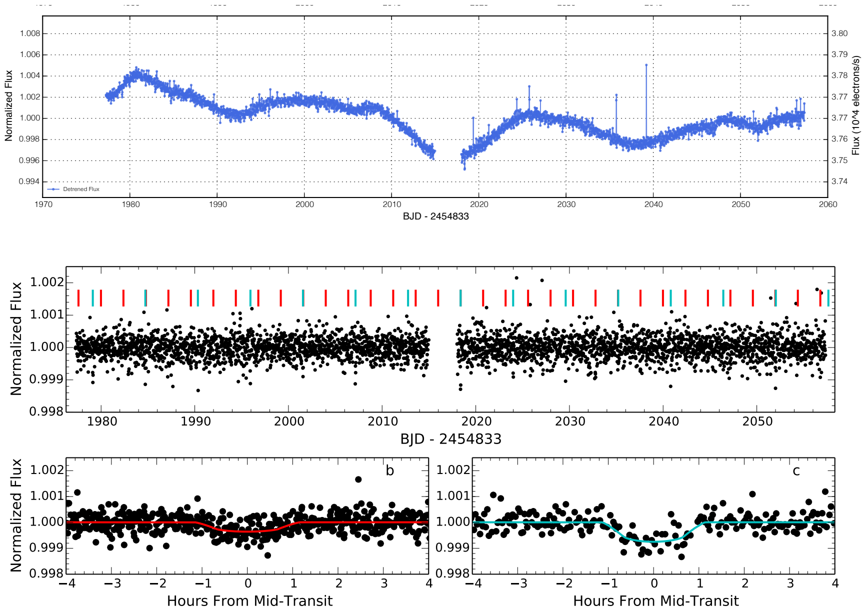

Figure 3.14: *Top*: *K2* photometry for K2-35 after subtracting variations caused by telescope roll. *Middle*: Calibrated *K2* photometry. Vertical ticks indicate times of planet transits. *Bottom*: Phase-folded photometry and best fitting light curves for each planet.

Table 3.11. Planet properties, K2-35

Parameter	Planet b	Planet c	Units
Transit Model			
T_0	810.5871 ± 0.0085	812.1158 ± 0.0049	$\mathrm{BJD_{TDB}}{-}2456000$
P	2.39984 ± 0.00039	5.60912 ± 0.00071	d
i	$86.10^{+2.67}_{-4.43}$	$87.85^{+1.51}_{-2.25}$	deg
$R_p/R_\star$	$0.01777^{+0.00234}_{-0.00166}$	$0.02661^{+0.00407}_{-0.00266}$	–
$R_\star/a$	$0.1237^{+0.0539}_{-0.0230}$	$0.0575^{+0.0319}_{-0.0133}$	–
u	0.72 ± 0.05	0.72 ± 0.05	–
b	$0.56^{+0.26}_{-0.35}$	$0.66^{+0.20}_{-0.40}$	–
t_{14}	2.064 ± 0.308	$2.050^{+0.343}_{-0.227}$	hrs
R_p	1.40 ± 0.17	$2.09^{+0.33}_{-0.24}$	$R_\oplus$
$\rho_{\star,\mathrm{circ}}$	1.73 ± 1.31	$3.16^{+3.79}_{-2.32}$	$\mathrm{g\,cm^{-3}}$
Derived Properties			
a	0.0320 ± 0.0005	0.0564 ± 0.0009	AU
S_{inc}	217.4 ± 25.5	70.1 ± 8.2	$S_\oplus$
T_{eq}	979 ± 29	737 ± 22	K

Same footnotes as Table 3.7

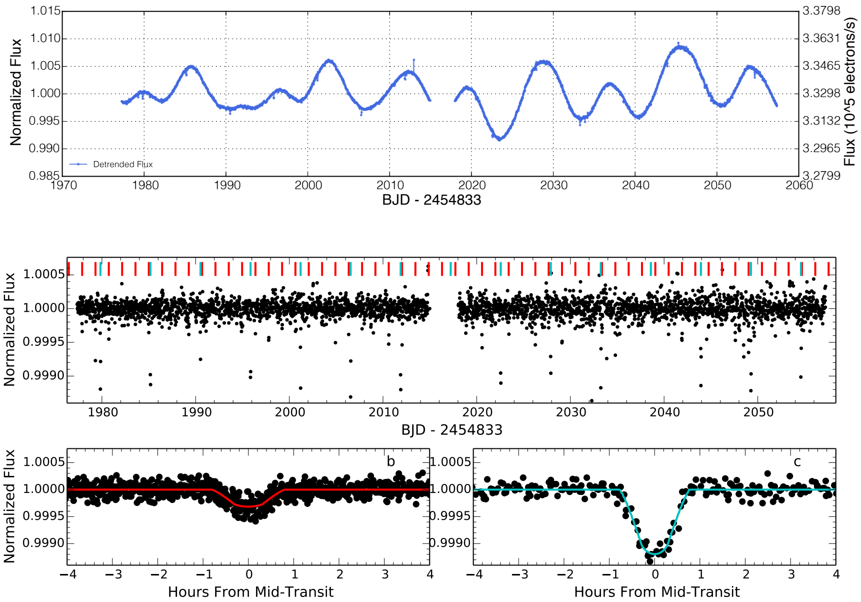

Figure 3.15: *Top*: *K2* photometry for K2-36 after subtracting variations caused by telescope roll. *Middle*: Calibrated *K2* photometry. Vertical ticks indicate times of planet transits. *Bottom*: Phase-folded photometry and best fitting light curves for each planet.

Table 3.12. Planet properties, K2-36

Parameter	Planet b	Planet c	Units
Transit Model			
T_0	809.4684 ± 0.0017	812.8422 ± 0.0008	$\mathrm{BJD_{TDB}}{-}2456000$
P	1.42266 ± 0.00005	5.34059 ± 0.00010	d
i	$87.75^{+1.62}_{-2.40}$	$88.33^{+1.19}_{-1.63}$	deg
$R_p/R_\star$	$0.01625^{+0.00093}_{-0.00060}$	$0.03468^{+0.00515}_{-0.00362}$	–
$R_\star/a$	$0.1124^{+0.0201}_{-0.0091}$	$0.0405^{+0.0250}_{-0.0117}$	–
u	0.69 ± 0.05	0.70 ± 0.05	–
b	0.36 ± 0.26	$0.72^{+0.16}_{-0.42}$	–
t_{14}	1.206 ± 0.078	$1.267^{+0.301}_{-0.104}$	hrs
R_p	1.32 ± 0.09	$2.80^{+0.43}_{-0.31}$	$R_\oplus$
$\rho_{\star,\mathrm{circ}}$	$6.57^{+1.89}_{-2.56}$	$9.96^{+17.74}_{-7.60}$	$\mathrm{g\,cm^{-3}}$
Derived Properties			
a	0.0230 ± 0.0004	0.0555 ± 0.0009	AU
S_{inc}	546.3 ± 63.5	93.6 ± 10.9	$S_\oplus$
T_{eq}	1232 ± 36	793 ± 23	K

Same footnotes as Table 3.7

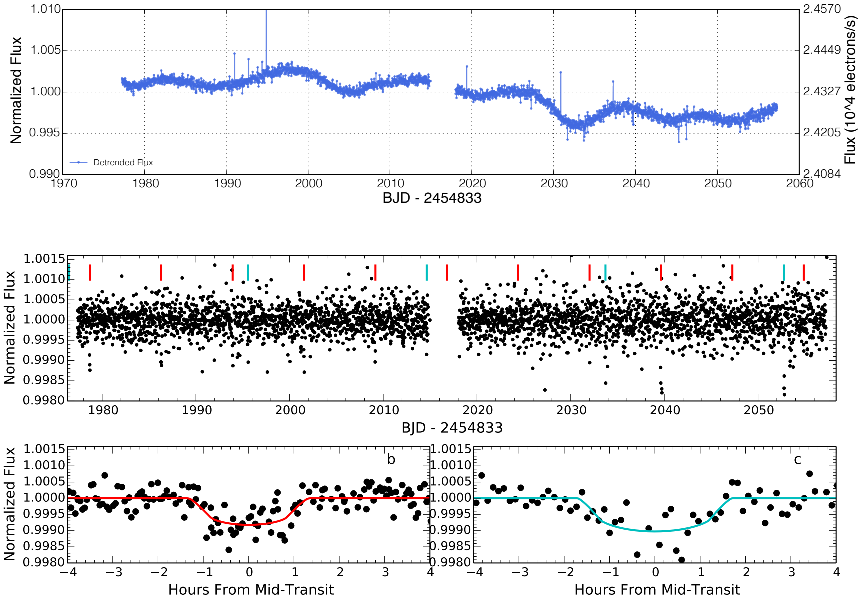

Figure 3.16: *Top*: *K2* photometry for K2-16 after subtracting variations caused by telescope roll. *Middle*: Calibrated *K2* photometry. Vertical ticks indicate times of planet transits. *Bottom*: Phase-folded photometry and best fitting light curves for each planet.

Table 3.13. Planet properties, K2-16

Parameter	Planet b	Planet c	Units
Transit Model			
T_0	811.6871 ± 0.0038	809.4800 ± 0.0091	$\mathrm{BJD_{TDB}}{-}2456000$
P	7.61880 ± 0.00087	19.07863 ± 0.00327	d
i	$87.97^{+1.47}_{-1.86}$	87.83 ± 1.68	deg
$R_p/R_\star$	$0.02796^{+0.00363}_{-0.00259}$	$0.03526^{+0.01553}_{-0.00650}$	–
$R_\star/a$	$0.0525^{+0.0268}_{-0.0127}$	$0.0439^{+0.0285}_{-0.0210}$	–
u	0.71 ± 0.05	0.72 ± 0.05	–
b	$0.68^{+0.18}_{-0.43}$	$0.86^{+0.07}_{-0.46}$	–
t_{14}	$2.487^{+0.382}_{-0.225}$	$3.859^{+1.640}_{-0.728}$	hrs
R_p	2.02 ± 0.24	$2.54^{+1.12}_{-0.47}$	$R_\oplus$
$\rho_{\star,\mathrm{circ}}$	$2.25^{+2.90}_{-1.59}$	$0.61^{+3.71}_{-0.48}$	$\mathrm{g\,cm^{-3}}$
Derived Properties			
a	0.0667 ± 0.0011	0.1229 ± 0.0021	AU
S_{inc}	44.5 ± 5.2	13.1 ± 1.5	$S_\oplus$
T_{eq}	658 ± 19	485 ± 14	K

Same footnotes as Table 3.7

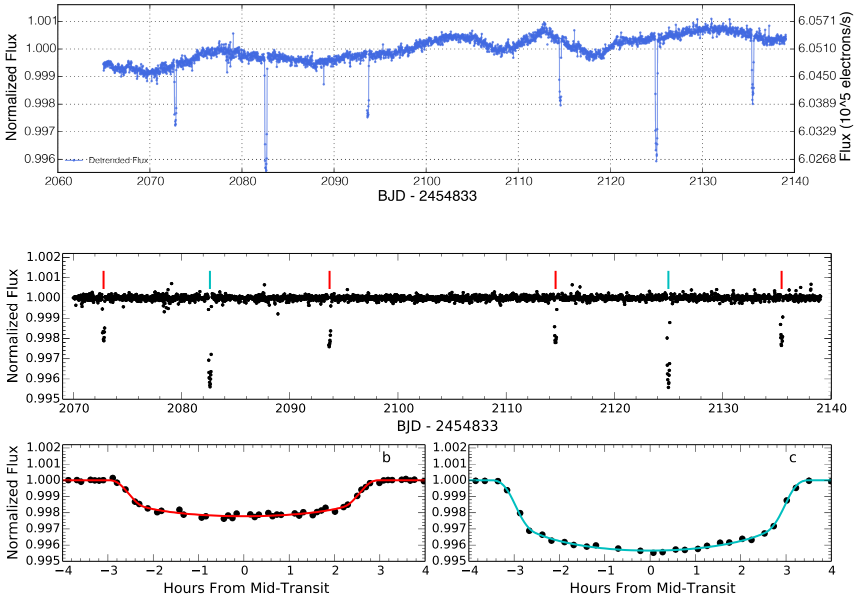

Figure 3.17: *Top*: *K2* photometry for K2-24 after subtracting variations caused by telescope roll. *Middle*: Calibrated *K2* photometry. Vertical ticks indicate times of planet transits. *Bottom*: Phase-folded photometry and best fitting light curves for each planet.

Table 3.14. Planet properties, K2-24

Parameter	Planet b	Planet c	Units
Transit Model			
T_0	905.7950 ± 0.0007	915.6250 ± 0.0005	$\mathrm{BJD_{TDB}}{-}2456000$
P	20.88508 ± 0.00036	42.36342 ± 0.00063	d
i	88.95 ± 0.62	$89.43^{+0.26}_{-0.17}$	deg
$R_p/R_\star$	0.04409 ± 0.00146	0.06147 ± 0.00122	–
$R_\star/a$	$0.0388^{+0.0062}_{-0.0041}$	0.0224 ± 0.0017	–
u	0.56 ± 0.03	0.57 ± 0.02	–
b	$0.47^{+0.16}_{-0.27}$	$0.44^{+0.09}_{-0.18}$	–
t_{14}	$5.881^{+0.269}_{-0.187}$	7.058 ± 0.179	hrs
R_p	5.83 ± 0.60	8.10 ± 0.82	$R_\oplus$
$\rho_{\star,\mathrm{circ}}$	0.74 ± 0.28	$0.94^{+0.27}_{-0.18}$	$\mathrm{g\,cm^{-3}}$
Derived Properties			
a	0.1542 ± 0.0026	0.2471 ± 0.0041	AU
S_{inc}	60.1 ± 12.4	23.4 ± 4.8	$S_\oplus$
T_{eq}	709 ± 36	560 ± 29	K

Same footnotes as Table 3.7

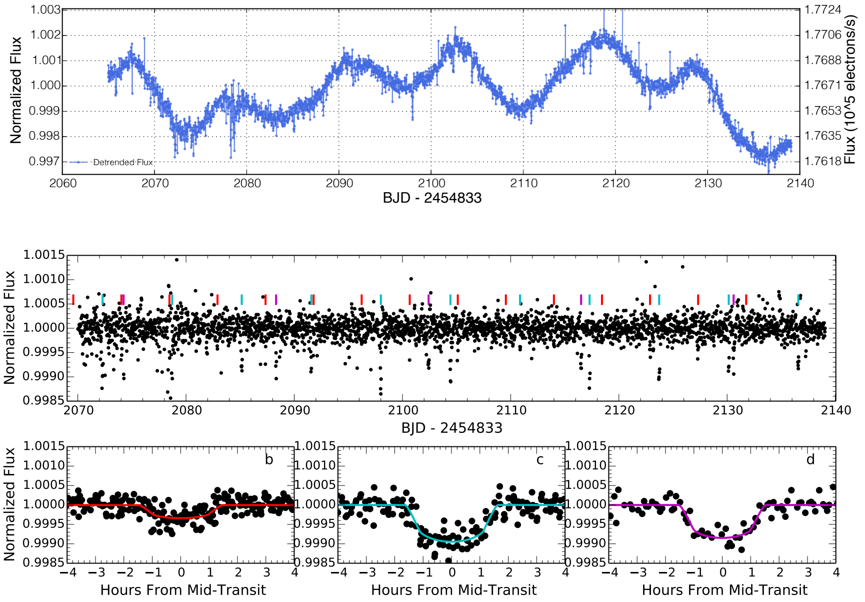

Figure 3.18: *Top*: *K2* photometry for K2-37 after subtracting variations caused by telescope roll. *Middle*: Calibrated *K2* photometry. Vertical ticks indicate times of planet transits. *Bottom*: Phase-folded photometry and best fitting light curves for each planet.

Table 3.15. Planet properties, K2-37

Parameter	Planet b	Planet c	Planet d	Units
Transit Model				
T_0	893.7013 ± 0.0080	898.8603 ± 0.0023	907.2315 ± 0.0031	$\mathrm{BJD_{TDB}}{-}2456000$
P	4.44117 ± 0.00075	6.42904 ± 0.00036	14.09189 ± 0.00135	d
i	$87.28^{+1.95}_{-3.37}$	$87.37^{+1.83}_{-2.50}$	$88.34^{+1.18}_{-1.65}$	deg
$R_p/R_\star$	$0.01728^{+0.00188}_{-0.00109}$	$0.02955^{+0.00312}_{-0.00187}$	0.02950 ± 0.00351	–
$R_\star/a$	$0.0878^{+0.0420}_{-0.0135}$	$0.0739^{+0.0340}_{-0.0147}$	$0.0382^{+0.0259}_{-0.0123}$	–
u	0.64 ± 0.05	0.64 ± 0.05	0.64 ± 0.05	–
b	$0.55^{+0.27}_{-0.36}$	$0.62^{+0.21}_{-0.39}$	$0.76^{+0.14}_{-0.43}$	–
t_{14}	$2.706^{+0.325}_{-0.222}$	$3.127^{+0.457}_{-0.198}$	$2.967^{+0.728}_{-0.261}$	hrs
R_p	1.61 ± 0.17	2.75 ± 0.27	2.73 ± 0.36	$R_\oplus$
$\rho_{\star,\mathrm{circ}}$	1.42 ± 0.95	$1.13^{+1.07}_{-0.77}$	$1.71^{+3.80}_{-1.34}$	$\mathrm{g\,cm^{-3}}$
Derived Properties				
a	0.0511 ± 0.0009	0.0654 ± 0.0011	0.1103 ± 0.0018	AU
S_{inc}	213.3 ± 27.8	130.3 ± 16.9	45.7 ± 6.0	$S_\oplus$
T_{eq}	974 ± 32	861 ± 28	663 ± 22	K

Same footnotes as Table 3.7

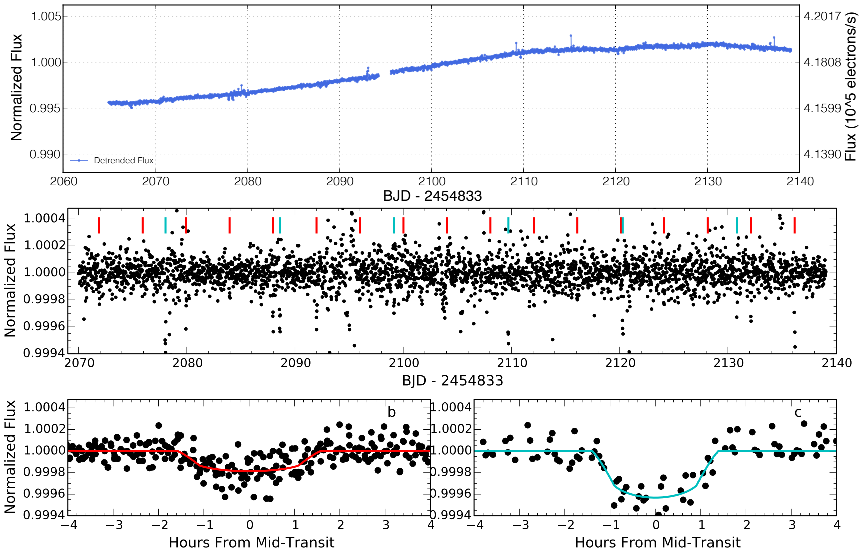

Figure 3.19: *Top*: *K2* photometry for K2-38 after subtracting variations caused by telescope roll. *Middle*: Calibrated *K2* photometry. Vertical ticks indicate times of planet transits. *Bottom*: Phase-folded photometry and best fitting light curves for each planet.

Table 3.16. Planet properties, K2-38

Parameter	Planet b	Planet c	Units
Transit Model			
T_0	896.8786 ± 0.0054	900.4752 ± 0.0033	$\mathrm{BJD_{TDB}}$–2456000
P	4.01593 ± 0.00050	10.56103 ± 0.00090	d
i	$87.28^{+1.88}_{-3.08}$	$88.61^{+1.00}_{-1.67}$	deg
$R_p/R_\star$	$0.01281^{+0.00105}_{-0.00064}$	$0.02004^{+0.00236}_{-0.00135}$	–
$R_\star/a$	$0.0993^{+0.0340}_{-0.0117}$	$0.0381^{+0.0234}_{-0.0079}$	–
u	0.62 ± 0.05	0.61 ± 0.05	–
b	0.48 ± 0.30	$0.64^{+0.23}_{-0.41}$	–
t_{14}	2.861 ± 0.220	$2.533^{+0.312}_{-0.144}$	hrs
R_p	1.55 ± 0.16	2.42 ± 0.29	$R_\oplus$
$\rho_{\star,\mathrm{circ}}$	$1.20^{+0.55}_{-0.70}$	3.06 ± 2.71	$\mathrm{g\,cm^{-3}}$
Derived Properties			
a	0.0506 ± 0.0008	0.0964 ± 0.0016	AU
S_{inc}	465.9 ± 80.1	128.3 ± 22.1	$S_\oplus$
T_{eq}	1184 ± 51	858 ± 37	K

Same footnotes as Table 3.7

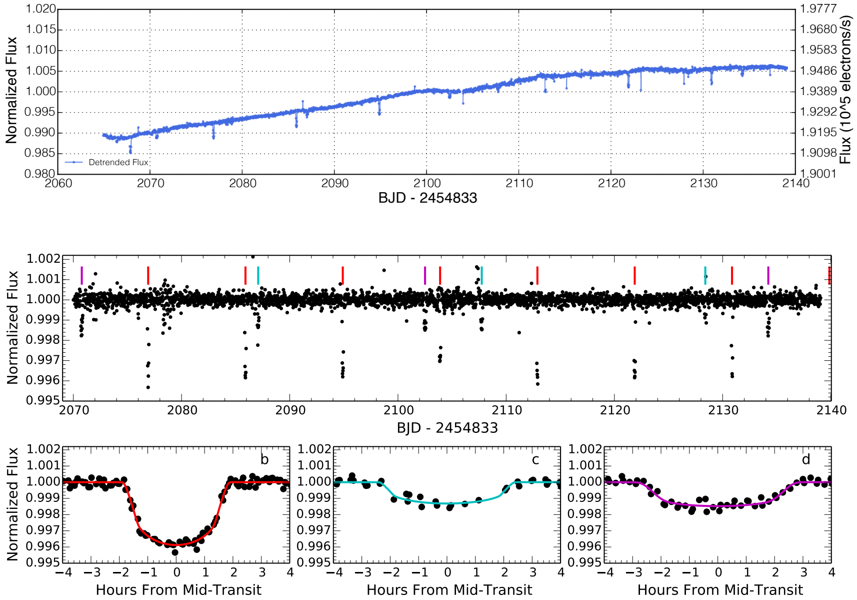

Figure 3.20: *Top*: *K2* photometry for K2-32 after subtracting variations caused by telescope roll. *Middle*: Calibrated *K2* photometry. Vertical ticks indicate times of planet transits. *Bottom*: Phase-folded photometry and best fitting light curves for each planet.

Table 3.17. Planet properties, K2-32

Parameter	Planet b	Planet c	Planet d	Units
Transit Model				
T_0	900.9258 ± 0.0009	899.4306 ± 0.0101	903.7846 ± 0.0031	$\mathrm{BJD_{TDB}}{-}2456000$
P	8.99218 ± 0.00020	20.65614 ± 0.00598	31.71922 ± 0.00236	d
i	$89.00^{+0.69}_{-0.90}$	$88.23^{+1.32}_{-2.68}$	$88.40^{+1.06}_{-0.65}$	deg
$R_p/R_\star$	$0.05635^{+0.00243}_{-0.00111}$	$0.03636^{+0.01024}_{-0.00384}$	$0.04004^{+0.00279}_{-0.00474}$	–
$R_\star/a$	$0.0526^{+0.0078}_{-0.0029}$	$0.0420^{+0.0427}_{-0.0132}$	0.0355 ± 0.0114	–
u	0.66 ± 0.04	0.66 ± 0.05	0.66 ± 0.05	–
b	0.33 ± 0.22	$0.74^{+0.18}_{-0.46}$	$0.79^{+0.07}_{-0.37}$	–
t_{14}	$3.693^{+0.193}_{-0.105}$	$5.024^{+2.307}_{-0.492}$	5.990 ± 0.729	hrs
R_p	5.38 ± 0.35	$3.48^{+0.97}_{-0.42}$	3.75 ± 0.40	$R_\oplus$
$\rho_{\star,\mathrm{circ}}$	$1.61^{+0.30}_{-0.54}$	$0.60^{+1.24}_{-0.52}$	$0.42^{+1.15}_{-0.22}$	$\mathrm{g\,cm^{-3}}$
Derived Properties				
a	0.0808 ± 0.0013	0.1407 ± 0.0024	0.1873 ± 0.0031	AU
S_{inc}	82.9 ± 10.6	27.4 ± 3.5	15.4 ± 2.0	$S_\oplus$
T_{eq}	769 ± 25	583 ± 19	505 ± 16	K

Same footnotes as Table 3.7

CHAPTER 4
K2-66b AND K2-106b: TWO EXTREMELY HOT SUB-NEPTUNE-SIZE PLANETS WITH HIGH DENSITIES

This chapter is a reproduction of Sinukoff et al. (2017a).

4.1 Introduction

Approximately one third of Sun-like stars host planets between the size of Earth and Neptune ("sub-Neptunes") with orbital periods $P < 100$ days (Howard et al., 2012; Fressin et al., 2013; Petigura et al., 2013b; Burke et al., 2015). Most sub-Neptunes detected to date were discovered by the prime *Kepler* mission (2009–2013). While *Kepler* provided a detailed measure of the distribution of planet radii, only a few tens of stars hosting sub-Neptunes were bright enough for secure mass-measurements by current generation precision radial velocity (RV) facilities (e.g. Marcy et al., 2014b). Many other planets have masses measured from transit timing variations (TTVs, Holman & Murray, 2005; Agol et al., 2005), a technique that is limited to compact, multiplanet systems (e.g. Carter et al., 2012; Hadden & Lithwick, 2014).

Mass and radius measurements yield planet densities, which can be used to infer bulk compositions and probe planet formation histories. From the dozens of sub-Neptunes with measured densities, bulk compositional trends have become apparent. Most notably, the majority of planets smaller than $\approx 1.6\,R_\oplus$ have primarily rocky compositions, whereas most larger planets have lower densities, consistent with the presence of extended envelopes of H/He and other low-density volatiles (Weiss & Marcy, 2014; Marcy et al., 2014b; Rogers, 2015; Dressing et al., 2015).

This overall trend in bulk compositions likely has a temperature dependence, which has yet to be fully explored. The gaseous envelopes of planets at extreme temperatures are subjected to photoevaporation by the incident radiation from their host stars (e.g. Owen & Wu, 2013; Lopez & Fortney, 2014). Probing planets at extreme temperatures is crucial to understand these sculpting effects and the formation histories of planets close to their host stars. If these planets did form as mini-Neptunes and/or giant planets, studying the masses and compositions of their remnants provides insight into the nature of the cores of such planets, specifically the mechanisms that formed them, put them so close to their host stars, and removed their surrounding envelopes.

Recent studies of planet occurrence as a function of radius and temperature have shed light on the formation and evolution of sub-Neptunes. The prime *Kepler* mission revealed that the occurrence of 2–4 $R_\oplus$ planets drops significantly at very short orbital periods (P¡ 10 days, Howard et al., 2012; Fressin et al., 2013). Moreover, from a study of Kepler planets and planet candidates, including 157 with astroseismically characterized host stars, Lundkvist et al. (2016) reported a complete absence of planets with radii 2.2–3.8 $R_\oplus$ and incident fluxes $S_{\mathrm{inc}} > 650\ S_\oplus$. Evolutionary models have explained this gap as a "photoevaporation desert", because planets in this size and temperature regime have their envelopes stripped by photoevaporation (Owen & Wu, 2013; Lopez & Fortney, 2013). Alternatively, smaller planet cores might form too late and/or too close to the star to accrete much gas and grow in size (Lee & Chiang, 2016).

Another rare sub-class of small planets are those with orbital periods $P < 1$ day, known as "ultra-short-period" planets (hereafter USPs). They exist around $\sim 1\%$ of Sun-like stars (Sanchis-Ojeda et al., 2014). While it is unclear how USPs form and how they end up so close to the star, there are several observational clues: Systems with USPs commonly host additional planets, which might have played a role in their formation and/or migration histories. Moreover, Sanchis-Ojeda et al. (2014) measured a sharp decrease in the occurrence of USPs larger than $\sim 1.4\,R_{\oplus}$, and a complete lack of USPs $>2.0\,R_{\oplus}$. Lopez (2017) showed that the observed dearth of USPs $R_P = 2$–$4\,R_{\oplus}$ suggests that they formed with water-poor H/He envelopes that were subsequently lost via photoevaporation.

Bulk density measurements of these two rare types of sub-Neptunes can reveal whether they are bare cores, or contain a significant amount of volatiles. Unfortunately, there have been few opportunities to study their compositions. The few of them discovered in the prime *Kepler* field orbit stars too faint for spectroscopic follow-up. However, in 2014, NASA's *K2* mission began a new chapter in the search for planets orbiting bright stars. The *Kepler* spacecraft has been collecting precise photometry of numerous fields along the ecliptic plane, each for nearly three continuous months (Howell et al., 2014). With 10,000–20,000 stars per campaign, hundreds of transiting planet candidates have been discovered (Vanderburg et al., 2015; Pope et al., 2016; Barros et al., 2016; Adams et al., 2016a), many of which have been statistically validated or confirmed as planets (Sinukoff et al., 2016; Crossfield et al., 2016). This includes several USPs around bright stars amenable to Doppler spectroscopy, including WASP-47e (Becker et al., 2015; Dai et al., 2015; Sinukoff et al., 2017b) and HD 3167b (Vanderburg et al., 2016b). *K2* also provides an opportunity to probe the compositions of planets in and at the boundaries of the photoevaporation desert.

Here we report the first mass and density measurements of a planet in the photoevaporation desert as well as the mass and density of a USP planet in a multiplanet system. K2-66 (EPIC 206153219) is a G1 subgiant star in *K2* Campaign 3 (C3), which hosts a transiting sub-Neptune in the photoevaporation desert. K2-106 (EPIC 220674823) is a G-star in *K2* Campaign 8 (C8) with two transiting sub-Neptunes, including a USP sub-Neptune (K2-106b). We note that K2-66b was first reported as a planet candidate by Vanderburg et al. (2015) and statistically validated by Crossfield et al. (2016). Both K2-106 planets were first reported and statistically validated by Adams et al. (2016b) as part of the Short-Period Planets Group effort (SuPerPiG).

In §5.2 we describe the methods by which we generate stellar light curves from raw *K2* photometry and summarize our adaptive optics imaging and Doppler observations. §5.3 explains our analysis of the resulting light curves, AO images, and RV time-series to precisely characterize the host stars and determine planet masses and radii. In §5.4, we present our results, discuss possible planet compositions, and place these planets in context with other sub-Neptunes. Concluding statements are provided in §6.6.

4.2 Observations

4.2.1 *K2* Photometry

NASA's *Kepler* Telescope collected nearly continuous photometry of K2-66 from 2014 November 15 – 2015 January 23 UT (69 days) as part of *K2* Campaign 3. K2-106 was observed from 2016 January 04 – 2016 March 23 UT (80 days) as part of *K2* Campaign 8. We generated stellar light curves from the respective target pixel files using the same procedures detailed in Sinukoff et al. (2016) and Crossfield et al. (2016). The same Gaussian process was used to model and subtract the spacecraft motion from *K2* pixel data. We use the same K2-66 light curve presented in Crossfield et al. (2016), so we do not display it in this work.

4.2.2 Adaptive Optics Imaging

We observed K2-106 on 2016 August 24 UT with the high-contrast adaptive optics (AO) system on the Keck-II telescope using the NIRC2 imaging instrument (PI: Keith Matthews). The images were obtained in the narrow camera mode using a 3-point dither pattern with nods of $2''$ in each cardinal direction to remove background light. The K$_s$ filter was used for all observations. Conditions were foggy and the star was at airmass 1.2 with seeing of 0.″8 during the observations. Crossfield et al. (2016) presented NIRC2 adaptive optics imaging of K2-66 obtained by our group, which we do not show here. The star was found to be single. Moreover, Adams et al. (2016b) presented similar NIRC2 observations of K2-106, finding no evidence of secondary sources.

4.2.3 Radial Velocity Measurements

RV measurements of K2-66 and K2-106 were made using HIRES (Vogt et al., 1994) at the W. M. Keck Observatory. We collected 38 RV measurements of K2-66 from 2015 September 20 UT to 2017 January 07 UT and 35 RV measurements of K2-106 from 2016 August 12 UT to 2017 January 22 UT. Observations and data reduction followed the usual methods of the California Planet Search (CPS; Howard et al., 2010a). An iodine cell was used for each observation as a wavelength calibrator and point spread function (PSF) reference. The "C2" decker (0.″87 × $14''$ slit) provided spectral resolution $R \approx 55{,}000$ and allowed for the sky background to be measured and subtracted. An exposure meter was used to automatically terminate exposures after reaching a target signal-to-noise ratio (SNR) per pixel at 550 nm. Most K2-66 exposures were terminated at SNR $\approx$ 100 and typically lasted 20 min. K2-106 exposures proceeded until SNR $\approx$ 125 ($\sim$ 25 min).

For each star, a single iodine-free exposure was taken at roughly twice the SNR using the "B3" decker ($0\farcs57 \times 14''$ slit). The standard CPS Doppler pipeline was used to measure RVs (Marcy & Butler, 1992; Valenti et al., 1995; Butler et al., 1996; Howard et al., 2009). RV measurements are listed in Tables 4.1 and 4.2 for K2-66 and K2-106, respectively.

4.3 Analysis

Here we describe the methods used to characterize planet host stars and to model our *K2* light curves and RV time series. Measured stellar parameters, light curve model parameters, and RV model parameters are listed in Tables 4.3 and 4.4 for K2-66 and K2-106, respectively.

4.3.1 Stellar characterization

From the iodine-free HIRES spectra, we measured the effective temperature ($T_{\rm eff}$), surface gravity ($\log g$), and metallicity ([Fe/H]) of K2-66 and K2-106, using the updated "Spectroscopy Made Easy" (SME) analysis tool described in Brewer et al. (2016). Previous comparison of SME results with astroseismic results demonstrated $\log g$ values accurate to 0.05 dex (Brewer et al., 2015). Stellar masses and radii were estimated using the `isochrones` Python package (Morton, 2015b), which fit our $T_{\rm eff}$, $\log g$, and [Fe/H] measurements to a grid of models from the Dartmouth Stellar Evolution Database (Dotter et al., 2008). **Posteriors were sampled using the `emcee` Markov Chain Monte Carlo (MCMC) package (Foreman-Mackey et al., 2013). The adopted uncertainties on stellar mass and radius correspond to 68.3% (1σ) confidence intervals of the resulting posterior distributions.** For K2-66, we measure a mass $M_\star = 1.11 \pm 0.04\,{\rm M}_\odot$ and radius $R_\star = 1.67 \pm 0.12\,{\rm R}_\odot$. These are consistent with the values $M_\star = 1.16 \pm 0.05\,{\rm M}_\odot$, and $R_\star = 1.71 \pm 0.14\,{\rm R}_\odot$ reported by Crossfield et al. (2016), who used the SpecMatch algorithm (Petigura, 2015) instead of SME. For K2-106, we measure a mass of $0.92 \pm 0.03\,{\rm M}_\odot$ and radius of $0.95 \pm 0.05\,{\rm R}_\odot$. Adams et al. (2016b) measured $M_\star = 0.93 \pm 0.01\ {\rm M}_\odot$, which is consistent with our measurement, but they estimated $R_\star = 0.83 \pm 0.04\,{\rm R}_\odot$, which is smaller than our measurement at the ~ 2.5-σ level (see discussion in §4.4.2).

To test for spectroscopic blends, we used the algorithm of Kolbl et al. (2015) to search for multiple sets of stellar lines. For both K2-66 and K2-106, we ruled out the possibility of companions in the $0\farcs87 \times 14''$ HIRES slit with $T_{\rm eff} = 3400$–$6100\,{\rm K}$, down to 1% contrast in V and R bands, and $\Delta RV > 10$ m s^{-1}.

The magnetic activity of each star was assessed by measuring $S_{\rm HK}$indices using the Ca II H & K spectral lines (Isaacson & Fischer, 2010). The $S_{\rm HK}$measurements are listed in Tables 4.1 and 4.2 for K2-66 and K2-106 respectively. The median $S_{\rm HK}$values from all spectra are 0.128 and 0.140. The measured $T_{\rm eff}$ and $S_{\rm HK}$were converted into $\log R'_{\rm HK}$values, a metric of the Ca II flux relative to the photospheric continuum (Middelkoop, 1982; Noyes et al., 1984). We measure median $\log R'_{\rm HK}$values

Table 4.1. K2-66 Relative radial velocities, Keck-HIRES

BJD	RV $[\mathrm{m\,s^{-1}}]$	Unc. $[\mathrm{m\,s^{-1}}]$[a]	S_{HK} [b]
2457286.044784	6.58	4.19	N/A
2457580.106140	7.14	2.24	0.127
2457583.113840	-13.31	2.18	0.127
2457585.922824	3.35	2.10	0.128
2457586.022505	2.63	2.17	0.128
2457586.073226	4.15	2.20	0.127
2457587.027388	-8.39	2.06	0.129
2457588.028820	-2.36	2.07	0.128
2457595.974851	9.66	2.63	0.116
2457596.997324	-3.35	4.25	N/A
2457599.015841	-7.50	2.21	0.125
2457600.041053	-0.06	1.99	0.128
2457601.008159	5.21	2.29	0.126
2457612.841886	-8.28	2.64	0.128
2457613.983431	-16.35	2.69	0.131
2457615.860156	6.51	2.99	0.133
2457616.885444	13.79	2.84	0.130
2457622.027461	14.11	3.09	0.126
2457622.093780	-1.18	3.37	0.125
2457651.964266	2.48	2.83	0.135
2457652.025942	9.88	2.80	0.128
2457652.937923	-9.59	2.88	0.133
2457653.926554	-7.16	2.76	0.136
2457653.968022	-7.98	2.67	0.135
2457668.732792	-0.47	2.71	0.118
2457678.880082	-1.04	3.05	0.125
2457679.758736	-0.64	2.65	0.130
2457697.840632	-2.61	2.70	0.124
2457711.713727	-3.43	2.79	0.124
2457712.717828	0.82	2.66	0.127
2457713.715934	5.43	2.68	0.129
2457714.779542	-8.83	3.03	0.128
2457716.765754	2.09	2.95	0.125
2457745.716553	-15.72	2.80	0.127
2457745.763482	-24.08	5.15	N/A
2457746.704085	-1.96	2.73	0.128
2457747.720099	-6.56	2.59	0.127
2457760.710967	-6.37	3.04	0.124

[a] Uncertainties estimated from the dispersion in the radial velocity measured from 718 chunks. These uncertainties do not include "jitter" which is incorporated as a free parameter during the RV modeling (σ_{jit}, Table 4.3).

[b] For three observations, the S_{HK} measurement failed due to a combination of poor seeing, scattered light, and overlapping orders at blue wavelengths. These measurements are listed as N/A.

Table 4.2. K2-106 Relative radial velocities, Keck-HIRES

BJD	RV [m s^{-1}]	Unc. [m s^{-1}][a]	S_{HK}
2457612.932644	-5.04	1.89	0.149
2457613.967264	-3.25	1.58	0.147
2457614.109833	-2.35	1.50	0.150
2457615.925879	-5.08	1.71	0.148
2457616.925922	-3.58	1.66	0.150
2457617.917421	4.13	1.53	0.148
2457618.926340	5.95	1.53	0.147
2457652.069904	10.72	1.53	0.143
2457653.036506	-0.86	1.64	0.139
2457668.986188	-11.42	1.72	0.137
2457671.780051	-24.84	1.94	0.150
2457672.066034	-5.93	1.66	0.152
2457672.780348	-6.86	1.69	0.153
2457672.964502	-12.31	1.61	0.153
2457697.825599	5.88	1.77	0.142
2457711.823439	-16.01	2.31	0.150
2457711.890113	-4.35	1.52	0.139
2457712.000267	1.74	1.94	0.132
2457712.760228	-0.49	1.75	0.137
2457713.803918	4.51	1.85	0.140
2457713.987377	-7.84	1.55	0.141
2457714.817690	1.62	1.57	0.136
2457714.952333	8.26	2.07	0.134
2457716.798647	1.70	1.91	0.139
2457717.971107	-7.35	2.40	0.124
2457718.905031	4.66	2.21	0.132
2457745.786321	1.55	1.80	0.144
2457746.762857	-5.93	1.74	0.135
2457747.817094	-9.04	1.83	0.134
2457761.774749	6.95	1.63	0.138
2457763.715781	-0.96	1.57	0.142
2457764.733619	2.21	1.79	0.139
2457765.800317	5.55	2.94	0.111
2457774.729422	-0.41	1.53	0.138
2457775.725113	2.53	1.65	0.138

[a] Uncertainties estimated from the dispersion in the radial velocity measured from 718 chunks. These uncertainties do not include “jitter” which is incorporated as a free parameter during the RV modeling (σ_{jit}, Table 4.4).

of −5.27 and −5.15 dex, consistent with magnetically quiet stars from the California Planet Search (Isaacson & Fischer, 2010). For comparison, the Sun ranges from log $R'_{\rm HK}$= −5.05 dex to −4.85 dex over a typical magnetic cycle (Meunier et al., 2010).

Our NIRC2 images were processed using a standard flat-field, background subtraction, and image stacking techniques (e.g Crepp et al., 2012). Figure 4.1a displays the final reduced image and angular scale. Both raw and stacked images were examined for companion sources. A speckle to the right of the host star was ruled out as a companion as stacked images in the J-band filter showed it moving as a function of wavelength. Figure 4.1b shows the sensitivity to nearby companions. Contrast levels reach ΔK = 7.7 for separations beyond $0\farcs75$. Adams et al. (2016b) achieve similar contrast limits from K-band observations of K2-106, also with Keck/NIRC2 AO.

4.3.2 Light curve analysis

We fit transit models to the detrended K2-106 light curve using the same MCMC analysis described in Crossfield et al. (2016). In brief, our code employs the Markov Chain Monte Carlo (MCMC) package `emcee` (Foreman-Mackey et al., 2013) and model light curves are generated using the Python package `BATMAN` (Kreidberg, 2015). The model parameters are: time of conjunction ($T_{\rm conj}$), orbital period, eccentricity, inclination, and longitude of periastron (P e, i, and ω), scaled semimajor axis ($a/R_\star$), ratio of planet radius to stellar radius ($R_p/R_\star$), a single multiplicative offset for the absolute flux level, and quadratic limb-darkening coefficients (u_0 and u_1). The detrended K2-106 light curve and fitted transit models for planets b and c are shown in Figure 4.2

4.3.3 RV Analysis

Methodology

To analyze the RV time-series of K2-66 and K2-106, we used the RV fitting package `RadVel` (B. Fulton & E. Petigura, in prep.), which is publicly available on GitHub[1]. `RadVel` is written in object-oriented Python. It uses a fast Kepler equation solver written in C and the affine-invariant sampler (Goodman & Weare, 2010) of the `emcee` package (Foreman-Mackey et al., 2013). `RadVel` is easily adaptable to a variety of maximum-likelihood fitting and MCMC applications. The standard version allows for modeling of multi-planet, multi-instrument RV time-series, and assumes no interaction between planets (e.g. Sinukoff et al., 2017b).

---

[1] https://github.com/California-Planet-Search/radvel
http://radvel.readthedocs.io/en/master/index.html

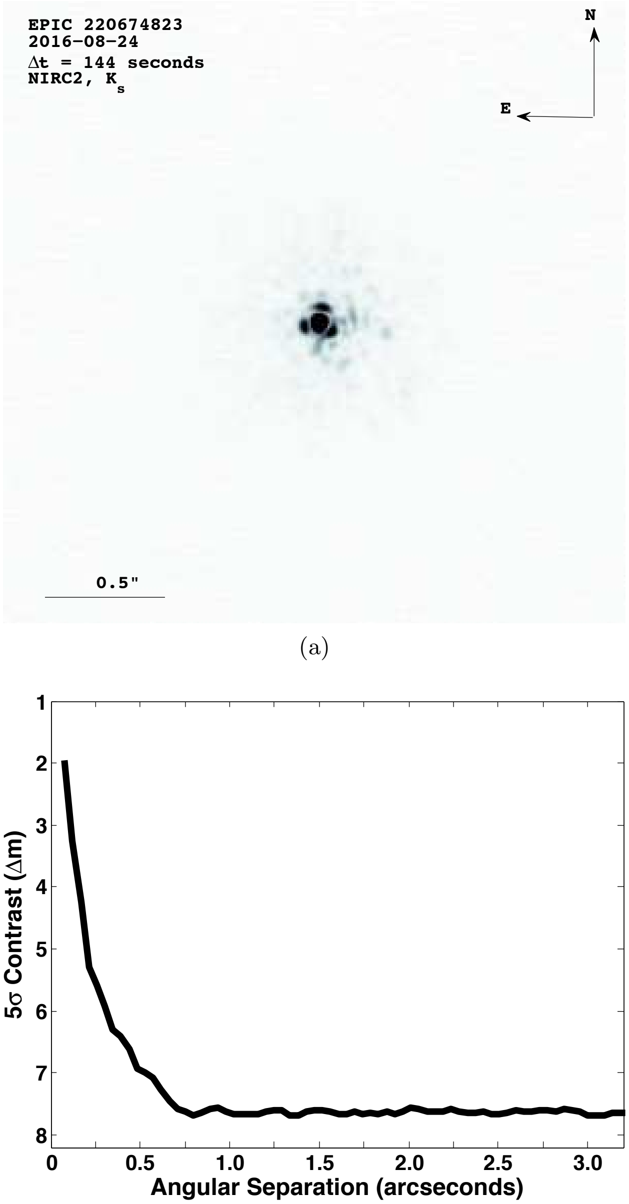

(a)

(b)

Figure 4.1: Keck/NIRC2 K_s-band adaptive optics imaging of K2-106. *(a)* Reduced image, showing no evidence of secondary stars. *(b)* 5σ contrast limits.

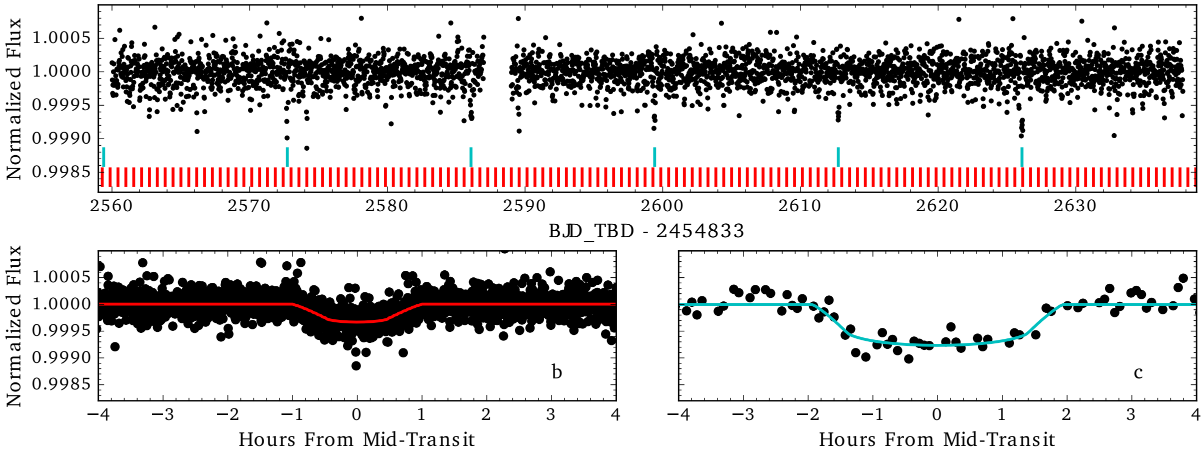

Figure 4.2: *Top*: Calibrated *K2* photometry for K2-106. Vertical ticks indicate the locations of each planets' transits. Bottom: Phase-folded photometry and best-fit light curves for each of the two planets.

We adopt the same likelihood function for RV modeling as Howard et al. (2014):

$$\ln \mathcal{L} = -\sum_i \left[\frac{(v_i - v_m(t_i))^2}{2\left(\sigma_i^2 + \sigma_{\rm jit}^2\right)} + \ln \sqrt{2\pi \left(\sigma_i^2 + \sigma_{\rm jit}^2\right)} \right], \tag{4.1}$$

where v_i and σ_i are the ith RV measurement and corresponding uncertainty, and $v_m(t_i)$ is the Keplerian model velocity at time t_i. The same RV model parameters are used as MCMC step parameters. Before starting the MCMC exploration, we first use the minimization technique of Powell (1964) to find the maximum-likelihood model. Fifty parallel MCMC chains ("walkers") are then initialized by perturbing each of the free parameters from the maximum likelihood values by as much as 3%. An initial round of MCMC exploration continues until the Gelman-Rubin (GR) statistic (Gelman & Rubin, 1992) drops below 1.10, at which point the chains are reset. Following this burn-in phase, the remaining chains are kept and the MCMC run proceeds until the GR $<$ 1.03 and the T_z statistic (Ford, 2006) exceeds 1000 for all free parameters. This ensures that the chains are well-mixed and converged.

The adopted basis for our RV model for both K2-66 and K2-106 is: $\{P, T_{\rm conj}, K, \gamma\}$, where P is orbital period, $T_{\rm conj}$ is the time of conjunction, K is the RV semi-amplitude and γ is a constant RV offset. For K2-106, we fit for P, $T_{\rm conj}$, and K of both planets. We lock the orbital periods and phases at the photometrically measured values in Tables 4.3 and 4.4. Since the orbital ephemeris is tightly constrained from photometry, it made no difference whether we fixed the ephemeris or assigned Gaussian priors according to uncertainties on P and T_{conj}. When testing non-circular orbits, we include two additional model parameters, $\sqrt{e}\cos\omega$ and $\sqrt{e}\sin\omega$, where e is the orbital eccentricity and ω is the longitude of periapsis of the star's orbit. This parameterization mitigates the Lucy-Sweeney bias toward non-zero eccentricity (Lucy & Sweeney, 1971; Eastman et al., 2013). We also search for additional bodies at orbital periods beyond the duration of RV observations by testing RV models that include a constant acceleration term, $\mathrm{d}v/\mathrm{d}t$ (i.e. a linear trend in the RV time series). To assess whether the addition of eccentricity and constant acceleration parameters are warranted, we use the Bayesian Information Criterion (BIC). When comparing models, we lock the RV jitter at the values in Tables 4.3 and 4.4.

In §4.3.3, we discuss our search for additional planets in these two systems. We found no conclusive evidence for additional planets.

K2-66

After testing several different RV model parameterizations for K2-66, we adopt a circular orbit (sinusoidal) model with zero acceleration ($\mathrm{d}v/\mathrm{d}t \equiv 0$). The adopted RV parameters for K2-66 are listed in Table 4.3, including $K = 7.4 \pm 1.2\,\mathrm{m\,s^{-1}}$. The maximum likelihood RV fit is shown in Figure 4.3. When the orbital eccentricity is allowed to float, the MCMC fit yields $e = 0.10^{+0.13}_{-0.07}$, and a planet mass consistent with the circular orbit model. The change in the BIC is $\Delta\mathrm{BIC} = \mathrm{BIC_{ecc}} - \mathrm{BIC_{circ}} = 1.0$, which indicates that the fit does not improve enough to justify the additional free parameters (Kass & Raftery, 1995). Similarly, introducing $\mathrm{d}v/\mathrm{d}t$ as a free parameter yields $\Delta\mathrm{BIC} = \mathrm{BIC}_{\mathrm{d}v/\mathrm{d}t} - \mathrm{BIC}_{\mathrm{d}v/\mathrm{d}t \equiv 0} = -0.7$, indicating no preference for the more complex model. Each of the different RV models that were tested resulted in a planet mass within 0.5σ of the adopted value.

K2-106

The adopted RV model for K2-106 is the sum of two sinusoids (two circular orbits), with $\mathrm{d}v/\mathrm{d}t \equiv 0$. The fitted RV parameters for K2-106 are listed in Table 4.4 and the adopted RV fit is displayed in Figure 4.4. Overall, the choice of model did not significantly affect the planet mass measurements — all of the RV models yielded planet mass constraints consistent with the adopted values. For planet b, we measure $K = 7.2 \pm 1.3\,\mathrm{m\,s^{-1}}$, for a 5.5σ detection. For planet c, we measure $K = 1.6 \pm 1.7\,\mathrm{m\,s^{-1}}$, which is not a reliable detection. From the posterior distribution, we place an upper limit, $K < 6.7\,\mathrm{m\,s^{-1}}$ ($M_P < 24.4\ M_\oplus$) at 99.7% confidence. Due to its proximity to the host star, the orbit of K2-106b has likely been circularized by tidal interactions with the star: We compute a circularization timescale of ≈ 6000 years using (Goldreich & Soter, 1966) assuming the same a tidal quality factor $Q = 100$ estimated for terrestrial planets in the Solar System (Goldreich & Soter, 1966; Henning et al., 2009; Lainey, 2016). Nevertheless, we tested a fit to the RV time series in which the eccentricity of planet b was allowed to float. The MCMC fit yielded $e = 0.11^{+0.11}_{-0.08}$, and a planet mass consistent with the best circular orbit model. Moreover, the eccentric model is not statistically favored (ΔBIC = 0.1). When the eccentricity of planet c was allowed to float, the preferred eccentricity was 0.75 and the MCMC chains did not converge. Any orbit $e \gtrsim 0.35$ would cross the stellar surface. We also ran a trial with $\mathrm{d}v/\mathrm{d}t$ as a free parameter, but found this additional model complexity was not statistically warranted (ΔBIC = 0.2). Finally, since planet c was not significantly detected, we also tried fitting for planet b alone but the measured mass changes by $< 0.5\sigma$.

There are several possible reasons why we do not detect the RV signal of planet c. One possibility is that K is sufficiently small that more data are needed to securely detect the planet. Alternatively, stellar activity on the timescale of the planet's orbital period (13 days) could partially wash out the planet signal. However, our $\log R'_{\mathrm{HK}}$measurement of -5.15 indicates a magnetically quiet star. Finally, the star might host additional planets not included in our RV model.

Search for Additional Planets

We conducted a search for additional planets in both systems using the planet search algorithm described in Howard & Fulton (2016), which utilizes a two-dimensional Keplerian Lomb-Scargle periodogram (2DKLS, O'Toole et al., 2009). The periodogram values represent the difference in χ^2 between an N-planet model (χ^2_N) and an N+1 planet model (χ^2_{N+1}) for each orbital period value. When searching for the first planet in a given system we compare χ^2 for a 1-planet model to χ^2 for a flat line. Figure 4.5 shows the periodograms for $N = 0$ and $N = 1$. We estimate an empirical false alarm probability (eFAP) for any peaks in the 2DKLS periodogram by fitting a log-linear function to a histogram of periodogram values.

For K2-66, we find no evidence of additional planet signals in the RV time series. In the $N = 0$ case, the tallest peak in the periodogram occurs at 5.1 days, corresponding to the known transiting planet K2-66b. For $N = 1$, which tests the 2-planet hypothesis, the tallest peak is at $P = 4.0$ days and has eFAP $> 90\%$. We note that when we tested a 2-planet RV model with an initial period guess of 4.0 days for the second Keplerian, the measured RV semi-amplitude for K2-66b remains consistent with the adopted 1-planet model at $\approx 0.3\ \sigma$. Therefore, even if there is an additional planet at $P \approx 4$ days, it does not significantly influence our mass measurement for K2-66b.

Similarly, for K2-106, our search for additional planets in the RV time-series yields a null result. The periodogram for $N = 0$ has a global maximum at the orbital period of K2-106b (0.57 days). The $N = 1$ periodogram does not have any significant peaks — the tallest is at $P = 35$ days with eFAP $> 90\%$. We conclude that more RV data are needed to confidently detect any additional bodies orbiting K2-106. We note that the measured RV semi-amplitude for K2-106b changes by $< 0.5\sigma$ when a 3-planet RV model is tested with an initial period guess of 35 days for the third Keplerian. Thus, even if there is an additional planet at $P \approx 35$ days, it has a negligible effect on our mass measurement for K2-106b.

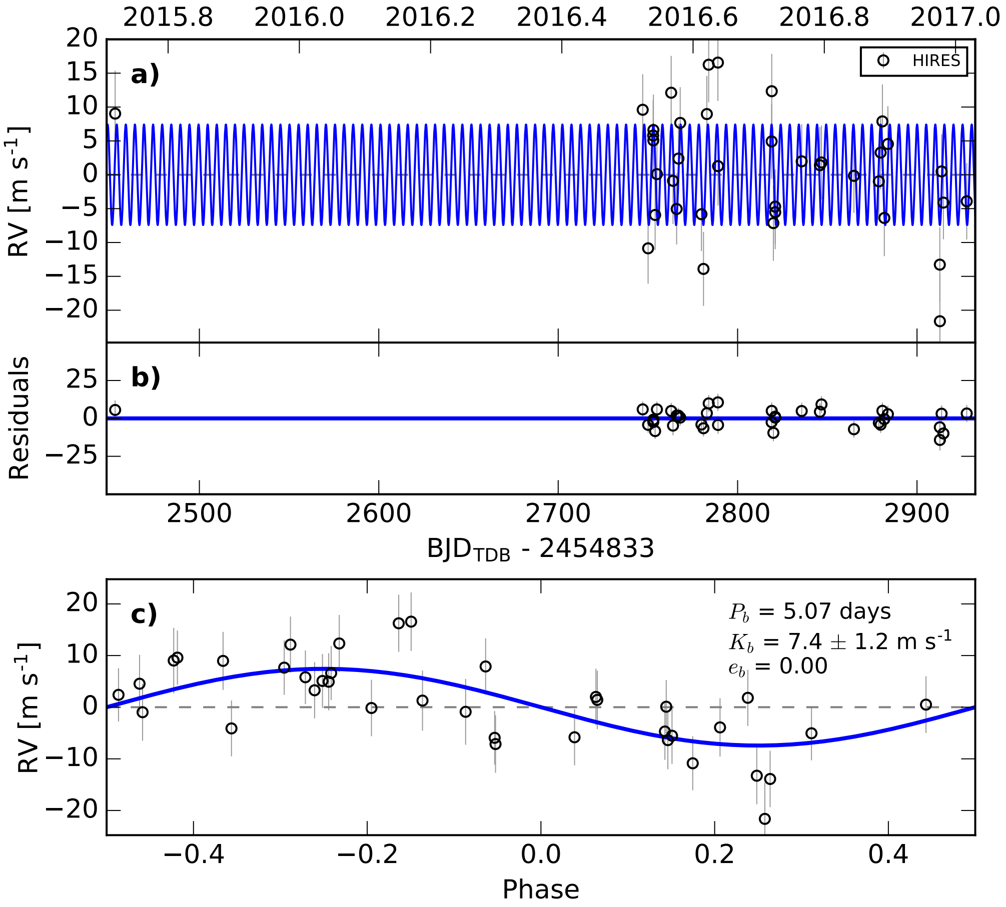

Figure 4.3: Single-planet RV model of K2-66, assuming a circular orbit and adopting the ephemeris from transit fits. *a)* The RV time-series. Open black circles indicate Keck/HIRES data. The solid blue line corresponds to the most likely model. Note that the orbital parameters listed in Table 4.3 are the median values of the posterior distributions. Error bars for each independent dataset include an RV jitter term listed in Table 4.3, which are added in quadrature to the measurement uncertainties. *b)* Residuals to the maximum-likelihood fit. *c)* The RV time-series phase folded at the orbital period of K2-66b.

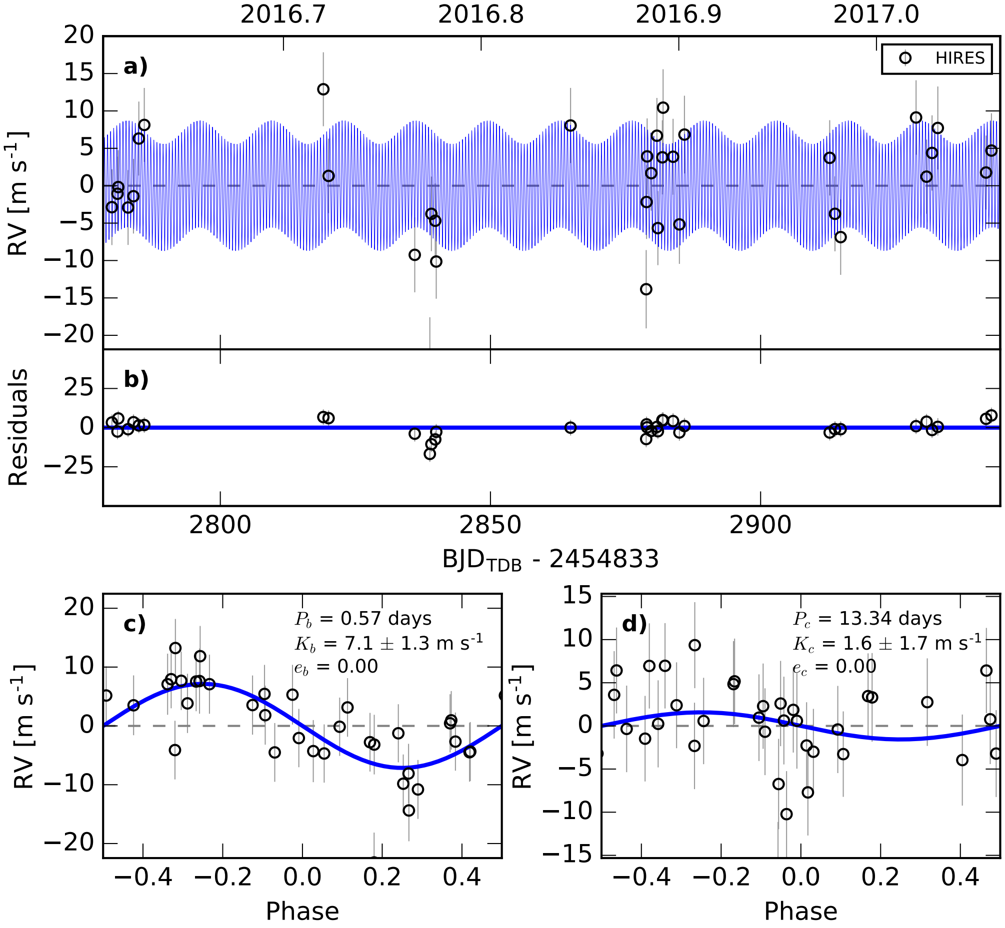

Figure 4.4: Two-planet RV model of K2-106, assuming circular orbits and adopting the ephemerides from transit fits. Details are same as Figure 4.3, with panels c and d showing the phase-folded light curves for planets b and c, after subtracting the signal of the other planet. We do not make a statistically significant measurement of the mass of planet c.

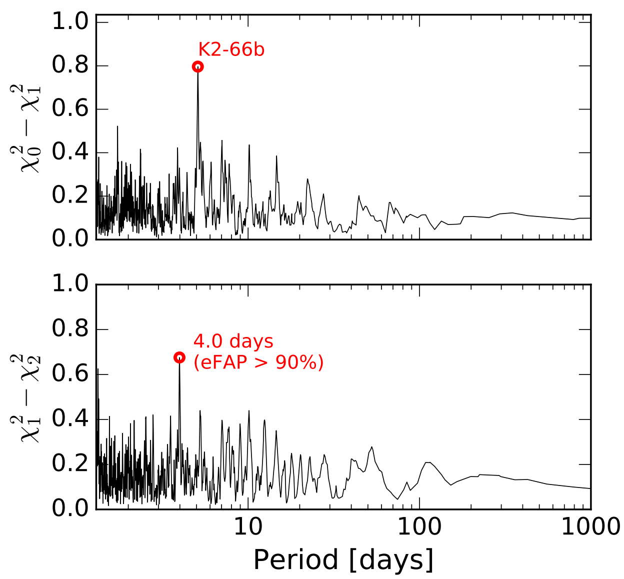

(a) (b)

Figure 4.5: Two-dimensional Keplerian Lomb-Scargle periodograms of the measured RV time series of **a)** K2-66 and **b)** K2-106. Values on the vertical axis represent the difference in χ^2 between an N-planet model (χ^2_N) and an N+1 planet model (χ^2_{N+1}) at each period. The tallest peaks in the $N = 0$ cases (top panels) correspond to the periods of known transiting planets, as labeled. For the $N = 1$ cases (bottom panels), empirical false alarm probabilities (eFAPs) for the tallest peaks are $> 90\%$. They are likely to be spurious signals rather than the signals of additional planets.

4.4 Results & Discussion

4.4.1 No Significant Dilution

Our RV detections of K2-66b and K2-106b confirm that they are bonafide planets. To verify that the planet radius measurements are accurate, we investigated the possibility that the photometric aperture contains a blend of multiple stars. Blends would dilute the transit depth, causing the planet radius to be underestimated (Ciardi et al., 2015). Figure 4.6 shows blend constraints from the spectroscopic analysis, AO images, and RV measurements. Together, these rule out the presence of companions that would significantly alter the measured planet radii. Contrasts in the NIRC2-AO bandpass were converted to the Kepler bandpass and to companion masses using $riJHK$ photometric calibrations of Kraus & Hillenbrand (2007). A blend with Kepler-band contrast $\Delta K_p \lesssim 2$ mag is required for a 10% error in the measured planet radius. Such companions within $\sim$ 100 AU of K2-66 or K2-106 would have been detected as a linear trend in the RV time-series and would have been detected inside $\sim$ 5 AU as secondary lines in the HIRES spectrum. AO imaging rules out problematic companions beyond $\sim$ 10 AU. We note that the plotted constraints from RV observations use Equation 1 of Winn et al. (2010), and conservatively assume dv/dt values equal to the 3-σ upper limits obtained when dv/dt is included as a free model parameter. The only conceivable problematic blend that would be undetected is a companion near apastron of a highly eccentric orbit (hence low dv/dt), at an orbital phase of low projected separation (hence undetected in AO images) and with a spectrum similar to that of the primary star (hence undetected spectral lines). However, such a scenario is highly improbable and we conclude that the likelihood of a problematic blend is negligibly low.

4.4.2 Planetary Bulk Compositions

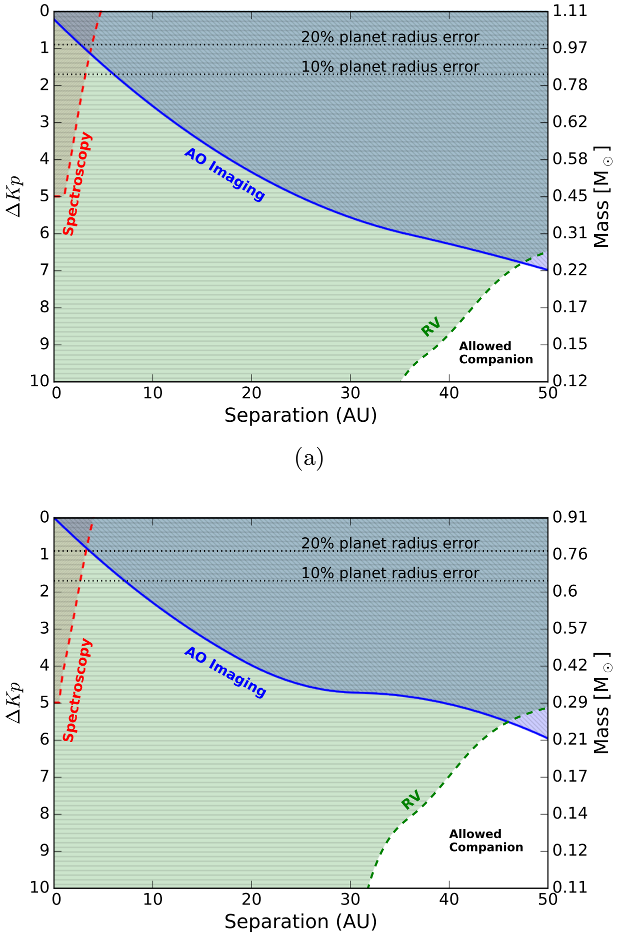

(a)

(b)

Figure 4.6: Constraints on the presence of other stars in the photometric aperture for *(a)* K2-66 and *(b)* K2-106, which would dilute the measure transit depth. The vertical axes show companion brightness contrast and companion mass plotted against orbital separation. NIRC2 AO imaging excludes companions in the hatched blue region, assuming distances of 400 pc and 250 pc to K2-66 and K2-106, respectively. The dashed red line shows the limits of our search for secondary lines in the HIRES spectrum. Companions in the hatched green region would induce a linear RV trend larger than the 3-σ upper limit determined from the RV time-series, assuming a circular, edge-on orbit. The horizontal dotted lines represent companion contrasts at which the dilution of the observed transit depths of K2-66b and K2-106b would cause planet radii to be overestimated by 10% and 20%. Together, AO imaging and spectroscopy, and RVs rule out companions that would cause systematic errors of > 10% in planet radius with high confidence (see §4.4.1 for discussion)

Table 4.3. K2-66 system parameters

Parameter	Value	Units
Stellar Parameters		
V	11.710 ± 0.186	mag
$T_{\rm eff}$	5887 ± 46	K
$\log g$	4.03 ± 0.05	dex
[Fe/H]	-0.047 ± 0.02	dex
$v \sin i$	3.7 ± 2.0	m s^{-1}
$M_\star$	1.11 ± 0.04	$M_\odot$
$R_\star$	1.67 ± 0.12	$R_\odot$
Planet b		
Transit Model		
P	5.06963 ± 0.00081	days
$T_{\rm conj}$	2455817.0092 ± 0.0051	BJD
$R_p/R_\star$	$0.01353^{+0.00174}_{-0.00080}$	—
$R_\star/a$	$0.127^{+0.048}_{-0.013}$	—
u_0	0.52 ± 0.01	—
u_1	0.19 ± 0.01	—
b	0.47 ± 0.31	—
i	$86.6^{+2.4}_{-4.4}$	deg
T_{14}	$4.71^{+0.45}_{-0.26}$	hrs
$\rho_\star$	$0.36^{+0.14}_{-0.22}$	$\mathrm{g\,cm^{-3}}$
RV Model (circular orbit assumed)		
K	7.4 ± 1.2	$\mathrm{m\,s^{-1}}$
Derived Planet Parameters		
a	0.05983 ± 0.00072	au
$S_{\rm inc}$	840 ± 125	$S_\oplus$
$T_{\rm eq}$	1372 ± 51	K
R_P	$2.49^{+0.34}_{-0.24}$	$R_\oplus$
M_P	21.3 ± 3.6	$M_\oplus$
ρ_p	7.8 ± 2.7	$\mathrm{g\,cm^{-3}}$
Other		
γ	-2.5 ± 1.0	$\mathrm{m\,s^{-1}}$
$\sigma_{\rm jit}$	5.0 ± 0.8	$\mathrm{m\,s^{-1}}$

Note. — $S_{\rm inc}$ = incident flux, $T_{\rm conj}$ = time of conjunction. $T_{\rm eq}$ = equilibrium temperature, assuming albedo = 0.3

Table 4.4. K2-106 system parameters

Parameter	Value	Units
Stellar Parameters		
V	12.102 ± 0.212	mag
$T_{\rm eff}$	5496 ± 46	K
$\log g$	4.42 ± 0.05	dex
[Fe/H]	0.06 ± 0.03	dex
$v \sin i$	< 2.0	m s^{-1}
$M_\star$	0.92 ± 0.03	$\mathrm{M}_\odot$
$R_\star$	0.95 ± 0.05	$\mathrm{R}_\odot$
Planet b		
Transit Model		
P	0.571336 ± 0.000020	days
$T_{\rm conj}$	2456226.4368 ± 0.0016	BJD
$R_p/R_\star$	$0.01745^{+0.00187}_{-0.00079}$	—
$R_\star/a$	$0.366^{+0.121}_{-0.036}$	—
u_0	0.459 ± 0.001	—
u_1	0.225 ± 0.001	—
b	0.47 ± 0.32	—
i	$80.2^{+7.0}_{-12.7}$	deg
T_{14}	$1.79^{+0.56}_{-0.23}$	hrs
$\rho_\star$	$1.18^{+0.43}_{-0.68}$	$\mathrm{g\,cm^{-3}}$
RV Model (circular orbit assumed)		
K	7.2 ± 1.3	$\mathrm{m\,s^{-1}}$
Derived Planet Parameters		
a	0.01312 ± 0.00014	au
$S_{\rm inc}$	4293 ± 483	$S_\oplus$
$T_{\rm eq}$	2063 ± 58	K
R_P	$1.82^{+0.20}_{-0.14}$	$R_\oplus$
M_P	9.0 ± 1.6	$M_\oplus$
ρ_p	$8.57^{+4.64}_{-2.80}$	$\mathrm{g\,cm^{-3}}$
Planet c		
Transit Model		
P	13.3387 ± 0.0018	days
$T_{\rm conj}$	2456238.7352 ± 0.0042	BJD
$R_p/R_\star$	$0.0265^{+0.0036}_{-0.0015}$	—
$R_\star/a$	$0.0368^{+0.0159}_{-0.0041}$	—
u_0	0.459 ± 0.001	—
u_1	0.225 ± 0.001	—
b	0.47 ± 0.32	—
i	$89.0^{+0.7}_{-1.4}$	deg
T_{14}	3.50 ± 0.21	hrs
$\rho_\star$	$2.13^{+0.92}_{-1.40}$	$\mathrm{g\,cm^{-3}}$
RV Model (circular orbit assumed)		
K	1.6 ± 1.7	$\mathrm{m\,s^{-1}}$
Derived Planet Parameters		
a	0.1071 ± 0.0015	au

Table 4.4 (cont'd)

Parameter	Value	Units
$S_{\rm inc}$	64 ± 7	$S_\oplus$
$T_{\rm eq}$	722 ± 20	K
R_P	$2.77^{+0.37}_{-0.23}$	$R_\oplus$
M_P	5.7 ± 6.1	$M_\oplus$
ρ_p	1.3 ± 1.6	$\mathrm{g\,cm^{-3}}$
Other		
γ	-2.2 ± 1.0	$\mathrm{m\,s^{-1}}$
$\sigma_{\rm jit}$	5.1 ± 0.7	$\mathrm{m\,s^{-1}}$

Note. — $S_{\rm inc}$ = incident flux, $T_{\rm conj}$ = time of conjunction. $T_{\rm eq}$ = equilibrium temperature, assuming albedo = 0.3

The derived planet properties for K2-66 and K2-106 are listed in Tables 4.3 and 4.4 respectively. Figure 4.7a shows the masses and radii of K2-66b and K2-106b along with all other planets smaller than $4\,R_\oplus$, whose masses and radii are each known to better than 50% precision[2]. Here we discuss possible planet bulk compositions.

K2-66

For K2-66b, we measure a radius $R_P = 2.49^{+0.34}_{-0.24}\ R_\oplus$, and a mass $M_P = 21.3{\pm}3.6\,M_\oplus$, corresponding to bulk density $\rho_p = 7.8 \pm 2.7\,\mathrm{g\,cm^{-3}}$. It is one of the most massive planets between 2 and 3 $R_\oplus$, and likely has a massive heavy-element core. The compositions of planets in this region of the mass radius diagram are not uniquely determined and could be a range of different admixtures of various chemical species including iron, rock, water and H/He (Rogers & Seager, 2010; Valencia et al., 2013). To assess possible compositions, we considered a couple of different two-layer planet models and in each case we constrained the mass fraction of each layer.

First, we assumed an Earth-composition core (33% iron, 67% rock) surrounded by a solar-composition H/He envelope. We used the work of Lopez & Fortney (2014), who started with a sample of 1–20 $M_\oplus$ cores surrounded by H/He envelopes that are 0.1–50% of the total planet mass and recorded the evolution of planet radius and envelope mass over a range of incident fluxes. Their models consist of planet radii (R_P) computed over a 4-D grid of planet core mass ($M_{\rm core}$), planet envelope mass ($M_{\rm env}$), age, and incident stellar flux ($S_{\rm inc}$), i.e. $R_P = R_P$ ($M_{\rm core}$, $M_{\rm env}$, age, $S_{\rm inc}$). Following Petigura et al. (2017a), we interpolated this grid to convert our measured M_P, R_P, $S_{\rm inc}$, and age into a core mass (envelope mass). We generated probability distributions for core mass fraction (CMF) by randomly sampling the posteriors of M_P, R_P, and $S_{\rm inc}$, assuming an age of 5

---

[2] NASA Exoplanet Archive, UT 08 February 2017, http://exoplanetarchive.ipac.caltech.edu

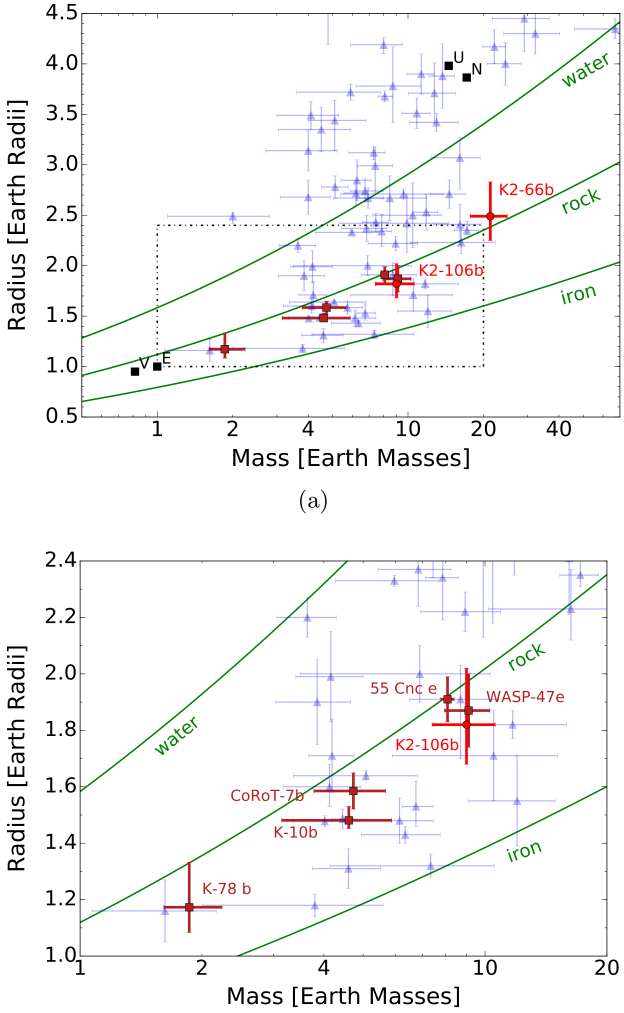

(a)

(b)

Figure 4.7: *(a)* Masses and radii of all confirmed planets whose mass and radius are measured to better than 50% (2σ) precision (blue triangles). Solar System planets are represented as black squares. Red circles indicate our measurements of K2-66b and K2-106b. Dark red squares represent other USP measurements from the literature. Green curves show the expected planet mass-radius curves for 100% iron, 100% rock (Mg_2SiO_4), and 100% water (ice) compositions according to models by Fortney et al. (2007). *(b)* A zoomed in look of the top panel. The five well-characterized USPs all have masses and radii consistent with mostly rocky compositions and little to no gaseous envelopes.

Gyr. Varying the age between 3–8 Gyr had negligible effect, which is explained by the fact that at Gyr ages, there is little dependence on age as the heating/cooling budget is close to a steady state value. From the resulting probability distribution, we constrain CMF > 0.96 and $M_{\rm core} > 10.8$ $M_\oplus$ at 99.7% confidence (3σ). One potential limitation of our method is that the Lopez & Fortney (2014) models assume the planet incident flux is constant. However, the luminosity of K2-66 has increased by a factor of $\sim$2 since evolving off of the main sequence and therefore the planet incident flux was twice as low for most of its lifetime. Nevertheless, when we repeated this analysis using half the incident flux, the 3σ lower limit on the CMF changes by a negligible amount, from 0.96 to 0.95. We conclude that if the planet consists of a H/He envelope atop an Earth-composition core, the envelope is <5% of the planet's mass and the core is $>$10.8 $M_\oplus$. If the iron mass fraction is larger (smaller) than that of Earth, then the planet would need a more (less) extended H/He atmosphere to maintain the same radius.

We also considered a composition of rock (Mg_2SiO_4) and water ice. We randomly drew 100,000 planet masses and radii from the posterior distributions, and converted them into a rock-mass-fraction (RMF) using Equation 7 of Fortney et al. (2007). From the resulting distribution of RMFs, we conclude that if the planet is indeed a mixture of rock and water ice, then RMF $> 81\%$ at 68.3% confidence (1σ). Moreover, the total mass of rock $M_{\rm rock} > 16\,M_\oplus$ at 68.3% confidence and the planet is denser than pure rock at 39% confidence.

K2-106

For the USP planet K2-106b, we measure radius, mass, and density $R_P = 1.82^{+0.20}_{-0.14}$ $R_\oplus$, $M_P = 9.0 \pm 1.6\,M_\oplus$, and $\rho_p = 8.57^{+4.64}_{-2.80}$ g cm^{-3}. These are consistent with an Earth-like composition. Assuming the planet is a mixture of iron and rock, we used Equation 8 of Fortney et al. (2007) to convert our mass and radius posteriors into an iron mass fraction (IMF) probability distribution. The median IMF is 19% with a 1σ upper limit of 33%, consistent with an Earth-like composition. With an extremely high incident flux of $4293 \pm 483\,S_\oplus$, and equilibrium temperature of 2063 ± 58 K, K2-106b is the hottest sub-Neptune with a measured density. At such close proximity to the star, any volatiles would likely have been lost by photoevaporation, leaving a bare ~ 9 $M_\oplus$ core.

The measured radii of planets b and c are larger than those reported by Adams et al. (2016b) at the $\sim 2.5\sigma$ and $\sim 1\sigma$ level respectively. Adams et al. (2016b) measure $R_P = 1.46 \pm 0.14\,R_\oplus$ for planet b and $R_P = 2.53 \pm 0.14\,R_\oplus$ for planet c. Adopting their measured radius for planet b with our measured mass yields an iron mass fraction, IMF $= 0.8 \pm 0.2$. Although such a large IMF is unlikely based on simulations of planet formation (e.g. Marcus et al., 2010), we investigated the source of the measurement discrepancy. We discovered that Adams et al. (2016b) underestimate the stellar radius due to an unreported error in the $T_{\rm eff}$-$R_\star$ relations of Boyajian et al. (2012), which they used to convert their spectroscopically measured $T_{\rm eff}$ (5590 ± 51 K) into a radius. Equation 8 of Boyajian et al. (2012) was reported as being a third-order polynomial fit to a sample of 33 K–M-dwarfs with precisely measured radii and $T_{\rm eff}$. Equation 9 was reported as a second polynomial fit that extends to hotter temperatures by including the Sun. However, these equations seem to have been mistakenly swapped — the polynomial coefficients in Equation 8 belong in Equation 9 and vice-versa. This can be seen by computing $R_\star$ (5778 K) = 1.00 and 0.86 $\mathrm{R}_\odot$ for Equations 8 and 9 respectively. The two equations diverge as $T_{\rm eff}$ exceeds $\sim 5300\,$K, which is particularly problematic. Adams et al. (2016b) used Equation 9 to compute $R_\star = 0.83\ \mathrm{R}_\odot$ but would have computed $R_\star = 0.91\ \mathrm{R}_\odot$ if they had used Equation 8, which is consistent with our measurement. Although Equation 8 is preferred for $T_{\rm eff} \gtrsim 5500\,$K, neither are particularly reliable for this temperature regime—the Sun is the only fitted data point beyond 5500 K, which is also where $R_\star$ and $T_{\rm eff}$ become significantly age-dependent because of main sequence evolution. We encourage the authors of any studies who have used Equations 8 and 9 of Boyajian et al. (2012) to verify their results. T. Boyajian has confirmed the error and is working to publish an erratum.

We note that the $T_{\rm eff}$ and $\log g$ measured by Adams et al. (2016b) are higher than our measurements. Our spectroscopic parameters for K2-106 are derived from SME, which has been well-validated by asteroseismically characterized stars (Brewer et al., 2015). Nevertheless, even if we run the `isochrones` Python package assuming the $T_{\rm eff}$, $\log g$, and [Fe/H] values from Adams et al. (2016b), we measure stellar parameters $M_\star = 0.96\,\mathrm{M}_\odot$ and $R_\star = 0.90\,\mathrm{M}_\odot$, which are within our measurement errors.

4.4.3 Photoevaporation Desert

The radius and temperature of K2-66b and K2-106b constitute the extremes of planet parameter space. Figure 4.8 shows the radius and incident flux of confirmed planets from the NASA Exoplanet Archive[3] (NEA). K2-106b ranks among the hottest sub-Neptunes found to date. There is a clear absence of very hot planets larger than $\sim 2\,R_\oplus$. Another noticeable feature is that hotter giant planets tend to have larger radii— the reason for which is highly debated (see Ginzburg & Sari, 2015, and references therein). It would be interesting to see if any trends exist for the larger sub-Neptunes of similar temperature. K2-66b occupies the region of parameter space found to be completely devoid of planets by Lundkvist et al. (2016) ($2.2\,R_\oplus$ ¡ R_P ¡ $3.8\,R_\oplus$, $S_{\rm inc}$ ¿ $650\,S_\oplus$), hereafter referred to as the "L16 desert".

We find that seven other planets fall within the L16 desert. To assess the reliability of these seven measurements, we examined constraints on the host stellar parameters from spectroscopic and imaging observations. None of them were asteroseismically characterized by Lundkvist et al. (2016). According to the Exoplanet Follow-up Observing Program (ExoFOP) database[4], five of these stars (K2-100, Kepler-480, Kepler-536, Kepler-656, and Kepler-1270) have properties constrained from spectroscopy and AO imaging. One of these five stars, Kepler-536, has a stellar companion at $0\farcs56$

---

[3] NASA Exoplanet Archive, UT 15 February 2017, http://exoplanetarchive.ipac.caltech.edu

[4] https://exofop.ipac.caltech.edu/cfop.php

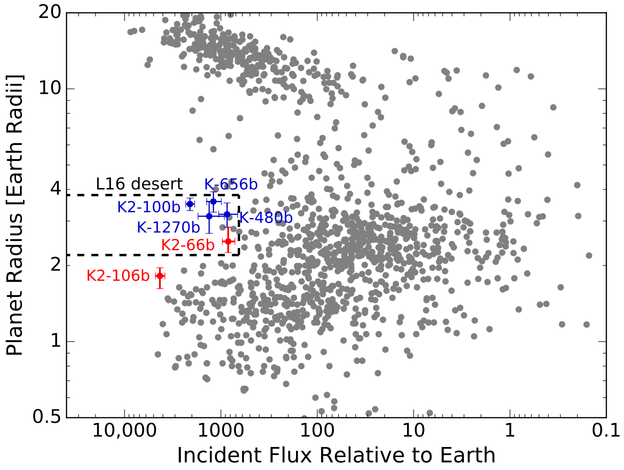

Figure 4.8: Radii and incident fluxes of all confirmed planets from the NASA Exoplanet Archive. K2-66b and K2-106b are shown in red. The black dashed box encloses the region of parameter space found by Lundkvist et al. (2016) to completely lack planets, which we refer to as the L16 desert. K2-66b, as well as three other planets (blue) occupy the L16 desert and have host stars characterized by both spectroscopic and AO observations. Four of these five planets have host stars with super-solar luminosities. K2-106b is one of the hottest sub-Neptunes found to date.

separation. The planet in this system would be much larger than $4\,R_\oplus$ if it orbits the companion star rather than the primary (Law et al., 2014; Furlan et al., 2017) so we deem this measurement unreliable. We consider the planet parameters for the other four systems to be reliable and confirm that planets remain in the L16 desert when spectroscopic stellar parameters are adopted. For K2-100, we adopt the stellar and planet parameters reported in (Mann et al., 2017). The star is a late F dwarf in the 800 Myr Praesepe Cluster. For Kepler 480, Kepler-656, and Kepler-1270, we had previously obtained HIRES spectra and used the SpecMatch algorithm (Petigura, 2015) to derive T_eff, $\log g$, and [Fe/H]. We computed stellar masses and radii using the `isochrones` package (see §4.3.1). We find that Kepler-480 is an F8 dwarf, Kepler-1270 is a K1 subgiant, and K2-656 is a high-metallicity G dwarf ($[\mathrm{Fe/H}] = 0.23 \pm 0.05$ dex). The planets in the L16 desert that orbit these four spectroscopically characterized host stars are plotted as blue points and labeled in Figure 4.8.

We examine whether the five planets in the L16 desert share common properties that can be linked to their origins. First, we note that none of them are USPs — they have orbital periods of 1.3–6.0 days. Moreover, four of the five host stars have luminosities $L > 1.7\,\mathrm{L}_\odot$. Based on these two observations, we speculate that planets in the L16 desert are 2–4 $R_\oplus$ cores of larger planets that were stripped of their gaseous envelopes by means of photoevaporation. Such 2–4 $R_\oplus$ cores would have higher surface gravities and orbit further from the star than the smaller cores of USPs. Therefore, the removal of their envelopes by photoevaporation would require stars that are systematically more luminous than USP hosts, consistent with observations. Mass measurements of other planets in the L16 desert are needed to test the hypothesis that they are cores surrounded by little to no gas.

Given that K2-66 is a subgiant star, we consider the evolution of the planet's irradiance since the star left the main sequence. According to Dartmouth stellar evolution models, a star with mass $M_\star = 1.1\,\mathrm{M}_\odot$ and [Fe/H] = 0.05 dex would have had a radius $R_\star \approx 1.1$ $\mathrm{R}_\odot$ during its main sequence lifetime and have luminosity $L_\star \approx 1.5$ $\mathrm{L}_\odot$. Its current luminosity is ≈ 3.0 $\mathrm{L}_\odot$, meaning that the planet incident flux has increased twofold, from ≈ 420 to $840\,S_\oplus$ since the main sequence era. This would have boosted the rate of photoevaporation of low-density volatiles in the planet's envelope. Alternatively, EPIC 206153219 might have formed in a gas-poor disk, preventing it from accumulating much H/He.

If K2-66b was stripped of its envelope as the star became a subgiant, then the rapid post-main sequence evolution explains the lack of known planets similar in size and density. Perhaps we are catching a glimpse of a planet from a population that quickly spirals into their host stars as they evolve off the main sequence (e.g. KELT-8b, Fulton et al., 2015). To test this scenario, we computed an inspiral time, $t_\mathrm{inspiral} \approx 370$ Gyr for K2-66b using Equation 1 of Lai (2012) assuming a nominal reduced tidal quality factor $Q'_\star = 10^7$. We conclude that the planet is not on the verge of spiraling into its host star.

4.4.4 Ultra-short-period Planets

Only five other USPs have measured masses and densities: 55 Cnc (Fischer et al., 2008; Dawson & Fabrycky, 2010; Nelson et al., 2014; Demory et al., 2016), CoRoT-7b (Léger et al., 2009; Bruntt et al., 2010; Haywood et al., 2014), Kepler-10b (Batalha et al., 2011; Esteves et al., 2015), Kepler-78b (Howard et al., 2013; Pepe et al., 2013; Grunblatt et al., 2015), and WASP-47e (Becker et al., 2015; Dai et al., 2015; Sinukoff et al., 2017b). These planets are plotted on the mass-radius diagram in Figure 4.7b. The properties of these planets and their host stars are provided in Table 4.5. All of them have masses and radii consistent with admixtures of rock and iron with little to no surrounding volatiles. This is consistent with the notion that USPs are the remnant cores of larger planets that lost their gaseous envelopes or formed without much gas in the first place. It is curious that three of the six well-characterized USPs have consistent masses and radii that are ~ 1.7–$2.0\,R_\oplus$ and ~ 8–$10\,M_\oplus$. Perhaps these planets constitute an upper size and mass limit to the cores of the larger planets from which they form. If all USPs have similar rocky compositions, then the observed absence of USPs $>2.0\,R_\oplus$ naturally translates to an upper mass limit. Some sub-Neptune-size planets with $P > 1$ day have cores $> 10\,M_\oplus$ (e.g. K2-66b), but there are no such examples of USPs. More well-characterized USPs are needed to reveal their core mass distribution.

We note that the three well-characterized USPs with ~ 8–$10\,M_\oplus$ cores (K2-106b, 55 Cnc e, WASP-47e) have host stars with super-solar metallicities, whereas two of the three well-characterized USPs with masses $\lesssim 5\,M_\oplus$ (Kepler-78b and Kepler-10b) have host stars with sub-solar metallicities. With only six data points, a correlation cannot be claimed, but this motivates a more complete analysis of all USPs beyond the scope of this study.

USPs are unlikely to be remnants of hot-Jupiters. While earlier studies argued that USPs could be the leftover cores of hot-Jupiters that experienced Roche lobe overflow (RLO, e.g. Valsecchi et al., 2014), simulations by Valsecchi et al. (2015) and Jackson et al. (2016) suggest that RLO of planets with cores $\lesssim 10\,M_\oplus$ would tend to expand their orbits to $P > 1$ day. Moreover, Winn et al. (2017) found that the [Fe/H] distribution of USP host stars is inconsistent with that of hot-Jupiter host stars, and consistent with that of stars hosting hot planets of Neptune-size or smaller. This suggests the that the majority of USPs are not remnants of hot-Jupiters but could be remnants of Neptune- or sub-Neptune-size planets.

Five of the six well-characterized USPs have known planetary companions. The single exception is Kepler-78b, which orbits an active star, hampering the ability to detect planets with longer orbital periods. The number of detected companions to USPs is consistent with a 50–100% occurrence rate of additional planets P ¡ 45 days, depending on the assumed distribution of mutual inclinations and assuming 100% detection completeness (Adams et al., 2016b).

It remains unclear how USPs settle so close to their host stars, but the multiplicity of these systems ($P < 50$ days) hints that they form via inward migration mechanisms involving multiple planets. For example, Hansen & Zink (2015) demonstrated that tidal decay of 55 Cnc e from beyond its current orbit would have sent the planet through multiple secular resonances, exciting its orbital eccentricity and inclination. A shrinking periastron distance would subsequently boost tidal evolution and increase the rate of orbital decay. However, unless the perturber has a mass comparable to Jupiter, secular interactions are usually too weak to overcome relativistic precession at short orbital periods (Lee & Chiang, 2017). Thus, secular interactions can only explain USP systems that also host close-in giant planets like 55 Cnc and WASP-47. Alternatively, USPs might have migrated through a gas disk to their current orbits via mean motion resonances (MMRs) with other planets. However, companions of USPs detected to date are not in MMR. It is possible that resonant companions were engulfed by the star or collided to form a single object. Formation of USPs via MMR would require the disk to extend very close to the star. USPs could also have been gravitationally scattered inwards by another companion, but this is difficult to reconcile with the observed presence of multiple companions on close-in orbits, which would be unstable at modest eccentricities. Lee & Chiang (2017) show that the observed USP population is consistent with in-situ formation or disk migration followed by tidal migration. Any complete theory of planet formation must account for the presence of these rocky $\sim$ 5-10 $M_\oplus$ USPs with close neighbors.

4.5 Conclusion

We have measured the masses and densities of two extremely hot sub-Neptunes, K2-66b and K2-106b. We have characterized their stellar hosts using high-resolution spectroscopy and adaptive optics imaging. The radius of K2-66b, $R_P = 2.49^{+0.34}_{-0.24}$ $R_\oplus$ measured from *K2* photometry and

Table 4.5. Ultra-short-period planets with measured masses.

Name	$M_\star$ ($M_\odot$)	$R_\star$ ($R_\odot$)	[Fe/H] (dex)	P (days)	R_P ($R_\oplus$)	M_P ($M_\oplus$)	ρ_p ($\mathrm{g\,cm^{-3}}$)	$N_{\rm pl}$	References
55 Cnc e	0.905 ± 0.015	0.943 ± 0.010	0.31 ± 0.04	0.74	1.92 ± 0.08	8.08 ± 0.31	$6.3^{+0.8}_{-0.7}$	5	V05, V11, D16
CoRot-7b	0.91 ± 0.03	0.82 ± 0.04	0.12 ± 0.06	0.85	1.585 ± 0.064	4.73 ± 0.95	6.61 ± 1.33	2	L09, B10, H14
Kepler-10b	0.913 ± 0.022	1.065 ± 0.009	-0.15 ± 0.04	0.84	$1.48^{+0.05}_{-0.03}$	$4.61^{+1.27}_{-1.46}$	8.0 ± 3.0	2	B11, E15
Kepler-78b	0.83 ± 0.05	0.74 ± 0.05	-0.08 ± 0.04	0.36	$1.18^{+0.16}_{-0.09}$	$1.86^{+0.38}_{-0.25}$	$5.57^{+3.02}_{-1.31}$	1	S13, H13, P13
WASP-47e	0.99 ± 0.05	1.18 ± 0.08	0.36 ± 0.05	0.79	1.87 ± 0.13	9.11 ± 1.17	7.63 ± 1.90	4	B15, S17
K2-106b	0.95 ± 0.05	0.92 ± 0.03	0.06 ± 0.03	0.57	$1.82^{+0.20}_{-0.14}$	9.0 ± 1.6	$8.57^{+4.64}_{-2.80}$	2	This study

Note. — V05: Valenti & Fischer (2005), V11: von Braun et al. (2011), D16: Demory et al. (2016), L09: Léger et al. (2009), B10: Bruntt et al. (2010), H14: Haywood et al. (2014), B11: Batalha et al. (2011), E15: Esteves et al. (2015), S13: Sanchis-Ojeda et al. (2013), H13: Howard et al. (2013), P13: Pepe et al. (2013), B15: Becker et al. (2015), S17: Sinukoff et al. (2017b).

mass, $M_P = 21.3 \pm 3.6\,M_\oplus$ measured from Keck-HIRES RVs are consistent with a mostly rocky composition and little to no low-density volatiles, making it one of the densest planets of its size. It is one of the few known planets in the "photoevaporation desert" ($R_P = 2.2$–$3.8\,R_\oplus$, $S_{\rm inc} \geq 650\,S_\oplus$), and the first such planet with a measured mass. These planets tend to orbit stars more luminous than the Sun, which suggests that they might have systematically higher densities due to increased photoevaporation. The measured radius, $R_P = 1.82^{+0.20}_{-0.14}\ R_\oplus$ and mass, $M_P = 21.3 \pm 3.6\,M_\oplus$ of K2-106b indicate an Earth-like composition, similar to the four other USPs with measured densities. It is the hottest sub-Neptune with a measured mass, and could be the stripped core of a more massive planet. K2-66b and K2-106b join the rare class of planets larger than 1.5 $R_\oplus$ with mostly rocky compositions.

CHAPTER 5
MASS CONSTRAINTS OF THE WASP-47 PLANETARY SYSTEM FROM RADIAL VELOCITIES

This chapter is a reproduction of Sinukoff et al. (2017b).

5.1 Introduction

Approximately 1% of Sun-like stars host giant planets on short-period orbits (P < 10 days), known as hot Jupiters (HJs, Howard et al., 2012; Wright et al., 2012). These planets are thought to have migrated to their observed locations from beyond the ice-line at several AU. One proposed migration mechanism involves dynamical interaction between the planet and protoplanetary disk (e.g. Lin et al., 1996). In this case, the planet maintains a low eccentricity. Other "high-eccentricity migration" (HEM) modes have been proposed including planet-planet scattering (e.g. Rasio & Ford, 1996), Kozai oscillations induced by either a nearby star (e.g. Wu & Murray, 2003) or planet (e.g. Naoz et al., 2011), and secular interactions (e.g. Wu & Lithwick, 2011). In the HEM scenario, gravitational perturbations excite planets onto eccentric orbits, which subsequently shrink and circularize due to stellar tides. Other proposed dynamical effects include misalignment between the orbital axis of the HJ and the stellar spin axis, as well as the destabilization of close-in planets encountered upon migration.

Observations of systems with HJs are difficult to reconcile with HEM theory. For example, Schlaufman & Winn (2016) found that HJ host stars are no more likely to host additional giant planets than stars with giant planets at $P > 10$ days. Knutson et al. (2014) found no difference between the occurrence of additional giant planets at 1–20 AU in systems with HJs whose orbits are eccentric or misaligned versus circular and aligned with the stellar spin. Moreover, Dawson et al. (2015) concluded that the number of migrating Jupiters on highly eccentric orbits is lower than predicted by HEM theory (Socrates et al., 2012).

In support of HEM theory, Steffen et al. (2012) found an absence of HJs in close proximity to smaller planets (0.7–5 $R_\oplus$) discovered by *Kepler*. However, it remains unclear whether HJs are intrinsically lonely or if their close neighbors have merely evaded detection. For example, Batygin et al. (2016) proposed a mechanism for in-situ formation of HJs, which predicts a population of small planets mutually inclined to the HJ, and therefore unlikely to transit. While HJs are observed to be lonely, Huang et al. (2016) found that roughly half of transiting "warm-Jupiters" ($P =$ 10–200 days) are accompanied by transiting planets $\sim$ 2–6 $R_\oplus$ on interior orbits $P < 50$ days. They proposed that the warm-Jupiters in these multi-planet systems formed in-situ and that occasionally this same mechanism might produce a very small fraction of HJs. These latest theories add to the diversity of theories to explain HJ formation.

WASP-47 is the first star known to host a Jovian-size planet with $P < 10$ days and additional close-in planets—proof that not all HJs are isolated and strengthening the argument that HEM alone cannot produce the entire population of HJs. The Jovian-size planet WASP-47b orbits the star every 4.2 days. It was first reported and confirmed by Hellier et al. (2012) who detected both its transit and radial velocity (RV) signatures. Becker et al. (2015) detected two additional transiting planets using *K2* photometry. One of these planets, WASP-47e, is an ultra-short-period (USP) super-Earth ($P = 0.79$ days). WASP-47d is Neptune-size ($P = 9.0$ days). Becker et al. (2015) detected transit timing variations (TTVs) of both planets. Their TTV signals are anticorrelated and have a super-period consistent with 52.67-days — the expected super-period for two such planets near 2:1 orbital mean-motion-resonance (Lithwick et al., 2012). Becker et al. (2015) reported planet mass constraints $M_b = 341^{+73}_{-55}\,M_\oplus$, $M_d = 15.2 \pm 7\,M_\oplus$, and $M_e < 22\,M_\oplus$ based on dynamical fits to the observed transit times. Measurements of the Rossiter-McLaughlin effect by (Sanchis-Ojeda et al., 2015) ruled out orbits that are strongly misaligned with the stellar spin axis. Crossfield et al. (2016) independently validated the planetary system by demonstrating that the star is unlikely to be a blend of multiple stars, via Keck-NIRC2 adaptive optics images and a search for secondary lines in the stellar spectrum.

A fourth planet, WASP-47c, was detected with an orbital period of 572 ± 7 days by Neveu-VanMalle et al. (2016) from 32 RV observations with the Euler/CORALIE instrument spanning almost 3 years[1]. Neveu-VanMalle et al. (2016) measure a minimum mass $M_c \sin i = 394 \pm 70\,M_\oplus$. WASP-47c joins the population of giant planets beyond 1 AU that have been found in systems with HJs (Knutson et al., 2014).

WASP-47d and WASP-47e are examples of super-Earth- and Neptune-size planets, which are common around Sun-like stars (Howard et al., 2012; Fressin et al., 2013; Petigura et al., 2013b; Burke et al., 2015). Only a handful of these planets have precisely measured masses and bulk densities. Compositional trends have emerged from this limited sample. Planets smaller than $\approx 1.6\,R_\oplus$ typically have high densities consistent with Earth-like bulk compositions, while most larger planets have low densities that require thick envelopes of H/He (Weiss & Marcy, 2014; Marcy et al., 2014b; Lopez & Fortney, 2014; Rogers, 2015; Dressing et al., 2015). However, there is significant scatter about the mean mass-radius relationship, indicating compositional diversity, even for a fixed planet radius. Due to the limited number of known sub-Neptunes with bright host stars, mass measurements are scarce, and this compositional diversity has yet to be fully explored.

Dai et al. (2015) obtained 26 RVs of WASP-47 with the Carnegie Planet Finder Spectrograph (PFS), measuring $M_b = 370 \pm 29\,M_\oplus$, $M_e = 12.2 \pm 3.7\,M_\oplus$, and $M_d = 10.4 \pm 8.4\,M_\oplus$, consistent with TTV measurements by Becker et al. (2015). Dai et al. (2015) measure a bulk density of WASP-47e of $11.2 \pm 3.6\,\mathrm{g\,cm^{-3}}$, consistent with a rocky and potentially iron-rich composition. Their $\sim$ 80% measurement uncertainty on the mass of planet d is insufficient to constrain the planet's bulk

---

[1] WASP-47d and WASP-47e were published before WASP-47c, which was named while the work of Neveu-VanMalle et al. (2016) was still under revision.

composition.

Here we present improved mass constraints of all four planets in the WASP-47 system by combining Keck-HIRES RVs with the previously published RVs of Hellier et al. (2012), Dai et al. (2015), and Neveu-VanMalle et al. (2016). This work is part of a NASA "Key Project" to measure *K2* planet masses using Keck-HIRES. Section 5.2 of this manuscript summarizes our Doppler observations and spectroscopic constraints of stellar parameters. Our analysis of the RV time-series and resulting planet mass measurements are detailed in Section 5.3. In Section 5.4, we discuss possible compositions of WASP-47e and WASP-47d, eccentricity constraints of the Hot-Jupiter, and interpret these in the context of planet formation and evolution.

5.2 Observations

5.2.1 *K2* Photometry

WASP-47 was observed by the Kepler Telescope for 69 consecutive days in Campaign 3 (C3) of NASA's *K2* mission (Howell et al., 2014). It was one of only 55 targets in *K2* Campaign 3 that was observed in short-cadence mode (60 sec), enabling precise measurement of transit parameters. We adopt the orbital ephemerides, and transit depths reported by Becker et al. (2015).

5.2.2 Radial Velocity Measurements

We collected RV measurements of WASP-47 using HIRES (Vogt et al., 1994) at the W. M. Keck Observatory from 2015 August 10 UT to 2016 October 7 UT (424 days). We followed standard procedures of the California Planet Search (CPS; Howard et al., 2010a). For each RV observation, we used the "C2" decker ($0\farcs87 \times 14''$ slit), which yields a spectral resolution $R = 55{,}000$ and is long enough for sky subtraction. Before the starlight entered the spectrometer slit, it first passed through a cell of iodine gas, which imprints a dense set of molecular absorption lines on the stellar spectrum. These iodine lines were used for wavelength calibration and PSF reference. We used an exposure meter to terminate exposures after reaching a SNR per pixel of $\sim$100 at 550 nm (typically $\sim$15 min). A single iodine-free spectrum was obtained as a stellar template using the "B3" decker ($0\farcs57 \times 14''$ slit). RVs were measured by forward modeling each observed spectrum as the product of an RV-shifted iodine-free spectrum and a high-resolution/high-SNR iodine transmission spectrum. The latter was first convolved with an instrumental PSF, modeled as the sum of 13 Gaussians with fixed centers and widths but variable amplitudes (Marcy & Butler, 1992; Valenti et al., 1995; Butler et al., 1996; Howard et al., 2009). Our measured RVs are listed in Table 5.3.

5.2.3 Stellar Parameters

We measured the effective temperature (T_{eff}), surface gravity ($\log g$), and metallicity ([Fe/H]) of WASP-47 from our iodine-free HIRES spectrum using the updated SME analysis of Brewer et al. (2016). This new methodology yields $\log g$ values that are accurate to 0.05 dex, as determined from careful comparisons against stars with $\log g$ determined from asteroseismology (Brewer et al., 2015). We find $T_{\text{eff}} = 5475 \pm 60$ K, $\log g = 4.27 \pm 0.05$ dex, and [Fe/H] $= 0.36 \pm 0.05$ dex. To estimate the stellar mass and radius, we fit our spectroscopic measurements of T_{eff}, $\log g$, & [Fe/H] to a grid of models from the Dartmouth Stellar Evolution Database (Dotter et al., 2008) using the `isochrones` Python package (Morton, 2015b) with uncertainties determined by the `emcee` Markov Chain Monte Carlo (MCMC) package (Foreman-Mackey et al., 2013). The derived stellar mass and radius are $0.99 \pm 0.03\,\mathrm{M}_\odot$ and $1.18 \pm 0.08\,\mathrm{R}_\odot$. These are consistent with the measurements of $1.04 \pm 0.08\,\mathrm{M}_\odot$ and $1.15 \pm 0.04\,R_\oplus$ by Mortier et al. (2013). Following Sinukoff et al. (2016), we conservatively adopt uncertainties of 5% on stellar mass to account for the intrinsic uncertainties of the Dartmouth models estimated by Feiden & Chaboyer (2012).

Following the prescription of Isaacson & Fischer (2010), we measure S_{HK}indices from the HIRES spectra, which serve as a proxy for stellar activity. Our S_{HK}measurements are listed in Table 5.3. The median S_{HK}index of 0.132 is consistent with other inactive stars in the California Planet Search (Isaacson & Fischer, 2010). Consistent with this picture, we measure the stellar jitter to be $3.7 \pm 0.6\,\mathrm{m\,s^{-1}}$ (Table 5.2).

5.3 Analysis

5.3.1 Radial Velocity Data Analysis

We analyzed the RV time-series using the RV fitting package `RadVel` (Fulton & Petigura, in prep.), which is publicly-available on GitHub[2]. We fit our Keck-HIRES RVs along with previously published RV datasets (Hellier et al., 2012; Dai et al., 2015; Neveu-VanMalle et al., 2016), summarized in Table 5.1. We omit the six RV measurements reported by Neveu-VanMalle et al. (2016) that were taken after a CORALIE instrument upgrade. These would have added two free parameters to our RV model, which was not worth the negligible gain in RV measurements. After omitting the 17 HIRES observations JD = 2457244.9366–2457245.07451, taken during a WASP-47b transit, we still have 12 out-of-transit observations from that night. RVs have astrophysical and instrumental errors that manifest on a variety of timescales from minutes to year. Therefore, the consecutive measurements during the same night don't constitute independent measurements. To guard against these data from having a disproportionate influence influence on the fit, we bin the 8 pre-transit RV

---

[2] https://github.com/California-Planet-Search/radvel
http://radvel.readthedocs.io/en/master/index.html

Table 5.1. RV datasets

Reference[a]	Instrument	$N_{\rm RV}$	Median Unc. [$\rm m\,s^{-1}$]	Δt [days]
This study	HIRES	47[b]	1.8	424
V16	CORALIE	26	11.4	745
D15	PFS	26	3.1	12
H12	CORALIE	19	11.0	560

[a] V16: Neveu-VanMalle et al. (2016), D15: Dai et al. (2015), H12: Hellier et al. (2012)

[b] We made 74 RV measurements with Keck-HIRES, but omit 17 RVs measured during the WASP-47b transit event on 2015 August 10 UT. We binned the remaining 12 RVs from that night into two measurements for a total of 47 RVs

measurements and bin the 4 post-transit measurements. We note that an analysis of our HIRES RVs alone gives the same planet masses to within 1σ.

We adopt a four-planet model that is the sum of four Keplerian components. For each of the four datasets, our model includes an RV offset, γ, as well as an RV "jitter" parameter, $\sigma_{\rm jit}$, to account for additional Doppler noise of astrophysical or instrumental origins.

Our likelihood function for this analysis follows that of Howard et al. (2014):

$$\ln \mathcal{L} = -\sum_i \left[\frac{(v_i - v_m(t_i))^2}{2\left(\sigma_i^2 + \sigma_{\rm jit}^2\right)} + \ln \sqrt{2\pi\left(\sigma_i^2 + \sigma_{\rm jit}^2\right)} \right], \tag{5.1}$$

where v_i and σ_i are the ith RV measurement and corresponding uncertainty, and $v_m(t_i)$ is the Keplerian model velocity at time t_i. To increase the rate of convergence and to to counter the bias toward non-zero eccentricity (Lucy & Sweeney, 1971), we adopt the following parametrization of our model RV curve: $\{P, T_c, \sqrt{e}\cos\omega, \sqrt{e}\sin\omega, K\}$, where P is orbital period, T_c is the time of conjunction, e is the orbital eccentricity, ω is the longitude of periastron and K is the RV semi-amplitude.

We first find the maximum-likelihood model using the minimization technique of Powell (1964), then perturb the best-fitting free parameters by up to 3% to start 100 parallel MCMC chains. The free parameters of the RV model are adopted as the MCMC step parameters. `RadVel` incorporates the affine-invariant sampler of the `emcee` package (Foreman-Mackey et al., 2013). The Gelman-Rubin (Gelman & Rubin, 1992) and T_z statistics (Ford, 2006) are checked in real-time during the MCMC exploration and the chains are deemed well-mixed and the MCMC run is halted when the Gelman-Rubin is within 3% of unity and $T_z > 1000$ for all free parameters.

We assume circular orbits for WASP-47d and WASP-47e while allowing the eccentricities of WASP-47b and WASP-47c to vary freely. An N-body dynamical stability analysis by Becker et al. (2015) showed that the orbits of the inner three planets are unstable when eccentricities of the three inner planets exceed ~ 0.05. For the $\sim$ 4–6 $\mathrm{m\,s^{-1}}$ RV signals of WASP-47d and WASP-47e, our signal-to-noise is too low to distinguish between eccentricities of 0.00 and 0.05. The orbital periods and orbital phases of WASP-47b, d, and e were locked at the values reported in Becker et al. (2015) from transits. We adopt uninformed priors (i.e. no priors) on all free step parameters and step in linear parameter space. The median values and the 68% credible intervals are reported in Table 5.2. The best-fitting RV model is shown in Figure 5.1

We searched for additional companions at large orbital distances by testing RV models with and without a constant radial acceleration term, $\mathrm{d}v/\mathrm{d}t$. We compared these two models using the Bayesian Information Criterion (BIC), with the RV jitter fixed at the values in Table 5.2. We compute $\Delta\mathrm{BIC} = \mathrm{BIC}_{\mathrm{d}v/\mathrm{d}t} - \mathrm{BIC}_{\mathrm{d}v/\mathrm{d}t=0} = 3.8$, indicating that the simpler model is preferred, so we adopt $\mathrm{d}v/\mathrm{d}t = 0$.

We investigated whether the Keplerian orbit approximation is valid for our RV model, given the dynamical influences of the three inner planets on each other. First, we considered the TTV amplitudes, which indicate the order of magnitude of non-Keplerian effects. The TTV amplitudes of planets b, d, and e measured by Becker et al. (2015) of 0.63 min, 7.3 min, and ¡ 1.2 min are 0.01%, 0.06%, and $< 0.1\%$ of the respective orbital periods. We assessed whether these deviations from Keplerian orbits are significant given the precision of our RV measurements. Given RV semi-amplitude K and assuming a phase shift equal to the TTV amplitude ΔT, the deviation of RV(t) is:

$$\begin{aligned}\Delta\mathrm{RV}(t) &= \frac{\partial\mathrm{RV}}{\partial t}\Delta T \\ &= \frac{2\pi K}{P}\cos\left(\frac{2\pi t}{P}\right)\Delta T.\end{aligned} \tag{5.2}$$

The maximum ΔRV is $2\pi K P^{-1}\Delta T$, which evaluates to $0.09\,\mathrm{m\,s^{-1}}$, $0.01\,\mathrm{m\,s^{-1}}$, and $< 0.03\,\mathrm{m\,s^{-1}}$ for planets b, d, and e respectively. These represent upper bounds to the orbit-averaged deviations from Keplerian over the K2 time baseline. These deviations are much smaller than our RV measurement uncertainties (1.5–2.0 m/s).

Since the RV time-series is much longer than the K2 baseline, one may wonder if there are large amplitude deviations from Keplerian orbits that build up over longer timescales. To verify that the TTVs remain small over the timescale of RV observations, we used the symplectic N-body integrator TTVFast (Deck et al., 2014) to numerically integrate the planet orbits over 2000 days. The orbital elements were initialized at the maximum-likelihood solution obtained from RVs. The TTV amplitudes of planets b, d, and e remained at 0.6 min, 7 min and < 1 min respectively over the 2000 day timespan.

We note that the orbital periods of planets b and d measured by Becker et al. (2015) do not accurately reflect the average orbital periods that would be measured over many years. Becker et al. (2015) measured P by fitting a linear ephemeris to the *K2* transits. Since the *K2* photometry only spans one TTV super-period, the Becker et al. (2015) orbital periods could be different from the average orbital periods over the time baseline of our RV measurements, which spans many TTV super-periods.

To quantify the additional uncertainties of average orbital periods, we used the 2000-day baseline of transit times obtained with TTVFast. For each planet, we performed a linear fit to every unique set of N consecutive transit times, where N is the number of transits observed in the K2 photometry. The resulting distribution of slopes (orbital periods) provides an estimate of the uncertainty of the average orbital period attributed to the limited timescale of *K2* observations. The 1-sigma uncertainties obtained from these orbital period distributions are $\pm$ 0.000019 days and $\pm$ 0.00074 days for planets b and d respectively. These are $\sim 4\times$ larger than the uncertainties reported by Becker et al. (2015). We refit our RV time-series using these larger orbital period uncertainties, but there was no change in the RV solution or corresponding uncertainties. The scale of these uncertainties is still a tiny fraction of the RV phase. Nevertheless we recommend that future studies adopt these larger uncertainties on average orbital period, which are listed in Table 5.2.

Table 5.2. WASP-47 system parameters

Parameter	Value	Units	Ref.
Stellar Parameters			
T_{eff}	5475 ± 60	K	A
$\log g$	4.27 ± 0.05	dex	A
[Fe/H]	0.36 ± 0.05	dex	A
$v \sin i$	$1.80^{+0.24}_{0.16}$	m s^{-1}	C
$M_\star$	0.99 ± 0.05	$\mathrm{M}_\odot$	A
$R_\star$	1.18 ± 0.08	$\mathrm{R}_\odot$	A
Planet Parameters			
WASP-47b			
P	4.1591287 ± 0.000019	days	A, B
T_{conj}	$2457007.932131 \pm 0.000023$	BJD	B
$R_p/R_\star$	0.10186 ± 0.00023	—	B
a	0.05047 ± 0.00085	AU	A
S_{inc}	441 ± 65	$S_\oplus$	A
R_P	13.11 ± 0.89	$R_\oplus$	A
e	$0.0036^{+0.0049}_{-0.0026}$	—	A
ω	91^{+183}_{-39}	deg	A
K	142.34 ± 0.85	$\mathrm{m\,s^{-1}}$	A
M_P	356 ± 12	$M_\oplus$	A
ρ_p	0.87 ± 0.18	$\mathrm{g\,cm^{-3}}$	A
WASP-47c			
P	595.7 ± 5.0	days	A
T_{conj}	2455992 ± 10	BJD	A
a	1.382 ± 0.023	AU	A
S_{inc}	0.59 ± 0.09	$S_\oplus$	A
e	0.27 ± 0.04	—	A
ω	136 ± 12	deg	A
K	32.62 ± 1.14	$\mathrm{m\,s^{-1}}$	A
M_P	411 ± 18	$\mathrm{M}_\oplus \sin i$	A
WASP-47d (circular orbit assumed)			

5.4 Discussion

Figure 5.2 shows the mass-radius distribution of all confirmed planets with $R_p < 4.0\,R_\oplus$ whose mass and radius are measured to better than 50% precision (2σ) either by RVs or TTVs[3]. Previous studies of small planets from the prime *Kepler* mission revealed a transition in the typical composition of planets from mostly rocky to planets having thick envelopes of low density H/He at $\approx 1.6\,R_\oplus$ (Weiss & Marcy, 2014; Marcy et al., 2014b; Lopez & Fortney, 2014; Rogers, 2015; Dressing et al., 2015). An important open question is if and how this transition depends on incident stellar flux. Jontof-Hutter et al. (2016) illustrate that the population of planets $< 30\ M_\oplus$ tend to have fewer volatiles as incident flux increases, consistent with atmospheric loss via photoevaporation. WASP-47e is among the most highly irradiated small planets with a well-measured mass, and thus helps us to probe the mass-radius relationship at extreme values of incident stellar flux, in a regime similar to Kepler-10b, Kepler-78b, and 55 Cnc e.

The measured mass of WASP-47e ($9.11 \pm 1.17\,M_\oplus$) is consistent with the measurement of Dai et al. (2015) ($12.2 \pm 3.7\,M_\oplus$) at the 1σ level. We improve the fractional uncertainty from 30% to 13%, allowing for a more detailed interpretation of composition. The measurements of Dai et al. (2015) favored an admixture of 50% iron and 50% rock. Assuming an iron-rock admixture, we sample our planet mass and radius posterior distributions and compute an iron mass fraction (IMF) using Equation 8 of Fortney et al. (2007). From 100,000 independent samples, we obtain a median IMF of 13% and a 1σ upper limit of 24%, suggesting that WASP-47e is mostly rock. Its IMF is lower than Earth's IMF (33%) at 80% confidence. Alternatively, WASP-47e could have an IMF similar to Earth but possess a significant atmosphere of a high mean molecular weight species, such as water or sulfur.

The measured mass and radius of WASP-47d ($12.75 \pm 2.70\,M_\oplus$ and $3.71 \pm 0.26\,R_\oplus$) are consistent with several other planets, including Kepler-94b, Kepler-95b, Kepler-30b, KOI-142b, and GJ 3470b. With an incident flux $S_{\rm inc} = 157 \pm 23\ \ S_\oplus$, the atmosphere of WASP-47d might have undergone significant photoevaporation. Nevertheless, it must still have an atmosphere containing some amount of H/He. There are a number of degenerate planet compositions in this region of the mass-radius diagram with different fractions of rock, iron, water, and H/He (Rogers & Seager, 2010; Valencia et al., 2013). Possible compositions include a small iron-rich or rocky core with an extended H/He or steam envelope, or a water-world with a modest H/He envelope. Future transmission spectroscopy observations would help to break these degeneracies.

WASP-47e is among the few known USP planets $> 1.5\,R_\oplus$. Lopez (2017) explains the dearth of larger USP planets as a consequence of photoevaporation of H/He envelopes of larger planets that formed water-poor. The one potential counter-example noted by Lopez (2017) is the $1.9\,R_\oplus$ USP planet 55 Cnc e. The most recent mass and radius constraints suggest the presence of a water-rich envelope, 8 ± 3% of the planet's mass.

---

[3] NASA Exoplanet Archive, UT 24 September 2016, http://exoplanetarchive.ipac.caltech.edu

Table 5.2 (cont'd)

Parameter	Value	Units	Ref.
P	9.03081 ± 0.00074	days	A, B
$T_{\rm conj}$	$2457006.36927 \pm 0.00044$	BJD	B
$R_p/R_\star$	0.02886 ± 0.00047	—	B
a	0.0846 ± 0.0014	AU	A
$S_{\rm inc}$	157 ± 23	$S_\oplus$	A
R_P	3.71 ± 0.26	$R_\oplus$	A
K	3.94 ± 0.82	$\rm m\,s^{-1}$	A
M_P	12.75 ± 2.70	$M_\oplus$	A
ρ_p	1.36 ± 0.42	$\rm g\,cm^{-3}$	A
WASP-47e (circular orbit assumed)			
P	0.789597 ± 0.000013	days	B
$T_{\rm conj}$	$2457011.34849 \pm 0.00038$	BJD	B
$R_p/R_\star$	0.01456 ± 0.00024	—	B
a	0.01667 ± 0.00028	AU	A
$S_{\rm inc}$	4043 ± 593	$S_\oplus$	A
R_P	1.87 ± 0.13	$R_\oplus$	A
K	6.34 ± 0.78	$\rm m\,s^{-1}$	A
M_P	9.11 ± 1.17	$M_\oplus$	A
ρ_p	7.63 ± 1.90	$\rm g\,cm^{-3}$	A
Other			
$\gamma_{\rm HIRES}$	6.4 ± 1.5	$\rm m\,s^{-1}$	A
$\gamma_{\rm PFS,D15}$	20.5 ± 2.9	$\rm m\,s^{-1}$	A
$\gamma_{\rm CORALIE,H12}$	-27070.3 ± 5.1	$\rm m\,s^{-1}$	A
$\gamma_{\rm CORALIE,V16}$	-27085.3 ± 2.7	$\rm m\,s^{-1}$	A
$\sigma_{\rm jit,HIRES}$	3.7 ± 0.6	$\rm m\,s^{-1}$	A
$\sigma_{\rm jit,PFS,D15}$	6.3 ± 1.2	$\rm m\,s^{-1}$	A
$\sigma_{\rm jit,CORALIE,H12}$	5.9 ± 3.5	$\rm m\,s^{-1}$	A
$\sigma_{\rm jit,CORALIE,V16}$	6.7 ± 3.3	$\rm m\,s^{-1}$	A

Note. — $S_{\rm inc}$ = Incident flux, $T_{\rm conj}$ = Time of conjunction, A: This study, B: Becker et al. (2015), C: Sanchis-Ojeda et al. (2015). H12: Hellier et al. (2012), D15: Dai et al. (2015), V16: Neveu-VanMalle et al. (2016). Orbital periods of planets b and d are those from Becker et al. (2015), but with larger uncertainties (See §3).

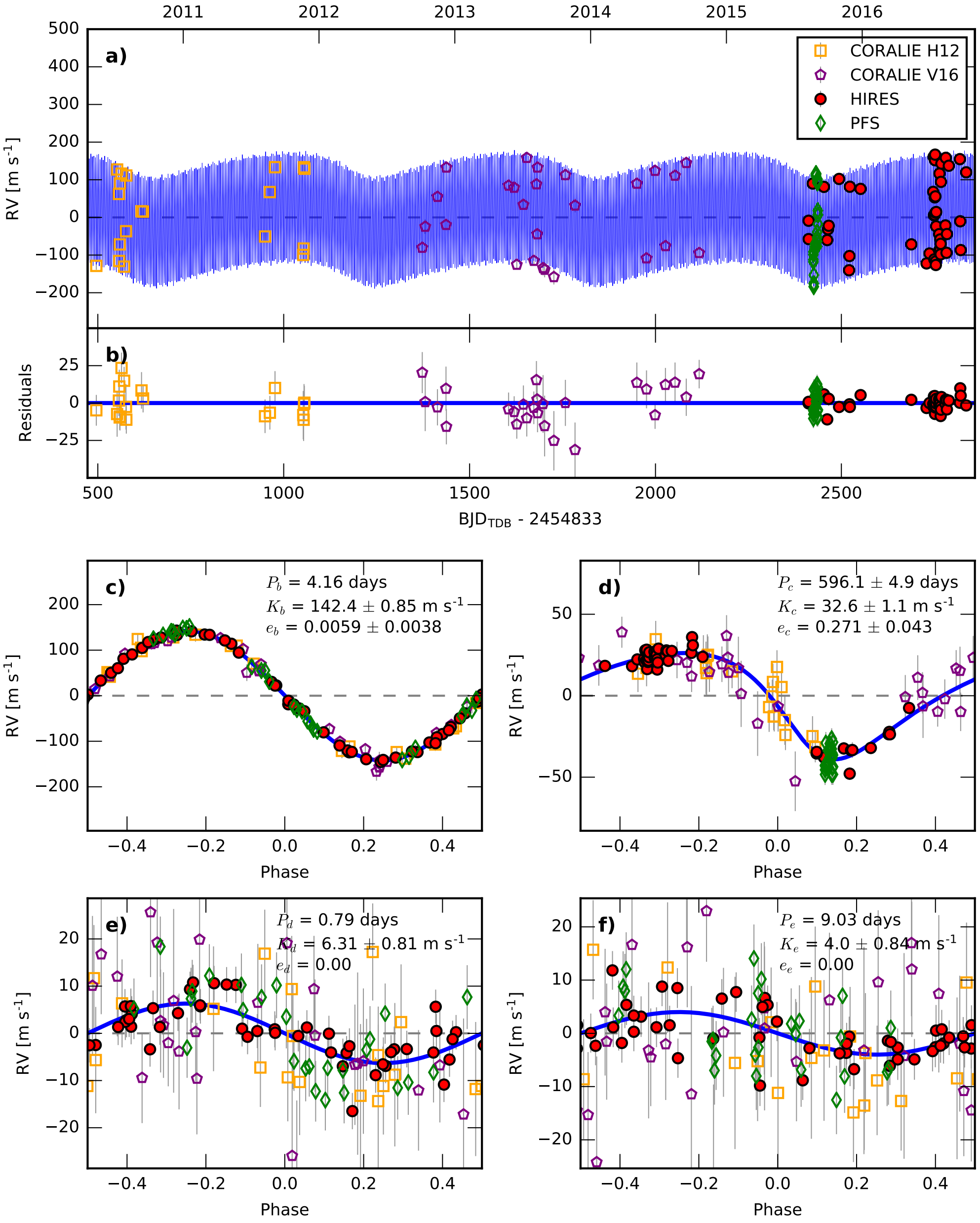

Figure 5.1: Four-planet RV model of WASP-47, assuming circular orbits for WASP-47d and WASP-47e **a)** The RV time-series. Filled red circles indicate Keck-HIRES data. Orange squares represent CORALIE data published by Hellier et al. (2012). Purple pentagons represent CORALIE data published by Neveu-VanMalle et al. (2016). Green diamonds indicate PFS data published by Dai et al. (2015). The solid blue line corresponds to the most likely model. Note that the orbital parameters listed in Table 5.2 are the median values of the posterior distributions. Error bars for each independent dataset include an RV jitter term listed in Table 5.2, which are added in quadrature to the measurement uncertainties. **b)** Residuals to the maximum-likelihood fit. **c-f)** The RV time-series phase folded at the orbital periods of each of the four planets after subtracting the other three planet signals.

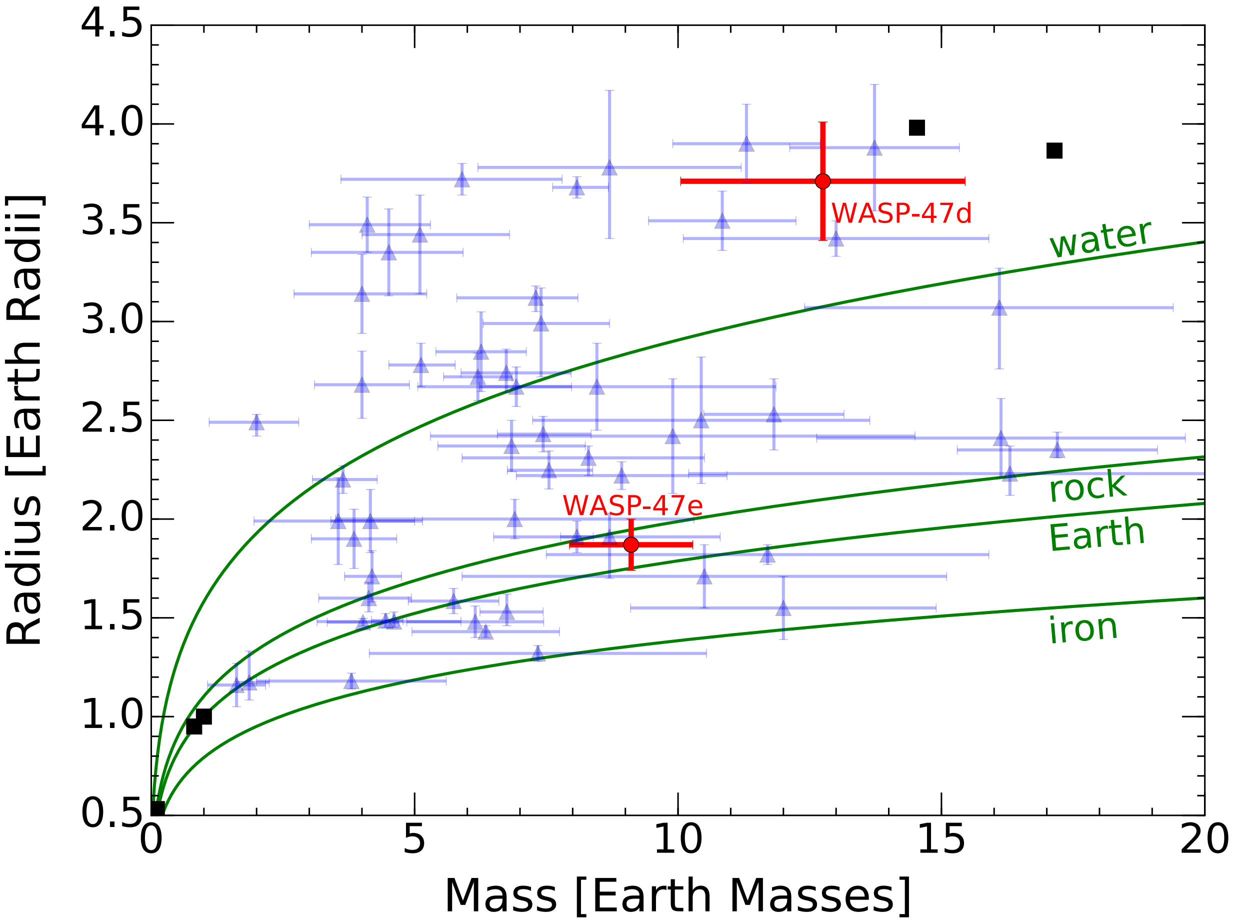

Figure 5.2: Radii and masses of all confirmed planets whose mass and radius are measured to better than 50% (2σ) precision (blue triangles). Solar System planets are represented as black squares. Red circles indicate our measurements of WASP-47d and WASP-47e. Green curves show the expected planet mass-radius curves for 100% iron, 100% rock (Mg_2SiO_4), 100% water (ice), and Earth-like (67% rock, 33% iron) compositions according to models by Fortney et al. (2007).

55 Cnc has remarkable similarities to WASP-47. It hosts a USP super-Earth (55 Cnc e), a non-transiting giant planet (55 Cnc b) at P=15 days, and three additional non-transiting planets at P = 44, 262, and $\sim$ 4800 days. The fact that these systems host both a HJ and a USP planet suggests that their formations are linked in some way. Moreover, the mass and radius of 55 Cnc e ($8.3 \pm 0.3\,M_{\oplus}$, $1.92 \pm 0.08\,R_{\oplus}$) are consistent with WASP-47e ($9.11 \pm 1.17\,M_{\oplus}$, $1.87 \pm 0.13\,R_{\oplus}$). Therefore, both planets could have water-rich envelopes. More well-characterized USP planets $\approx 2\,R_{\oplus}$ are needed to determine if they represent a distinct population of USP planets spawning from unique formation and/or evolutionary processes. In particular, as proposed by Huang et al. (2016), WASP-47b and 55 Cnc b might represent the rare close-in extremes of in-situ formation hypothesized to produce the $\sim$ 50% of warm-Jupiters (P = 10–200 days) that have small companions at shorter orbital distances. This highlights the limitations of classifying HJs and warm-Jupiters based on orbital period alone, without taking the more complete system architecture into account.

One clue about the formation history of 55 Cnc e is the fact that it transits whereas the outer planet (P $\sim$4800 days) is claimed, on the basis of HST astrometry, to be inclined to the line of sight by 30 degrees (McArthur et al., 2004). Hansen & Zink (2015) showed that if 55 Cnc e formed slightly beyond its current orbit, and migrated inwards through tidal dissipation, it would have crossed a pair of secular resonances in the system, which could have boosted its inclination and/or eccentricity. This would increase the tidal heating and potentially devolatilize the planet or drive it to Roche lobe overflow. The WASP-47 system also shows a potential secular resonance if WASP-47e once had a semi-major axis of 0.022 AU. Although this system clearly did not experience pumping of the inclination, a small but finite initial eccentricity for WASP-47d could have driven tidal evolution of WASP-47e through this resonance and rapidly increased the tidal heating, potentially leading to strong devolatilization. If WASP-47e and WASP-47d both formed as Neptune-size planets,, but WASP-47e was heated or tidally stripped, then their current difference in densities reflects their evolution rather than their origins.

From our MCMC analysis of the RV time-series, we determine the orbital eccentricity of the HJ to be < 0.021 at 99.7% (3σ) confidence. The very low eccentricity and the alignment between the orbital axis and stellar spin (Sanchis-Ojeda et al., 2015) are consistent with disk migration, in-situ formation, and the aforementioned secular interaction scenario. In future, this eccentricity constraint can be used to inform TTV models.

WASP-47 has a high metallicity (0.36 ± 0.05 dex) which has been shown to be associated with HJ occurrence and giant planet occurrence (e.g. Fischer & Valenti, 2005; Buchhave et al., 2014). The Kepler sample of Earth-size planets were found around stars of widely varying metallicity (Buchhave et al., 2014). However, if USPs are associated with metal-rich stars, it suggests different formation pathway than the bulk of known Earth-size planets—one that may be more closely associated with HJs. Although it is beyond the scope of this study, a comparison between the metallicities of stars hosting HJs with those hosting USPs will provide a useful test of the relationship between the formation of USPs and HJs.

We note that while this manuscript was under review, Almenara et al. (2016) reported mass and radius constraints of the WASP-47 system using a photodynamical model. They simultaneously fit the *K2* photometry and the RV measurements of Hellier et al. (2012), Dai et al. (2015), and Neveu-VanMalle et al. (2016). Their planet mass measurements are consistent with this study at the 1-σ level. Future incorporation of our Keck-HIRES RVs into a photodynamical analysis would further improve constraints of the WASP-47 system.

Table 5.3. Relative radial velocities, Keck-HIRES

BJD	RV $[\mathrm{m\,s^{-1}}]^{\mathrm{a}}$	Unc. $[\mathrm{m\,s^{-1}}]^{\mathrm{b}}$	S_{HK}
2457244.871067	0.48	1.67	0.126
2457244.878949	5.92	1.77	0.132
2457244.887016	-1.84	1.66	0.133
2457244.895257	-3.04	1.82	0.135
2457244.903486	-1.37	1.64	0.132
2457244.911878	-3.26	1.84	0.127
2457244.920153	-5.65	1.59	0.135
2457244.928510	-8.04	1.76	0.133
2457244.936600	-8.56	1.66	0.135
2457244.944818	-2.06	1.71	0.135
2457244.953082	-0.15	1.66	0.130
2457244.961427	-0.13	1.62	0.132
2457244.969923	-4.30	1.73	0.131
2457244.978731	-9.13	1.77	0.131
2457244.987215	-20.02	1.73	0.130
2457244.995815	-20.64	1.68	0.136
2457245.004993	-29.55	1.73	0.121
2457245.013720	-32.44	1.66	0.127
2457245.022227	-39.56	1.67	0.135
2457245.030607	-39.94	1.59	0.136
2457245.038917	-43.69	1.62	0.104
2457245.047448	-48.47	1.65	0.129
2457245.056198	-53.78	1.52	0.129
2457245.065700	-50.95	1.79	0.114
2457245.074508	-46.85	1.60	0.123
2457245.083096	-44.16	1.65	0.130
2457245.091812	-48.39	1.52	0.133
2457245.100712	-57.42	1.53	0.129
2457245.110018	-52.81	1.68	0.134
2457256.103458	96.66	2.11	0.135
2457286.030224	87.81	2.19	0.089
2457294.949126	-53.43	2.17	0.115
2457296.992830	-24.59	2.00	0.137
2457298.980931	-15.40	3.62	0.131
2457326.879645	108.91	1.96	0.036
2457353.819776	-133.61	2.05	0.142
2457354.803856	-95.88	1.95	0.128
2457355.794764	88.20	1.99	0.127
2457384.711392	82.45	1.93	0.127
2457521.108185	-64.84	1.86	0.126
2457562.108559	-115.52	1.81	0.160
2457570.076758	-89.15	2.05	0.151
2457580.060228	74.59	1.83	0.140
2457581.046494	167.52	1.81	0.131
2457582.043488	12.38	1.98	0.135

Table 5.3 (cont'd)

BJD	RV $[\mathrm{m\,s^{-1}}]$[a]	Unc. $[\mathrm{m\,s^{-1}}]$[b]	S_{HK}
2457583.061003	-104.76	1.83	0.136
2457583.922512	13.32	1.83	0.133
2457584.109907	59.97	1.80	0.127
2457584.914664	158.68	1.90	0.137
2457585.068538	173.44	1.79	0.135
2457585.911306	62.57	1.98	0.140
2457586.089591	19.48	2.04	0.127
2457586.909613	-110.17	1.72	0.131
2457587.088454	-119.61	1.67	0.138
2457587.950710	-16.79	2.01	0.136
2457588.097234	21.03	1.80	0.141
2457595.894592	-81.36	2.24	0.138
2457596.120574	-37.76	2.18	0.121
2457596.917828	123.24	2.11	0.131
2457598.938091	-51.78	2.07	0.119
2457599.106292	-79.28	1.95	0.135
2457599.928092	-91.45	1.83	0.140
2457600.118064	-63.52	1.87	0.135
2457600.927270	101.12	2.06	0.138
2457602.055444	149.79	2.09	0.132
2457612.852525	-14.58	1.83	0.136
2457614.023768	164.96	1.77	0.135
2457615.871589	-87.25	1.96	0.132
2457616.894897	-37.49	1.90	0.133
2457622.042983	143.94	2.30	0.129
2457651.804239	161.48	1.74	0.128
2457652.803402	-3.55	1.77	0.145
2457653.938888	-80.03	1.86	0.142
2457668.749161	126.48	2.14	0.143

[a] RVs do not include zero point offset (γ_{HIRES}, Table 5.2)

[b] Uncertainties do not include jitter ($\sigma_{\mathrm{jit,HIRES}}$, Table 5.2)

CHAPTER 6
BULK PROPERTIES OF ROCKY AND GAS-DOMINATED PLANETS: DISTRIBUTIONS AND INTERPRETATIONS

6.1 Introduction

NASAs Kepler mission discovered thousands of planets transiting their host stars, mapping out the distribution of planet radii and orbital periods. However, only a small fraction of *Kepler* planet hosts are bright enough for Doppler follow-up to measure planet masses and constrain their compositions — one of the best links to their formation histories.

By the end of the prime *Kepler* mission in 2013, only a few dozen planets smaller than Neptune ($< 4\ R_\oplus$) had precisely measured masses. A transition from rocky to gaseous planets was observed at a radius of ~ 1.5–$2 R_\oplus$ (Weiss & Marcy, 2014). However, there is significant scatter about the mean mass-radius relation, indicating compositional diversity (e.g. Wolfgang & Lopez, 2015; Wolfgang et al., 2016). For example, Kepler-138d, a "fluffy", ~ 1.3 g cm^{-3} planet, which seems to be an exception to the otherwise rocky population of planets smaller than $\sim$1.5 $\mathrm{R}_\oplus$.

This noticeable diversity suggested that the planets mass-radius relation might be partially driven by environmental factors like temperature and host star properties. There is growing evidence that photoevaporation of planetary envelopes by incident X-ray and EUV radiation plays a key role in sculpting planet radii and densitites. The discovery of valley in the planet radius distribution at 1.5–2.0 $R_\oplus$ by the California Kepler Survey (CKS Petigura et al., 2017b; Fulton et al., 2017) divided the population of small planets into "super-Earths" and "sub-Neptunes". This valley has been interpreted as a natural effect of photoevaporation. Owen & Wu (2017) showed that planets are least susceptible to photoevaporation when the core radius is half of the total planet radius ($R_{\mathrm{core}} = 0.5 R_P$). Puffier planets quickly shrink to twice the size of their core (f_{env} $\approx$ 1%), while planets that form with modest envelopes ($f_{\mathrm{env}} \lesssim 1\%$) are rapidly stripped to their cores, creating a gap in planet radius. In order for photoevaporation models to correctly predict the observed radius distribution, simulated planets had to posses cores with Earth-like compositions and form with H/He envelopes. In other words, these small worlds had to be water-poor.

In this paper, we study the transition from rocky to gaseous planets (super-Earths to sub-Neptunes) by examining the mass-radius relation of planets 1–8 $R_\oplus$ in unprecedented detail. We leverage dozens of recent measurements of masses of small planets from the *K2* mission to construct a catalog of 139 planets with measured densities. This includes planets from *Kepler*, *K2*, and other sources. We spectroscopically characterize all of the host stars and incorporating parallaxes from Gaia to measure precise planet masses and radii. Armed with a large and precise statistical sample, we investigate the distribution of planet core masses and the role of photoevaporation in sculpting the mass-radius relation.

Table 6.1. Sample Summary

Type	N_{stars}	N_{planets}
Kepler TTV	19	30
Kepler RV	20	27
K2 RV	54	73
Other RV	8	9
Total	101	139

In Section 6.2, we outline our sample selection and vetting processes. Our stellar characterization methods are described in Section 6.3, while Section 6.4 summarized our derivations of planet radii, masses, and core masses. We present and interpret the resulting catalog of planet masses and radii in Section 6.5. We observe a gap in the distribution of planet compositions and a positive correlation between planet core masses and host star metallicities. Concluding statements are provided in Section 6.6.

6.2 Sample Selection

Our goal is to construct a comprehensive catalog of transiting planets 1–8 Earth radii, whose masses are constrained either by radial velocities (RVs), or transit timing variations (TTVs). After selecting the sample, we re-derive properties of each planetary system according to a uniform set of stellar host parameters derived from spectroscopy of the host star. Since most sub-Jovian planets were discovered via the transit method, we chose to filter our sample based on planet radius rather than planet mass. Here, we outline the different resources from which we gathered our sample of planets.

6.2.1 NASA Exoplanet Archive

We first queried the NASA Exoplanet Archive (NEA) Extended Planet Database[1](Akeson et al., 2013) for all confirmed planets with mass constraints (1461 planets, 2529 references as of March 13 2018) and separately for all confirmed planets with radius constraints (2947 planets, 5119 references).[2] We selected the 316 planets returned from both queries and had at least one reference citing Rp < 8 Re. We exclude circumbinary planets (Kepler-38b, Kepler-47b and c, Kepler-64b, Kepler-413b, Kepler-453b)

---

[1] https://exoplanetarchive.ipac.caltech.edu/cgi-bin/TblSearch/nph-tblSearchInit?app=ExoTbls&config=exomultpars

[2] A joint query of mass and radius would have excluded references that did not include both mass and radius measurements.

6.2.2 Hadden & Lithwick (2017)

We also select planets from Hadden & Lithwick (2017), hereafter HL17, who analyzed the TTVs of 145 planets from 55 Kepler multiplanet systems. Their measurements of planet masses and eccentricities are not listed in the NEA. The HL17 catalog is a favorable resource for our study for several reasons: First, it constitutes a uniform analysis of TTVs including most of the planetary systems that have been analyzed by previous TTV studies. Therefore, it is a natural choice to avoid selection biases. Second, HL17 use the TTV measurements from Holczer et al. (2016), which are derived using all 17 quarters of Kepler long-cadence photometry. Finally, HL17 assess the robustness of each mass constraint. They perform MCMC fits of the TTVs using numerical N-body integration and use analytical fits as a sanity-check. For the MCMC analysis, they separately measure masses using two different priors — A "high" mass prior weighted towards high masses and low eccentricities as well as a "default" mass prior weighted towards low masses and high eccentricities. When the posteriors from the two different trials agree, it indicates that the mass-eccentricity degeneracy is broken by chopping and second-harmonic signals, and that the mass measurement is reliable.

We select the planets listed by HL17 as $R_P < 8\ R_\oplus$ with a "robust" mass disposition. These are planets with a $>$1-σ mass detection for which the the peak of the "high" mass posterior is within the 1-σ confidence interval of the "default" mass posterior. We note that for Kepler-138, we adopt the masses from Almenara et al. (2018), derived from a photodynamical analysis.

We discovered that several of the planet mass uncertainties in the machine readable versions of H17 Table 1 are erroneous when compared to the actual table included in the manuscript. In most cases where the uncertainty is $\geq 10\ M_\oplus$, the digits to the left of the ones digit are missing. For example, the manuscript lists Kepler-56c as $32.0^{+11.2}_{-10.5}\ M_\oplus$, but the machine-readable tables list $32.0^{+11.2}_{-0.5}\ M_\oplus$. We have corrected our uncertainties to match those in the H17 manuscript and notified the authors about the error.

6.2.3 Howard et al. K2 planet mass catalog

Howard et al. (in prep), hereafter H18, report masses of ~ 50 planets discovered by NASA's *K2* mission. Masses were measured by fitting multiple years of Doppler observations of *K2* planet hosts conducted using Keck-HIRES. The HIRES RVs were jointly fit with RVs reported by other studies, where available. Host stars were precisely characterized using Keck-HIRES spectra and AO images from a suite of AO instruments. Observations stemmed from a larger K2 follow-up program dedicated to validation and characterization of K2 planet candidates. Selection of candidates for RV follow-up was based primarily on the likelihood and efficiency of detecting planet signals — on the measured orbital period, radius, and host star activity and brightness. Stars were typically not observed if the RV signals predicted using the mean mass-radius relations of Weiss & Marcy (2014) and Wolfgang et al. (2016) were $\lesssim 1.5\ \mathrm{m\,s^{-1}}$ (see H18 for details). This introduces a bias against the detection of planets denser than predicted by these relations.

6.2.4 Removal of stellar blends

While the planets in our sample have confirmed dispositions, some of their radii may be significantly underestimated because of transit dilution caused by the presence of secondary stars in the photometric aperture (Ciardi et al., 2015). We tested each star for blend scenarios using our HIRES spectra, and previous analyses of adaptive-optics images.

Each HIRES spectrum was examined for multiple sets of stellar lines using the algorithm of Kolbl et al. (2015). This algorithm can detect secondary stars $T_{\rm eff} = 3400$–$6100\,{\rm K}$, down to 1% contrast in V and R bands, and $\Delta RV > 10$ m s^{-1}.

Furlan et al. (2017) generated a catalog of KOI stellar companions including those previously discovered by several other high-resolution imaging surveys at optical to near-IR wavelengths (e.g Lillo-Box et al., 2012, 2014; Law et al., 2014; Baranec et al., 2016; Kraus et al., 2016; Ziegler et al., 2017). The catalog includes each of the Kepler stars in our sample. They identified and characterized blends and provide correction factors for planet radii based on the expected dilution of the transit depth. We exclude all stars with companions bright enough to cause our planet radii to be underestimated by more than our typical radius measurement uncertainty of 5%, assuming the planet transits the primary star. In total, we excluded two Kepler stars based on this criterion (Kepler-345, Kepler-326).

All of the K2 host stars in our sample have been observed by AO instruments. The other host stars (i.e. non-Kepler/K2) in our sample have been thoroughly vetted for blends using high-resolution imaging. These stars host some of the first small planets ever discovered and have since been secured by numerous follow-up observations. We verified that all of these stars have been validated by high-resolution imaging. Moreover, many of these other stars are nearby and have high-proper motions. In many cases, archival images from decades ago have been used identify presently blended background stars that were previously at much larger separations.

6.2.5 Other sample cuts

We further remove all planets with grazing or near-grazing transits. Specifically, we exclude all planets with transit impact parameter $b > 0.7$. When the planet grazes the stellar disk, planet radius uncertainties can be very large and dependent on the choice of stellar limb-darkening models. We also exclude stars with effective temperatures $T_{\rm eff} < 3400$ K. The empirical library of stellar spectra that we use to model our observed spectra has few stars cooler than 3400 K, so that our empirical matching methods become unreliable (see Section 6.3.1). Finally, we exclude two stars, WASP-156 and CoRoTID 223977153, as their planets were published recently. So far, we have been unable to acquire Keck-HIRES spectra of these stars.

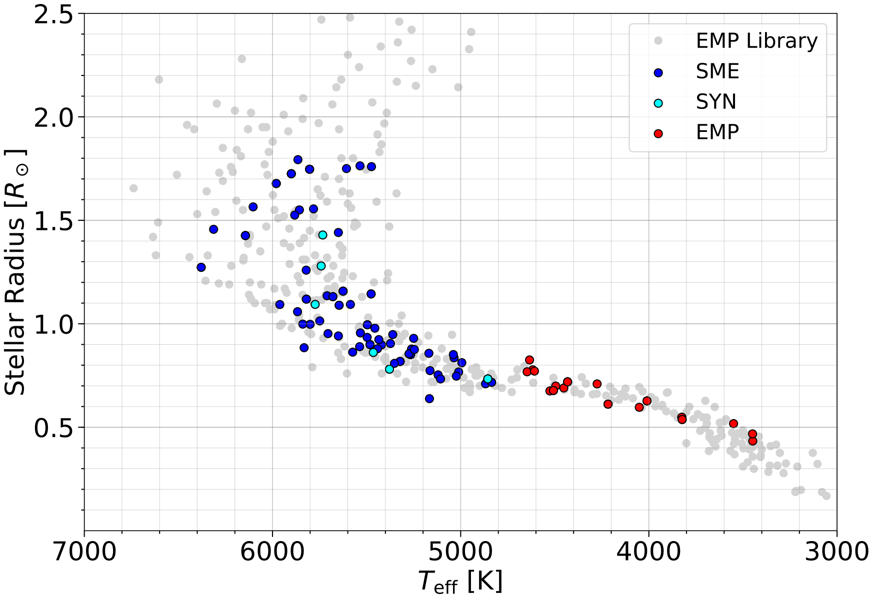

Figure 6.1: Radii and effective temperatures of host stars in our sample. Dark blue circles correspond to stars spectroscopically characterized using Spectroscopy Made Easy (Brewer et al., 2015). Cyan circles indicate stars characterized with SpecMatch "synthetic" (Petigura et al., 2013b), and red circles represent stars characterized using SpecMatch-Emp (Yee et al., 2017). The library of stars used by SpecMatch-Emp are shown as gray points. The sample becomes sparse below ~ 3400 K, so we exclude cooler stars from our sample.

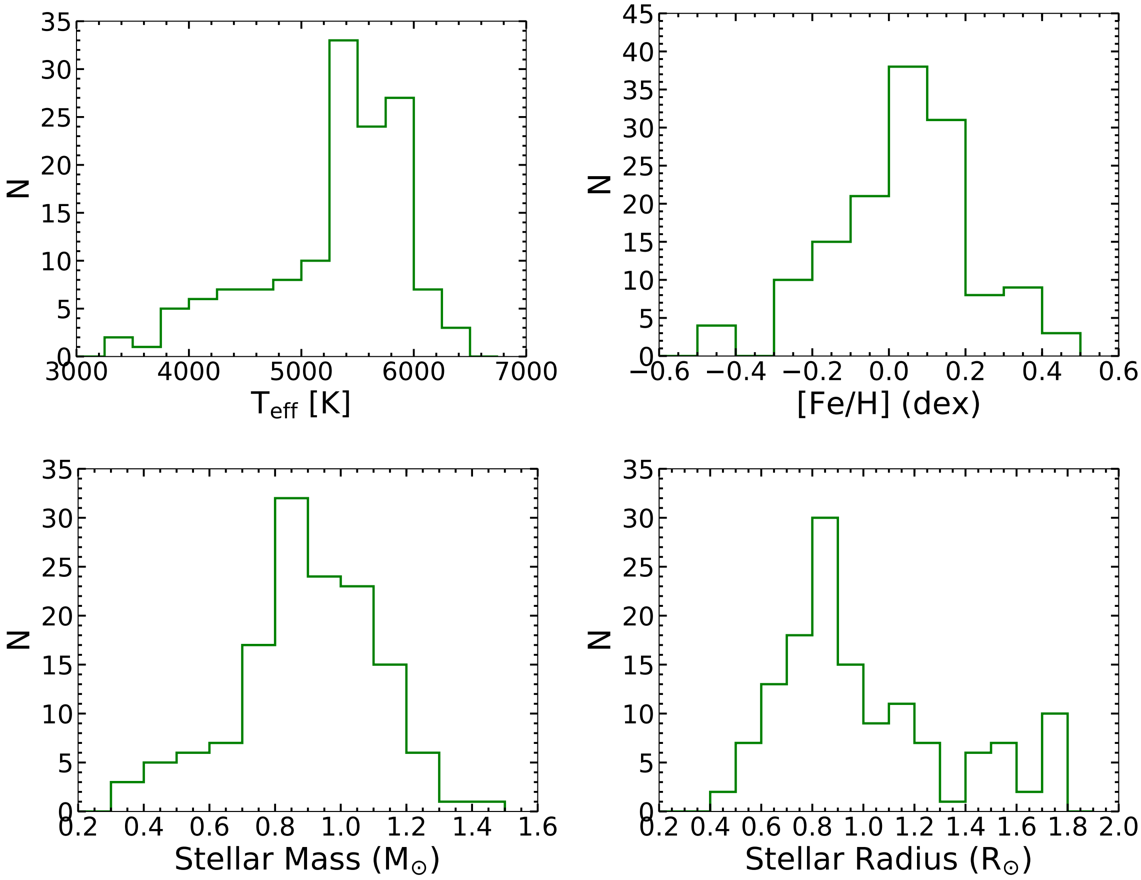

Figure 6.2: The distributions of stellar properties $T_{\rm eff}$, [Fe/H], $M_\star$, and $R_\star$ for our adopted planet sample.

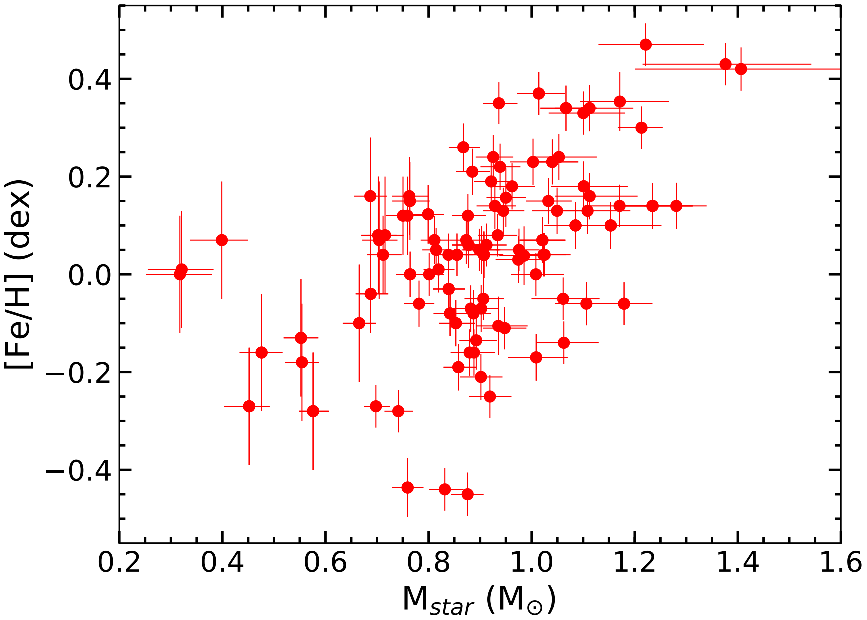

Figure 6.3: There is a significant correlation between stellar metallicity and stellar mass, which is important to the analysis in Section 6.5.3

6.3 Stellar Characterization

Many properties of the planets in our sample, including their masses and radii, are measured in relation to those of their stellar hosts. Typically, multiple estimates of the same planet parameter exist in the literature, from a suite of different studies. Systematic differences between stellar characterization methods used by those studies can manifest as systematic differences in derived planet properties. These systematics should be considered when stitching together a catalog of planets from the literature, especially when examining how the distribution of planet bulk properties depends on characteristics of the host star.

We mitigate these systematic errors by re-deriving the physical properties of every planet in our sample using a homogeneously generated catalog of of host star properties. The rank-orders of our measured stellar properties (i.e relative values) are more secure than if we had assumed values from the literature.

To this end, we obtained a Keck-HIRES spectrum of each star, many of which were previously acquired as part of the California Planet Search and *K2* planet search. We collected HIRES spectra of the remaining planet hosts in our sample, with the exception of a two recently identified planet hosts WASP-156, and CoRoTID 223977153. These stars had already set for the season by the time we identified them as suitable targets for our sample. Since we do not have a HIRES spectrum, we omit these stars and their planets from our final sample.

Our complete catalog of stellar properties is listed in Table 6.5. Figure 6.2 displays the distributions of T_{eff}, [Fe/H], $M_\star$, and $R_\star$. Here we describe our stellar characterization methods.

6.3.1 Effective Temperatures, surface gravities, and metal abundances

Stellar parameters were derived from each HIRES spectrum using different spectroscopic analysis tools for stars hotter and cooler than 4700 K (hereafter "hot" and "cool" stars respectively). For the hot stars we measured T_{eff}, $\log g$, and the abundances of various metals using Spectroscopy Made Easy (SME, Brewer et al., 2015). Many of the same HIRES spectra were previously analyzed by Brewer et al. (2016) and Brewer & Fischer (2018) using SME, in which case we adopted the measurements from those catalogs. We ran SME on the remaining spectra and report those results here for the first time. We followed Brewer & Fischer (2018) equations 1 and 2 to estimate uncertainties on T_{eff}, $\log g$, and metal abundances as a function of spectral SNR. This yielded T_{eff} uncertainties smaller than 50 K. However, conservatively adopted 100 K uncertainties for all hot stars to account for systematic differences between temperatures measured by SME and other spectroscopic modeling tools like SpecMatch (Petigura, 2015) as well as other techniques like interferometry and the infrared flux method.

The SME code did not successfully run for a small subset of our hot stars, possibly due to inadequacies in a few of our calibration spectra. In such cases we used SpecMatch (Petigura, 2015), which matches HIRES spectra to an interpolated library of model spectra from Coelho et al. (2005). It has been previously demonstrated that spectroscopic parameters derived from SpecMatch and SME are in good agreement (Petigura et al., 2017b).

Below 4700 K, the onset of dense forests of molecular lines complicates spectral synthesis, limiting the reliability of stellar characterization pipelines such as SME and SpecMatch. Therefore, for the cool stars we used SpecMatch-Emp (Yee et al., 2017), to measure T_{eff} and [Fe/H]. SpecMatch-Emp derives these parameters by comparing the spectra with a library of well-characterized stars spanning $\sim$ 3000–7000 K. We exclude stars with $T_{\mathrm{eff}} < 3400$ K because SpecMatch-Emp's spectral library is sparse at these temperatures, limiting its accuracy.

We derived stellar masses and radii by combining constraints from spectroscopy, astrometry, and photometry using the publicly available `isoclassify` code (Huber et al., 2017). Our methodology is described in detail in Fulton & Petigura (2018). In brief, stellar radius may be determined from the Stefan-Boltzmann Law given an absolute bolometric magnitude M_{bol} and an effective temperature. We derived bolometric magnitudes according to

$$M_{\mathrm{bol}} = m_K - A_K - \mu - BC_K. \tag{6.1}$$

where m_K is the apparent K-band magnitude, A_K is the line-of-sight K-band extinction, μ is the distance modulus, and BC_K is the K-band bolometric correction. In our modeling, constraints on m_K come from 2MASS (Skrutskie et al., 2006) and constraints on μ come from Gaia DR2 (Gaia Collaboration et al., 2018). We derived BC_K by interpolating of the grid of BC_K computed by

Conroy et al., (in prep). We account for K-band extinction using the using the 3D dust map from Bovy et al. (2016). For most targets $A_K < 0.01$ mag, so neglecting extinction entirely would only amount to a 0.5% error on stellar radius.

Figure 6.1 shows our measured stellar radii as a function of T_{eff}. Typical errors on our stellar masses and radii are 3–5%.

6.4 Derived Planet Properties

Table 6.6 provides a list of planet parameters. Here we discuss the procedures used to determine planet radii, masses, and core masses.

6.4.1 Radius

Planet radii were computed by multiplying our measured stellar radii by $R_p/R_\star$ measurements, most of which come from the literature. For the Kepler planets, we adopted $R_p/R_\star$ values from the Kepler DR25 catalog Thompson et al. (2018). Kepler-78b was not published in Thompson et al. (2018), so we utilized the transit parameters listed in (Howard et al., 2013).

For the *K2* stars we generate the light curves as described in H18. The same methods were used to produce light curves of a few additional *K2* stars in our sample that were not in H18. These include K2-56, K2-131, K2-141, and HIP 116454. To summarize, we tested both the `k2phot` and EVEREST 2.0 (Luger et al., 2016, 2017) pipelines. The `everest` pipeline yielded better overall photometric precision than `k2phot`, but the `everest` light curves had more significant outliers. The excess of outliers is partially due to the fact that `everest` does not automatically exclude measurements close in time to spacecraft thruster firings, which occur every ∼6 hours. The `k2phot` pipeline flags and removes photometry simultaneous with thruster firings by identifying the abrupt changes in the motion of stars across the detector. We retrieved the points flagged by the `k2phot` pipeline and masked the corresponding `everest` measurements.

We used the same methodology to fit the `k2phot` and `everest` light curves. After using a median filter to remove any long term trends caused by stellar variability or instrument systematics, we used the Python package `emcee` (Foreman-Mackey et al., 2013) for Markov Chain Monte Carlo (MCMC) exploration of the posterior probability surface. To reduce unnecessary computational expense, we only fit the light curves in $3\times T_{14}$ windows centered on the individual mid-transit times. In order to obtain robust parameter estimates for multi-planet systems, we removed the transits of all other planets from the light curve before fitting each individual planet. We adopted a Gaussian likelihood function and the analytic transit model of Mandel & Agol (2002) as implemented in the Python package `batman` (Kreidberg, 2015), assuming a linear ephemeris and quadratic limb darkening.

The transit model free parameters we used are orbital period P_{orb}, mid-transit time T_0, scaled

Table 6.2. Source of transit parameters

Stars	Light curve	Transit parameters
Kepler	Thompson et al. (2018)	Thompson et al. (2018)
K2	EVEREST 2.0	BATMAN
Other	best literature	best literature

planet radius $R_p/R_\star$, scaled semi-major axis $a/R_\star$, impact parameter $b \equiv a\cos i/R_\star$, and quadratic limb-darkening coefficients (q_1 and q_2) under the transformation of Kipping (2013). We also fit for the logarithm of the Gaussian errors ($\log\sigma$) and a constant out-of-transit baseline offset, which was included to minimize any potential biases in parameter estimates arising from the normalization of the light curves. We imposed Gaussian priors on the limb darkening coefficients, with mean and standard deviation determined by Monte Carlo sampling an interpolated grid of the theoretical limb darkening coefficients tabulated by Claret et al. (2012), enabling the propagation of uncertainties in host star effective temperature $T_{\rm eff}$, surface gravity $\log g$, and metallicity [Fe/H]. We refined initial parameter estimates by performing a preliminary nonlinear least squares fit using the Python package `lmfit` (Newville et al., 2014), and then initialized 100 "walkers" in a Gaussian ball around the least squares solution. We ran the MCMC for 5000 steps and visually inspected the chains and posteriors to ensure they were smooth and unimodal. Finally, we computed the autocorrelation time[3] of each parameter to ensure that we had collected 1000's of effectively independent samples after discarding the first 3000 steps as "burn-in."

For all non-*Kepler*/*K2* stars ("other"), we adopt $R_p/R_\star$ measurements from the literature. When multiple measurements of $R_p/R_\star$ exist in the literature with similar precision, we select the measurement obtained at the wavelengths closest to the Kepler bandpass for consistency.

6.4.2 Mass

Planet masses were derived by scaling the mass measurements from the literature by a factor $(M_\star/M_\star^{\rm lit})^x$, where $M_\star$ is our measured stellar mass and $M_\star^{\rm lit}$ is the stellar mass from which the planet mass was derived in the literature. For RV detections, the measured planet mass is proportional to the RV semi-amplitudes, which scales as $M_\star^{-2/3}$. Therefore, for RV systems we adopt x=2/3. TTV analyses measure $M_P/M_\star$, so we adopt x=1. Some TTV studies directly reported the ratio of planet mass to stellar mass, in which case we simply multiplied that ratio by our measured $M_\star$.

---

[3] `https://github.com/dfm/acor`

Table 6.3. Planet Groups

Group	P (days)	R_P ($R_\oplus$)	Number
sub-Saturn	any	$4-8$	29
sub-Neptune	any	$2-4$	66
super-Earth	any	$1-2$	45
ultra-short-period	<1	>1	9

6.4.3 Core Mass

We estimate planet core mass, using the planet structure and thermal evolution models of Lopez & Fortney (2014), which assume each planet is comprised of an Earth-composition core (30% Fe, 70% Mg_2SiO_4) surrounded by a solar-composition H/He envelope. Lopez & Fortney (2014) simulated the radius evolution of such planets over a grid of planet masses, core mass fractions (CMF), and incident flux ($S_{\rm inc}$). We interpolated this grid to estimate core mass fractions given our measured, planet masses, radii, incident fluxes, and ages. Note that here, and throughout this text we refer to Mg_2SiO_4 as "rock".

6.5 Results & Analysis

Throughout this analysis, we group planets according to their radius and orbital period as outlined in Table 6.3. Figure 6.4 shows the distribution of measured planet radii and orbital periods. Our sample includes nine ultra-short-period planets (USPs, $P < 1$ day). We note that sub-Saturns (4–8 $R_\oplus$) are overrepresented in our sample due to their higher detectability and Doppler programs which have specifically targeted them (e.g. Petigura et al., 2017a). While they comprise $\sim$ 25% of our planet sample, their occurrence rate is only ∼4% that of 1–4 $R_\oplus$ planets for $P < 100$ days (Fulton et al., 2017). The fact that most of the planets with $P \lesssim 3$ days are smaller than 2 $R_\oplus$ is a characteristic of the general planet population and not the results of detection biases, as observations are more sensitive to larger planets. However, these small, short-period planets are overrepresented in our sample due to their high detectability and scientific interest — follow-up observations are usually conducted at every opportunity. These planets are intrinsically rare, as planet occurrence drops steadily inside P < 10 days (Howard et al., 2012).

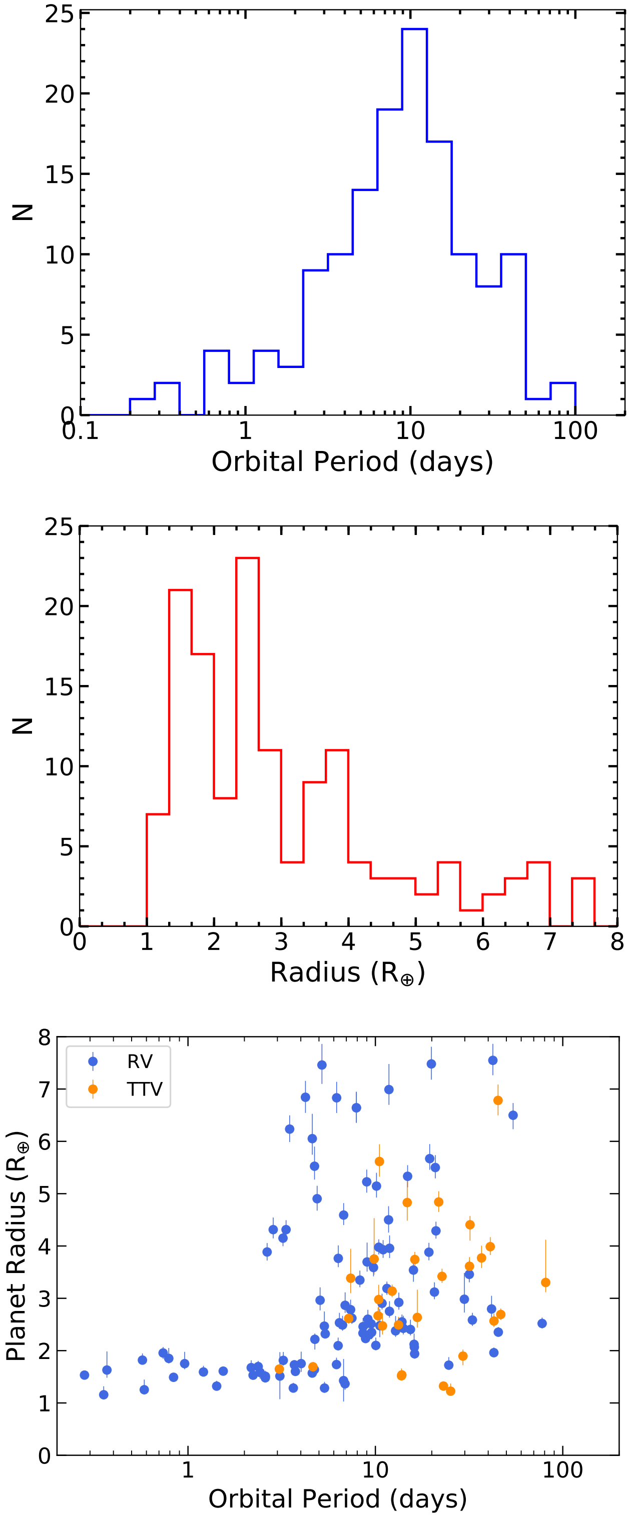

Figure 6.4: The distributions of planet orbital periods and radii in our sample.

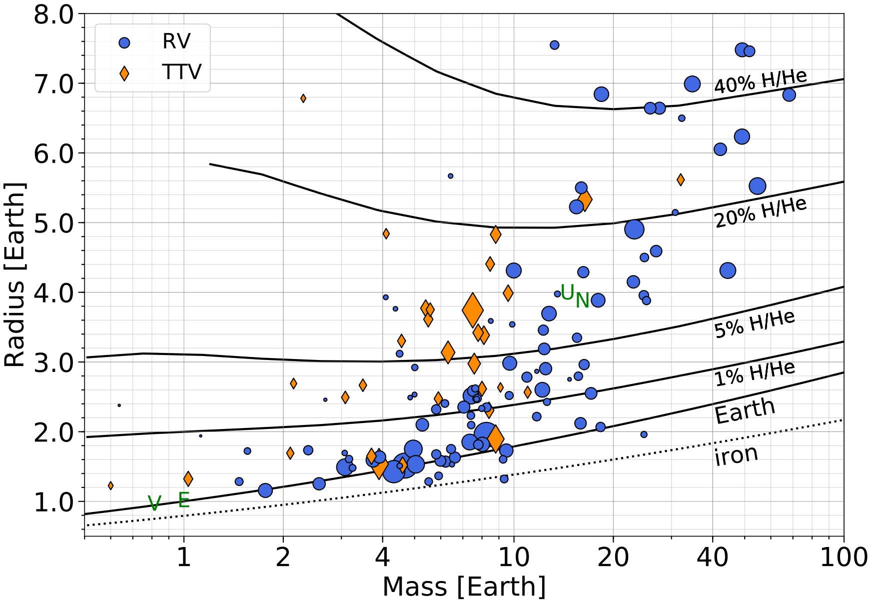

Figure 6.5: Planet mass-radius diagram for our entire catalog of planets from 1–8$R_\oplus$. Blue circles and orange diamonds indicate planets whose masses were measured from RVs and TTVs respectively. The size of each point scales as $1/\sigma_{M_P}$ Green letters denote Solar System planets Venus, Earth, Uranus, and Neptune. Solid black curves show the mass-radius relations of Lopez & Fortney (2014) for planets with Earth-composition cores surrounded by H/He envelopes with mass fractions of 0%, 1%, 5%, 20% and 40%. These assume an incident flux of $100S_\oplus$ and an age of 5 Gyr. The dashed black line indicates the mass-radius relation of a pure iron planet modeled by Fortney et al. (2007).

6.5.1 A gap in planet composition

The observed gap in the planet radius distribution (Fulton et al., 2017) indicates two distinct populations of small planets — “super-Earths” comprised of Earth-composition cores, and “sub-Neptunes” which are similar cores surrounded by H/He envelopes, comprising a few percent of their total mass. If the radius gap is caused by the complete photoevaporation of tenuous atmospheres ($\lesssim$ 1% H/He), then there should be similar gap in the planet density-radius distribution, precisely where planets with tenous atmospheres would reside.

Figure 6.6 reveals a bimodal density-radius distribution that is consistent with the photoevaporative interpretation of the planet radius gap. The left panel shows all planets, while the right panel excludes planets whose masses are measured to better than 33% precision (i.e. a 3-σ detection). The background shading scales with the number density of points, weighted by measurement uncertainties. Specifically, we generated 1000 draws of planet density and radius from the mass and radius posteriors of each planet. We then constructed a 2-D histogram of the entire set of draws and smoothed it using a 2-D Gaussian kernel.

The resulting distribution is bimodal. The population of $\sim$ 1–2-$R_{\oplus}$ planets with high densities is consistent with solid cores surrounded by little to no gas (“super-Earths”). Most of these planets are highly irradiated ($S_{\mathrm{inc}} > 100\ S_{\oplus}$), and susceptible to photoevaporation. The second population consists of planets 2.2-3$R_{\oplus}$, with lower densities consistent with Earth-composition cores surrounded by a few percent H/He. Between these two populations, where planets with trace amounts of H/He ($< 1\%$), there is a deficit of planets. Note that the compositional curve corresponding to a 1% H/He envelope assumes an incident flux of 100 $S_{\oplus}$ and age of 5 Gyr.

Th compositional gap becomes even sharper when we exclude planets with poorly constrained masses ($<$ 3-σ). This is not an artifact of detection biases, as planets in the gap are more detectable than the super-Earth population. Moreover, there is almost no change in planet mass across the gap, only a change in radius. Interestingly, there is a small population of 1–2 $R_{\oplus}$ planets, with low densities consistent with $<$ 1% H/He atmospheres (e.g. Kepler-138d, GJ 9827d). These planets are relatively cool ($S_{\mathrm{inc}} < 100\ S_{\oplus}$) and less susceptible to photoevaporation. They are almost certainly underrepresented in our sample — their detectability is low because of their small size and long orbital periods.

6.5.2 Distribution of core masses and compositions

The distributions of planet masses and planet core masses are shown in the top panel of Figure 6.7. While the observed core mass distribution peaks at $\sim$ 6–9 $M_{\oplus}$, smaller cores are likely undersampled due to lower detectability. On the other hand, the steady drop of planet core masses beyond $\sim 10 M_{\oplus}$ is likely real. Only 13 planets have cores $> 10\ M_{\oplus}$ at $> 2\sigma$ confidence, and 11 of these are sub-Saturns. The core mass distribution of our sample indicates that super-Earths and sub-Neptunes, which comprise the bulk of the planet population, rarely possess cores $> 10 M_{\oplus}$. If larger cores

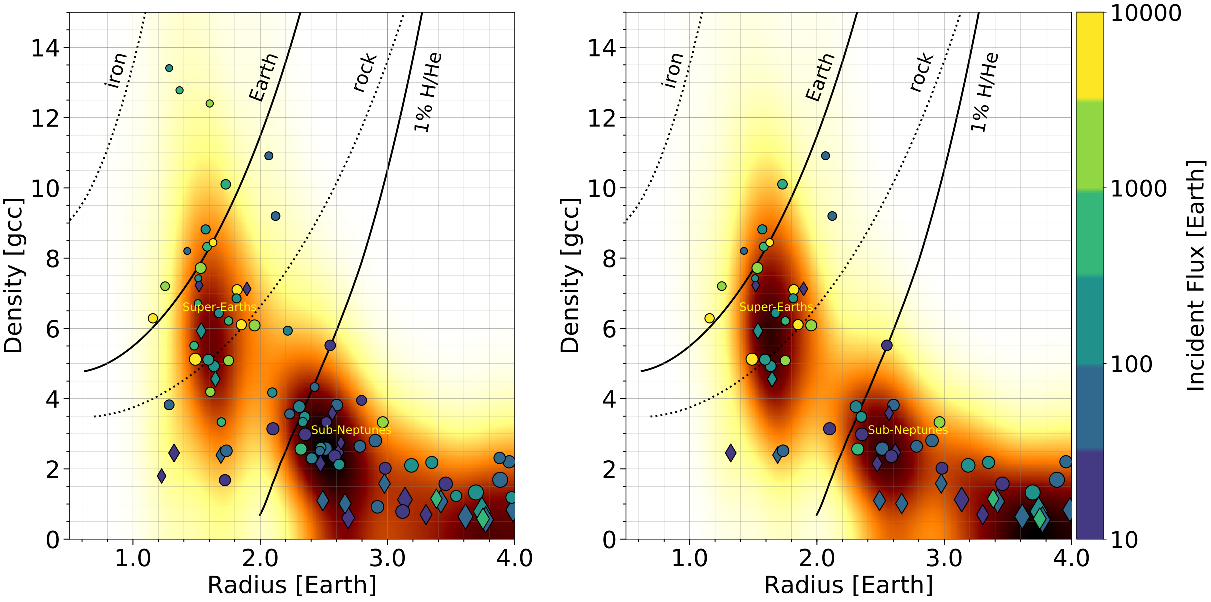

Figure 6.6: The density-radius distribution of our sample. The left panel shows all planets, while the right panel excludes planets whose masses are measured to better than 33% precision (i.e. a 3-σ detection). Points are colored according to planet incident flux and sizes scale as $1/\sqrt{\sigma_{\rho_p}}$. The background shading scales with the number density of points, weighted according to measurement uncertainties and smoothed using a Gaussian kernel. Distinct super-Earth and sub-Neptune populations are evident, with a gap between them, which is where planets with Earth-composition cores and $\lesssim 1\%$ H/He envelopes would reside. This gap is likely caused by the complete photoevaporation of planets with tenuous envelopes. There is a residual population of 1–2 $R_\oplus$ planets with lower densities. These planets experience low levels of irradiation, so they are less susceptible to photoevaporation.

form before most of the gas disperses from the disk, they are likely to experience runaway accretion and become giant planets.

The bottom panel of Figure 6.7 shows how the distribution of core masses changes with orbital period. At $P \lesssim 3$ days, cores do not exceed 10 $M_\oplus$. In contrast, from 3–10 days, there is a large diversity of core masses ranging from $\sim$ 1–40 $M_\oplus$. There appears to be a pile-up of 20–40 $M_\oplus$ cores, which are not observed beyond 10 days. This resembles the pile-up of hot-Jupiters observed at similar orbital periods, which has been attributed to net effect of disk migration and planet-star tides (e.g. Heller, 2018). The sub-Saturn population we observe with 20-40 $M_\oplus$ cores could arise from similar migration and tidal mechanisms. These planets might be former hot-Jupiters that lost part of their envelopes via photoevaporation or never accreted enough gas to exceed 8 $R_\oplus$.

The observed peak in the core mass distribution at 6–9 $M_\oplus$ is consistent with the typical core mass of $\sim 8M_\oplus$ inferred by Wu (2018) from the observed planet radius distribution. Assuming Earth-composition cores, she simulated the effects of photoevaporation on planet populations with different core and envelope mass distributions and found that the resulting radius distribution best matched observations when the characteristic core masses was $\sim 8M_\oplus$.

The assumption of an Earth-composition core was justified based on theoretical expectations of the efficiency of photoevaporation — cores of lower density (e.g. water ice) must have lower masses to maintain radii consistent with the "super-Earth" peak of the radius distribution, but these low-mass cores are expected to be too susceptible to photoevaporation for enough planets to retain envelopes and preserve the equal height of the two peaks in the radius distribution. For the two peaks to be equal in height, the cores must have Earth-like compositions, assuming the photoevaporation efficiency of $\sim$ 10% predicted by simulations. At least some of the USP planets are known to have Earth-like compositions (e.g. Kepler-78b). However, it is possible that photoevaporation models are inaccurate and that the typical core composition differs from Earth.

Fortunately, we can investigate the compositional diversity of small planet cores by directly examining the density-radius distribution of our super-Earth sample. For this analysis, we select all planets 1–$2R_\oplus$ with $\rho_p > 4\,\mathrm{g\,cm^{-3}}$, as these are likely to be bare cores (super-Earths), or at least have minimal atmospheres.

We place limits on the compositions of these planets in three different scenarios, each assuming a different two-component compositional model:

1. Iron/Rock core
2. Rock/Water core
3. Earth-like core + H/He

For Scenario 1, we sample the mass and radius posteriors of each planet 1000 times and, for each draw, we compute the rock mass fraction, f_rock, using equation 8 of Fortney et al. (2007). In cases where the density exceeds that of pure iron, we set $f_\mathrm{rock} = 0$. If the density is lower than that of pure rock, we set $f_{\mathrm{rock}} = M_{\mathrm{rock}} \;/\; M_P$, where M_{rock} is the mass of a planet with the same radius and $f_{\mathrm{rock}} = 1$ — this is a purely analytic continuation. The median of the resulting f_{rock} distribution is 0.82 (82% rock 18% iron), with a wide 1-σ confidence interval of 0.4–1.3.

We assess whether the breadth of the f_{rock} distribution of can be explained by measurement uncertainties. That is, we test whether our measured distribution is consistent with the scenario that all of these planets have the same f_{rock}. To conduct this test, we simulate a population of planets that have the same masses as our measured masses, but have radii that are computed assuming Earth-composition cores. We draw 1000 mass and radius measurements of each simulated planet assuming the same noise properties as our real mass and radius measurements. For each draw, we compute f_{rock}. The same steps are repeated using the observed masses and radii and their uncertainties.

Figure 6.8 compares the observed f_{rock} distribution with that from our simulated observations of Earth-composition cores (f_{rock} =0.7). The observed distribution is still broader than the simulated one, suggesting that there is an intrinsic spread of core compositions, some of which are Earth-like. We repeated the same simulations assuming cores with $f_{\mathrm{rock}} = 0.82$, to match the median of the observed population, but the simulated distribution was still wider than the observed one by the same amount. We also tried increasing our mass and radius uncertainties, and found that they had to be scaled by $\gtrsim 50\%$ before there was reasonable agreement with the observed population.

For Scenario 2, we seek to constrain the fraction of cores comprised of more than 10% water ice ($f_{\mathrm{ice}} > 0.1$). Again, we sample the mass and radius posteriors of each planet 1000 times and, for each draw, we compute f_{ice}, this time using equation 7 of Fortney et al. (2007). If the density is higher than that of pure rock, we set $f_{\mathrm{ice}} = 0$. For each planet, we compute the probability that $f_{\mathrm{ice}} > 0.1$. The mean of these probabilities is 0.18, suggesting that, at most, $\sim 18\%$ of these cores have $f_{\mathrm{ice}} > 0.1$, assuming they are composed of rock and water.

For Scenario 3, we sample the f_{env} posteriors for each of these planets 1000 times. We find that for all draws, $f_{\mathrm{env}} < 10^{-4}$. According to the models of Lopez & Fortney (2014), the addition of H/He at such extreme temperatures rapidly expands the planet radius beyond the measured value — the atmospheric scale height, H is proportional to planet temperature. Envelopes of these highly irradiated planets would be quickly photoevaporated, but tenuous hydrogen envelopes could be maintained by outgassing from the planet interior (Elkins-Tanton & Seager, 2008). While our conclusions are limited to the uncertainties of the Lopez & Fortney (2014) models, which are difficult to quantify, it is unlikely that these planets have $f_{\mathrm{env}} > 10^{-3}$.

In summary, our mass and radius measurements suggest that there is some intrinsic dispersion in the compositions of super-Earth cores. If most cores are mixtures of iron and rock, then the typical f_{rock} is $\sim 80\%$, slightly less iron-rich than Earth. If most cores are mixtures of rock and water ice, then $\lesssim 20\%$ of them have $f_{\mathrm{ice}} > 10\%$. Finally, if the cores are mostly Earth-like in composition, then they have little to no H/He ($f_{\mathrm{env}} \lesssim 10^{-3}$).

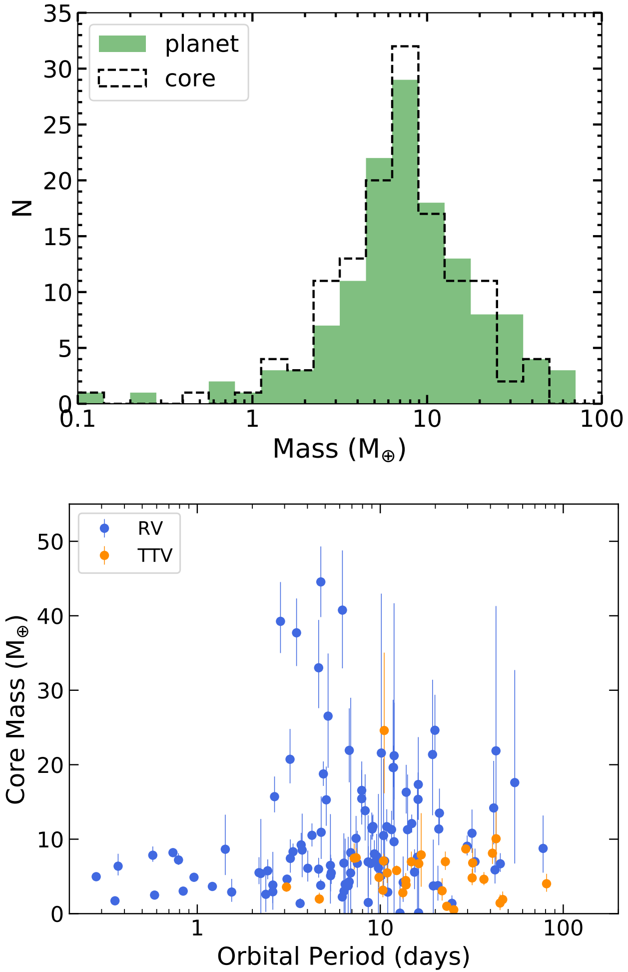

Figure 6.7: Top: Planet mass and planet core mass distributions for our sample. Bottom: Planet core mass plotted against planet orbital period.

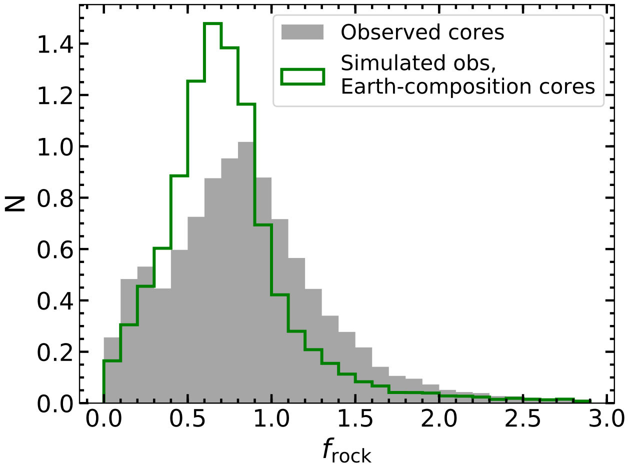

Figure 6.8: Distribution of rock mass fractions for super-Earth cores. The gray histogram shows the normalized observed distribution. The green histogram shows the simulated observed $f_{\rm rock}$ distribution for planets having the same masses, but a single Earth-like composition ($f_{\rm rock}$ =0.7). The observed distribution is still broader than the simulated one, suggesting that there is an intrinsic spread of core compositions, some of which are Earth-like.

6.5.3 A correlation between core mass and host star metallicity

In the canonical picture of planet formation, cores of planets assemble from solids in the protoplanetary disk. The surface density of disk solids, which dictates core growth, presumably scales with stellar metallicity, as both star and disk emerge from the same nebula of gas and dust. Since the efficiency of core growth depends on the available reservoir of solid material, one might expect the occurrence and outcome of planet formation to be strongly correlated with stellar metallicity.

Studies comparing the occurrence patterns of planets around stars of different metallicities have already shed light on the planet formation process. The first Doppler detections of giant planets revealed that metal-rich stars are more likely to host Jovian-mass planets (Gonzalez, 1997; Reid, 2002; Santos et al., 2004; Fischer & Valenti, 2005), which is a key prediction of core accretion theory. More recently, numerous studies have used the *Kepler* sample to investigate the occurrence-metallicity relation for smaller planets. The emerging consensus is that planets smaller than $4R_\oplus$ orbit stars with a broad range of metallicities, lower on average than the metallicities of giant planet hosts (Buchhave et al., 2012, 2014; Petigura et al., 2018). There has been much debate about if and how the metallicity distribution varies with planet radius for $R_P < 4\ R_\oplus$. While Buchhave et al. (2014) favored the existence of distinct metallicity distributions for planets $R_P < 1.7\ R_\oplus$ and those 1.7–4.0 $R_\oplus$, Schlaufman (2015) rebutted that their statistical methods were flawed and suggested the data favored a linear increase in average host star metallicity with planet radius, extending from Earth- to Jovian-size planets.

Petigura et al. (2018) used a sample of 1305 spectroscopically characterized planet hosts from the California Kepler Survey (CKS) to study the metallicity-radius relationship with unprecedented precision, including its dependence on orbital period. They found that for $P < 10$ days, the occurrence of planets 1.0–1.7 $R_\oplus$ and 1.7-4.0 $R_\oplus$ both show a positive correlation with stellar metallicity, consistent with previous studies (Mulders et al., 2016; Dong et al., 2018). Beyond 10 days, this trend vanishes for the super-Earths, but remains for sub-Neptunes. They also found that the vast majority of planets 4–8 $R_\oplus$ orbit stars with super-solar metallicities.

The dependence between planet mass and stellar metallicity has been investigated much less extensively than the radius-metallicity relationship. This is mostly due to a relative lack of mass measurements for small planets. Studies of masses and radii as a function of metallicity can offer complementary insights about planet formation. Planet masses provide a more direct assessment of the cores of planets whereas radii are very sensitive to changes in envelope mass (Lopez & Fortney, 2014).

The absence of strong trends between planet radius and host star metallicity does not necessarily reduce the likelihood of a strong mass-metallicity correlation. Radius-metallicity trends might be weaker than mass-metallicity trends. First, while cores can presumably grow larger and more efficiently in higher metallicity disks, the envelopes of planets within these disks would tend to have higher opacities, lowering the rate of cooling and suppressing further gas accretion and overall expansion. Moreover, the radii of small planet cores grow slowly with mass as $\sim M_{\mathrm{core}}{}^{1/4}$ (Fortney et al., 2007), so an increase in core mass with metallicity would show weakly in planet radius space. On the other hand, the efficiency of photoevaporation is lower for metal-enriched atmospheres, which would tend to strengthen the correlation between planet radius and stellar metallicity.

These complicating factors can be sidestepped by directly examining the distribution of planet masses as a function of stellar metallicities rather than planet radii. Our large sample of planet masses allows for such an investigation, isolating the importance of stellar metallicity in the core assembly process, and the degree to which it affects bulk compositions. We address these questions in this section.

Figure 6.9 shows planet core masses (M_{core}) plotted against host star iron abundances ([Fe/H]) for our entire planet sample (1–8 $R_\oplus$) as well as separately for 1–4 $R_\oplus$ planets and 4–8 $R_\oplus$ planets. RV and TTV populations are distinguished to capture any systematic differences that might result from different formation pathways or detection biases. One striking feature of the entire population is an overall increase in both the mean and variance of core mass with host star metallicity. For example, for stars with [Fe/H] < –0.2 dex, core masses are typically 1–8 $M_\oplus$, whereas stars with [Fe/H] > +0.2 dex have planets spanning $\sim$ 4–50 $M_\oplus$ This is consistent with the analysis by Petigura et al. (2018), which demonstrated that metal rich stars host planets with a greater diversity of radii.

To quantify the strength and significance of correlations, we perform a weighted-least-squares regression, using weights of 1 / $\sigma_{M_{\mathrm{core}}}$. We compute Pearson correlation coefficients (r) and p-values, which are listed in Table 6.4. We assume correlations are significant if p-values are less than 0.01. We observe significant positive correlations between planet core mass and host star metallicity over the full range of planet sizes (1–8 $R_\oplus$), and similarly significant correlations for 1–4 $R_\oplus$ planets and 4–8 $R_\oplus$ planets individually. Metallicity is evidently an important predictor of the core masses of planets between the size of Earth and Saturn. This suggests that the assembly of cores — even those of small planets — is limited by the solid surface density of the protoplanetary disks.

Core mass is better predicted by stellar metallicity than stellar mass

Here we demonstrate that even though stellar metallicity is correlated with stellar mass, metallicity is a better predictor of planet core mass for both 1–4 $R_\oplus$ planets and 4–8 $R_\oplus$ planets.

Even though we observe a correlation between M_core and [Fe/H], it is important to consider that metallicity is strongly correlated with stellar mass. Figure 6.3 shows this correlation in our sample, which naturally arises because high-mass stars have shorter lifespans, so those observed today formed relatively recently, at times when the Galaxy was more enriched with metals.

Comparing the left and middle columns of Figure 6.10, we see that in every radius bin core mass correlates more strongly with stellar metallicity than stellar mass. Across the 1–8 $R_\oplus$ sample, there is a significant correlation, but there are a number of outliers, which are better explained by metallicity effects. For example, GJ 436b, and GJ 3470b, and K2-55b have unusually high core masses for planets orbiting low-mass stars, yet their host star metallicities are also atypically high.

Within the 4–8 $R_\oplus$ range, there is no evidence that core mass and stellar mass are correlated. The vast majority of these planets orbit stars more massive than 0.8, and the few exceptions have super-solar metallicities. For planets 1-4$R_\oplus$, the correlation between M_core and $M_\star$ is of marginal significance (p-value = 0.02).

There is theoretical and observational evidence that planet core mass scales with *both* stellar mass and metallicity. The masses of protoplanetary disks scale with that of the host star, although there is much scatter in the regime of Sun-like stars (Williams & Cieza, 2011). Therefore, it is likely that the total reservoir of solid material and the growth of planet cores scales with both stellar mass and metallicity. Moreover, the planet radius valley shifts to larger radii with increasing stellar mass, indicating that the core masses of small planets increases with stellar mass (Fulton & Petigura, 2018; Wu, 2018). Fulton & Petigura (2018) noted that the shifting radius valley could be a metallicity effect rather than a stellar mass effect.

Wu (2018) came to the opposite conclusion, namely that that planet mass correlates with stellar mass and not metallicity. This conclusion is based on a statistical analysis of planet radii (for $R_p = 1 - 4R_\oplus$), not measured planet masses. Wu (2018) noted that the gap radius shifts as a function of stellar mass and that this shift can be accounted for semi-analytically by $R_\mathrm{core} \propto M_\star^{1/4}$ and $M_\mathrm{core} \propto M_\star^{0.95-1.45} \approx M_\star^{1.0}$. Wu (2018) finds no additional variability in gap radius that correlates with stellar metallicity, after de-correlating against stellar mass. This is in tension with our observation that stellar metallicity drives planet mass. We note differences between the two studies. First, Wu (2018) is based on planet radii scaled to planet masses, not mass measurements (as is in our study). Second, the Wu (2018)) conclusion is based on first fitting out the stellar mass dependence and then failing to find an dependence on stellar metallicity. Wu (2018) did not describe in their paper running the analysis with stellar metallicity (instead of stellar mass) as the independent variable. Third, their analysis considers 1–4 Re planets while ours spans 1–8 Re planets.

Our observations disfavor the conclusion of Wu (2018) that the size of small planet cores increase with stellar mass, uninfluenced by metallicity. We conclude that core mass is more sensitive to stellar metallicity than stellar mass.

Negligible influence of detection bias

Here, we show that unlike our planet core masses, our planet radiii are not significantly correlated with stellar metallicity, suggesting that the observed correlation between core mass and metallicity is unlikely to arise from biases against detecting small cores around metal-rich stars. These results are summarized visually in Figure 6.10 and quantitatively in Table 6.4.

For small planets, it is conceivable that the observed correlation between core mass and metallicity is, in part an artifact of detection biases — for a given planet radius, larger stars, which are more metal-rich than smaller stars on average, yield shallower transits. This limits the detectability of small planets orbiting high metallicity stars. If this bias is present in our sample, it should manifest as a correlation between planet radius and stellar metallicity. However, the right column of Figure 6.10 shows a weak and insignificant correlation for planets 1-4$R_\oplus$ (r=0.14, p-value=0.12). For planets 1–2$R_\oplus$, which are most likely to suffer from detection biases, the correlation is even weaker (r=0.09, p-value=0.52). We conclude that the observed correlation is not significantly swayed by detection biases. Regardless, this bias can not explain the observed deficit of massive cores around low-metallicity stars, where they are easily detectable, and more detectable than those orbiting higher metallicity stars.

The trend between core-mass and host star metallicity appears consistent across the entire population of 1–8 $R_\oplus$ planets. However, we cannot simply assume a continuum of planet formation in the range 1–8 $R_\oplus$. Planets spanning 4–8 $R_\oplus$ are intrinsically much rarer than 1–4 $R_\oplus$ planets and may have different formation pathways with high-metallicity thresholds. On average, these "sub-Saturns" form around stars with even higher metallicities than Jovian planets, suggesting they represent the fringes of planet formation rather than the norm. Some might be the byproducts of collisions between two massive cores, the formation of which requires an abundance of disk solids.

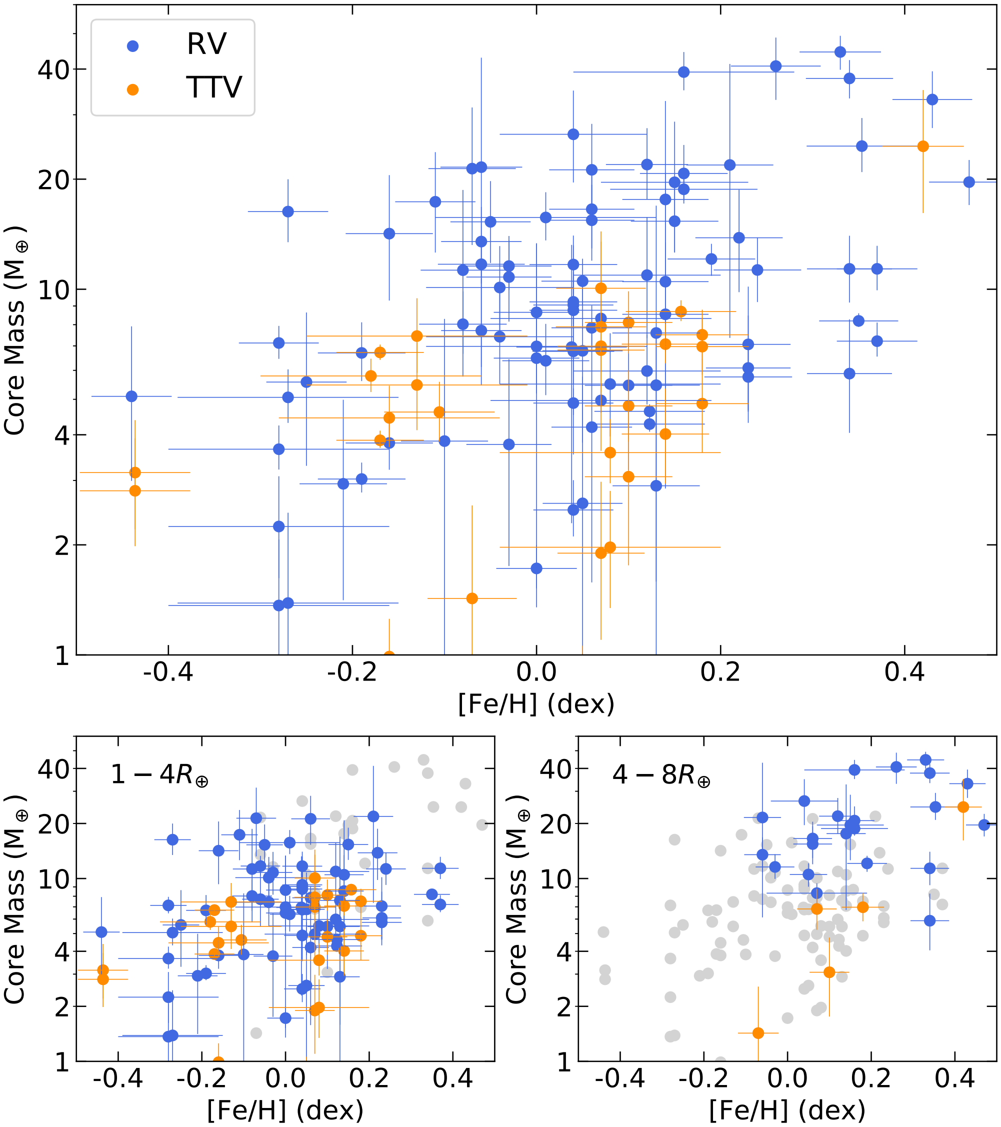

Figure 6.9: Planet Core mass plotted against host star metallicity for all planets 1–$8R_{\oplus}$ (top), 1–$4R_{\oplus}$ (bottom-left) and 4–$8R_{\oplus}$ (bottom-right). Blue and orange circles distinguish planets with masses measured from RVs and TTVs respectively. There is a significant positive correlation for all populations.

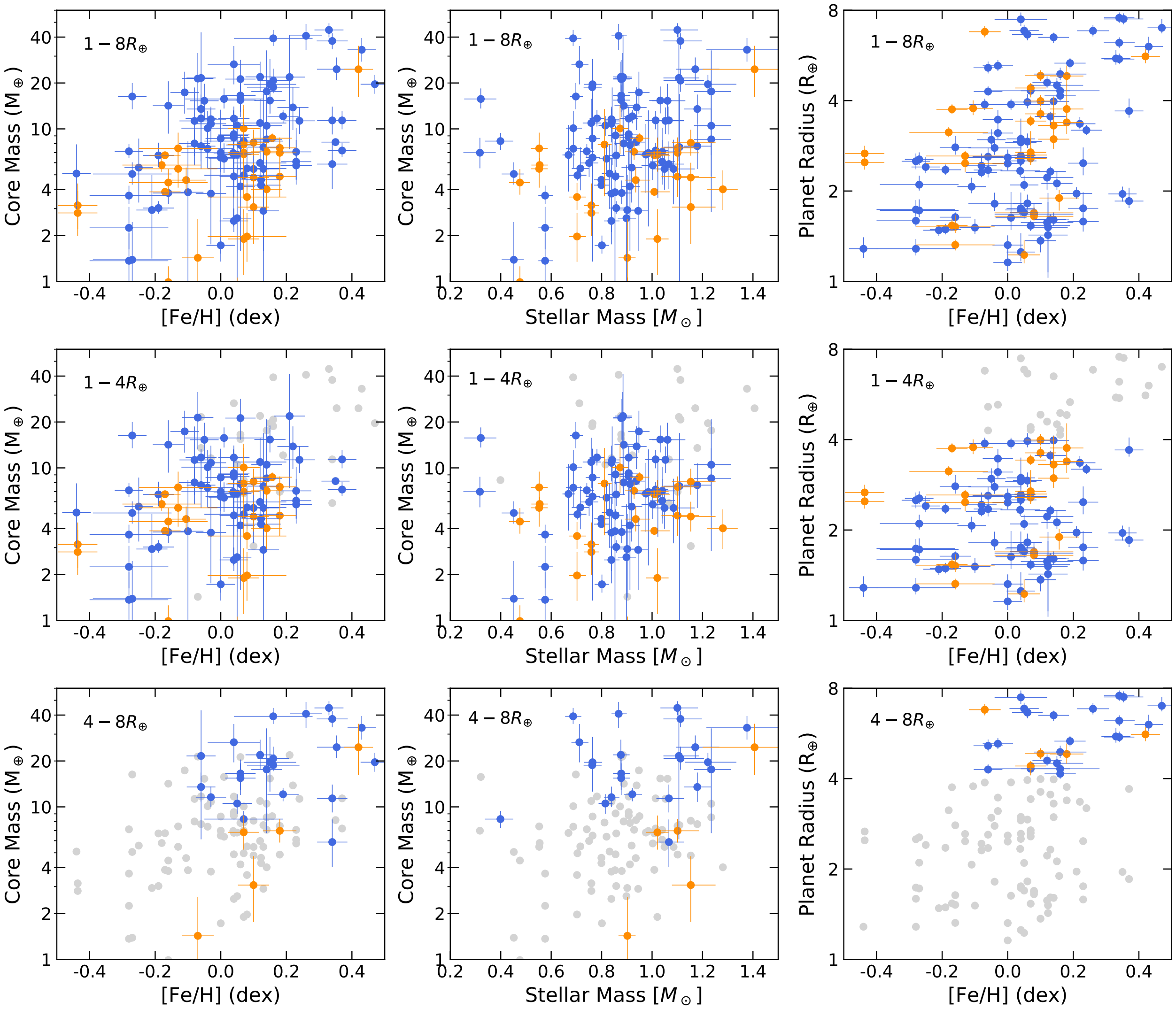

Figure 6.10: Left column: Same as Figure 6.9. Middle column: Core mass versus stellar mass for the same three planet radius bins. In all radius bins, core mass correlates more strongly with stellar metallicity than stellar mass. Right column: Planet radius versus stellar metallicity. For 1–4 $R_\oplus$ planets (middle row), planet radius us not significantly correlated with stellar metallicity, suggesting that the observed correlation between core mass and stellar metallicity is not driven by detection biases.

Table 6.4. Correlations between planet and and host star properties for different planet radius bins

R_P ($R_\oplus$)	Var Y	Var X	r[a]	p-value	Sig.[b]
1–4	$M_{\rm core}$	[Fe/H]	0.32	7×10^{-4}	Y
1–8	$M_{\rm core}$	[Fe/H]	0.39	2×10^{-6}	Y
4–8	$M_{\rm core}$	[Fe/H]	0.48	8×10^{-3}	Y
1–4	$M_{\rm core}$	$M_\star$	0.23	2×10^{-2}	N
1–8	$M_{\rm core}$	$M_\star$	0.24	5×10^{-3}	Y
4–8	$M_{\rm core}$	$M_\star$	0.10	6×10^{-1}	N
1–4	R_P	[Fe/H]	0.14	1×10^{-1}	N
1–8	R_P	[Fe/H]	0.34	2×10^{-5}	Y
4–8	R_P	[Fe/H]	0.32	8×10^{-2}	N

[a] Pearson correlation coefficient

[b] Correlation considered significant if p-value $\leq 1\times10^{-2}$

6.6 Conclusion

We assembled a catalog of 139 planets spanning 1–8$R_\oplus$ that have measured masses. By characterizing their 101 host stars using HIRES spectra and Gaia parallaxes, we derived precise stellar and planet properties with minimal systematic biases in methodology. This constitutes the most comprehensive and precise catalog of small planet masses to date. The updated mass-radius diagram provides an updated picture of the compositional diversity of small planets.

A gap exists in the planet density-radius distribution, separating super-Earths with bare cores from sub-Neptunes, which possess H/He envelopes comprising a few percent of their mass. Planets with tenuous H/He envelopes ($f_{\rm env} \lesssim 1\%$) are completely eroded by photoevaporation consistent with the leading interpretation of the observed planet radius valley. The few 1–2 $R_\oplus$ planets with H/He envelopes have low incident flux ($S_{\rm inc} < 100$ $R_\oplus$) and are therefore less susceptible photoevaporation. Collectively, these observations indicate that close to stars, nature produces cores similar in composition to Earth, surrounded by H/He envelopes, which are then sculpted by photoevaporation.

We find that small planet cores have typical masses of 6–9 $M_\oplus$, although detection biases limit the number of smaller cores in our sample. All of the planets in our sample with orbital periods less than 2.5 days have cores smaller than 10 $M_\oplus$. The overall core mass distribution drops steadily beyond 10$M_\oplus$ and the majority of cores in our sample that exceed 10 $M_\oplus$ belong to sub-Saturns

(4–8 $R_\oplus$), some of which have cores exceeeding 40 $M_\oplus$.

We find evidence that small planet cores have a diversity of bulk compositions. The observed density-radius distribution of super-Earth cores is broader than would be expected for a single composition. Assuming these cores are admixtures of iron and rock, the median rock fraction of these cores is 82%, which is slightly larger than that of Earth (70%). If these cores are comprised of rock and water, then less than 20% of them are more than 10% water by mass.

A positive correlation exists between the core masses of small planets and the metallicity of their host stars. It is unlikely to be the result of detection biases, as we do not observe a correlation between planet radii and stellar metallicity. Moreover, even though stellar metallicities strongly correlate with stellar mass, we find that metallicities are a better predictor of core mass than stellar mass. The assembly of planet cores is more sensitive to stellar metallicity than stellar mass.

Table 6.5. Host Star Properties

Name	Npl	T_{eff} [K]	log g [dex]	[Fe/H] [dex]	Spec[a] Method	$M_\star$ [$\mathrm{M}_\odot$]	$R_\star$ [$\mathrm{R}_\odot$]	Age [Gyr]	Iso[b] Method
55 Cnc	5	5250 ± 100	4.360 ± 0.079	0.350 ± 0.043	sme	0.94 ± 0.03	0.930 ± 0.039	$10.2^{+2.5}_{-4.1}$	direct
BD+20 594	1	5710 ± 100	4.420 ± 0.085	-0.160 ± 0.047	sme	0.89 ± 0.04	1.135 ± 0.041	7.4 ± 3.8	direct
CoRoT-24	2	4634 ± 110	4.49 ± 0.20	0.150 ± 0.080	emp	0.76 ± 0.04	0.825 ± 0.046	6.6 ± 4.7	direct
CoRoT-7	2	5256 ± 100	4.490 ± 0.083	0.080 ± 0.046	sme	0.87 ± 0.03	0.846 ± 0.033	7.3 ± 4.4	direct
CoRoT-8	1	5035 ± 100	4.400 ± 0.086	0.260 ± 0.049	sme	0.87 ± 0.03	0.835 ± 0.035	$9.5^{+3.2}_{-5.0}$	direct
EPIC 201357835	1	5942 ± 100	4.580 ± 0.081	-0.450 ± 0.045	sme	0.88 ± 0.03	$0.840^{+0.047}_{-0.034}$	$3.0^{+3.1}_{-2.0}$	grid
EPIC 202089657	1	6132 ± 100	4.130 ± 0.080	-0.140 ± 0.044	sme	$1.06^{+0.07}_{-0.05}$	1.554 ± 0.058	5.8 ± 1.3	direct
EPIC 206011496	1	5435 ± 100	4.470 ± 0.080	0.050 ± 0.043	sme	0.90 ± 0.04	0.924 ± 0.036	6.7 ± 4.1	direct
EPIC 211945201	1	6019 ± 100	4.180 ± 0.080	0.140 ± 0.044	sme	1.17 ± 0.07	1.387 ± 0.049	$4.29^{+1.42}_{-0.94}$	direct
EPIC 212357477	1	5705 ± 100	4.450 ± 0.080	0.050 ± 0.044	sme	0.98 ± 0.04	0.952 ± 0.035	4.6 ± 3.1	direct
EPIC 213546283	1	5685 ± 100	4.23 ± 0.10	-0.135 ± 0.060	syn	0.89 ± 0.04	1.154 ± 0.044	$11.2^{+1.7}_{-2.6}$	direct
EPIC 216494238	1	5741 ± 100	4.14 ± 0.10	0.353 ± 0.060	syn	1.17 ± 0.09	1.279 ± 0.052	$5.3^{+1.9}_{-1.3}$	direct
EPIC 229004835	1	5839 ± 100	4.420 ± 0.080	-0.110 ± 0.044	sme	0.95 ± 0.04	0.998 ± 0.036	5.3 ± 3.1	direct
EPIC 245943455	1	5310 ± 100	4.420 ± 0.081	0.240 ± 0.045	sme	0.93 ± 0.04	0.910 ± 0.038	8.4 ± 4.1	direct
EPIC 245991048	1	5773 ± 100	4.31 ± 0.10	0.038 ± 0.060	syn	0.99 ± 0.05	1.094 ± 0.041	7.1 ± 2.9	direct
EPIC 247418783	1	5520 ± 100	4.500 ± 0.080	0.080 ± 0.044	sme	0.93 ± 0.04	0.899 ± 0.034	$4.8^{+4.0}_{-3.1}$	direct
GJ 3470	1	3550 ± 70	4.61 ± 0.20	0.07 ± 0.12	emp	0.40 ± 0.06	0.518 ± 0.021	7.0 ± 4.6	direct
GJ 436	1	3448 ± 70	4.67 ± 0.20	0.01 ± 0.12	emp	0.32 ± 0.06	0.433 ± 0.018	7.0 ± 4.6	direct
GJ 9827	3	4217 ± 70	4.62 ± 0.20	-0.28 ± 0.12	emp	0.58 ± 0.03	0.612 ± 0.021	6.8 ± 4.7	direct
HAT-P-11	2	4617 ± 110	4.54 ± 0.20	0.160 ± 0.080	emp	0.76 ± 0.04	0.778 ± 0.038	6.6 ± 4.7	direct
HAT-P-26	1	5039 ± 100	4.450 ± 0.081	0.050 ± 0.045	sme	0.81 ± 0.03	0.851 ± 0.035	$9.0^{+3.5}_{-4.9}$	direct
HD 106315	2	6379 ± 100	4.230 ± 0.080	-0.060 ± 0.044	sme	1.18 ± 0.05	1.273 ± 0.042	2.84 ± 0.88	direct
HD 219134	6	4856 ± 100	4.49 ± 0.10	0.123 ± 0.060	syn	0.80 ± 0.03	0.73 ± 0.11	7.7 ± 4.6	direct
HD 3167	3	5261 ± 100	4.470 ± 0.080	0.040 ± 0.043	sme	0.86 ± 0.03	0.878 ± 0.034	8.1 ± 4.3	direct
HD 89345	1	5607 ± 100	4.010 ± 0.080	0.470 ± 0.044	sme	1.22 ± 0.10	1.750 ± 0.065	5.8 ± 1.8	direct
HD 97658	1	5120 ± 100	4.570 ± 0.080	-0.280 ± 0.043	sme	0.74 ± 0.03	0.753 ± 0.030	7.2 ± 4.5	direct
HIP 116454	1	5011 ± 100	4.540 ± 0.085	-0.060 ± 0.047	sme	0.78 ± 0.03	0.767 ± 0.031	7.3 ± 4.6	direct
K2-10	1	5533 ± 100	4.470 ± 0.085	-0.070 ± 0.047	sme	0.88 ± 0.04	0.956 ± 0.037	6.6 ± 4.1	direct
K2-100	1	6044 ± 100	4.400 ± 0.080	0.300 ± 0.044	sme	1.21 ± 0.04	1.227 ± 0.045	$1.49^{+1.28}_{-0.95}$	direct
K2-105	1	5373 ± 100	4.450 ± 0.085	0.220 ± 0.047	sme	0.94 ± 0.04	0.905 ± 0.035	6.9 ± 4.2	direct
K2-106	2	5496 ± 100	4.420 ± 0.080	0.060 ± 0.044	sme	0.91 ± 0.04	0.995 ± 0.039	7.8 ± 3.9	direct
K2-108	1	5474 ± 100	3.990 ± 0.081	0.330 ± 0.044	sme	1.10 ± 0.07	1.760 ± 0.075	8.6 ± 2.0	direct
K2-110	1	4868 ± 100	4.530 ± 0.080	-0.270 ± 0.044	sme	0.70 ± 0.03	0.710 ± 0.030	8.0 ± 4.5	direct
K2-111	1	5832 ± 100	4.430 ± 0.080	-0.440 ± 0.044	sme	0.83 ± 0.03	0.884 ± 0.063	8.2 ± 3.7	grid
K2-121	1	4526 ± 110	4.63 ± 0.20	0.040 ± 0.080	emp	0.71 ± 0.03	0.675 ± 0.033	6.6 ± 4.7	direct
K2-131	1	5107 ± 100	4.540 ± 0.085	0.010 ± 0.047	sme	0.82 ± 0.03	0.733 ± 0.030	6.9 ± 4.5	direct
K2-141	2	4452 ± 70	4.61 ± 0.20	0.07 ± 0.12	emp	0.70 ± 0.03	0.690 ± 0.023	6.6 ± 4.7	direct
K2-18	1	3449 ± 70	4.60 ± 0.20	0.00 ± 0.12	emp	0.32 ± 0.06	0.468 ± 0.019	7.0 ± 4.6	direct
K2-180	1	5166 ± 100	4.630 ± 0.081	-0.710 ± 0.045	sme	0.67 ± 0.02	0.638 ± 0.020	6.9 ± 4.6	grid
K2-181	1	5528 ± 100	4.350 ± 0.085	0.180 ± 0.047	sme	0.96 ± 0.04	1.060 ± 0.042	8.7 ± 3.3	direct
K2-189	2	5442 ± 100	4.510 ± 0.085	-0.100 ± 0.047	sme	0.85 ± 0.03	0.879 ± 0.034	6.4 ± 4.3	direct
K2-19	3	5322 ± 100	4.510 ± 0.083	0.060 ± 0.046	sme	0.88 ± 0.03	0.818 ± 0.036	6.4 ± 4.3	direct
K2-199	2	4507 ± 110	4.61 ± 0.20	-0.040 ± 0.080	emp	0.69 ± 0.03	0.678 ± 0.034	6.6 ± 4.7	direct
K2-214	1	5875 ± 100	4.280 ± 0.081	0.040 ± 0.044	sme	1.03 ± 0.05	1.236 ± 0.047	6.3 ± 2.0	direct
K2-216	1	4495 ± 70	4.60 ± 0.20	0.08 ± 0.12	emp	0.72 ± 0.03	0.699 ± 0.023	6.7 ± 4.6	direct
K2-220	1	5612 ± 100	4.450 ± 0.080	-0.050 ± 0.044	sme	0.91 ± 0.04	1.026 ± 0.040	6.4 ± 3.8	direct
K2-222	1	5961 ± 100	4.330 ± 0.080	-0.250 ± 0.044	sme	0.92 ± 0.04	1.093 ± 0.038	7.6 ± 2.6	direct
K2-229	3	5163 ± 100	4.530 ± 0.080	0.040 ± 0.043	sme	0.84 ± 0.03	0.774 ± 0.032	6.8 ± 4.4	direct
K2-24	2	5625 ± 100	4.290 ± 0.083	0.340 ± 0.046	sme	1.07 ± 0.05	1.158 ± 0.043	6.5 ± 2.2	direct
K2-27	1	5246 ± 100	4.480 ± 0.081	0.120 ± 0.045	sme	0.88 ± 0.03	0.876 ± 0.036	7.5 ± 4.4	direct
K2-3	3	3825 ± 70	4.61 ± 0.20	-0.27 ± 0.12	emp	0.45 ± 0.04	0.548 ± 0.021	6.9 ± 4.7	direct
K2-32	3	5274 ± 100	4.490 ± 0.083	-0.030 ± 0.046	sme	0.84 ± 0.03	0.855 ± 0.034	7.7 ± 4.4	direct
K2-36	2	4836 ± 100	4.550 ± 0.084	0.000 ± 0.046	sme	0.76 ± 0.03	0.717 ± 0.031	7.3 ± 4.6	direct
K2-37	3	5352 ± 100	4.530 ± 0.083	-0.080 ± 0.046	sme	0.84 ± 0.03	0.809 ± 0.032	6.4 ± 4.3	direct
K2-38	2	5679 ± 100	4.320 ± 0.083	0.230 ± 0.046	sme	1.04 ± 0.05	$1.131^{+0.123}_{-0.095}$	6.4 ± 2.5	grid
K2-39	1	4915 ± 100	3.580 ± 0.080	0.430 ± 0.043	sme	1.38 ± 0.16	3.08 ± 0.14	$4.2^{+2.5}_{-1.4}$	direct
K2-55	1	4275 ± 70	4.57 ± 0.20	0.16 ± 0.12	emp	0.69 ± 0.03	0.709 ± 0.025	6.8 ± 4.7	direct
K2-61	1	5748 ± 100	4.380 ± 0.085	0.030 ± 0.048	sme	0.97 ± 0.04	0.995 ± 0.042	6.2 ± 3.1	direct
K2-62	2	4455 ± 70	4.57 ± 0.20	-0.10 ± 0.12	emp	0.67 ± 0.03	0.696 ± 0.023	6.6 ± 4.7	direct
K2-66	1	5865 ± 100	3.990 ± 0.080	-0.050 ± 0.044	sme	1.06 ± 0.07	1.79 ± 0.10	7.3 ± 1.6	direct
K2-73	1	5867 ± 100	4.390 ± 0.081	0.040 ± 0.044	sme	1.02 ± 0.04	1.058 ± 0.039	4.4 ± 2.5	direct

Table 6.5 (cont'd)

Name	Npl	$T_{\rm eff}$ [K]	$\log g$ [dex]	[Fe/H] [dex]	Spec[a] Method	$M_\star$ [$M_\odot$]	$R_\star$ [$R_\odot$]	Age [Gyr]	Iso[b] Method
K2-79	1	5853 ± 100	4.180 ± 0.081	-0.000 ± 0.044	sme	1.01 ± 0.05	1.247 ± 0.045	8.0 ± 1.8	direct
K2-98	1	6103 ± 100	4.120 ± 0.081	-0.060 ± 0.044	sme	$1.11^{+0.08}_{-0.06}$	1.565 ± 0.065	5.3 ± 1.3	direct
KOI-142	2	5393 ± 100	4.410 ± 0.084	0.200 ± 0.046	sme	0.93 ± 0.04	0.926 ± 0.035	8.2 ± 4.0	direct
Kepler-10	2	5646 ± 100	4.330 ± 0.085	-0.190 ± 0.048	sme	0.86 ± 0.03	1.090 ± 0.040	$10.8^{+2.1}_{-3.5}$	direct
Kepler-100	3	5857 ± 100	4.130 ± 0.085	0.100 ± 0.048	sme	$1.09^{+0.08}_{-0.06}$	1.550 ± 0.054	6.6 ± 1.7	direct
Kepler-101	2	5535 ± 100	4.010 ± 0.085	0.340 ± 0.047	sme	$1.11^{+0.08}_{-0.07}$	1.763 ± 0.072	8.1 ± 2.0	direct
Kepler-102	5	4811 ± 100	4.560 ± 0.085	0.130 ± 0.047	sme	0.79 ± 0.03	0.738 ± 0.031	6.8 ± 4.6	direct
Kepler-103	2	5882 ± 100	4.160 ± 0.085	0.130 ± 0.048	sme	$1.11^{+0.08}_{-0.06}$	1.525 ± 0.056	5.9 ± 1.6	direct
Kepler-105	2	5957 ± 100	4.420 ± 0.084	-0.110 ± 0.046	sme	0.99 ± 0.04	1.047 ± 0.038	4.0 ± 2.6	direct
Kepler-106	4	5933 ± 100	4.460 ± 0.085	-0.070 ± 0.047	sme	1.00 ± 0.04	1.064 ± 0.040	$3.2^{+2.7}_{-2.1}$	direct
Kepler-11	6	5820 ± 100	4.430 ± 0.085	0.070 ± 0.047	sme	1.02 ± 0.04	1.119 ± 0.041	3.8 ± 2.6	direct
Kepler-113	2	4647 ± 110	4.55 ± 0.20	0.120 ± 0.080	emp	0.76 ± 0.04	0.768 ± 0.037	6.6 ± 4.7	direct
Kepler-131	2	5749 ± 100	4.460 ± 0.085	0.150 ± 0.048	sme	1.03 ± 0.04	1.014 ± 0.036	$3.4^{+2.9}_{-2.2}$	direct
Kepler-138	3	3823 ± 70	4.65 ± 0.20	-0.16 ± 0.12	emp	0.48 ± 0.04	0.537 ± 0.020	6.9 ± 4.7	direct
Kepler-1655	1	6047 ± 100	4.370 ± 0.085	-0.280 ± 0.048	sme	0.94 ± 0.04	1.058 ± 0.036	5.7 ± 2.7	direct
Kepler-177	2	5733 ± 100	4.11 ± 0.10	-0.106 ± 0.060	syn	$0.94^{+0.06}_{-0.04}$	1.429 ± 0.071	10.7 ± 1.9	direct
Kepler-18	3	5361 ± 100	4.380 ± 0.085	0.190 ± 0.048	sme	0.92 ± 0.04	0.948 ± 0.037	$9.4^{+3.0}_{-4.5}$	direct
Kepler-19	3	5537 ± 100	4.550 ± 0.085	-0.080 ± 0.048	sme	0.89 ± 0.04	0.889 ± 0.033	$4.4^{+4.3}_{-3.0}$	direct
Kepler-20	6	5482 ± 100	4.470 ± 0.085	0.040 ± 0.048	sme	0.91 ± 0.04	0.900 ± 0.033	6.3 ± 4.1	direct
Kepler-21	1	6207 ± 100	4.060 ± 0.085	0.030 ± 0.047	sme	1.25 ± 0.09	1.947 ± 0.065	$3.45^{+1.19}_{-0.66}$	direct
Kepler-22	1	5614 ± 100	4.590 ± 0.085	-0.260 ± 0.048	sme	0.85 ± 0.03	0.849 ± 0.031	$4.1^{+4.3}_{-2.8}$	direct
Kepler-223	4	5803 ± 100	4.160 ± 0.089	0.180 ± 0.051	sme	$1.10^{+0.09}_{-0.06}$	1.75 ± 0.13	6.4 ± 1.8	direct
Kepler-26	4	4051 ± 70	4.63 ± 0.20	-0.18 ± 0.12	emp	0.55 ± 0.03	0.596 ± 0.022	6.8 ± 4.7	direct
Kepler-279	3	6631 ± 100	4.42 ± 0.10	-0.049 ± 0.060	syn	$1.25^{+0.05}_{-0.04}$	1.439 ± 0.054	$0.91^{+0.80}_{-0.55}$	direct
Kepler-29	2	5378 ± 100	4.64 ± 0.10	-0.436 ± 0.060	syn	0.76 ± 0.03	0.781 ± 0.042	$5.7^{+5.0}_{-3.9}$	direct
Kepler-30	3	5464 ± 100	4.66 ± 0.10	0.157 ± 0.060	syn	0.95 ± 0.04	0.861 ± 0.045	$2.9^{+3.5}_{-2.0}$	direct
Kepler-305	3	4994 ± 100	4.410 ± 0.087	0.070 ± 0.049	sme	0.81 ± 0.03	0.812 ± 0.044	$9.5^{+3.2}_{-5.0}$	direct
Kepler-307	2	5456 ± 100	4.390 ± 0.085	0.140 ± 0.047	sme	0.93 ± 0.04	0.979 ± 0.038	8.6 ± 3.8	direct
Kepler-310	3	5429 ± 100	4.580 ± 0.086	-0.210 ± 0.048	sme	0.82 ± 0.03	0.868 ± 0.034	$5.5^{+4.8}_{-3.7}$	direct
Kepler-33	6	5900 ± 100	4.020 ± 0.085	0.100 ± 0.048	sme	$1.15^{+0.10}_{-0.07}$	1.725 ± 0.069	5.7 ± 1.5	direct
Kepler-359	3	5659 ± 100	4.610 ± 0.087	-0.360 ± 0.049	sme	0.83 ± 0.03	0.898 ± 0.077	$4.0^{+4.3}_{-2.7}$	direct
Kepler-36	2	5980 ± 100	4.050 ± 0.085	-0.170 ± 0.048	sme	1.01 ± 0.06	1.678 ± 0.061	7.7 ± 1.5	direct
Kepler-4	1	5782 ± 100	4.060 ± 0.085	0.160 ± 0.048	sme	$1.11^{+0.09}_{-0.07}$	1.555 ± 0.059	6.9 ± 1.8	direct
Kepler-406	2	5586 ± 100	4.340 ± 0.085	0.230 ± 0.048	sme	1.00 ± 0.05	1.094 ± 0.041	7.5 ± 3.1	direct
Kepler-454	2	5620 ± 100	4.280 ± 0.085	0.220 ± 0.048	sme	1.01 ± 0.05	1.090 ± 0.040	8.2 ± 2.5	direct
Kepler-48	4	5169 ± 100	4.460 ± 0.085	0.210 ± 0.047	sme	0.88 ± 0.03	0.857 ± 0.035	8.0 ± 4.4	direct
Kepler-49	4	4010 ± 70	4.58 ± 0.20	-0.13 ± 0.12	emp	0.55 ± 0.03	0.627 ± 0.023	6.8 ± 4.7	direct
Kepler-51	3	5574 ± 100	4.600 ± 0.086	-0.070 ± 0.048	sme	0.90 ± 0.03	0.863 ± 0.037	$3.3^{+3.7}_{-2.2}$	direct
Kepler-549	2	5266 ± 100	4.590 ± 0.086	0.070 ± 0.049	sme	0.87 ± 0.03	0.850 ± 0.036	$4.7^{+4.7}_{-3.3}$	direct
Kepler-56	3	4790 ± 100	3.270 ± 0.081	0.420 ± 0.044	sme	1.41 ± 0.21	4.32 ± 0.22	$4.0^{+3.1}_{-1.6}$	direct
Kepler-60	3	5887 ± 100	4.200 ± 0.085	-0.030 ± 0.047	sme	1.00 ± 0.05	1.507 ± 0.060	7.7 ± 1.8	direct
Kepler-68	3	5821 ± 100	4.300 ± 0.085	0.130 ± 0.047	sme	1.05 ± 0.05	1.259 ± 0.045	5.8 ± 2.2	direct
Kepler-78	1	5023 ± 100	4.550 ± 0.080	0.000 ± 0.044	sme	0.80 ± 0.03	0.747 ± 0.030	6.9 ± 4.5	direct
Kepler-79	4	6313 ± 100	4.210 ± 0.085	0.140 ± 0.047	sme	1.28 ± 0.06	1.457 ± 0.057	$2.27^{+0.64}_{-0.86}$	direct
Kepler-80	5	4432 ± 70	4.57 ± 0.20	0.08 ± 0.12	emp	0.70 ± 0.03	0.720 ± 0.024	6.6 ± 4.7	direct
Kepler-85	4	5421 ± 100	4.560 ± 0.087	0.050 ± 0.049	sme	0.90 ± 0.04	0.898 ± 0.038	$4.4^{+4.4}_{-3.0}$	direct
Kepler-89	4	6144 ± 100	4.160 ± 0.084	0.140 ± 0.047	sme	1.23 ± 0.07	1.426 ± 0.050	$3.30^{+0.89}_{-0.68}$	direct
Kepler-93	2	5650 ± 100	4.480 ± 0.085	-0.160 ± 0.047	sme	0.88 ± 0.04	0.941 ± 0.034	6.0 ± 3.9	direct
Kepler-94	2	4452 ± 70	4.52 ± 0.20	0.22 ± 0.12	emp	0.74 ± 0.03	0.781 ± 0.025	6.7 ± 4.6	direct
Kepler-95	1	5650 ± 100	4.180 ± 0.085	0.240 ± 0.048	sme	$1.05^{+0.07}_{-0.05}$	1.441 ± 0.055	8.2 ± 2.2	direct
Kepler-96	1	5740 ± 100	4.530 ± 0.085	0.070 ± 0.047	sme	1.00 ± 0.04	0.953 ± 0.034	$2.7^{+2.9}_{-1.9}$	direct
Kepler-97	2	5800 ± 100	4.480 ± 0.085	-0.210 ± 0.047	sme	0.90 ± 0.04	0.997 ± 0.037	5.0 ± 3.4	direct
Kepler-98	1	5497 ± 100	4.490 ± 0.085	0.130 ± 0.047	sme	0.94 ± 0.04	0.934 ± 0.035	5.1 ± 3.7	direct
Kepler-99	1	4608 ± 110	4.54 ± 0.20	0.120 ± 0.080	emp	0.75 ± 0.03	0.771 ± 0.037	6.6 ± 4.7	direct
WASP-47	4	5476 ± 100	4.270 ± 0.080	0.370 ± 0.044	sme	1.01 ± 0.05	1.144 ± 0.049	9.2 ± 2.5	direct

[a] Spectral characterization tool used: SME = Spectroscopy Made Easy (Brewer et al., 2015, 2016; Brewer & Fischer, 2018), EMP = SpecMatch-Emp (Yee et al., 2017), SYN = SpecMatch-Syn (Petigura, 2015)

[b] Direct: Rstar, Lum, Distance estimated from Isoclassify "Direct" method (Huber et al., 2017) using $T_{\rm eff}$, $\log g$, [Fe/H], K mag and parallax as inputs.
Grid: Mstar, Rstar, Lum, age, Distance posteriors estimated by interpolation of MIST isochrones using $T_{\rm eff}$, $\log g$, [Fe/H] and K mag (no parallax)

Table 6.6. Planet Properties

Name	Per	$R_p/R_\star$	R_P	M_P	ρ_p	$f_{\rm env}$	$S_{\rm inc}$
55 Cnce	0.737	1.929 ± 0.076	1.96 ± 0.11	8.25 ± 0.34	6.09 ± 1.08	0 ± 0	2412 ± 271
BD+20 594b	41.685	$2.259^{+0.185}_{-0.094}$	$2.80^{+0.25}_{-0.15}$	15.67 ± 5.51	3.95 ± 1.64	$2.7^{+1.7}_{-1.3}$	24.0 ± 2.5
CoRoT-24c	11.759	5.000 ± 0.010	4.50 ± 0.25	24.84 ± 8.62	1.50 ± 0.58	15.2 ± 3.1	33.0 ± 4.6
CoRoT-7b	0.854	1.784 ± 0.047	1.65 ± 0.08	4.61 ± 0.91	5.70 ± 1.39	0 ± 0	1741 ± 191
CoRoT-8b	6.212	7.50 ± 0.10	6.83 ± 0.30	68.20 ± 10.55	1.18 ± 0.24	$39.8^{+3.4}_{-4.6}$	101 ± 11
EPIC 201357835b	11.894	$3.002^{+0.127}_{-0.053}$	$2.75^{+0.19}_{-0.12}$	14.73 ± 26.83	3.58 ± 6.83	$0.19^{+1.78}_{-0.19}$	83.1 ± 8.7
EPIC 202089657b	1.315	$1.968^{+0.102}_{-0.049}$	$3.34^{+0.22}_{-0.15}$	-4.20 ± 5.45	-0.52 ± 0.78	0^{+1}_{-0}	5321 ± 578
EPIC 206011496b	2.369	$1.683^{+0.084}_{-0.039}$	$1.69^{+0.11}_{-0.08}$	3.07 ± 2.64	3.33 ± 3.00	0 ± 0	592 ± 66
EPIC 211945201b	19.491	$3.749^{+0.127}_{-0.058}$	$5.67^{+0.28}_{-0.21}$	6.43 ± 7.65	0.20 ± 0.22	$23.6^{+4.3}_{-23.6}$	101 ± 12
EPIC 212357477b	6.327	$2.017^{+0.127}_{-0.050}$	$2.09^{+0.15}_{-0.09}$	7.42 ± 3.34	4.17 ± 2.13	$0.33^{+0.48}_{-0.33}$	195 ± 21
EPIC 213546283b	9.771	$2.853^{+0.171}_{-0.083}$	$3.59^{+0.26}_{-0.17}$	8.50 ± 9.23	0.97 ± 1.10	$7.4^{+2.3}_{-7.4}$	168 ± 18
EPIC 216494238b	19.895	$5.362^{+0.077}_{-0.038}$	7.48 ± 0.31	49.14 ± 6.39	0.64 ± 0.12	48.2 ± 3.9	69.4 ± 10.0
EPIC 229004835b	16.139	$1.899^{+0.115}_{-0.065}$	$2.07^{+0.15}_{-0.10}$	18.29 ± 5.30	10.91 ± 3.88	0 ± 0	68.9 ± 7.4
EPIC 245943455b	6.339	$3.791^{+0.192}_{-0.072}$	$3.76^{+0.25}_{-0.17}$	4.37 ± 5.33	0.44 ± 0.56	$9.1^{+2.3}_{-9.1}$	138 ± 16
EPIC 245991048b	8.583	$1.957^{+0.101}_{-0.049}$	$2.33^{+0.15}_{-0.10}$	7.99 ± 5.26	3.33 ± 2.27	$0.84^{+0.95}_{-0.62}$	179 ± 20
EPIC 247418783b	2.225	$1.561^{+0.122}_{-0.044}$	$1.53^{+0.13}_{-0.07}$	$6.49^{+4.75}_{-7.42}$	9.43 ± 8.23	0 ± 0	633 ± 71
GJ 3470b	3.337	7.642 ± 0.037	4.31 ± 0.18	9.98 ± 1.12	0.69 ± 0.11	$15.9^{+1.5}_{-2.1}$	36.7 ± 6.8
GJ 436b	2.644	8.22 ± 0.11	3.89 ± 0.17	17.99 ± 2.41	1.69 ± 0.32	$10.0^{+2.0}_{-1.4}$	$36.3^{+10.3}_{-7.8}$
GJ 9827b	1.209	$2.387^{+0.155}_{-0.064}$	$1.59^{+0.12}_{-0.07}$	3.74 ± 0.49	$5.11^{+1.33}_{-0.93}$	0 ± 0	310 ± 35
GJ 9827c	3.648	$1.926^{+0.132}_{-0.071}$	$1.28^{+0.10}_{-0.06}$	1.47 ± 0.58	3.82 ± 1.69	0 ± 0	71.4 ± 7.9
GJ 9827d	6.201	$2.601^{+0.173}_{-0.091}$	$1.73^{+0.13}_{-0.08}$	2.38 ± 0.70	2.52 ± 0.88	$0.31^{+0.23}_{-0.16}$	35.0 ± 4.0
HAT-P-11b	4.888	$5.782^{+0.035}_{-0.017}$	4.90 ± 0.24	23.16 ± 1.57	1.08 ± 0.17	19.0 ± 2.6	93 ± 13
HAT-P-26b	4.235	7.37 ± 0.12	6.84 ± 0.31	18.40 ± 2.19	0.32 ± 0.06	42.5 ± 3.3	183 ± 20
HD 106315b	9.550	$1.692^{+0.108}_{-0.076}$	$2.35^{+0.17}_{-0.13}$	8.26 ± 2.56	3.48 ± 1.29	0.97 ± 0.58	277 ± 29
HD 106315c	21.056	$3.090^{+0.071}_{-0.038}$	4.29 ± 0.16	16.22 ± 3.27	1.09 ± 0.25	13.6 ± 1.6	96 ± 10
HD 219134b	3.093	1.89 ± 0.49	1.51 ± 0.45	4.67 ± 0.19	7.43 ± 6.63	0 ± 0	180 ± 36
HD 219134c	6.765	1.78 ± 0.44	1.43 ± 0.41	4.32 ± 0.22	8.20 ± 7.02	0 ± 0	64 ± 12
HD 3167b	0.960	$1.830^{+0.224}_{-0.088}$	$1.75^{+0.23}_{-0.11}$	4.95 ± 0.39	$5.08^{+2.01}_{-1.01}$	0 ± 0	1620 ± 177
HD 3167c	29.845	$3.12^{+0.51}_{-0.24}$	$2.98^{+0.50}_{-0.25}$	9.71 ± 1.26	$2.02^{+1.06}_{-0.57}$	4.9 ± 2.5	16.6 ± 1.8
HD 89345b	11.815	$3.663^{+0.215}_{-0.078}$	$6.99^{+0.49}_{-0.29}$	34.70 ± 3.48	0.53 ± 0.10	$43.1^{+3.6}_{-5.6}$	231 ± 31
HD 97658b	9.490	3.06 ± 0.14	2.51 ± 0.15	7.42 ± 0.72	2.58 ± 0.53	2.04 ± 0.79	55.4 ± 6.2
HIP 116454b	9.120	3.11 ± 0.17	2.60 ± 0.18	12.19 ± 1.42	3.82 ± 0.90	$1.80^{+1.09}_{-0.84}$	53.7 ± 6.2
K2-10b	19.306	$3.724^{+0.088}_{-0.047}$	3.88 ± 0.17	25.21 ± 9.42	2.31 ± 0.95	$9.1^{+2.4}_{-1.9}$	42.0 ± 4.6
K2-100b	1.674	$2.669^{+0.074}_{-0.030}$	3.57 ± 0.15	-1.53 ± 20.21	-0.06 ± 2.49	0^{+3}_{-0}	2078 ± 207
K2-105b	8.267	$3.395^{+0.126}_{-0.053}$	$3.35^{+0.18}_{-0.14}$	15.52 ± 4.52	2.18 ± 0.75	6.0 ± 1.5	99 ± 11
K2-106b	0.571	$1.676^{+0.096}_{-0.042}$	$1.82^{+0.13}_{-0.08}$	8.02 ± 0.98	7.10 ± 1.50	0 ± 0	4741 ± 515
K2-106c	13.339	$2.692^{+0.134}_{-0.077}$	$2.92^{+0.19}_{-0.14}$	5.01 ± 3.12	0.92 ± 0.64	4.5 ± 1.2	71.1 ± 7.8
K2-108b	4.734	$2.879^{+0.149}_{-0.058}$	$5.52^{+0.38}_{-0.26}$	54.69 ± 4.94	1.74 ± 0.34	18.1 ± 2.7	767 ± 94
K2-110b	13.864	$3.293^{+0.110}_{-0.047}$	$2.55^{+0.14}_{-0.11}$	17.12 ± 3.15	5.52 ± 1.30	$1.11^{+0.81}_{-0.52}$	25.3 ± 3.0
K2-111b	5.352	$1.332^{+0.063}_{-0.038}$	$1.28^{+0.12}_{-0.09}$	5.51 ± 2.35	$13.41^{+7.95}_{-5.88}$	0 ± 0	256 ± 33
K2-121b	5.186	$10.127^{+0.176}_{-0.081}$	7.46 ± 0.38	51.68 ± 11.09	0.67 ± 0.18	47.8 ± 5.4	62.7 ± 9.0
K2-131b	0.369	$2.04^{+0.44}_{-0.16}$	$1.63^{+0.36}_{-0.15}$	6.62 ± 1.39	$8.44^{+5.81}_{-2.89}$	0 ± 0	3680 ± 434
K2-141b	0.280	2.037 ± 0.046	1.53 ± 0.06	5.04 ± 0.42	7.72 ± 1.13	0 ± 0	3009 ± 328
K2-18b	32.941	$5.066^{+0.161}_{-0.092}$	2.59 ± 0.13	7.51 ± 1.60	2.36 ± 0.62	3.4 ± 1.0	1.49 ± 0.35
K2-180b	8.866	$3.207^{+0.162}_{-0.079}$	$2.23^{+0.13}_{-0.09}$	7.40 ± 3.23	3.57 ± 1.64	$0.81^{+0.80}_{-0.43}$	48.3 ± 5.2
K2-181b	6.894	$2.479^{+0.189}_{-0.081}$	$2.87^{+0.25}_{-0.15}$	11.72 ± 17.71	2.51 ± 4.07	$1.4^{+2.7}_{-1.4}$	192 ± 22
K2-189b	2.588	$1.575^{+0.089}_{-0.049}$	$1.51^{+0.10}_{-0.07}$	4.51 ± 3.70	6.71 ± 5.62	0 ± 0	497 ± 55
K2-189c	6.679	$2.596^{+0.151}_{-0.059}$	$2.49^{+0.18}_{-0.11}$	4.85 ± 5.59	1.40 ± 1.91	1.3 ± 1.3	140 ± 16
K2-19b	7.919	$7.446^{+0.070}_{-0.044}$	6.64 ± 0.30	27.59 ± 4.81	0.52 ± 0.11	$39.9^{+3.5}_{-5.0}$	87 ± 10
K2-19c	11.907	$4.436^{+0.193}_{-0.089}$	$3.96^{+0.25}_{-0.19}$	24.74 ± 6.73	2.20 ± 0.70	$9.5^{+3.0}_{-2.0}$	50.5 ± 5.9
K2-199b	3.225	$2.455^{+0.177}_{-0.064}$	$1.81^{+0.16}_{-0.10}$	7.80 ± 2.13	6.86 ± 2.43	0 ± 0	119 ± 17
K2-199c	7.374	$3.766^{+0.171}_{-0.069}$	$2.78^{+0.19}_{-0.14}$	10.94 ± 2.70	2.64 ± 0.85	3.0 ± 1.2	39.6 ± 5.7
K2-214b	8.597	$1.824^{+0.100}_{-0.053}$	$2.46^{+0.17}_{-0.12}$	2.68 ± 6.43	0.82 ± 2.31	$0.79^{+1.41}_{-0.79}$	238 ± 26
K2-216b	2.175	$2.197^{+0.169}_{-0.064}$	$1.68^{+0.14}_{-0.07}$	5.81 ± 1.73	6.44 ± 2.36	0 ± 0	207 ± 23
K2-220b	13.682	$2.153^{+0.125}_{-0.061}$	$2.41^{+0.17}_{-0.11}$	0.12 ± 4.08	0.02 ± 1.55	0^{+2}_{-0}	79.7 ± 8.8
K2-222b	15.386	$2.017^{+0.138}_{-0.066}$	$2.40^{+0.19}_{-0.11}$	6.18 ± 2.63	2.30 ± 1.08	$1.72^{+1.06}_{-0.75}$	97.4 ± 10.0
K2-229b	0.584	$1.485^{+0.221}_{-0.084}$	$1.25^{+0.19}_{-0.09}$	2.57 ± 0.43	$7.20^{+3.55}_{-1.91}$	0 ± 0	2289 ± 265
K2-24b	20.885	$4.356^{+0.085}_{-0.040}$	5.50 ± 0.22	15.99 ± 2.91	0.53 ± 0.13	$27.2^{+1.8}_{-2.6}$	52.2 ± 6.2
K2-24c	42.363	$5.978^{+0.099}_{-0.054}$	7.55 ± 0.30	13.27 ± 4.44	0.16 ± 0.06	$51.2^{+5.2}_{-3.7}$	20.4 ± 2.4
K2-27b	6.771	$4.808^{+0.131}_{-0.058}$	4.59 ± 0.21	26.96 ± 5.16	1.47 ± 0.35	15.6 ± 2.3	116 ± 13
K2-3b	10.054	$3.513^{+0.210}_{-0.084}$	$2.10^{+0.15}_{-0.09}$	5.28 ± 0.84	$3.14^{+0.85}_{-0.63}$	$0.85^{+0.54}_{-0.40}$	11.7 ± 1.7
K2-3c	24.644	$2.882^{+0.231}_{-0.098}$	$1.72^{+0.15}_{-0.09}$	1.56 ± 0.89	1.68 ± 1.03	$0.47^{+0.43}_{-0.29}$	3.57 ± 0.52

Table 6.6 (cont'd)

Name	Per	$R_p/R_\star$	R_P	M_P	ρ_p	$f_{\rm env}$	$S_{\rm inc}$
K2-3d	44.560	$2.35^{+0.17}_{-0.12}$	$1.40^{+0.12}_{-0.09}$	-0.68 ± 1.62	-1.36 ± 3.23	0 ± 0	1.62 ± 0.24
K2-32b	8.992	$5.606^{+0.107}_{-0.049}$	5.23 ± 0.22	15.46 ± 2.01	0.59 ± 0.11	23.9 ± 2.4	79.3 ± 8.7
K2-32c	20.661	$3.346^{+0.148}_{-0.070}$	$3.12^{+0.19}_{-0.14}$	4.50 ± 2.47	0.79 ± 0.46	6.1 ± 1.3	26.3 ± 2.9
K2-32d	31.717	$3.708^{+0.241}_{-0.078}$	$3.46^{+0.26}_{-0.15}$	12.27 ± 2.99	1.58 ± 0.49	8.2 ± 1.8	14.8 ± 1.6
K2-36b	1.423	$1.690^{+0.107}_{-0.049}$	$1.32^{+0.10}_{-0.07}$	9.34 ± 3.86	21.03 ± 9.65	0 ± 0	493 ± 59
K2-36c	5.341	$3.156^{+0.330}_{-0.089}$	$2.47^{+0.28}_{-0.12}$	7.70 ± 5.88	2.51 ± 2.14	$1.19^{+1.63}_{-0.99}$	84 ± 10
K2-37b	4.443	$1.654^{+0.124}_{-0.058}$	$1.46^{+0.12}_{-0.08}$	-0.98 ± 5.34	-1.75 ± 9.43	0 ± 0	192 ± 21
K2-37c	6.430	$2.872^{+0.181}_{-0.069}$	$2.53^{+0.19}_{-0.11}$	5.00 ± 5.24	1.54 ± 1.73	1.6 ± 1.6	118 ± 13
K2-37d	14.092	$2.753^{+0.247}_{-0.082}$	$2.43^{+0.24}_{-0.12}$	12.59 ± 6.26	4.33 ± 2.69	$0.95^{+1.27}_{-0.69}$	41.3 ± 4.5
K2-38b	4.017	$1.420^{+0.103}_{-0.049}$	$1.75^{+0.23}_{-0.16}$	6.45 ± 1.99	$6.21^{+3.82}_{-2.52}$	0 ± 0	476 ± 72
K2-38c	10.561	$2.008^{+0.135}_{-0.060}$	$2.48^{+0.32}_{-0.22}$	7.73 ± 2.71	$2.61^{+1.71}_{-1.13}$	$1.8^{+1.6}_{-1.2}$	131 ± 20
K2-39b	4.605	$1.800^{+0.114}_{-0.048}$	$6.05^{+0.47}_{-0.31}$	42.19 ± 6.85	1.03 ± 0.26	19.8 ± 2.9	1374 ± 204
K2-55b	2.849	$5.58^{+0.22}_{-0.10}$	$4.31^{+0.23}_{-0.17}$	44.46 ± 4.47	2.99 ± 0.51	$9.9^{+2.4}_{-1.6}$	125 ± 13
K2-61b	2.573	$1.733^{+0.098}_{-0.048}$	$1.88^{+0.13}_{-0.09}$	0.22 ± 7.90	0.04 ± 6.03	0 ± 0	728 ± 85
K2-62b	6.672	$2.602^{+0.217}_{-0.075}$	$1.98^{+0.18}_{-0.09}$	-0.99 ± 4.28	-0.54 ± 2.82	0^{+1}_{-0}	46.6 ± 5.0
K2-62c	16.197	$2.555^{+0.242}_{-0.091}$	$1.94^{+0.20}_{-0.09}$	1.12 ± 5.72	1.10 ± 3.89	0 ± 0	14.3 ± 1.5
K2-66b	5.069	$1.515^{+0.087}_{-0.053}$	$2.96^{+0.25}_{-0.19}$	16.31 ± 3.93	3.33 ± 1.14	1.77 ± 0.90	984 ± 123
K2-73b	7.496	$2.270^{+0.110}_{-0.049}$	$2.62^{+0.16}_{-0.11}$	7.63 ± 3.74	2.12 ± 1.13	$2.13^{+1.02}_{-0.71}$	209 ± 22
K2-79b	10.995	$2.890^{+0.082}_{-0.050}$	3.93 ± 0.17	4.09 ± 4.40	0.35 ± 0.39	$10.2^{+2.1}_{-10.2}$	174 ± 20
K2-98b	10.137	$3.015^{+0.076}_{-0.041}$	5.14 ± 0.24	30.80 ± 21.69	1.17 ± 0.90	17.9 ± 2.6	339 ± 41
KOI-142b	10.954	$3.863^{+0.041}_{-0.310}$	$3.90^{+0.16}_{-0.34}$	8.71 ± 2.58	0.81 ± 0.29	11.8 ± 2.3	72.8 ± 8.1
Kepler-10b	0.837	$1.255^{+0.026}_{-0.015}$	1.49 ± 0.06	3.08 ± 0.27	5.12 ± 0.77	0 ± 0	3960 ± 402
Kepler-10c	45.294	$1.981^{+0.033}_{-0.013}$	2.35 ± 0.09	7.05 ± 1.23	2.98 ± 0.62	1.68 ± 0.54	19.3 ± 2.0
Kepler-100b	6.887	$0.80820^{+0.00080}_{-0.06320}$	$1.37^{+0.05}_{-0.12}$	5.91 ± 2.52	12.78 ± 5.99	0 ± 0	478 ± 57
Kepler-100c	12.816	$1.407^{+0.159}_{-0.049}$	$2.38^{+0.28}_{-0.12}$	0.64 ± 3.19	0.26 ± 1.31	0^{+2}_{-0}	209 ± 25
Kepler-100d	35.333	$0.962^{+0.198}_{-0.054}$	$1.63^{+0.34}_{-0.11}$	-3.93 ± 5.47	-5.04 ± 7.39	0 ± 0	54.1 ± 6.5
Kepler-101b	3.488	$3.2422^{+0.0231}_{-0.0080}$	6.23 ± 0.26	49.07 ± 5.34	1.12 ± 0.18	$22.5^{+2.0}_{-2.8}$	1201 ± 145
Kepler-102d	10.312	$1.656^{+0.018}_{-0.146}$	$1.33^{+0.06}_{-0.13}$	4.00 ± 1.71	9.31 ± 4.49	0 ± 0	35.5 ± 4.2
Kepler-102e	16.146	$3.064^{+0.027}_{-0.257}$	$2.47^{+0.11}_{-0.23}$	9.19 ± 2.04	$3.38^{+0.85}_{-1.22}$	$1.63^{+1.27}_{-0.78}$	19.6 ± 2.3
Kepler-103b	15.965	$2.128^{+0.014}_{-0.110}$	$3.54^{+0.13}_{-0.22}$	9.88 ± 8.53	1.23 ± 1.08	$7.2^{+1.7}_{-4.3}$	151 ± 18
Kepler-103c	179.612	$3.495^{+0.100}_{-0.193}$	$5.81^{+0.27}_{-0.38}$	37.69 ± 25.70	1.06 ± 0.74	$27.9^{+7.1}_{-3.9}$	6.00 ± 0.73
Kepler-105c	7.126	$1.512^{+0.032}_{-0.219}$	$1.73^{+0.07}_{-0.26}$	3.60 ± 1.30	$3.85^{+1.48}_{-2.22}$	0 ± 0	237 ± 25
Kepler-106c	13.571	$2.391^{+0.041}_{-0.263}$	$2.77^{+0.12}_{-0.32}$	9.87 ± 3.07	2.55 ± 1.03	2.7 ± 1.3	101 ± 11
Kepler-106e	43.844	$2.5934^{+0.0027}_{-0.3042}$	$3.01^{+0.11}_{-0.37}$	10.56 ± 5.32	2.14 ± 1.22	$3.9^{+2.2}_{-1.7}$	21.2 ± 2.3
Kepler-11d	22.684	$2.802^{+0.055}_{-0.018}$	3.42 ± 0.14	$7.79^{+0.88}_{-1.64}$	$1.07^{+0.18}_{-0.26}$	7.5 ± 1.1	51.6 ± 5.6
Kepler-11e	32.000	$3.611^{+0.025}_{-0.214}$	$4.41^{+0.17}_{-0.30}$	$8.47^{+1.65}_{-2.27}$	$0.55^{+0.12}_{-0.19}$	15.8 ± 2.3	32.6 ± 3.5
Kepler-11f	46.689	2.206 ± 0.041	2.69 ± 0.11	2.15 ± 0.95	0.61 ± 0.28	$3.55^{+0.73}_{-1.20}$	19.7 ± 2.1
Kepler-113b	4.754	$2.6463^{+0.0091}_{-0.1978}$	$2.22^{+0.11}_{-0.20}$	11.72 ± 4.03	5.94 ± 2.41	$0.37^{+0.65}_{-0.37}$	97 ± 13
Kepler-131b	16.092	$1.918^{+0.172}_{-0.063}$	$2.12^{+0.21}_{-0.10}$	15.91 ± 3.03	$9.20^{+3.18}_{-2.23}$	0 ± 0	63.1 ± 7.0
Kepler-138c	13.781	$2.593^{+0.220}_{-0.073}$	$1.52^{+0.14}_{-0.07}$	$4.60^{+0.71}_{-0.95}$	$7.23^{+2.31}_{-1.79}$	0 ± 0	7.2 ± 1.1
Kepler-138d	23.088	$2.258^{+0.033}_{-0.047}$	1.32 ± 0.05	1.03 ± 0.22	2.45 ± 0.61	$0.156^{+0.059}_{-0.156}$	3.60 ± 0.52
Kepler-1655b	11.873	$1.9838^{+0.0054}_{-0.2721}$	$2.29^{+0.08}_{-0.32}$	4.95 ± 2.88	2.28 ± 1.50	$1.00^{+1.04}_{-0.57}$	134 ± 14
Kepler-177b	36.855	$2.420^{+0.088}_{-0.045}$	3.77 ± 0.22	5.40 ± 0.95	0.55 ± 0.14	$11.9^{+1.5}_{-2.2}$	43.9 ± 5.1
Kepler-18b	3.505	1.76 ± 0.16	1.82 ± 0.18	6.90 ± 3.40	6.27 ± 3.60	0 ± 0	344 ± 39
Kepler-18d	14.859	$5.1590^{+0.0075}_{-0.0570}$	5.33 ± 0.21	16.40 ± 1.40	0.60 ± 0.09	25.9 ± 2.2	50.2 ± 5.7
Kepler-19b	9.287	$2.378^{+0.035}_{-0.011}$	2.31 ± 0.09	8.40 ± 1.55	3.77 ± 0.82	$0.85^{+0.52}_{-0.35}$	97 ± 10
Kepler-20b	3.696	$1.763^{+0.038}_{-0.011}$	1.73 ± 0.07	9.48 ± 1.34	10.10 ± 1.88	0 ± 0	319 ± 35
Kepler-20c	10.854	$2.960^{+0.149}_{-0.052}$	$2.90^{+0.18}_{-0.12}$	12.47 ± 2.11	$2.81^{+0.73}_{-0.56}$	3.5 ± 1.0	75.9 ± 8.4
Kepler-20d	77.611	$2.568^{+0.060}_{-0.027}$	2.52 ± 0.10	9.67 ± 3.74	3.33 ± 1.36	$2.09^{+1.18}_{-0.81}$	5.51 ± 0.61
Kepler-21b	2.786	$0.8919^{+0.0063}_{-0.1163}$	$1.89^{+0.07}_{-0.25}$	5.11 ± 1.62	$4.15^{+1.43}_{-2.10}$	0 ± 0	2893 ± 335
Kepler-22b	289.862	$2.423^{+0.095}_{-0.324}$	$2.24^{+0.12}_{-0.31}$	44.47 ± 62.49	21.74 ± 31.33	0 ± 0	0.97 ± 0.10
Kepler-223b	7.384	$1.777^{+0.260}_{-0.084}$	$3.38^{+0.56}_{-0.29}$	8.10 ± 1.16	$1.15^{+0.60}_{-0.33}$	5.3 ± 2.4	530 ± 76
Kepler-223c	9.846	$1.969^{+0.380}_{-0.075}$	$3.75^{+0.78}_{-0.30}$	$5.57^{+1.76}_{-1.21}$	$0.58^{+0.41}_{-0.19}$	9.0 ± 3.6	360 ± 53
Kepler-223d	14.789	$2.536^{+0.076}_{-0.035}$	4.83 ± 0.38	8.80 ± 1.36	0.43 ± 0.12	19.2 ± 3.0	209 ± 30
Kepler-26b	12.283	$4.823^{+0.049}_{-0.024}$	3.14 ± 0.12	6.31 ± 0.60	1.13 ± 0.17	6.6 ± 1.1	11.7 ± 1.4
Kepler-26c	17.256	4.50 ± 0.36	2.93 ± 0.26	6.31 ± 0.60	1.39 ± 0.39	5.2 ± 1.9	7.43 ± 0.91
Kepler-279c	35.735	$2.954^{+0.071}_{-0.316}$	$4.64^{+0.21}_{-0.52}$	$7.40^{+2.20}_{-1.50}$	0.41 ± 0.15	13.9 ± 3.4	68.7 ± 6.8
Kepler-279d	54.414	$2.745^{+0.029}_{-0.412}$	$4.31^{+0.17}_{-0.67}$	$4.50^{+1.20}_{-0.90}$	$0.31^{+0.09}_{-0.16}$	10.9 ± 3.1	39.3 ± 3.9
Kepler-29b	10.338	$3.133^{+0.080}_{-0.043}$	2.67 ± 0.15	3.49 ± 1.10	1.01 ± 0.36	3.40 ± 0.93	63.6 ± 7.6
Kepler-29c	13.288	$2.928^{+0.079}_{-0.048}$	2.49 ± 0.14	3.08 ± 0.96	1.10 ± 0.39	2.66 ± 0.85	45.5 ± 5.6
Kepler-30b	29.334	$2.018^{+0.076}_{-0.154}$	$1.90^{+0.12}_{-0.17}$	8.80 ± 0.55	$7.12^{+1.49}_{-2.00}$	0 ± 0	17.7 ± 2.2
Kepler-305d	16.739	$2.97^{+0.58}_{-0.15}$	$2.63^{+0.53}_{-0.19}$	$9.10^{+6.10}_{-3.80}$	$2.74^{+2.48}_{-1.30}$	$2.3^{+2.6}_{-1.7}$	25.7 ± 3.1

Table 6.6 (cont'd)

Name	Per	$R_p/R_\star$	R_P	M_P	ρ_p	$f_{\rm env}$	$S_{\rm inc}$
Kepler-307b	10.421	$2.79^{+0.24}_{-0.17}$	$2.98^{+0.28}_{-0.21}$	7.58 ± 0.86	$1.58^{+0.49}_{-0.38}$	4.9 ± 1.5	91 ± 10
Kepler-307c	13.073	$2.51^{+0.25}_{-0.18}$	$2.68^{+0.29}_{-0.22}$	3.73 ± 0.60	$1.07^{+0.39}_{-0.31}$	$3.9^{+1.0}_{-1.5}$	67.8 ± 7.5
Kepler-310d	92.876	$2.885^{+0.014}_{-0.497}$	$2.73^{+0.11}_{-0.48}$	7.00 ± 3.75	$1.89^{+0.95}_{-1.50}$	3.4 ± 2.0	4.16 ± 0.44
Kepler-33d	21.776	$2.573^{+0.031}_{-0.013}$	4.84 ± 0.20	4.10 ± 1.85	0.20 ± 0.09	17.6 ± 1.9	126 ± 16
Kepler-33e	31.784	$1.921^{+0.050}_{-0.021}$	3.61 ± 0.16	5.50 ± 1.15	0.64 ± 0.16	$9.32^{+0.84}_{-1.14}$	76.1 ± 9.7
Kepler-33f	41.029	$2.119^{+0.042}_{-0.017}$	3.99 ± 0.17	9.60 ± 1.75	0.83 ± 0.19	$12.6^{+1.3}_{-1.9}$	54.3 ± 7.1
Kepler-359c	57.688	$4.49^{+0.10}_{-0.74}$	$4.40^{+0.41}_{-0.80}$	$2.90^{+2.40}_{-1.90}$	0.19 ± 0.16	$11.7^{+6.3}_{-9.3}$	9.8 ± 1.4
Kepler-36b	13.840	$0.840^{+0.027}_{-0.018}$	1.54 ± 0.07	3.90 ± 0.20	5.93 ± 0.87	0 ± 0	252 ± 27
Kepler-36c	16.239	$2.0452^{+0.0203}_{-0.0074}$	3.74 ± 0.14	7.50 ± 0.30	0.79 ± 0.09	9.9 ± 1.1	204 ± 22
Kepler-4b	3.213	$2.4470^{+0.0140}_{-0.0055}$	4.15 ± 0.16	23.00 ± 3.75	1.77 ± 0.35	7.28 ± 0.91	1242 ± 157
Kepler-406b	2.426	$1.327^{+0.112}_{-0.086}$	$1.58^{+0.15}_{-0.12}$	5.99 ± 1.27	8.32 ± 2.74	0 ± 0	834 ± 91
Kepler-454b	10.574	$1.7524^{+0.0017}_{-0.1673}$	$2.08^{+0.08}_{-0.21}$	6.66 ± 1.34	$4.07^{+0.95}_{-1.48}$	$0.44^{+0.55}_{-0.30}$	118 ± 13
Kepler-48d	42.896	$2.097^{+0.060}_{-0.023}$	1.96 ± 0.09	24.76 ± 16.17	18.11 ± 12.09	0 ± 0	8.9 ± 1.0
Kepler-49b	7.204	$3.824^{+0.050}_{-0.023}$	2.62 ± 0.10	8.00 ± 1.75	2.46 ± 0.61	2.70 ± 0.79	25.4 ± 3.1
Kepler-49c	10.913	$3.62^{+0.32}_{-0.20}$	$2.47^{+0.24}_{-0.16}$	5.90 ± 1.50	2.15 ± 0.76	2.4 ± 1.2	14.6 ± 1.8
Kepler-51b	45.155	$7.207^{+0.039}_{-0.022}$	6.78 ± 0.30	2.30 ± 1.65	0.04 ± 0.03	25^{+11}_{-22}	11.2 ± 1.2
Kepler-549b	42.950	$2.767^{+0.098}_{-0.051}$	2.57 ± 0.13	$11.00^{+4.20}_{-3.20}$	$3.59^{+1.50}_{-1.15}$	$1.89^{+1.24}_{-0.77}$	9.5 ± 1.1
Kepler-56b	10.510	$1.192^{+0.034}_{-0.021}$	5.62 ± 0.31	32.00 ± 10.85	1.00 ± 0.38	18.2 ± 2.1	798 ± 132
Kepler-60d	11.898	$1.185^{+0.304}_{-0.092}$	$1.95^{+0.51}_{-0.17}$	3.90 ± 0.65	$2.91^{+2.33}_{-0.88}$	$0.44^{+0.97}_{-0.44}$	235 ± 25
Kepler-68b	5.399	$1.690^{+0.026}_{-0.011}$	2.32 ± 0.09	5.81 ± 1.67	2.56 ± 0.79	0.86 ± 0.28	435 ± 47
Kepler-78b	0.355	$1.420^{+0.190}_{-0.070}$	$1.16^{+0.16}_{-0.07}$	1.77 ± 0.23	$6.29^{+2.76}_{-1.44}$	0 ± 0	3827 ± 434
Kepler-79e	81.066	$2.079^{+0.509}_{-0.087}$	$3.30^{+0.82}_{-0.19}$	4.56 ± 1.26	$0.70^{+0.55}_{-0.22}$	$7.2^{+2.3}_{-3.2}$	19.0 ± 2.0
Kepler-80d	3.072	$2.100^{+0.062}_{-0.016}$	$1.65^{+0.07}_{-0.06}$	$3.70^{+0.80}_{-0.60}$	$4.56^{+1.17}_{-0.87}$	0 ± 0	133 ± 15
Kepler-80e	4.645	$2.155^{+0.059}_{-0.033}$	1.69 ± 0.07	2.10 ± 0.70	2.39 ± 0.85	$0.23^{+0.17}_{-0.23}$	76.3 ± 8.3
Kepler-85e	25.215	$1.251^{+0.140}_{-0.059}$	$1.23^{+0.15}_{-0.08}$	$0.60^{+0.50}_{-0.40}$	$1.80^{+1.63}_{-1.25}$	0 ± 0	23.7 ± 2.7
Kepler-89b	3.743	$1.031^{+0.048}_{-0.022}$	$1.60^{+0.09}_{-0.07}$	9.27 ± 4.07	12.40 ± 5.76	0 ± 0	1012 ± 116
Kepler-89c	10.424	$2.5563^{+0.0305}_{-0.0046}$	3.98 ± 0.14	13.54 ± 9.68	1.19 ± 0.86	$9.5^{+1.7}_{-1.3}$	259 ± 30
Kepler-89e	54.320	$4.178^{+0.011}_{-0.093}$	6.50 ± 0.25	32.23 ± 19.52	0.65 ± 0.40	36.2 ± 3.9	28.6 ± 3.3
Kepler-93b	4.727	$1.5943^{+0.0040}_{-0.0836}$	$1.64^{+0.06}_{-0.10}$	3.92 ± 0.66	4.93 ± 1.12	0 ± 0	290 ± 31
Kepler-94b	2.508	$3.911^{+0.040}_{-0.264}$	$3.33^{+0.11}_{-0.25}$	10.68 ± 1.39	$1.59^{+0.25}_{-0.42}$	6.3 ± 1.5	201 ± 19
Kepler-95b	11.523	$2.029^{+0.027}_{-0.013}$	3.19 ± 0.13	12.35 ± 2.30	2.10 ± 0.46	$5.24^{+1.24}_{-0.89}$	184 ± 22
Kepler-96b	16.238	$2.546^{+0.026}_{-0.203}$	$2.65^{+0.10}_{-0.23}$	9.13 ± 4.38	2.72 ± 1.42	$1.98^{+1.43}_{-0.91}$	56.2 ± 6.0
Kepler-97b	2.587	$1.361^{+0.015}_{-0.032}$	1.48 ± 0.06	3.24 ± 1.70	5.51 ± 2.97	0 ± 0	794 ± 89
Kepler-98b	1.542	$1.579^{+0.014}_{-0.046}$	1.61 ± 0.07	3.16 ± 1.47	4.19 ± 2.02	0 ± 0	1086 ± 121
Kepler-99b	4.604	1.868 ± 0.043	1.57 ± 0.08	6.20 ± 1.27	8.82 ± 2.29	0 ± 0	99 ± 14
WASP-47d	9.031	$2.961^{+0.268}_{-0.082}$	$3.69^{+0.37}_{-0.18}$	12.77 ± 1.52	1.33 ± 0.32	9.4 ± 2.2	145 ± 17
WASP-47e	0.790	$1.484^{+0.146}_{-0.046}$	$1.85^{+0.20}_{-0.10}$	7.35 ± 0.75	6.10 ± 1.47	0 ± 0	3744 ± 438

CHAPTER 7
CONCLUSION

The work compiled in this thesis improves our understanding of the compositional diversity of small planets, and the processes that govern their formation and evolution. By nearly doubling of the number of small planets with measured masses, we were able to explore the transition from rocky to gaseous planets and its dependence on environmental parameters like temperature and host-star properties.

In Chapter 2, we provided a review of the formation of small planets and the future detectability of planets smaller than Earth. The occurrence patterns and compositions of these "sub-Earths" will be studied by future generations of telescopes. So far, we've only been able to measure the masses and compositions of the three sub-Earths in the Solar system, Mercury, Venus, and Mars.

Following the prime *Kepler* mission, *K2* enabled us to discover hundreds of small planets orbiting bright stars. These discoveries required a large collaborative effort. Countless hours were spent examining the *K2* photometry for planet candidates and conducting follow-up spectroscopic and AO imaging observations in order to validate them and precisely characterize their host stars. With each new *K2* campaign, new catalogs of bona-fide planets were assembled, including the catalog of eleven multi-planet systems presented in Chapter 3. There, we also quantified the *K2* "multiplicity boost", demonstrating that in the first two *K2* campaigns, planet candidates in multi-candidate systems were a priori ~ 25 times less likely to be false positives than those in single-candidate systems. This boost was used to validate several planet candidates.

Dozens of planets in these new *K2* catalogs orbit stars bright enough for Doppler observations. Over the course of three years, we took RV measurements of more than 50 planet hosts, and developed tools to model our RV time-series to estimate planet masses (Fulton et al., 2018). Chapters 3–5 feature mass measurements and compositional constraints of nine of these planets in four different systems. K2-38 hosts a hot super-Earth likely to have been stripped of its H/He envelope by photoevaporation and a cooler sub-Neptune, which has retained at least part of its envelope. Similarly, K2-106 hosts an ultra-short-period planet with an Earth-like composition and a cooler sub-Neptune companion. K2-66 is a subgiant star that hosts a sub-Neptune that is particularly dense for its size, comprised of a $\sim 15 M_{\oplus}$ core. Finally, WASP-47 is one of the few stars with a Hot-Jupiter in close proximity to sub-Neptune-size planets — an ultra-short-period planet with an Earth-like composition and a sub-Neptune with a similar mass, which orbits beyond the hot-Jupiter. There is also a giant planet on a several year eccentric orbit, which might have played a role in the formation of the inner planets.

Leveraging the dozens of new mass measurements made by our collaboration, this thesis culminates in Chapter 6 with the construction and analysis of a catalog of nearly all of the planets 1–8 $R_{\oplus}$ with measured masses — 139 planets in total. We derived stellar temperatures and metallicities from HIRES spectra of all 101 host stars, and determined precise stellar radii using our spectroscopic constraints in conjunction with Gaia parallaxes. To further minimize systematic biases in our planet radii, adopted transit parameters for each planet using a consistent methodology for all *Kepler*, *K2*, and other planets.

This constitutes the most comprehensive and precise catalog of small planet masses to date and we use it study the bulk compositions of small planets with greater fidelity. The concurrent discovery of a gap in the planet radius distribution by the California Kepler Survey (Fulton et al., 2017), and follow-up theoretical work by Owen & Wu (2017), suggested that photoevaporation is an important sculptor of planet bulk compositions, and provided us a framework within which to analyze and interpret the mass-radius relationship.

We discover a gap in the planet density-radius distribution, separating two distinct populations — "super-Earths" consisting of 1–2 $R_\oplus$ cores with little to no gas, and "sub-Neptunes" with H/He envelopes comprising $\gtrsim$ 1% of their total mass. The gap between these populations would be occupied by cores with <1% H/He, indicating that such planets are completely stripped of their envelopes by photoevaporation. We also observe a population of cooler super-Earths, which have lower densities, suggesting that their lower levels of irradiation have enabled the preservation of their H/He envelopes.

The typical core of a small planet is 6–9 $M_\oplus$ or slightly less considering potential detection biases. At orbital periods less than 3 days, cores do not exceed 10 $M_\oplus$. Beyond 3 days, the majority of cores are <10 $M_\oplus$. Some sub-Saturns, particularly those orbiting metal-rich stars, have cores as large as $40 M_\oplus$. After analyzing the measured density-radius distribution of super-Earth cores, and accounting for our measurement errors, we conclude that small planet cores likely have a diversity of bulk compositions. The majority of them may have Earth-like compositions, but not all of them. Assuming admixtures of iron and rock, we find the median core rock fraction is 82% — slightly less iron-rich than Earth (70%). Alternatively, if these cores are admixtures of rock and water, then less than 20% of them are more than 10% water by mass. The lack of water in these cores suggests that most of them formed interior to the ice-line.

Finally, we discover a positive correlation between the core masses of small planets and the metallicities of their host stars. Metallicities are a better predictor of core mass than stellar mass. Even though both parameters have been linked to the availability of solid-material in the protoplanetary disk, it appears that the assembly of planet cores is more sensitive to stellar metallicity than stellar mass.

This thesis constitutes an important milestone in the understanding of the compositions of small planets. We have many more planet hunting and planet characterization missions to look forward to in the next few years. TESS will find nearly all of the nearby transiting planets orbiting close to their host stars, and JWST will allow precise characterization of the atmospheres of small planets, offering new clues about their formation and evolution.

BIBLIOGRAPHY

Adams, E. R., Jackson, B., & Endl, M. 2016a, AJ, 152, 47

Adams, E. R., Seager, S., & Elkins-Tanton, L. 2008, ApJ, 673, 1160

Adams, E. R., Jackson, B., Endl, M., et al. 2016b, ArXiv e-prints, arXiv:1611.00397

Agnor, C. B., & Hamilton, D. P. 2006, Nature, 441, 192

Agol, E., Steffen, J., Sari, R., & Clarkson, W. 2005, MNRAS, 359, 567

Ahn, C. P., Alexandroff, R., Allende Prieto, C., et al. 2012, ApJS, 203, 21

Ahrens, T. J. 1993, Annual Review of Earth and Planetary Sciences, 21, 525

Akeson, R. L., Chen, X., Ciardi, D., et al. 2013, PASP, 125, 989

Alibert, Y., Mordasini, C., & Benz, W. 2011, A&A, 526, A63

Almenara, J. M., Díaz, R. F., Bonfils, X., & Udry, S. 2016, A&A, 595, L5

Almenara, J. M., Díaz, R. F., Dorn, C., Bonfils, X., & Udry, S. 2018, MNRAS, 478, 460

Almenara, J. M., Astudillo-Defru, N., Bonfils, X., et al. 2015, A&A, 581, L7

Andrews, S. M., Rosenfeld, K. A., Kraus, A. L., & Wilner, D. J. 2013, ArXiv e-prints, arXiv:1305.5262

Armstrong, D. J., Santerne, A., Veras, D., et al. 2015, A&A, 582, A33

Bailes, M., Bates, S. D., Bhalerao, V., et al. 2011, Science, 333, 1717

Baranec, C., Ziegler, C., Law, N. M., et al. 2016, AJ, 152, 18

Baranec, C., Riddle, R., Law, N. M., et al. 2013, Journal of Visualized Experiments, 72, e50021

—. 2014, ApJ, 790, L8

Barclay, T., Rowe, J. F., Lissauer, J. J., et al. 2013, Nature, 494, 452

Barros, S. C. C., Demangeon, O., & Deleuil, M. 2016, A&A, 594, A100

Barros, S. C. C., Almenara, J. M., Demangeon, O., et al. 2015, MNRAS, 454, 4267

Barry, R., Kruk, J., Anderson, J., et al. 2011, in Society of Photo-Optical Instrumentation Engineers (SPIE) Conference Series, Vol. 8151, Society of Photo-Optical Instrumentation Engineers (SPIE) Conference Series

Batalha, N. M., Borucki, W. J., Bryson, S. T., et al. 2011, ApJ, 729, 27

Batalha, N. M., Rowe, J. F., Bryson, S. T., et al. 2013, ApJS, 204, 24

Batygin, K., Bodenheimer, P. H., & Laughlin, G. P. 2016, ApJ, 829, 114

Batygin, K., & Morbidelli, A. 2013, AJ, 145, 1

Bean, J. L., Seifahrt, A., Hartman, H., et al. 2010, ApJ, 713, 410

Becker, J. C., Vanderburg, A., Adams, F. C., Rappaport, S. A., & Schwengeler, H. M. 2015, ApJ, 812, L18

Beichman, C., Livingston, J., Werner, M., et al. 2016, ApJ, 822, 39

Bennett, D. P. 2008, Detection of Extrasolar Planets by Gravitational Microlensing, ed. J. W. Mason (Praxis Publishing Ltd.), 47

Bennett, D. P., & Rhie, S. H. 1996, ApJ, 472, 660

—. 2002, ApJ, 574, 985

Benz, W., Anic, A., Horner, J., & Whitby, J. A. 2007, Space Sci. Rev., 132, 189

Benz, W., Slattery, W. L., & Cameron, A. G. W. 1988, Icarus, 74, 516

Berger, T. A., Huber, D., Gaidos, E., & van Saders, J. L. 2018, ArXiv e-prints, arXiv:1805.00231

Blum, J., & Wurm, G. 2000, Icarus, 143, 138

Borucki, W. J., Koch, D., Basri, G., et al. 2010, Science, 327, 977

Borucki, W. J., Koch, D. G., Basri, G., et al. 2011, ApJ, 736, 19

Borucki, W. J., Agol, E., Fressin, F., et al. 2013, Science, 340, 587

Bouchy, F., Díaz, R. F., Hébrard, G., et al. 2013, A&A, 549, A49

Bovy, J., Rix, H.-W., Green, G. M., Schlafly, E. F., & Finkbeiner, D. P. 2016, ApJ, 818, 130

Boyajian, T. S., von Braun, K., van Belle, G., et al. 2012, ApJ, 757, 112

Brewer, J. M., & Fischer, D. A. 2018, ArXiv e-prints, arXiv:1804.00673

Brewer, J. M., Fischer, D. A., Basu, S., Valenti, J. A., & Piskunov, N. 2015, ApJ, 805, 126

Brewer, J. M., Fischer, D. A., Valenti, J. A., & Piskunov, N. 2016, ApJS, 225, 32

Brown, T. M., Charbonneau, D., Gilliland, R. L., Noyes, R. W., & Burrows, A. 2001, ApJ, 552, 699

Brown, T. M., Latham, D. W., Everett, M. E., & Esquerdo, G. A. 2011, AJ, 142, 112

Bruntt, H., Deleuil, M., Fridlund, M., et al. 2010, A&A, 519, A51

Buchhave, L. A., Latham, D. W., Johansen, A., et al. 2012, Nature, 486, 375

Buchhave, L. A., Bizzarro, M., Latham, D. W., et al. 2014, Nature, 509, 593

Burke, C. J., Bryson, S. T., Mullally, F., et al. 2014, ApJS, 210, 19

Burke, C. J., Christiansen, J. L., Mullally, F., et al. 2015, ApJ, 809, 8

Butler, R. P., Marcy, G. W., Williams, E., et al. 1996, PASP, 108, 500

Butler, R. P., Tinney, C. G., Marcy, G. W., et al. 2001, ApJ, 555, 410

Cameron, A. G. W. 1985, Icarus, 64, 285

Canup, R. M., & Ward, W. R. 2006, Nature, 441, 834

Carter, J. A., Agol, E., Chaplin, W. J., et al. 2012, Science, 337, 556

Chambers, J. 2006, Icarus, 180, 496

Charpinet, S., Fontaine, G., Brassard, P., et al. 2011, Nature, 480, 496

Chen, H., & Rogers, L. A. 2016, ApJ, 831, 180

Chiang, E., & Laughlin, G. 2013, MNRAS, 431, 3444

Chiang, E., & Youdin, A. N. 2010, Annual Review of Earth and Planetary Sciences, 38, 493

Ciardi, D. R., Beichman, C. A., Horch, E. P., & Howell, S. B. 2015, ApJ, 805, 16

Clampin, M. C. 2012, in Society of Photo-Optical Instrumentation Engineers (SPIE) Conference Series, Vol. 8442, Society of Photo-Optical Instrumentation Engineers (SPIE) Conference Series

Claret, A., Hauschildt, P. H., & Witte, S. 2012, A&A, 546, A14

—. 2013, A&A, 552, A16

Coelho, P., Barbuy, B., Meléndez, J., Schiavon, R. P., & Castilho, B. V. 2005, A&A, 443, 735

Colón, K. D., Ford, E. B., & Morehead, R. C. 2012, MNRAS, 426, 342

Cosentino, R., Lovis, C., Pepe, F., et al. 2012, in Society of Photo-Optical Instrumentation Engineers (SPIE) Conference Series, Vol. 8446, Society of Photo-Optical Instrumentation Engineers (SPIE) Conference Series

Cowan, N. B., & Agol, E. 2011, ApJ, 729, 54

Cox, A. N., & Pilachowski, C. A. 2000, Physics Today, 53, 100000

Crepp, J. R., Johnson, J. A., Howard, A. W., et al. 2012, ApJ, 761, 39

Crossfield, I. J. M., Petigura, E., Schlieder, J. E., et al. 2015, ApJ, 804, 10

Crossfield, I. J. M., Ciardi, D. R., Petigura, E. A., et al. 2016, ApJS, 226, 7

Ćuk, M., & Burns, J. A. 2004, AJ, 128, 2518

Cushing, M. C., Rayner, J. T., & Vacca, W. D. 2005, ApJ, 623, 1115

Cushing, M. C., Vacca, W. D., & Rayner, J. T. 2004, PASP, 116, 362

Dai, F., Winn, J. N., Arriagada, P., et al. 2015, ApJ, 813, L9

Dai, F., Winn, J. N., Albrecht, S., et al. 2016, ArXiv e-prints, arXiv:1604.01413

Dalgarno, A., & Smith, F. J. 1962, Planetary and Space Science, 9, 1

Dawson, R. I., & Fabrycky, D. C. 2010, ApJ, 722, 937

Dawson, R. I., Murray-Clay, R. A., & Johnson, J. A. 2015, ApJ, 798, 66

Deck, K. M., Agol, E., Holman, M. J., & Nesvorný, D. 2014, ApJ, 787, 132

Dekany, R., Roberts, J., Burruss, R., et al. 2013, ApJ, 776, 130

Demory, B.-O., Gillon, M., Madhusudhan, N., & Queloz, D. 2016, MNRAS, 455, 2018

Demory, B.-O., Gillon, M., Seager, S., et al. 2012, ApJ, 751, L28

Dong, S., Xie, J.-W., Zhou, J.-L., Zheng, Z., & Luo, A. 2018, Proceedings of the National Academy of Science, 115, 266

Dotter, A., Chaboyer, B., Jevremović, D., et al. 2008, ApJS, 178, 89

Dressing, C. D., Charbonneau, D., Dumusque, X., et al. 2015, ApJ, 800, 135

Dressler, A., Spergel, D., Mountain, M., et al. 2012, ArXiv e-prints, arXiv:1210.7809

Dumusque, X., Udry, S., Lovis, C., Santos, N. C., & Monteiro, M. J. P. F. G. 2011, A&A, 525, A140

Dumusque, X., Pepe, F., Lovis, C., et al. 2012, Nature, 491, 207

Eastman, J., Gaudi, B. S., & Agol, E. 2013, PASP, 125, 83

Ebel, D. S., & Alexander, C. M. O. 2011, Planetary and Space Science, 59, 1888

Elkins-Tanton, L. T., & Seager, S. 2008, ApJ, 685, 1237

Elser, S., Moore, B., Stadel, J., & Morishima, R. 2011, Icarus, 214, 357

Endl, M., Kürster, M., & Els, S. 2000, A&A, 362, 585

Esteves, L. J., De Mooij, E. J. W., & Jayawardhana, R. 2015, ApJ, 804, 150

Fabrycky, D. C., Lissauer, J. J., Ragozzine, D., et al. 2014, ApJ, 790, 146

Fang, J., & Margot, J.-L. 2012, ApJ, 761, 92

—. 2013, ApJ, 767, 115

Fegley, B., & Cameron, A. G. W. 1987, Earth and Planetary Science Letters, 82, 207

Feiden, G. A., & Chaboyer, B. 2012, ApJ, 757, 42

Fischer, D. A., & Valenti, J. 2005, ApJ, 622, 1102

Fischer, D. A., Marcy, G. W., Butler, R. P., et al. 2008, ApJ, 675, 790

Fogg, M. J., & Nelson, R. P. 2007, A&A, 472, 1003

Ford, E. B. 2006, ApJ, 642, 505

Ford, E. B., Rowe, J. F., Fabrycky, D. C., et al. 2011, ApJS, 197, 2

Foreman-Mackey, D., Hogg, D. W., Lang, D., & Goodman, J. 2013, PASP, 125, 306

Foreman-Mackey, D., Montet, B. T., Hogg, D. W., et al. 2015, ApJ, 806, 215

Fortney, J. J., Marley, M. S., & Barnes, J. W. 2007, ApJ, 659, 1661

Fortney, J. J., Mordasini, C., Nettelmann, N., et al. 2013, ApJ, 775, 80

Fressin, F., Torres, G., Rowe, J. F., et al. 2012, Nature, 482, 195

Fressin, F., Torres, G., Charbonneau, D., et al. 2013, ApJ, 766, 81

Fulton, B. J., & Petigura, E. A. 2018, ArXiv e-prints, arXiv:1805.01453

Fulton, B. J., Petigura, E. A., Blunt, S., & Sinukoff, E. 2018, PASP, 130, 044504

Fulton, B. J., Shporer, A., Winn, J. N., et al. 2011, AJ, 142, 84

Fulton, B. J., Collins, K. A., Gaudi, B. S., et al. 2015, ApJ, 810, 30

Fulton, B. J., Petigura, E. A., Howard, A. W., et al. 2017, AJ, 154, 109

Furlan, E., Ciardi, D. R., Everett, M. E., et al. 2017, AJ, 153, 71

Gaia Collaboration, Brown, A. G. A., Vallenari, A., et al. 2018, ArXiv e-prints, arXiv:1804.09365

Gaidos, E., Fischer, D. A., Mann, A. W., & Lépine, S. 2012, ApJ, 746, 36

Gaidos, E., & Williams, D. M. 2004, New Astronomy, 10, 67

Gelman, A., & Rubin, D. B. 1992, Statist. Sci., 7, 457

Gilliland, R. L., Chaplin, W. J., Dunham, E. W., et al. 2011, ApJS, 197, 6

Ginzburg, S., & Sari, R. 2015, ApJ, 803, 111

Ginzburg, S., Schlichting, H. E., & Sari, R. 2018, MNRAS, 476, 759

Gladman, B. 1993, Icarus, 106, 247

Gladman, B., & Coffey, J. 2009, Meteoritics and Planetary Science, 44, 285

Goldreich, P., & Soter, S. 1966, Icarus, 5, 375

Gong, Y.-X., Zhou, J.-L., Xie, J.-W., & Wu, X.-M. 2013, ApJ, 769, L14

Gonzalez, G. 1997, MNRAS, 285, 403

Goodman, J., & Weare, J. 2010, Communications in Applied Mathematics and Computational Science, 5, 65

Grasset, O., Schneider, J., & Sotin, C. 2009, ApJ, 693, 722

Grunblatt, S. K., Howard, A. W., & Haywood, R. D. 2015, arXiv:1501.00369, arXiv:1501.00369

Guilloteau, S., Dutrey, A., Piétu, V., & Boehler, Y. 2011, A&A, 529, A105

Hadden, S., & Lithwick, Y. 2014, ApJ, 787, 80

—. 2017, AJ, 154, 5

Haghighipour, N. 2013, Annual Review of Earth and Planetary Sciences, 41, 469

Hansen, B. M. S., & Murray, N. 2012, ApJ, 751, 158

—. 2013, ApJ, 775, 53

Hansen, B. M. S., Shih, H.-Y., & Currie, T. 2009, ApJ, 691, 382

Hansen, B. M. S., & Zink, J. 2015, MNRAS, 450, 4505

Hatzes, A. P. 2013, ApJ, 770, 133

Hauck, S. A., Margot, J.-L., Solomon, S. C., et al. 2013, Journal of Geophysical Research (Planets), 118, 1204

Hayashi, C. 1981, Progress of Theoretical Physics Supplement, 70, 35

Haywood, R. D., Collier Cameron, A., Queloz, D., et al. 2014, MNRAS, 443, 2517

Hébrard, G., Lecavelier Des Étangs, A., Vidal-Madjar, A., Désert, J.-M., & Ferlet, R. 2004, in Astronomical Society of the Pacific Conference Series, Vol. 321, Extrasolar Planets: Today and Tomorrow, ed. J. Beaulieu, A. Lecavelier Des Etangs, & C. Terquem, 203

Heller, R. 2018, ArXiv e-prints, arXiv:1806.06601

Hellier, C., Anderson, D. R., Collier Cameron, A., et al. 2012, MNRAS, 426, 739

Henning, W. G., O'Connell, R. J., & Sasselov, D. D. 2009, ApJ, 707, 1000

Hirano, T., Narita, N., Sato, B., et al. 2012, ApJ, 759, L36

Holczer, T., Mazeh, T., Nachmani, G., et al. 2016, ApJS, 225, 9

Holman, M. J., & Murray, N. W. 2005, Science, 307, 1288

Howard, A. W., & Fulton, B. J. 2016, PASP, 128, 114401

Howard, A. W., Johnson, J. A., Marcy, G. W., et al. 2009, ApJ, 696, 75

—. 2010a, ApJ, 721, 1467

Howard, A. W., Marcy, G. W., Johnson, J. A., et al. 2010b, Science, 330, 653

Howard, A. W., Marcy, G. W., Bryson, S. T., et al. 2012, ApJS, 201, 15

Howard, A. W., Sanchis-Ojeda, R., Marcy, G. W., et al. 2013, Nature, 503, 381

Howard, A. W., Marcy, G. W., Fischer, D. A., et al. 2014, ApJ, 794, 51

Howell, S. B., Sobeck, C., Haas, M., et al. 2014, PASP, 126, 398

Huang, C., Wu, Y., & Triaud, A. H. M. J. 2016, ApJ, 825, 98

Huber, D., Zinn, J., Bojsen-Hansen, M., et al. 2017, ApJ, 844, 102

Hunten, D. M. 1982, Planetary and Space Science, 30, 773

Ida, S., & Lin, D. N. C. 2010, ApJ, 719, 810

Isaacson, H., & Fischer, D. 2010, ApJ, 725, 875

Isella, A., Carpenter, J. M., & Sargent, A. I. 2009, ApJ, 701, 260

Jackson, B., Jensen, E., Peacock, S., Arras, P., & Penev, K. 2016, Celestial Mechanics and Dynamical Astronomy, 126, 227

Jenkins, J. M., Caldwell, D. A., Chandrasekaran, H., et al. 2010, ApJ, 713, L87

Jin, S., Mordasini, C., Parmentier, V., et al. 2014, ApJ, 795, 65

Johnson, J. A., Petigura, E. A., Fulton, B. J., et al. 2017, AJ, 154, 108

Johnson, R. E. 2010, ApJ, 716, 1573

Jontof-Hutter, D., Ford, E. B., Rowe, J. F., et al. 2016, ApJ, 820, 39

Kaiser, N., Burgett, W., Chambers, K., et al. 2010, in Society of Photo-Optical Instrumentation Engineers (SPIE) Conference Series, Vol. 7733, Society of Photo-Optical Instrumentation Engineers (SPIE) Conference Series, 0

Kambe, E., Ando, H., Sato, B., et al. 2008, PASJ, 60, 45

Kass, R. E., & Raftery, A. E. 1995, Journal of the American Statistical Association, 90, 773

Kasting, J. F., & Pollack, J. B. 1983, Icarus, 53, 479

Kennedy, G. M., & Kenyon, S. J. 2008, ApJ, 682, 1264

Kenyon, S. J., & Bromley, B. C. 2006, AJ, 131, 1837

Kipping, D. M. 2013, MNRAS, 435, 2152

Kipping, D. M., Fossey, S. J., & Campanella, G. 2009, MNRAS, 400, 398

Kipping, D. M., Hartman, J., Buchhave, L. A., et al. 2013, ArXiv e-prints, arXiv:1301.1853

Knutson, H. A., Fulton, B. J., Montet, B. T., et al. 2014, ApJ, 785, 126

Koch, D. G., Borucki, W. J., Basri, G., et al. 2010, ApJ, 713, L79

Kokubo, E., & Ida, S. 1998, Icarus, 131, 171

—. 2000, Icarus, 143, 15

Kokubo, E., Kominami, J., & Ida, S. 2006, ApJ, 642, 1131

Kolbl, R., Marcy, G. W., Isaacson, H., & Howard, A. W. 2015, AJ, 149, 18

Kraus, A. L., & Hillenbrand, L. A. 2007, AJ, 134, 2340

Kraus, A. L., Ireland, M. J., Huber, D., Mann, A. W., & Dupuy, T. J. 2016, AJ, 152, 8

Kreidberg, L. 2015, PASP, 127, 1161

Kubas, D., Beaulieu, J. P., Bennett, D. P., et al. 2012, A&A, 540, A78

Kuchner, M. J. 2003, ApJ, 596, L105

Lai, D. 2012, MNRAS, 423, 486

Lainey, V. 2016, Celestial Mechanics and Dynamical Astronomy, 126, 145

Law, N. M., Morton, T., Baranec, C., et al. 2014, ApJ, 791, 35

Lee, E. J., & Chiang, E. 2016, ApJ, 817, 90

—. 2017, ArXiv e-prints, arXiv:1702.08461

Léger, A., Selsis, F., Sotin, C., et al. 2004, Icarus, 169, 499

Léger, A., Rouan, D., Schneider, J., et al. 2009, A&A, 506, 287

Léger, A., Grasset, O., Fegley, B., et al. 2011, Icarus, 213, 1

Lewis, J. S. 1972, Earth and Planetary Science Letters, 15, 286

Lewis, N. K., Showman, A. P., Fortney, J. J., et al. 2010, ApJ, 720, 344

Li, C.-H., Glenday, A. G., Phillips, D. F., et al. 2012, in Society of Photo-Optical Instrumentation Engineers (SPIE) Conference Series, Vol. 8446, Society of Photo-Optical Instrumentation Engineers (SPIE) Conference Series

Liddle, A. R. 2007, MNRAS, 377, L74

Lillo-Box, J., Barrado, D., & Bouy, H. 2012, A&A, 546, A10

—. 2014, A&A, 566, A103

Lin, D. N. C., Bodenheimer, P., & Richardson, D. C. 1996, Nature, 380, 606

Lissauer, J. J., Fabrycky, D. C., Ford, E. B., et al. 2011a, Nature, 470, 53

Lissauer, J. J., Ragozzine, D., Fabrycky, D. C., et al. 2011b, ApJS, 197, 8

Lissauer, J. J., Marcy, G. W., Rowe, J. F., et al. 2012, ApJ, 750, 112

Lissauer, J. J., Marcy, G. W., Bryson, S. T., et al. 2014, ApJ, 784, 44

Lithwick, Y., & Wu, Y. 2012, ApJ, 756, L11

Lithwick, Y., Xie, J., & Wu, Y. 2012, ApJ, 761, 122

Lopez, E. D. 2017, MNRAS, 472, 245

Lopez, E. D., & Fortney, J. J. 2013, ApJ, 776, 2

—. 2014, ApJ, 792, 1

Lopez, E. D., Fortney, J. J., & Miller, N. 2012, ApJ, 761, 59

Lovis, C., Mayor, M., Pepe, F., et al. 2006, Nature, 441, 305

Lucy, L. B., & Sweeney, M. A. 1971, AJ, 76, 544

Luger, R., Agol, E., Kruse, E., et al. 2016, AJ, 152, 100

Luger, R., Kruse, E., Foreman-Mackey, D., Agol, E., & Saunders, N. 2017, ArXiv e-prints, arXiv:1702.05488

Lundkvist, M. S., Kjeldsen, H., Albrecht, S., et al. 2016, Nature Communications, 7, 11201

Maciejewski, G., Dimitrov, D., Seeliger, M., et al. 2013, A&A, 551, A108

Mandel, K., & Agol, E. 2002, ApJ, 580, L171

Mandell, A. M., Raymond, S. N., & Sigurdsson, S. 2007, ApJ, 660, 823

Mann, A. W., Gaidos, E., & Ansdell, M. 2013a, ApJ, 779, 188

Mann, A. W., Gaidos, E., Kraus, A., & Hilton, E. J. 2013b, ApJ, 770, 43

Mann, A. W., Gaidos, E., Lépine, S., & Hilton, E. J. 2012, ApJ, 753, 90

Mann, A. W., Gaidos, E., Vanderburg, A., et al. 2017, AJ, 153, 64

Mao, S., & Paczynski, B. 1991, ApJ, 374, L37

Marcus, R. A., Sasselov, D., Hernquist, L., & Stewart, S. T. 2010, ApJ, 712, L73

Marcy, G. W., & Butler, R. P. 1992, PASP, 104, 270

Marcy, G. W., Weiss, L. M., Petigura, E. A., et al. 2014a, Proceedings of the National Academy of Science, 111, 12655

Marcy, G. W., Isaacson, H., Howard, A. W., et al. 2014b, ApJS, 210, 20

Mayor, M., & Queloz, D. 1995, Nature, 378, 355

Mazeh, T., Holczer, T., & Faigler, S. 2016, A&A, 589, A75

McArthur, B. E., Endl, M., Cochran, W. D., et al. 2004, ApJ, 614, L81

Meunier, N., Desort, M., & Lagrange, A.-M. 2010, A&A, 512, A39

Middelkoop, F. 1982, A&A, 107, 31

Miguel, Y., Kaltenegger, L., Fegley, B., & Schaefer, L. 2011, ApJ, 742, L19

Miller, M. C., & Hamilton, D. P. 2001, ApJ, 550, 863

Miralda-Escudé, J. 2002, ApJ, 564, 1019

Montet, B. T., Johnson, J. A., Muirhead, P. S., et al. 2015a, ApJ, 800, 134

Montet, B. T., Morton, T. D., Foreman-Mackey, D., et al. 2015b, ApJ, 809, 25

Montgomery, R., & Laughlin, G. 2009, Icarus, 202, 1

Morbidelli, A., Lunine, J. I., O'Brien, D. P., Raymond, S. N., & Walsh, K. J. 2012, Annual Review of Earth and Planetary Sciences, 40, 251

Mortier, A., Santos, N. C., Sousa, S. G., et al. 2013, A&A, 558, A106

Morton, T. D. 2012, ApJ, 761, 6

—. 2015a, isochrones: Stellar model grid package, Astrophysics Source Code Library, , , ascl:1503.010

—. 2015b, isochrones: Stellar model grid package, Astrophysics Source Code Library, , , ascl:1503.010

Morton, T. D., & Johnson, J. A. 2011, ApJ, 738, 170

Muirhead, P. S., Hamren, K., Schlawin, E., et al. 2012a, ApJ, 750, L37

Muirhead, P. S., Johnson, J. A., Apps, K., et al. 2012b, ApJ, 747, 144

Mulders, G. D., Pascucci, I., Apai, D., Frasca, A., & Molenda-Żakowicz, J. 2016, AJ, 152, 187

Mullally, F., Coughlin, J. L., Thompson, S. E., et al. 2015, ApJS, 217, 31

Naoz, S., Farr, W. M., Lithwick, Y., Rasio, F. A., & Teyssandier, J. 2011, Nature, 473, 187

Narita, N., Hirano, T., Fukui, A., et al. 2015, ApJ, 815, 47

Nelson, B. E., Ford, E. B., Wright, J. T., et al. 2014, MNRAS, 441, 442

Neveu-VanMalle, M., Queloz, D., Anderson, D. R., et al. 2016, A&A, 586, A93

Newton, E. R., Charbonneau, D., Irwin, J., & Mann, A. W. 2015, ApJ, 800, 85

Newville, M., Stensitzki, T., Allen, D. B., & Ingargiola, A. 2014, LMFIT: Non-Linear Least-Square Minimization and Curve-Fitting for Python, , , doi:10.5281/zenodo.11813

Noyes, R. W., Hartmann, L. W., Baliunas, S. L., Duncan, D. K., & Vaughan, A. H. 1984, ApJ, 279, 763

O'Brien, D. P., Morbidelli, A., & Levison, H. F. 2006, Icarus, 184, 39

O'Toole, S. J., Tinney, C. G., Jones, H. R. A., et al. 2009, MNRAS, 392, 641

Owen, J. E., & Wu, Y. 2013, ApJ, 775, 105

—. 2017, ApJ, 847, 29

Pál, A. 2012, MNRAS, 420, 1630

Pasquini, L., Cristiani, S., García López, R., et al. 2010, in Society of Photo-Optical Instrumentation Engineers (SPIE) Conference Series, Vol. 7735, Society of Photo-Optical Instrumentation Engineers (SPIE) Conference Series

Penny, M. T., Kerins, E., Rattenbury, N., et al. 2012, ArXiv e-prints, arXiv:1206.5296

Pepe, F., Cameron, A. C., Latham, D. W., et al. 2013, Nature, 503, 377

Pepe, F. A., Cristiani, S., Rebolo Lopez, R., et al. 2010, in Society of Photo-Optical Instrumentation Engineers (SPIE) Conference Series, Vol. 7735, Society of Photo-Optical Instrumentation Engineers (SPIE) Conference Series

Peplowski, P. N., Evans, L. G., Hauck, S. A., et al. 2011, Science, 333, 1850

Petigura, E. A. 2015, PhD thesis, University of California, Berkeley, arXiv:1510.03902

Petigura, E. A., Howard, A. W., & Marcy, G. W. 2013a, Proceedings of the National Academy of Science, 110, 19273

Petigura, E. A., & Marcy, G. W. 2012, PASP, 124, 1073

Petigura, E. A., Marcy, G. W., & Howard, A. W. 2013b, ApJ, 770, 69

Petigura, E. A., Schlieder, J. E., Crossfield, I. J. M., et al. 2015, ApJ, 811, 102

Petigura, E. A., Howard, A. W., Lopez, E. D., et al. 2016, ApJ, 818, 36

Petigura, E. A., Sinukoff, E., Lopez, E., et al. 2017a, ArXiv e-prints, arXiv:1702.00013

Petigura, E. A., Howard, A. W., Marcy, G. W., et al. 2017b, AJ, 154, 107

Petigura, E. A., Marcy, G. W., Winn, J. N., et al. 2018, AJ, 155, 89

Phillips, J. A., & Thorsett, S. E. 1994, Ap&SS, 212, 91

Pierrehumbert, R., & Gaidos, E. 2011, ApJ, 734, L13

Pont, F., Gilliland, R. L., Moutou, C., et al. 2007, A&A, 476, 1347

Pope, B. J. S., Parviainen, H., & Aigrain, S. 2016, MNRAS, 461, 3399

Porter, S. B., & Grundy, W. M. 2011, ApJ, 736, L14

Powell, M. J. D. 1964, The Computer Journal, 7, 155

Queloz, D., Bouchy, F., Moutou, C., et al. 2009, A&A, 506, 303

Radovan, M. V., Cabak, G. F., Laiterman, L. H., Lockwood, C. T., & Vogt, S. S. 2010, in Society of Photo-Optical Instrumentation Engineers (SPIE) Conference Series, Vol. 7735, Society of Photo-Optical Instrumentation Engineers (SPIE) Conference Series

Ragozzine, D., & Holman, M. J. 2010, ArXiv e-prints, arXiv:1006.3727

Rappaport, S., Levine, A., Chiang, E., et al. 2012, ApJ, 752, 1

Rasio, F. A., & Ford, E. B. 1996, Science, 274, 954

Raymond, S. N., Barnes, R., & Mandell, A. M. 2008, MNRAS, 384, 663

Raymond, S. N., Mandell, A. M., & Sigurdsson, S. 2006, Science, 313, 1413

Raymond, S. N., O'Brien, D. P., Morbidelli, A., & Kaib, N. A. 2009, Icarus, 203, 644

Raymond, S. N., Scalo, J., & Meadows, V. S. 2007, ApJ, 669, 606

Rayner, J. T., Cushing, M. C., & Vacca, W. D. 2009, ApJS, 185, 289

Rayner, J. T., Toomey, D. W., Onaka, P. M., et al. 2003, PASP, 115, 362

Reid, I. N. 2002, PASP, 114, 306

Reiners, A., Bean, J. L., Huber, K. F., et al. 2010, ApJ, 710, 432

Ribas, I., Guinan, E. F., Güdel, M., & Audard, M. 2005, ApJ, 622, 680

Rice, K. 2015, arXiv:1501.03304, arXiv:1501.03304

Rivera, E. J., Lissauer, J. J., Butler, R. P., et al. 2005, ApJ, 634, 625

Rogers, L. A. 2015, ApJ, 801, 41

Rogers, L. A., Bodenheimer, P., Lissauer, J. J., & Seager, S. 2011, ApJ, 738, 59

Rogers, L. A., & Seager, S. 2010, ApJ, 712, 974

Rojas-Ayala, B., Covey, K. R., Muirhead, P. S., & Lloyd, J. P. 2012, ApJ, 748, 93

Rowe, J. F., Bryson, S. T., Marcy, G. W., et al. 2014, ApJ, 784, 45

Rowe, J. F., Coughlin, J. L., Antoci, V., et al. 2015, ApJS, 217, 16

Rupprecht, G., Pepe, F., Mayor, M., et al. 2004, in Society of Photo-Optical Instrumentation Engineers (SPIE) Conference Series, Vol. 5492, Society of Photo-Optical Instrumentation Engineers (SPIE) Conference Series, ed. A. F. M. Moorwood & M. Iye, 148–159

Sanchis-Ojeda, R., Rappaport, S., Winn, J. N., et al. 2014, ApJ, 787, 47

—. 2013, ApJ, 774, 54

Sanchis-Ojeda, R., Fabrycky, D. C., Winn, J. N., et al. 2012, Nature, 487, 449

Sanchis-Ojeda, R., Winn, J. N., Dai, F., et al. 2015, ApJ, 812, L11

Santos, N. C., Israelian, G., & Mayor, M. 2004, A&A, 415, 1153

Sanz-Forcada, J., Micela, G., Ribas, I., et al. 2011, A&A, 532, A6

Sasaki, T., Stewart, G. R., & Ida, S. 2010, ApJ, 714, 1052

Schlaufman, K. C. 2015, ApJ, 799, L26

Schlaufman, K. C., & Winn, J. N. 2016, ApJ, 825, 62

Schmitt, J. R., Wang, J., Fischer, D. A., et al. 2014, AJ, 148, 28

Schneider, J., Dedieu, C., Le Sidaner, P., Savalle, R., & Zolotukhin, I. 2011, A&A, 532, A79

Schwab, C., Spronck, J. F. P., Tokovinin, A., et al. 2012, in Society of Photo-Optical Instrumentation Engineers (SPIE) Conference Series, Vol. 8446, Society of Photo-Optical Instrumentation Engineers (SPIE) Conference Series

Schwarz, G. 1978, Ann. Statist., 6, 461

Seager, S., Kuchner, M., Hier-Majumder, C. A., & Militzer, B. 2007, ApJ, 669, 1279

Sigurdsson, S. 1993, ApJ, 415, L43

Sinukoff, E., Fulton, B., Scuderi, L., & Gaidos, E. 2013, Space Sci. Rev., 180, 71

Sinukoff, E., Howard, A. W., Petigura, E. A., et al. 2016, ApJ, 827, 78

—. 2017a, AJ, 153, 271

—. 2017b, AJ, 153, 70

Skrutskie, M. F., Cutri, R. M., Stiening, R., et al. 2006, AJ, 131, 1163

Socrates, A., Katz, B., Dong, S., & Tremaine, S. 2012, ApJ, 750, 106

Sohl, F., Schubert, G., & Spohn, T. 2005, Journal of Geophysical Research (Planets), 110, 12008

Southworth, J. 2011, MNRAS, 417, 2166

Southworth, J., Maxted, P. F. L., & Smalley, B. 2004, MNRAS, 351, 1277

Spronck, J. F. P., Fischer, D. A., Kaplan, Z. A., & Schwab, C. 2012, in Society of Photo-Optical Instrumentation Engineers (SPIE) Conference Series, Vol. 8446, Society of Photo-Optical Instrumentation Engineers (SPIE) Conference Series

Steffen, J. H., Ragozzine, D., Fabrycky, D. C., et al. 2012, Proceedings of the National Academy of Science, 109, 7982

Steinmetz, T., Wilken, T., Araujo-Hauck, C., et al. 2008, Science, 321, 1335

Stevenson, K. B., Harrington, J., Lust, N. B., et al. 2012, ApJ, 755, 9

Tanaka, H., & Ida, S. 1999, Icarus, 139, 350

Tenenbaum, P., Christiansen, J. L., Jenkins, J. M., et al. 2012, ApJS, 199, 24

Terquem, C., & Papaloizou, J. C. B. 2007, ApJ, 654, 1110

Terrien, R. C., Mahadevan, S., Bender, C. F., et al. 2012, ApJ, 747, L38

Thompson, S. E., Coughlin, J. L., Hoffman, K., et al. 2018, ApJS, 235, 38

Tian, F. 2009, ApJ, 703, 905

Torres, G., Andersen, J., & Giménez, A. 2010, A&A Rev., 18, 67

Tully, C., & Johnson, R. E. 2001, Planetary and Space Science, 49, 533

Vacca, W. D., Cushing, M. C., & Rayner, J. T. 2003, PASP, 115, 389

Valencia, D., Guillot, T., Parmentier, V., & Freedman, R. S. 2013, ApJ, 775, 10

Valencia, D., Ikoma, M., Guillot, T., & Nettelmann, N. 2010, A&A, 516, A20

Valencia, D., Sasselov, D. D., & O'Connell, R. J. 2007, ApJ, 665, 1413

Valenti, J. A., Butler, R. P., & Marcy, G. W. 1995, PASP, 107, 966

Valenti, J. A., & Fischer, D. A. 2005, ApJS, 159, 141

Valsecchi, F., Rappaport, S., Rasio, F. A., Marchant, P., & Rogers, L. A. 2015, ApJ, 813, 101

Valsecchi, F., Rasio, F. A., & Steffen, J. H. 2014, ApJ, 793, L3

van Haaften, L. M., Nelemans, G., Voss, R., & Jonker, P. G. 2012, A&A, 541, A22

Vanderburg, A., Montet, B. T., Johnson, J. A., et al. 2015, ApJ, 800, 59

Vanderburg, A., Latham, D. W., Buchhave, L. A., et al. 2016a, ApJS, 222, 14

Vanderburg, A., Bieryla, A., Duev, D. A., et al. 2016b, ApJ, 829, L9

Vogt, S. S., Allen, S. L., Bigelow, B. C., et al. 1994, in Society of Photo-Optical Instrumentation Engineers (SPIE) Conference Series, Vol. 2198, Instrumentation in Astronomy VIII, ed. D. L. Crawford & E. R. Craine, 362

von Braun, K., Boyajian, T. S., ten Brummelaar, T. A., et al. 2011, ApJ, 740, 49

Walsh, K. J., Morbidelli, A., Raymond, S. N., O'Brien, D. P., & Mandell, A. M. 2011, Nature, 475, 206

Ward, W. R. 1997, Icarus, 126, 261

Weidenschilling, S. J. 1977a, MNRAS, 180, 57

—. 1977b, Ap&SS, 51, 153

—. 1978, Icarus, 35, 99

Weidling, R., Güttler, C., & Blum, J. 2012, Icarus, 218, 688

Weiss, L. M., & Marcy, G. W. 2014, ApJ, 783, L6

Williams, J. P., & Cieza, L. A. 2011, ARA&A, 49, 67

Wilson, O. C. 1968, ApJ, 153, 221

Winn, J. N., Johnson, J. A., Howard, A. W., et al. 2010, ApJ, 718, 575

Winn, J. N., Sanchis-Ojeda, R., Rogers, L., et al. 2017, AJ, 154, 60

Wolfgang, A., & Lopez, E. 2015, ApJ, 806, 183

Wolfgang, A., Rogers, L. A., & Ford, E. B. 2016, ApJ, 825, 19

Wolszczan, A. 1994, Science, 264, 538

—. 2012, New Astronomy Reviews, 56, 2

Wright, J. T. 2005, PASP, 117, 657

Wright, J. T., & Gaudi, B. S. 2012, ArXiv e-prints, arXiv:1210.2471

Wright, J. T., & Howard, A. W. 2009, ApJS, 182, 205

Wright, J. T., Marcy, G. W., Howard, A. W., et al. 2012, ApJ, 753, 160

Wright, J. T., Upadhyay, S., Marcy, G. W., et al. 2009, ApJ, 693, 1084

Wu, Y. 2018, ArXiv e-prints, arXiv:1806.04693

Wu, Y., & Lithwick, Y. 2011, ApJ, 735, 109

Wu, Y., & Murray, N. 2003, ApJ, 589, 605

Wurm, G., Trieloff, M., & Rauer, H. 2013, ApJ, 769, 78

Yee, S. W., Petigura, E. A., & von Braun, K. 2017, ApJ, 836, 77

Youdin, A. N., & Kenyon, S. J. 2013, From Disks to Planets, ed. T. D. Oswalt, L. M. French, & P. Kalas, 1

Zendejas, J., Segura, A., & Raga, A. C. 2010, Icarus, 210, 539

Zeng, L., & Sasselov, D. 2013, PASP, 125, 227

Zhou, J.-L., Aarseth, S. J., Lin, D. N. C., & Nagasawa, M. 2005, ApJ, 631, L85

Ziegler, C., Law, N. M., Morton, T., et al. 2017, AJ, 153, 66

Zsom, A., Ormel, C. W., Güttler, C., Blum, J., & Dullemond, C. P. 2010, A&A, 513, A57